Title
Tuning Magnetic Order in Transition Metal Oxide Thin Films

Author
Grutter, Alexander John

Publication Date
2013

Peer reviewed|Thesis/dissertation

Tuning Magnetic Order in Transition Metal Oxide Thin Films

by

Alexander John Grutter

A dissertation submitted in partial satisfaction of the

requirements for the degree of

Doctor of Philosophy

in

Engineering - Materials Science and Engineering

in the

Graduate Division

of the

University of California, Berkeley

Committee in charge:

Professor Yuri Suzuki, Co-Chair

Professor Oscar Dubon, Co-Chair

Professor Frances Hellman

Professor David Attwood

Fall 2013

Tuning Magnetic Order in Transition Metal Oxide Thin Films

Abstract

Tuning Magnetic Order in Transition Metal Oxide Thin Films

by

Alexander John Grutter

Doctor of Philosophy in Engineering - Materials Science and Engineering

University of California, Berkeley

Professor Yuri Suzuki, Co-Chair

Professor Oscar Dubon, Co-Chair

In recent decades, one of the most active and promising areas of condensed matter research has been that of complex oxides. With the advent of new growth techniques such as pulsed laser deposition and molecular beam epitaxy, a wealth of new magnetic and electronic ground states have emerged in complex oxide heterostructures. The wide variety of ground states in complex oxides is well known and generally attributed to the unprecedented variety of valence, structure, and bonding available in these systems. The tunability of this already diverse playground of states and interactions is greatly multiplied in thin films and heterostructures by the addition of parameters such as substrate induced strain and interfacial electronic reconstruction. Thus, recent studies have shown emergent properties such as the stabilization of ferromagnetism in a paramagnetic system, conductivity at the interface of two insulators, and even exchange bias at the interface between a paramagnet and a ferromagnet. Despite these steps forward, there remains remarkable disagreement on the mechanisms by which these emergent phenomena are stabilized. The contributions of strain, stoichiometry, defects, intermixing, and electronic reconstruction are often very difficult to isolate in thin films and superlattices.

This thesis will present model systems for isolating the effects of strain and interfacial electronic interactions on the magnetic state of complex oxides from alternative contributions. We will focus first on $SrRuO_3$, an ideal system in which to isolate substrate induced strain effects. We explore the effects of structural distortions in the simplest case of growth on (100) oriented substrates. We find that parameters including saturated magnetic moment and Curie temperature are all highly tunable through substrate induced lattice distortions. We also report the stabilization of a nonmagnetic spin-zero configuration of Ru^{4+} in tetragonally distorted films under tensile strain. Through growth on (110) and (111) oriented substrates we explore the effects of different distortion symmetries on $SrRuO_3$ and demonstrate the first reported strain induced transition to a high-spin state of Ru^{4+}. Finally, we examine the effects of strain on $SrRuO_3$ thin films and demonstrate a completely reversible universal out-of-plane magnetic easy axis on films grown on different substrate orientations. Having demonstrated the ability to tune nearly every magnetic parameter of $SrRuO_3$ through strain, we turn to magnetic properties at interfaces.

We study the emergent interfacial ferromagnetism in superlattices of the paramagnetic metal $CaRuO_3$ and the antiferromagnetic insulator $CaMnO_3$ and demonstrate that the interfacial ferromagnetic layer in this system is confined to a single unit cell of $CaMnO_3$ at

the interface. We discuss the remarkable oscillatory dependence of the saturated magnetic moment on the thickness of the $CaMnO_3$ layers and explore mechanisms by which this oscillation may be stabilized. We find long range coherence of the antiferromagnetism of the $CaMnO_3$ layers across intervening layers of paramagnetic $CaRuO_3$. Finally, we utilize the system of $LaNiO_3/CaMnO_3$ to separate the effects of intermixing and interfacial electronic reconstruction and conclusively demonstrate intrinsic interfacial ferromagnetism at the interface between a paramagnetic metal and an antiferromagnetic insulator. We find that the emergent ferromagnetism is stabilized through interfacial double exchange and that the leakage of conduction electrons from the paramagnetic metal to the antiferromagnetic insulator is critical to establishing the ferromagnetic ground state.

To my family

Contents

List of Figures **v**

List of Tables **x**

I Background 1

1 Introduction **2**
1.1 Tunable Ground States in Transition Metal Oxides . . . 2
1.2 Structure and Distortions in Perovskites . . . 3
1.3 Crystal Fields in Perovskite Transition Metal Oxides . . . 5
1.4 Magnetic Coupling in Transition Metal Oxides . . . 8
1.4.1 The Tight Binding Model and The Hubbard Hamiltonian . . . 8
1.4.2 Antiferromagnetic Superexchange . . . 10
1.4.3 Double Exchange . . . 12
1.4.4 Itinerant Ferromagnetism . . . 13
1.4.5 Magnetic Anisotropy . . . 15
1.5 Controlling Magnetism in Transition Metal Oxide Thin Films . . . 16
1.6 Thesis Goals and Chapter Summary . . . 18

2 Experimental Methods **20**
2.1 Thin Film Growth . . . 20
2.1.1 Pulsed Laser Deposition . . . 20
2.1.2 Reflection High Energy Electron Diffraction . . . 22
2.2 Structural Characterization . . . 24
2.2.1 Atomic Force Microscopy . . . 24
2.2.2 X-Ray Diffraction . . . 24
2.2.3 X-Ray Reflectometry . . . 28
2.2.4 Scanning Transmission Electron Microscopy . . . 31
2.3 Stoichiometry and Valence . . . 32
2.3.1 Rutherford Backscattering Spectrometry . . . 32
2.3.2 X-Ray Absorption Spectroscopy . . . 33
2.3.3 Electron Energy Loss Spectroscopy . . . 36
2.4 Magnetic Characterization . . . 36
2.4.1 SQUID Magnetometry . . . 36

2.4.2 X-Ray Magnetic Circular Dichroism . . . 39
2.4.3 Polarized Neutron Reflectometry . . . 40
2.4.4 Neutron Diffraction . . . 42
2.5 Electron Transport . . . 43

II Strain Tuning Magnetism in $SrRuO_3$ 47

3 Tuning Ferromagnetism in $SrRuO_3$ Films Using Epitaxial Strain 48
3.1 An Introduction to $SrRuO_3$ . . . 48
3.2 Sample Growth and Structure . . . 49
3.3 Relationship Between Thin Film Magnetism and Structure . . . 56
3.4 Understanding the Mechanism for Tuning the Saturated Magnetic Moment . 59
3.5 Outlook and Concluding Remarks . . . 66

4 Stabilizing High Spin Ru^{4+} in $SrRuO_3$ 68
4.1 $SrRuO_3$ on (110) and (111) Substrates . . . 68
4.2 Structure and Film Quality . . . 69
4.3 Strain and Magnetism . . . 72
4.4 Probing the Density of States . . . 77
4.5 Discussion and Conclusions . . . 80

5 Tuning Magnetic Anisotropy in $SrRuO_3$ 82
5.1 Magnetocrystalline Anisotropy . . . 82
5.2 Probing Anisotropy Through SQUID Magnetometry . . . 84
5.3 Strain as a Control Variable for Anisotropy . . . 87
5.4 Conclusions and Outlook . . . 90

III Inducing Magnetism at Interfaces in $CaMnO_3$-based Superlattices 92

6 Probing Interfacial Ferromagnetism in $CaRuO_3/CaMnO_3$ Superlattices 93
6.1 An Introduction to Interfacial Ferromagnetism . . . 93
6.2 Samples Studied . . . 96
6.3 Magnetic Characterization and Thickness Dependence . . . 97
6.4 Constructing the Magnetic Depth Profile . . . 99
6.5 X-Ray Magnetic Circular Dichroism . . . 103
6.6 Probing Oscillatory Coupling and Magnetic Structure Through Neutron Diffraction . . . 107
6.7 Detailed Crystal Structure Probing . . . 111
6.8 Concluding Thoughts . . . 115

7 Inducing Ferromagnetism at the $LaNiO_3/CaMnO_3$ Interface **117**
7.1 The Challenge of Intermixing at Interfaces 117
7.2 Superlattice Structure and Quality 119
7.3 Magnetism and Conductivity 123
7.4 Probing the Magnetic Depth Profile 125
7.5 Discussion and Concluding Thoughts 128

8 Summary and Outlook **133**

Bibliography **136**

A X-ray Magnetic Circular Dichroism **150**
A.1 Theoretical Basis 150
A.2 Example System 152
A.3 Sum Rules 160

B Strain in Epitaxial Thin Films **163**
B.1 Stress/Strain Notation 163
B.2 (100) Oriented substrates 165
B.3 (110) Oriented Substrates 166
B.4 (111) Oriented Substrates 167

List of Figures

1.1 The perovskite unit cell 4
1.2 Perovskite unit cell distorted by octahedral tilting 5
1.3 a) σ and b) π bonding in BO_6 octahedra 6
1.4 Crystal field splitting in BO_6 octahedra 7
1.5 Double exchange mechanism in Mn^{3+} and Mn^{4+} ions 13
1.6 Spin splitting and the Stoner model of itinerant ferromagnetism 14
1.7 A simple picture of a strain distorted perovskite structure 17

2.1 Schematic of one pulsed laser deposition chamber used to fabricate samples for this work 21
2.2 a) Schematic RHEED setup. b) Typical RHEED diffraction pattern from a film during deposition. c) Oscillation of the intensity of the $(\bar{1}00)$ and (100) reflections for a typical $LaAlO_3/LaNiO_3$ superlattice during deposition. . . . 23
2.3 Tapping mode atomic force microscopy 25
2.4 Ewald sphere construction of thin film X-ray diffraction 26
2.5 a) Real and b) reciprocal space construction of reciprocal space mapping with component along the growth and film axes 27
2.6 X-Ray diffraction geometry 27
2.7 X-Ray reflectometry geometry 28
2.8 a)X-ray absorption mechanism b) X-ray fluorescense interaction c) Auger electron emission 34
2.9 Electron mean free path as a function of kinetic energy, produced using theoretical calculations by the NIST inelastic mean free path database and confirmed Seah and Dench.[119, 136] Electron mean free path has been calculated as a function of energy for three important materials used in the thesis: $CaMnO_3$, $CaRuO_3$, and $LaNiO_3$. Note the very similar of all three systems. . 35
2.10 Magnetization vs. applied field measurement of a blank $SrTiO_3$ substrate contaminated with ferromagnetic iron oxide. The measurement was taken using SQUID magnetometry at 10 K, and a linear diamagnetic background was subtracted. 38
2.11 Schematic of L-edge X-ray absorption in a system with a ferromagnetically ordered d band, showcasing the requirements for observing X-ray magnetic circular dichroism 40
2.12 Schematic of the Polarized Beam Reflectometer and the NIST Center for Neutron Research.[10] 42

2.13 Schematic of the BT7 triple axis diffractometer, reproduced from Lynn et al..[87] 43
2.14 van der Pauw geometry for electrical characterization 44

3.1 Schematic of the crystal structure of $SrRuO_3$ at 300 K, as determined through neutron powder diffraction by Gardner et al.[43] the rotation of the Ru-O octahedra can be clearly seen. Structure is shown along a) the $(110)_{pc}$ or $(100)_O$ axis and b) $(001)_{pc}$ or $(001)_O$ axis. These two views show the rotation of the RuO_6 octahedra. c) Schematic of the $SrRuO_3$ crystal structure showing only the RuO_6 octahedra. d) Schematic showing the relationship between the pseudocubic (black) and orthorhombic (red) unit cells for perovskite systems with octahedral rotations as those found in $SrRuO_3$, $CaMnO_3$, and many others. Note that the a and b axes are at a 45° angle to the a' and b' axes while the c and c' axes are parallel. 50
3.2 Atomic force micrographs of $SrRuO_3$ on a) LSAT, b) $SrTiO_3$, c) $LaAlO_3$, d) $KTaO_3$ 52
3.3 a) Representative x-ray diffraction θ-2θ scans and b) ω rocking curves for films on all (100) substrates 53
3.4 (103) Reflection reciprocal lattice maps of typical $SrRuO_3$ films grown on a) 100 LSAT, b) (100) $SrTiO_3$, c) (100) $LaAlO_3$, and d) (100) $KTaO_3$. All films shown are between 50-70 nm thick. 55
3.5 Resistivity vs. Temperature measurements for representative 70-80 nm thick films on $SrTiO_3$, LSAT, and $LaAlO_3$ substrates (Inset) $d\rho/dT$ showing a peak at the T_C 56
3.6 a) Magnetization vs. temperature, b) T_C vs. growth axis strain, and c) T_C vs. in-plane strain for films on all (100) substrates. The thicknesses of the films shown here range from 50-120 nm. 57
3.7 a) Easy axis magnetic hysteresis loops and b) relationship between saturated moment and in-plane strain for films on all (100) substrates. Samples shown are representative films between 60-80 nm thick. 58
3.8 a) Ru $M^{3,2}$ edge and b) O K edge X-ray absorption and X-ray magnetic circular dichroism 60
3.9 Film unit cell volume vs. a) saturated magnetic moment and b) Curie temperature for films on all (100) substrates 64
3.10 a) Octahedra distorted by compressive strain and b) Example splitting of the t_{2g} orbitals which may result in a reduced moment 65
3.11 a) Reciprocal lattice maps of a series of (301) type reflections taken at 90° ϕ intervals for a representative $SrRuO_3$ film on (100) $KTaO_3$ 65

4.1 Compressive stresses applied to a cubic system by a) (110) and b) (111) oriented substrates 69

4.2 θ-2θ X-ray diffraction scans of $SrRuO_3$ films on a) (110) and b) (111) oriented substrates. The reader may take note of the substrate peaks, which occasionally exhibit small shoulders or, in the case of $LaAlO_3$, multiple peaks. This is common in commercially produced oxide substrates and is typically the result of twinning in the sample. All samples shown are representative films between 50-80 nm in thickness. 71
4.3 ω X-ray diffraction rocking curves of $SrRuO_3$ films on a) $SrTiO_3$ and b) (111) $KTaO_3$ substrates. All samples shown are representative films between 50-80 nm in thickness. 72
4.4 10 μm atomic force micrographs of films on (110) and (111) $SrTiO_3$ 73
4.5 a) Magnetic hysteresis loops and b) magnetization vs. temperature plots of representative films on (100), (110), and (111) $SrTiO_3$ 74
4.6 a) Saturated magnetic moment vs. thickness of representative films on (100), (110), and (111) $SrTiO_3$. b) Saturated magnetic moment vs. in-plane strain for films on (111) $SrTiO_3$ along with (Insets) (321) reciprocal lattice maps associated with representative films. c) Data shown in plot (a) against a model which describes the (111) oriented films as a contamination effect using equation 4.3. As can be seen, the (111) oriented films do not show a 1/T dependence. 75
4.7 Magnetization vs. applied field of a typical (111) oriented $SrTiO_3$ substrate from the same batch as those used for $SrRuO_3$ film depositions 76
4.8 Resistivity vs. temperature for a series of 70-80 nm thick films on (001), (110), and (111) $SrTiO_3$ 78
4.9 a) ρ_{xy} as a function of applied field for representative (100) and (110) oriented films on $SrTiO_3$. b) Saturated magnetic moment vs. nominal carrier concentration for films on $SrTiO_3$. The films shows represent a wide range of thicknesses from 30-120 nm for all substrate orientations. As described in the text, the data displayed was taken at 50 K, and general agreement was found below the Curie temperature. 80

5.1 Typical magnetic hysteresis loops with the field applied out-of-plane and in-plane of $SrRuO_3$ films on a) (100), b) (110), and c) (111) oriented $SrTiO_3$ . . 85
5.2 Typical magnetic hysteresis loops with the field applied out-of-plane and in-plane of $SrRuO_3$ films on a) (100), b) (110), and c) (111) oriented $KTaO_3$ . . 86
5.3 Typical magnetic hysteresis loops with the field applied out-of-plane and in-plane of $SrRuO_3$ films on a) (100) LSAT, b) (110) LSAT, and c) (100) $LaAlO_3$ and d) (110) $LaAlO_3$ 88
5.4 $M_S^{In-Plane}/M_S^{Out-of-Plane}$ vs. Tetragonal distortion for a series of 40-80 nm thick films on (100) $SrTiO_3$, LSAT, $LaAlO_3$, and $KTaO_3$ 89
5.5 X-ray absorption and X-ray magnetic circular dichroism of the a) Ru $M_{5,4}$ and b) O K edge of a representative (100) oriented $SrTiO_3$ film on $SrTiO_3$ with field applied in normal and grazing incidence 90
5.6 X-ray absorption and X-ray magnetic circular dichroism of the a) Ru $M_{5,4}$ and b) O K edge of a representative (100) oriented $KTaO_3$ film on $SrTiO_3$ with field applied in normal and grazing incidence 91

6.1 a) Magnetic moment vs. applied field for a (3/15) $CaRuO_3/CaMnO_3$ superlattice after cooling to 10 K in an applied field of ± 7 T. The superlattice can be seen to exhibit both ferromagnetism and exchange bias. b) A close up view of the hysteresis loop after cooling in -7 T. The exchange field by which the hysteresis loop is biased can be clearly seen. 95
6.2 X-ray reflectivity of a) a $(3,17)_{10}$ superlattice with fit and b) a $(3,17)_{10}$ and $(3,10)_{10}$ superlattice. 97
6.3 a) Saturated magnetic moment, b) exchange field, and c) coercive field of $CaRuO_3/CaMnO_3$ superlattices as a function of $CaMnO_3$ layer thickness. . . 98
6.4 Polarized neutron reflectometry spectra with fit for a) $(3/17)_{10}$ superlattice and b) $(3/18)_8$ superlattice. In both reflectivity spectra the data points are the actual Fresnel reflectivities while the lines represent the reflectivity spectrum of best fit depth profile. Red points and lines represent spin-up neutrons while blue represents spin down neutrons. c) Typical nuclear and magnetic depth profile assuming 1 unit cell of ferromagnetism at the interface. 100
6.5 Theoretical polarized neutron reflectometry spectra. a), c), and e) are for a $(3/17)_{10}$ superlattice and assume magnetic layers 1, 2, and 3 unit cells thick. b), d), and f) are for a $(3/18)_8$ superlattice and assume magnetic layers 1, 2, and 3 unit cells thick. 102
6.6 X-ray absorption and X-ray magnetic circular dichroism spectra of a $(3/3)_{10}$, $(3/4)_{10}$, and $(3/5)_{10}$ superlattice. (a) Unscaled, (b) Scaled using a symmetric interface model, (c) Scaled assuing only $CaRuO_3/CaMnO_3$ interfaces are magnetic for m = odd samples, and (d) Scaled assuing only $CaMnO_3/CaRuO_3$ interfaces are magnetic for m = odd samples, ... 106
6.7 Neutron diffraction spectra of a) $({}^1/_2,{}^1/_2,{}^1/_2)$ $SrTiO_3$ distortion peak with temperature dependence, b) $({}^1/_2,{}^1/_2,{}^1/_2)$ $CaMnO_3$ antiferromagnetic peak as a shoulder of the $SrTiO_3$ distortion, c) Improved resolution of the $({}^1/_2,{}^1/_2,{}^1/_2)$ $CaMnO_3$ antiferromagnetic peak, all taken at BT7. d) $({}^1/_2,{}^1/_2,{}^1/_2)$ $SrTiO_3$ distortion peak and $CaMnO_3$ magnetic $({}^1/_2,{}^1/_2,{}^1/_2)$ peak taken at BT4. . . 108
6.8 Neutron diffraction spectra of $({}^1/_2,{}^1/_2,{}^1/_2)$ $CaMnO_3$ antiferromagnetic peak at a) 25 K, b) 50 K, c) 75 K, d) 100 K. All spectra taken at beamline BT7. . 110
6.9 Schematic reciprocal lattice arrangement showing Q, Growth Axis, and In-Plane scanning directions used in neutron diffraction. Peaks appearing in Q-scans may not appear in Growth Axis or In-Plane scans. 111
6.10 a) Neutron diffraction scan of the expected C-type antiferromagnetic peak location taken at 5 K. b) $({}^3/_2,{}^1/_2,{}^1/_2)$ $CaMnO_3$ structural peak. 112
6.11 Reciprocal lattice maps of the $(\bar{1}03)$ peak of $CaRuO_3/CaMnO_3$ superlattices with periodicities of a) (3/4) and b) (3/5). Significant relaxation is evident. . 113
6.12 ω rocking curves of the (200) film peaks of (3/4) and (3/5) superlattices taken at SSRL beamline 2-1 114
6.13 l direction scans of the a) $(10^5/_2)$ and b) $(01^5/_2)$ diffraction peaks for (3/4) and (3/5) superlattices taken at SSRL beamline 2-1 115

7.1 a) 5 micron atomic force micrograph showing smooth atomic terraces on the film surface. b) X-ray reflectivity and theoretical fit of a $(6,8)_{10}$ film showing total thickness fringes as well as first, second, and third order superlattice reflections (marked by arrows). c) X-ray diffraction scan of a (6/14) sample showing substrate, film, and superlattice peaks. d) Reciprocal lattice map of the (301) reflection of a typical (6/20) superlattice. 121
7.2 High resolution STEM Z-constrast image of a (6/8) superlattice. 122
7.3 a) Mn L-edge spectra for a typical (6,8) $LaNiO_3/CaMnO_3$ superlattice highlighting the signatures of Mn^{4+}. b) Ni L-edge spectra for a typical (6,8) $LaNiO_3/CaMnO_3$ superlattice. Despite overlap with the La M-edge, clear signatures of Ni^{3+} are observable. 123
7.4 Resistivity vs. Temperature of a series of (n,8) superlattices 124
7.5 a) Magnetic hysteresis loops for a series of typical (2,8), (4,8), and (6,8) superlattices. b) Magnetic moment vs. temperature from 10-150 K. A ferromagnetic transition is observed between 75-80 K only in n $\geq$ 4 superlattices. c) Hysteresis loops for typical (6,8) and (7,8) superlattice illustrating the significant difference in saturated moments of n = even and n = odd samples. d) Magnetic hysteresis loops showing scaling of the magnetic moment with the number of interfaces rather than $CaMnO_3$ layer thickness. 126
7.6 a) Mn L-edge X-ray absorption and XMCD of a typical (6/8) $LaNiO_3$ superlattice. The X-ray absorption linshape is in excellent agreement with a Mn^{4+} state and indicates that the Mn^{3+} contribution must be at most 5%. The Mn XMCD linshape is also in excellent agreement with examples in the literature of Mn^{4+} XMCD b) Rescaling of the XMCD signal to reflect the interfacial nature of the ferromagnetism, as in Chapter 6.6 c) Plot comparing the area of rescaled Mn $L_{3,2}$ XMCD curves of the (6/8) $LaNiO_3/CaMnO_3$ superlattice with a $LaMnO_3$ standard as well as the $CaRuO_3/CaMnO_3$ samples shown in Chapter 6.6 as a function of electron escape depth. Note the excellent agreement at the theoretically expected scattering length of 2-3 nm. d) Ni L_2 edge X-ray absorption and XMCD showing no discerable dichroism. This indicates not only a lack of ferromagnetism in the Ni ions, but also a very weak paramagnetic response. All measurements shown were taken at 20 K and (for XMCD) at fields of $\pm$ 1.5 T. 129
7.7 (color online) a) Fitted polarized neutron reflectivity with standard error at 800 mT and 15 K at the first order superlattice reflection of a (5,8) superlattice. b) We show below the model used to obtain this fit, in which we assume one unit cell of magnetized $CaMnO_3$. 130

B.1 a) Normal stress b) Normal strain c) Shear stress d) Shear strain 164

List of Tables

A.1 Transition matrix element coefficients for positively circularly polarized light 153
A.2 Transition matrix element coefficients for negatively circularly polarized light 153

Acknowledgments

First and most obviously, this dissertation would not exist without Yuri. In the last six years, it has become clear to me that thesis advisors have a mind-boggling number of tasks to juggle. I look back and wonder how on earth you had time to read and edit my first few papers dozens of times, always managing to give feedback that was just specific enough to fix the paper while still forcing me to figure it out how to do it myself. Whether it's twenty paper drafts or a three-hour critique practice talk session, advisers who take so much time to train students to represent themselves professionaly are rare. You cared about my scientific development, always finding new collaborations and scientific experiences for me. You pushed me when I needed to be pushed and somehow got me through despite the move to Stanford. Only in the last six months or so did I really begin to realize how carefully you have been training me. Thank you.

I also want to extend a very special thanks to Franklin Wong. You spent so much time training and teaching me that I'm surprised you had time to write your own thesis. Your guidance would have been invaluable even without the addition of your boundless entertainment value. Thank you for everything.

To the many lab members who guided me at one point or another, especially Rajesh Chopdekar, Marco Liberati, and Virat Mehta. Thank you for your patience and willingness to draw the same bonding diagrams over and over. I think I'm starting to get it.

I am also grateful for the help of many of my lab contemporaries, Chunyong He, Jodi Iwata, Urusa Alaan, Matthew Gray, Ted Sanders, and Charles Flint. Thank you for the encouragement, understanding, and the occasional help with LHe fills. For those of you who are not done yet - good luck! You'll get there!

I would like to thank my collaborators Brian Kirby, Julie Borchers, Arturas Vailionis, Michael Fitzsimmons, Catherine Jenkins, Elke Arenholz, Kin Man Yu, Hao Yang, and Nigel Browning. Many of you have become additional mentors to me, spending many hours filling my brain with the deep mysteries of Neutrons and X-rays. I will always appreciate not just the massive amount of data gathering you made possible, but also the guidance and the time you took to teach me. Without you, this thesis would be much shorter. As a final note, despite the many equations and book chapters you've tried to make clear to me, I'm still convinced you are all science wizards.

To my friends who walked through this journey with me, bringing cookies, prayer, encouragement, and whatever else I needed to keep going - especially during the difficult times. I want to especially thank the Veritas Tuesday men's Bible study. I would also like to specifically thank William Hedberg, Onsi Fakhouri, Daniel Garcia, Hannah Fakhouri, and Melissa Filbin, who I could always turn to when research went ... not so well. To my cousin Arwen Long Declan, thank you for the many, many times you helped me gain some perspective. It's amazing you were able to be so supportive from so far away.

My family has always been completely supportive, so I didn't really expect anything else over the last six years. However, you exceeded even my wildest hopes. Mom and Dad, you guided me and prepared me for all of this, and I could never have done it without you. You taught me science, you taught me how to think things through, how to stay calm, how to prioritize. You proofread proposals, papers, even this thesis. Even when you weren't visiting, you walked with me through my Ph.D. every step of the way. Aaron, you've been

as supportive as anyone, with the added bonus that when I really, really need to blow up some tanks online you always make the time. I love you all.

Finally, Karen. You always believed that I could do this even when I was sure I couldn't. You were patient when I was cranky. You were kind when I was upset. You gave me space when I needed to work, and brought me out of it when I needed a break (whether I knew it or not). You proofread and helped me talk through the data analysis and theoretical processes over and over for hours until I had convinced myself of the direction I needed to go. You did everything possible to make sure that this thesis actually happened and I could not ask for a more loving, kind, generous, supportive wife.

Part I

Background

Chapter 1

Introduction

This dissertation is most fundamentally about the control of magnetism at the nanoscale. Through the deposition of transition metal complex oxides and heterostructures, we seek to identify and implement mechanisms for tuning many aspects of magnetic order. We will identify model systems uniquely suited to granting us additional insight into strain and interfacial effects, especially systems in which these effects may be isolated from external considerations. Before we can discuss this, however, it is critical to come to an understanding of the relevant physics in these systems, from their structure to mechanisms for magnetic interaction. Therefore, this chapter will introduce complex oxides as a physicists playground, with a wealth of exciting magnetic phenomena. We will explore the aspects of this material class leading to such diverse properties and, finally, discuss some of the most commonly applied models used to describe magnetism in oxides.

1.1 Tunable Ground States in Transition Metal Oxides

The ability of the scientific community to fabricate and manipulate materials at the nanoscale has undergone a rapid expansion in recent decades. As our understanding of thin film deposition has grown through the development of techniques such as pulsed laser ablation, molecular beam epitaxy, and many others, so too has it become increasingly necessary to understand the unique physics of low dimensional systems.[21, 117, 159, 22] The emergence of novel electronic and magnetic ground states in nanostructures which differ wildly from that of the bulk materials has sent the community into an intensive search for the specific mechanisms by which these novel states are induced, and parameters by which they may be controlled and functionalized. One of the most promising and active classes of materials in this search is that of transition metal complex oxides.

The transition metal complex oxides, often referred to simply as complex oxides, are a broad category of systems encompassing oxides with a number of crystal structures and a myriad of chemical compositions. However, the most commonly studied complex oxides fall into the perovskite, layered perovskite, or spinel structures and are composed of at least one (often several) different transition metals and some combination of alkali metal, alkali earth metal, or rare earth metal. The addition of strong electron correlation effects, due to the highly ionic nature of bonding in oxide system, further expands the range of electronic

interactions.[30] From these simple statements, it is clear that the complex oxides represent an enormous diversity of states even in the bulk systems. Complex oxides with the perovskite structure, which will be the focus of this thesis, exhibit properties as diverse and unusual as the strongest known $4d$ itinerant ferromagnetism in $SrRuO_3$, colossal magnetoresistance in $La_xSr_{1-x}MnO_3$, metal-insulator transitions in the rare-earth nickelates (RNO_3), superconductivity at the $LaAlO_3/SrTiO_3$ interface and in many layered perovskites, ferromagnetism, antiferromagnetism, charge and orbital ordering to name just a few.[2, 125, 5, 89, 41] These effects are possible through both electron correlation effects and the range of different ionic sizes and accessible valence states, which result in a range of electronic, magnetic, and optical properties.

With the additional opportunity to incorporate complex oxides into high quality thin film heterostructures through new growth techniques, interfacial interactions result in even more remarkable emergent properties. The most famous example is that of the $SrTiO_3/LaAlO_3$ in which a conductive 2-dimensional electron gas emerges at the interface between two band insulators.[114] Although there is still some debate, it now appears that this conductive interface emerges as a consequence of interfacial electronic reconstruction. Similar electronic reconstruction and interfacial exchange effects have been suggested to be responsible for ferromagnetism at antiferromagnet-antiferromagnet interfaces such as $LaFeO_3/LaCrO_3$ and paramagnet-antiferromagnet interfaces such as $CaRuO_3/CaMnO_3$.[150, 145] At the same time, strain effects have been implicated in the spin transition and ferromagnetism which emerges in thin films of the cobaltites.[103, 102]

Clearly, one of the most important questions in the physics of complex oxides is the identification of specific mechanisms for tuning these emergent phenomena. Achieving this goal requires both parameters to tune and measurements by which interfacial effects may be decoupled from effects such as films quality or intermixing. This thesis will focus on the identification of several systems in which strain and interfacial effects may be isolated from other contributions. In $SrRuO_3$ thin films, we will see that strain is a parameter which governs the ferromagnetic order. In $CaMnO_3$-based superlattices, the precise nature by which interfacial ferromagnetism is induced will be explored, and a mechanism by which the interfacial coupling may be activated and deactivated will be implemented.

1.2 Structure and Distortions in Perovskites

Many of the so-called "complex oxides" are highly ionic and take the form of the perovskite crystal structure. The prototypical example of the perovskite structure is $CaTiO_3$, from which the name of the strucure is derived. The generalized perovskite crystal has a chemical composition of ABO_3 in a simple cubic lattice decorated as shown in Figure 1.1 with a motif of $(0,0,0)_A$, $(0.5,\ 0.5,\ 0.5)_B$, $(0,\ 0.5,\ 0.5)_O$, $(0.5,\ 0,\ 0.5)_O$, $(0.5,\ 0.5,\ 0)_O$. In most perovskites, A is a larger cation, typically an alkaline earth metal ($CaTiO_3$, $SrRuO_3$), lanthanide ($LaAlO_3$), or more rarely an alkali metal ($KTaO_3$). The A cations are 12-fold coordinated and bonded to the neighboring oxygens, but not to the B-site cation. In most perovskite structures, the A-site cation will assume an ionic state without any valence electrons (Sr^{2+}, La^{3+}, Pr^{3+}). Thus, the vast majority of the electronic interactions related to magnetism and electron transport will be confined to the B-site cations and oxygen anions.

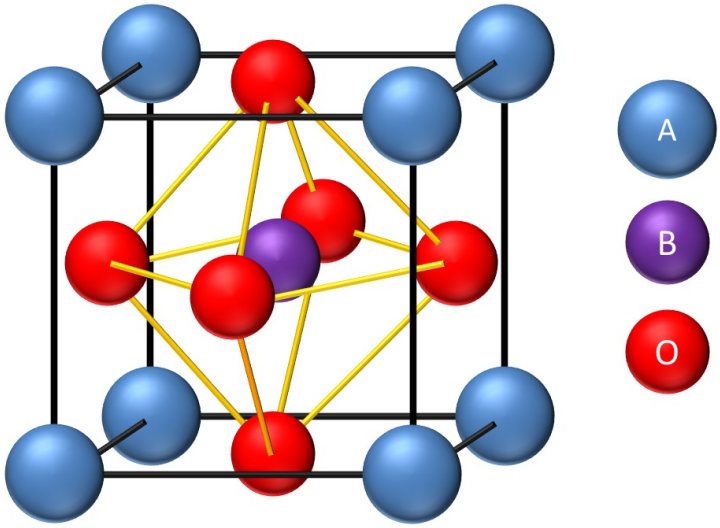

Figure 1.1: The perovskite unit cell

The typically far more interesting B-site cations are housed in an octahedral cage of oxygen atoms, as illustrated in Figure 1.1. The B cations are most commonly transition metals in a variety of valence states with partially filled $3d$ or $4d$ levels. In fact, the perovskite structure can accommodate different or even fractional valence states for a given transition metal. For example, the system $La_xSr_{1-x}MnO_3$ results in a Mn^{3+} valence when x=1, a Mn^{4+} valence when x=0, and a $Mn^{(4-x)+}$ for various alloy compositions.[125] This opportunity for the co-existence of multiple valence states is in fact one of the reasons that complex oxides in the perovskite structure offer such exciting opportunities for tuning the electronic and magnetic ground states. Equally important in creating such a unique class of materials are the strong correlation effects first described by Mott in his description of the surprising insulating state of NiO.[107] These electron-electron interactions are partly due to the inherent localization of the d-electrons and partly due to the increased electron localization present in ionic systems.

Despite the robust nature of the perovskite structure and its ability to incorporate many different cations and valence states, it is prone to structural distortions based on the relative ionic radii of the constituent materials. A parameter, called the tolerance factor, is defined below in Eq. 1.1 and describes the situations in which a perovskite compound is likely to be distorted rather from a simple cubic structure.[158]

$$t = \frac{(r_A + r_B)}{\sqrt{2}(r_B + r_O)} \tag{1.1}$$

The tolerance factor is thus defined by the atomic radii of the A-cation (r_A), the B-cation (r_B), and the oxygen atoms (r_O). An ideal cubic perovskite will have a tolerance factor of one, and deviation from ideal requires a distortion to accommodate the size mismatch. These distortions can take several forms, but usually include rotation and tilting of the oxygen octahedral, as shown in Figure 1.2.

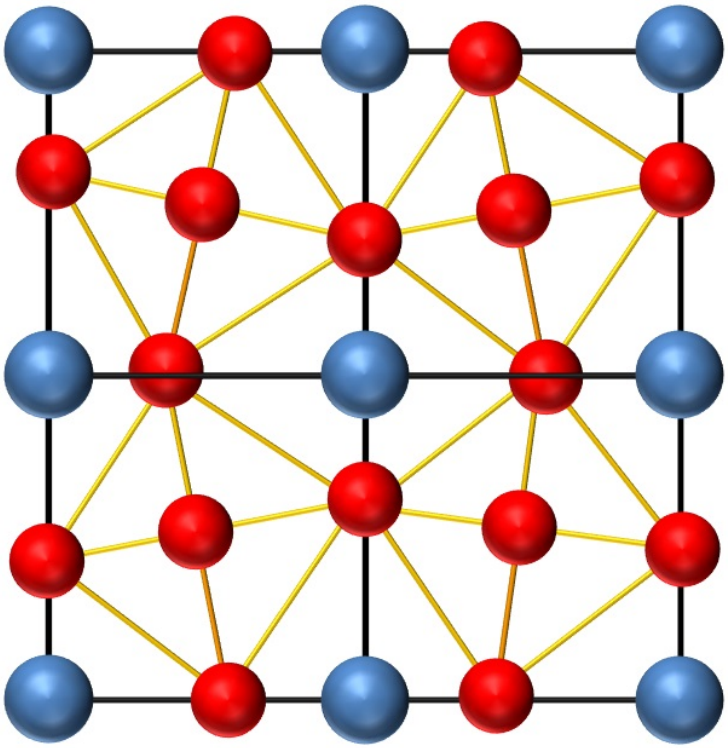

Figure 1.2: Perovskite unit cell distorted by octahedral tilting

A classic example illustrating the relationship between the tolerance factor and structural distortions is the series of compounds $CaRuO_3$, $SrRuO_3$, $BaRuO_3$, with tolerance factors of 0.96, 0.99, and 1.05, respectively.[124] Although both $CaRuO_3$ and $SrRuO_3$ are orthorhombically distorted, $SrRuO_3$ is very nearly cubic while the Ca ions in $CaRuO_3$ are simply too small for the structure and result in a large distortion. The large Ba ion in $BaRuO_3$ results in a distortion to a hexagonal perovskite structure.[124] These slight alterations in crystal structure can have profound effects on the behavior of a given system and are in fact largely credited with preventing ferromagnetic order in $CaRuO_3$ while the smaller distortion in $SrRuO_3$ results in ferromagnetism.

1.3 Crystal Fields in Perovskite Transition Metal Oxides

In any chemically bonded substance, the proximity of additional nuclei introduces coulombic interactions which result in perturbations of the single-atom electronic ground state. In the most general description, crystal field theory deals with the breaking of the degeneracy in the otherwise symmetric electronic ground state. Through symmetry arguments and the study of electron orbital overlap, it is possible to describe the splitting of, for example, the $3d$ states into multiple separate degenerate energy levels. The splitting of these energy levels is called the crystal field.

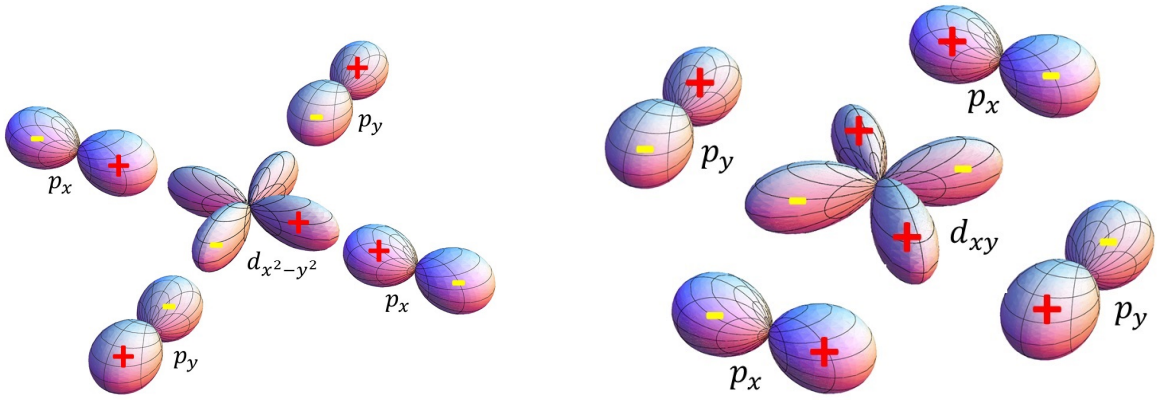

(a) (b)

Figure 1.3: a) σ and b) π bonding in BO_6 octahedra

As most interesting magnetism in perovskite complex oxides arises as a result of interactions between B-site d-electrons mediated by the p-orbitals of the intervening oxygens, it is important to have a basic understanding of the electronic structure and crystal field in this case. The B-site cation is surrounded by an octahedral cage of oxygens. As a result of bonding interactions with p orbitals of neighboring oxygen atoms, the d-states of the B-site cations split into two distinct energy levels, the e_g, associated with σ bonding, and the t_{2g}, associated with π bonding, as illustrated below in Figure 1.3. More precisely, the e_g levels are formed from the $d_{3z^2-r^2}$ and $d_{x^2-y^2}$ states, while the t_{2g} levels are formed from the d_{xy}, d_{xz}, and d_{yz} states. In terms of the hydrogenic orbitals $|l, m_l>$, these d-states may be written as follows:

$$d_{3z^2-r^2} = |2, 0\rangle \tag{1.2}$$

$$d_{xz} = \frac{1}{\sqrt{2}}(|2, 1\rangle + |2, -1\rangle) \tag{1.3}$$

$$d_{xy} = \frac{1}{\sqrt{2}i}(|2, 1\rangle - |2, -1\rangle) \tag{1.4}$$

$$d_{x^2-y^2} = \frac{1}{\sqrt{2}}(|2, 2\rangle + |2, -2\rangle) \tag{1.5}$$

$$d_{xy} = \frac{1}{\sqrt{2}i}(|2, 2\rangle - |2, -2\rangle) \tag{1.6}$$

and the bonding p orbitals are

$$p_z = |1, 0\rangle \tag{1.7}$$

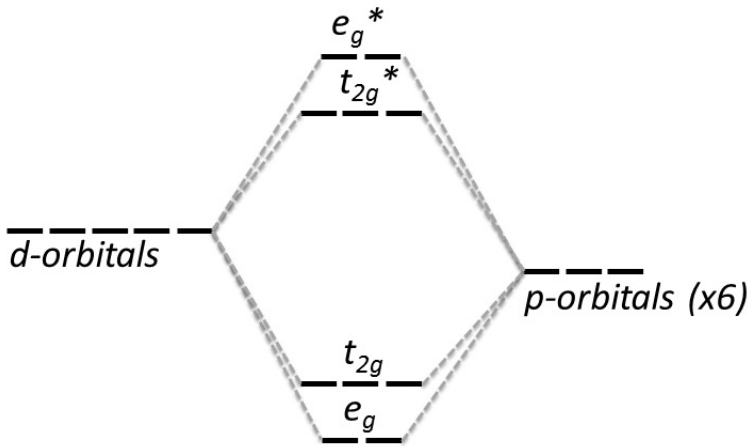

Figure 1.4: Crystal field splitting in BO_6 octahedra

$$p_x = \frac{1}{\sqrt{2}}\left(|1,1\rangle + |1,-1\rangle\right) \tag{1.8}$$

$$p_y = \frac{1}{\sqrt{2}i}\left(|1,1\rangle - |1,-1\rangle\right) \tag{1.9}$$

We can see some examples of σ and π-bonding between the oxygen p orbitals and the above d orbitals in Figure 1.3.

We can now describe the bonding in such an octahedral compound fairly completely. Each of the six ligands (oxygen in the cases we are interested in) contributes two π-bonding orbitals and one σ-bonding orbital. Three of the π-bonding orbitals overlap with a given central cation (generally a transition metal in this work) and form the t_{2g} and t^*_{2g} orbitals. Of the σ-bonding orbitals, two will overlap with any given cation and form the e_g and e^*_g orbitals. The rest remain as nonbonding ligand orbitals. Thus there are 18 ligand orbitals - 2 e_g, 3 t_{2g}, and 13 nonbonding. This bonded electron configuration is shown in Figure 1.4. Using an ionic model to describe the oxygen as O^{2-} and neglecting the nonbonding s-electrons, each oxygen contributes 6 electrons, all 36 of which completely fill the ligand orbitals and leave the antibonding e^*_g and t^*_{2g} states for the electrons around the transition metal cation.

As a result of the greater transfer integral in σ-bonded orbitals relative to π-bonded ones, the interactions of the e_g states are stronger than those of the t_{2g}. This explains the greater energy splitting between bonding and antibonding e_g levels relative to the t_{2g} levels. It also explains also why magnetically ordered systems in which the exchange is mediated through e_g orbitals tend to have much higher ordering temperatures than systems with t_{2g} exchange.

Reflecting the highly ionic nature of the bonding and the high electron affinity of oxygen, the energy levels equivalent to the metal cation d states are actually antibonding states. Thus, the more strongly interacting e_g states are higher in energy and are typically filled last. Alternatively, we may describe the system in terms of $2p$-$3d$ hybridization. Such a hybridization results in states with mixed character. Some will have more $3d$ character

while others will have more $2p$ character. As the $2p$ states are lower in energy, the states with the most $3d$ character are filled last. These two pictures are roughly equivalent, as they result in a slighly higher electron density around the oxygen anions relative to an unbonded state.

1.4 Magnetic Coupling in Transition Metal Oxides

Now that we have an understanding of the structure, bonding, and electronic configuration in perovskite transition metal oxides, we are nearly prepared to discuss magnetic interactions in these systems. First, however, we must introduce the model Hamiltonian most commonly used to describe magnetic exchange in oxides, as it differs from typically applied to other materials. These models are the nearly free electron model and the tight binding model, described extensively in the textbooks by Kittel, Ashcroft, and Mermin.[72, 4] The nearly free electron model treats valence electrons as free particles moving through the crystal and experiencing only slight perturbations as a consequence of the periodic potential of the lattice. The ionic cores are assumed to be immobile and the electrons are assumed to be completely independent. That is, we may fill up the electron levels sequentially from lowest to highest energy without worrying that the addition of an eletron will modify the energies of the other states. Additionally neglecting interactions between neighboring nuclei, we may write a model Hamiltonian in the nearly free electron model as

$$H = \sum_i \frac{p^2}{2m} - \sum_{i,j} \frac{Z_j e^2}{4\pi\epsilon_0 |r_i - R_j|} \tag{1.10}$$

where i is summed over all electrons and j is summed over all nuclei. r_i is the position of the i^{th} electron and R_j is the position of the j^{th} nuclei. Z is the charge of the nucleus, and p is the electron momentum. Obviously there are many ways to simplify the model to make it more tractable mathematically, most notably by including the single electron approximation in which only a single electron is assumed to occupy the system. Similarly there are many ways to make it more accurate, for example to including the possibility of phonons and electron-phonon interactions. It is quite clear, however, that attempting to describe a highly localized oxide system using a model in which the electrons are only marginally perturbed by the periodic lattice is problematic at best. For a better approach, we turn to the tight binding model.

1.4.1 The Tight Binding Model and The Hubbard Hamiltonian

A much more promising approach to modeling electrons in oxides can be found in the tight binding model. The tight binding model is both an independent electron model and a single electron model. A basis is constructed from the bonded atomic orbitals, and the tendency of electrons to move between orbitals is taken into account through a hopping term t_{ij}. Therefore a tight binding Hamiltonian may be written as

$$H_{tb} = -t \sum_{i,j,\sigma} \left(c^\dagger_{i\sigma} c_{j\sigma} + c^\dagger_{j\sigma} c_{i\sigma} \right) \tag{1.11}$$

where i and j are summed over all bonding orbitals and σ is summed over the available electron spin states. t is the orbital overlap integral, also known as the transfer integral or hopping parameter. $c^\dagger$ and c are the creation and destruction operators, so $c^\dagger_{i\sigma}c_{j\sigma}$ destroys a spin σ electron on orbital j and creates one on i, effectively "hopping" and electron from one state to another. Obviously we must not violate the Pauli Exclusion Principle, so the following constraint must apply:

$$c^\dagger_{i\sigma}|i,\sigma>=0 \tag{1.12}$$

The tight binding Hamiltonian is associated with the kinetic energy of the system and represents the energetic favorability of electron delocalization. This somewhat counterintuitive concept may be demonstrated in a number of ways, and we will begin with the kinetic energy of a single electron confined to a spherical volume with diameter d. According to the position-momentum uncertainty principle

$$\Delta x \Delta p \geq \frac{\hbar}{2} \tag{1.13}$$

so if Δx is the area or diameter to which the electron is confined and we assume the minimum possible uncertainty, we can approximate that

$$p \approx \frac{\hbar}{2d} \tag{1.14}$$

and the momentum and kinetic energy are related by

$$KE = \frac{p^2}{2m} = \frac{\hbar^2}{8md^2} \tag{1.15}$$

Thus, we can see that the uncertainty principle requires an inverse relationship between the kinetic energy of an electron and its delocalization. Alternatively we may examine the centrifugal term of the electron kinetic energy in a hydrogenic wave function to see

$$KE = l(l+1)\frac{\hbar^2}{2mr^2} = l(l+1)\frac{4\hbar^2}{2md^2} \tag{1.16}$$

An increase in the transfer integral can be interpreted as an increase in the hopping of electrons between sites and an increase in the delocalization of electrons. Kinetic energy decreases as hopping increases.

Despite the advantage offered by the tight binding approach in describing localized systems such as the transition metal oxides, the tight binding model has also been highly unsuccessful in describing these systems. The most significant reason for this is the complete neglect of electron-electron interactions. We attempt to address this through the adoptions of the Hubbard Hamiltonian. The Hubbard Hamiltonian is a modification of the tight binding approach first developed as an attempt to deal with the failure of conventional band theory and the single electron approximation to accurately describe electrical transport in transition metal oxides. Materials such as NiO were predicted to be conductive but experimentally proved insulating.[107] Mott attributed this observation to strong electron-electron correlations in transition metal oxides, and the materials have been known as Mott insulators

ever since.[107] In the Hubbard model, this takes the form of a second term added to the tight binding Hamiltonian as shown below:

$$H_{Hubbard} = -t \sum_{i,j,\sigma} \left(c^{\dagger}_{i\sigma} c_{j\sigma} + c^{\dagger}_{j\sigma} c_{i\sigma} \right) + U \sum i \left(n_{i\uparrow} n_{i\downarrow} \right) \tag{1.17}$$

The second term in the Hubbard Hamiltonian represents the Coulomb repulsion energy associated with adding an electron to an already occupied state. U represents the magnitude of this term and is variously referred to as the on-site potential, pairing energy, or simply the Hubbard U term. The operator $n_{i\sigma}$ returns 1 if an electron with spin σ occupies state i. Therefore it is easy to see that any state occupied by two electrons increases the total energy of the system by U. We now have two competing energy interests manifested in the Hubbard model. The kinetic energy term favors electron delocalization, hopping and conduction while the on-site potential term favors localization and insulating behavior.

The Hubbard Hamiltonian is one of the most useful tools available to us for describing the electronic state of correlated transition metal oxides. Not only does it successfully explain the transport behavior of Mott insulators through the formation of upper and lower Hubbard bands, but it also has profound implications for the description of magnetic ordering in these systems, as we shall see in the following sections. In describing the formulation and effects of the Hubbard model, we have largely followed the treatment of Stohr, and the reader is encouraged to refer to his excellent textbook on magnetism for further details.

1.4.2 Antiferromagnetic Superexchange

One of the most difficult magnetic exchange interactions to describe is superexchange. Although capable of inducing either ferromagnetic or antiferromagnetic interactions as described by Goodenough and Kanamori, superexchange across 180° metal-oxygen-metal bonds such as those extant in perovskites are exclusively antiferromagnetic in nature. We will confine ourselves, then, to a discussion of antiferromagnetic superexchange interactions.

Central to an understanding of superexchange is the realization, pioneered by Kondo in his description of the Kondo effect, that virtual states can impact observable ones. In this case, when we describe something as a virtual state we refer to an excited energy state with an occupation lifetime so short that the energy-time uncertainty principle prohibits its observation. Of equal importance to our understanding of superexchange is the fact that electron transfer between two metal cations separated by a mutually bonded oxygen may be facilitated by the oxygen atom, allowing an electron to "hop" from one cation to another.

In a highly correlated system such as many complex oxides, the implications of these two statements become immediately clear; electrons may hop from one metal atom to a partially occupied state in another metal atom as long as the Pauli exclusion principle is not violated. Thus, for an electron transfer to occur between half-filled orbitals, the orbitals must be antiferromagnetically aligned. Although this will be a virtual state due to the addition of the pairing energy, this transition can have real effects on the electronic and magnetic ground state of the system. There are now two competing energies - the decreased kinetic energy from delocalization into virtual states and the increased energy from the Hubbard U. This competition was treated in detail as a second order perturbation by Goodenough-Kanamori and an excellent description may also be found in the textbook by Stohr.

To explore the consequences, we will follow the method of Stohr and examine the toy system of two half-filled orbitals. We may describe the system with the wave function $|B, O, B' >$ where B represents the electron configuration on the interacting orbital of the first B-site cation, O is the electron configuration of the oxygen p-orbital mediating the interaction, and B' is the interacting orbital of the second B-site cation. Thus, the distinct configurations of our toy system in the antiferromagnetic configuration and their associated energies are:

$$\begin{aligned} &1.|\uparrow, \uparrow\downarrow, \downarrow>: E = 0 \\ &2.|0, \uparrow\downarrow, \uparrow\downarrow>: E = U \\ &3.|\uparrow\downarrow, \uparrow, \downarrow>: E = \Delta \end{aligned} \tag{1.18}$$

while the distinct configurations of the ferromagnetic arrangement are:

$$\begin{aligned} &4.|\uparrow, \uparrow\downarrow, \uparrow>: E = 0 \\ &5.|\uparrow, \downarrow, \uparrow\downarrow>: E = \Delta \end{aligned} \tag{1.19}$$

Here, U is the on-site coulomb repulsion and Δ is the energy required to transfer an electron from an oxygen site to a metal. Since in general $\Delta >>$ U and we cannot, in fact, distinguish energetically between states 3 and 5, we may simplify the problem and find the Hubbard Hamiltonian matrix in terms of states 1, 2 and 4, as shown below.

$$\begin{aligned} &\langle\uparrow, \downarrow |H_{Hubbard}| \uparrow, \downarrow> = 0 \\ &\langle\uparrow, \downarrow |H_{Hubbard}|0, \uparrow\downarrow> = -t\langle\uparrow, \downarrow | (|\uparrow, \downarrow\rangle + |\downarrow, \uparrow\rangle) = -t \\ &\langle\uparrow, \downarrow |H_{Hubbard}|0, \uparrow, \uparrow> = 0 \\ &\langle 0, \uparrow\downarrow |H_{Hubbard}| \uparrow, \downarrow> = -t\langle 0, \uparrow\downarrow | (|0, \uparrow\downarrow\rangle + |\uparrow\downarrow, 0\rangle) = -t \\ &\langle 0, \uparrow\downarrow |H_{Hubbard}|0, \uparrow\downarrow> = U \\ &\langle 0, \uparrow\downarrow |H_{Hubbard}| \uparrow, \uparrow> = 0 \\ &\langle\uparrow, \uparrow |H_{Hubbard}| \uparrow, \downarrow> = 0 \\ &\langle\uparrow, \uparrow |H_{Hubbard}|0, \uparrow\downarrow> = 0 \\ &\langle\uparrow, \uparrow |H_{Hubbard}| \uparrow, \uparrow> = 0 \end{aligned} \tag{1.20}$$

where we have omitted explicit writing of the oxygen configuration since it is invariant across the chosen basis. Note that the first term in the Hubbard Hamiltonian deals with state mixing and will only yield a nonzero value for off-diagonal terms. Since the $|\uparrow, \uparrow\rangle$ state *cannot* be mixed with any of the other states through electron hopping, only the terms involving both the $|\uparrow, \downarrow\rangle$ and $|0, \uparrow\downarrow\rangle$ off-diagonal terms are nonzero. The second term, on the other hand, deals with on-site coulomb repulsion rather than state mixing. Therefore it will only yield nonzero values on diagonal matrix elements, particularly ones in which the two electrons occupy the same transition metal orbital. Thus we may write the final Hamiltonian matrix of our toy system as

$$H = \begin{pmatrix} U & -t & 0 \\ -t & 0 & 0 \\ 0 & 0 & 0 \end{pmatrix} \tag{1.21}$$

When these states are used as a basis they result in perturbed eigenstates, Utilizing Mathematica to evade the actual math and diagonalize the Hubbard Hamiltonian matrix, we find that the lowest energy perturbed state is

$$\phi = |\uparrow,\downarrow> + \frac{t}{U}|0,\uparrow\downarrow> \tag{1.22}$$

which is antiferromagnetic with an energy of -t^2/U. Antiferromagnetism has been stabilized in this example system by the decrease in kinetic energy which comes from delocalizing, even if the delocalization occurs through the occupation of virtual states.

1.4.3 Double Exchange

One common form of ferromagnetic exchange in perovskite transition metal oxides is double exchange, in which electron transfer between ions of the same element but different valence is responsible for the exchange. To illustrate this mechanism, we will examine the classic example of double exchange, (La,Sr)MnO_3 (LSMO). LSMO is a ferromagnetic conducting oxide where the electron transport occurs through a hopping mechanism. Since the stable oxidation states of La and Sr are 3+ and 2+, respectively, the Mn ions are left in a combination of 3+ and 4+ oxidation states. These Mn oxidation states correspond to electron configurations of $t_{2g}^3 e_g^1$ and t_{2g}^3 as shown in Figure 1.5. Looking at Figure 1.5, it is tempting to say that the fourth electron in Mn^{3+} should occupy the t_{2g} level in the spin down configuration. Here, we have stated a commonly occuring competition between the crystal field energy, which splits the $3d$ levels and favors occupation of the t_{2g} states, and Hund's pairing energy, which favors a maximization of the total spin quantum number. Hund's pairing energy is fundamentally an electron correlation effect rooted in the increased coulombic repulsion associated with two electrons occupying the same energy level. The final electron configuration will therefore be determined by the relative strength of the crystal field and pairing energy. In some systems, such as $4d$ Ru, the crystal field is very large and an electron configuration of t_{2g}^4 results. However, in Mn the pairing energy dominates.

In this case movement of the e_g electron of the Mn^{3+} ion through the crystal is facilitated by overlap between the Mn d-orbitals and the O p-orbitals. The e_g electron is free to move through the crystal and the kinetic energy term dominates the Hubbard Hamiltonian. The t_{2g} elections cannot hop across atomic sites without encountering the on-site repulsion and are consequently localized. Thus, the e_g electrons are solely responsible for the conductivity and magnetic exchange. According to Hund's rules, an electron transfer is more energetically favorable if neighboring moments are aligned, so reduction of the kinetic energy term favors parallel spin alignment and ferromagnetism.

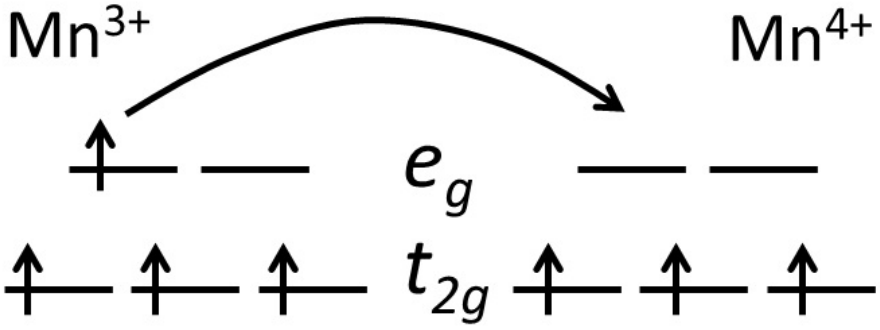

Figure 1.5: Double exchange mechanism in Mn^{3+} and Mn^{4+} ions

1.4.4 Itinerant Ferromagnetism

Addressing ferromagnetic interactions in a metallic system, the Stoner model treats the valence band as a system in which the density of states may be considered as two separate bands each populated exclusively by either spin-up or spin-down electrons. In a ferromagnetic system, the spin-up and spin-down bands must be split by an energy, called the exchange (E_{ex}) energy, in order to stabilize the spin polarization necessary for a ferromagnetic moment. Thus, the density of states for the conduction band of a ferromagnetic metallic system may be represented schematically as shown in Figure 1.6a. We will now examine the conditions necessary for such a splitting to be energetically favorable. For a more detailed reference on the subject the reader is encouraged to examine the textbook published by Coey, upon which this derivation is based.[23]

Obviously in the absence of an exchange interaction there is a kinetic energy cost to promote states from one spin band (the minority band) to the other (the majority band), as shown in Figure 1.6b. If we consider moving the top n electrons, located in an energy range δE, the increase in the kinetic energy of the system may be written as

$$\Delta E_{kin} = n \times \delta E = D(E_F)\delta E \times \delta E = D(E_F)\delta E^2 \tag{1.23}$$

where $D(E_F)$ is the density of states at the Fermi level. Clearly then, we must recover at least ΔE_{kin} from other factors if the ferromagnetic band splitting is to be stable.

The reason that this splitting may be energetically favorable can be found in the final term of the Hubbard Hamiltonian, which represents the correlation energy associated with two electrons occupying a single state. Although referred to variously as Hund's pairing energy, spin splitting, the exchange energy, or the Hubbard U term, the fundamental cause is the increased Coulomb repulsion associated with the overlapping electron wave functions. Therefore we will write the Coulombic repulsion energy represented by the final term of the Hubbard Hamiltonian as

$$E_C = U \sum_i \hat{n}_{i\uparrow}\hat{n}_{i\downarrow} \tag{1.24}$$

where U is the energy cost of adding an electron to a singly occupied state of the repulsion energy term and $\hat{n}_{i\uparrow}$ and $\hat{n}_{i\downarrow}$ are operators that return unity if there is a spin up or spin down

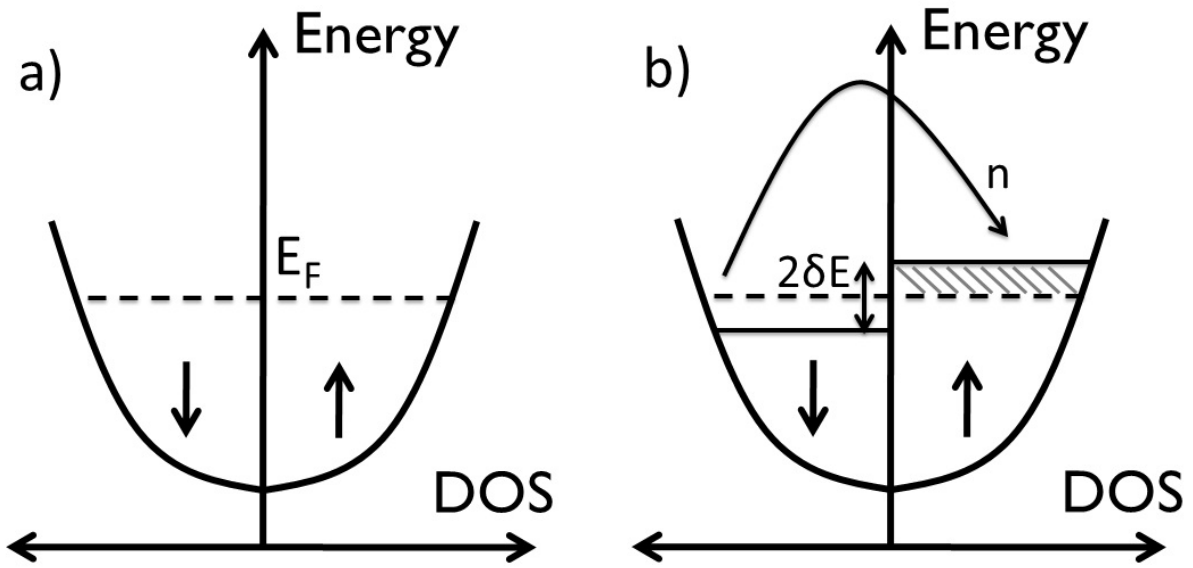

(a) (b)

Figure 1.6: Spin splitting and the Stoner model of itinerant ferromagnetism

electron in the ith state and zero if there is not. We now define an operator

$$\hat{n} = \hat{n}_\uparrow + \hat{n}_\downarrow \tag{1.25}$$

and rewrite E_C as

$$E_C = \frac{U}{4}(\hat{n}^2 - (\hat{n}_\uparrow - \hat{n}_\downarrow)^2) \tag{1.26}$$

so that now the decrease in energy when the top n electrons are promoted is

$$\Delta E_C = \frac{\partial}{\partial E}\left(\frac{U}{4}(\hat{n}^2 - (\hat{n}_\uparrow - \hat{n}_\downarrow)^2)\right) \times \delta E = -\frac{U}{4}(n_\uparrow - n_\downarrow) \times 2\left(\frac{\partial n_\uparrow}{\partial E} - \frac{\partial n_\downarrow}{\partial E}\right) \tag{1.27}$$

However, n, the total number of electrons does not change during this operation; only the distribution of spin up and spin down electrons does. If we remember that

$$\frac{\partial n_\uparrow}{\partial E} = -\frac{\partial n_\downarrow}{\partial E} \tag{1.28}$$

and

$$\frac{\partial n_\uparrow}{\partial E} = D(E_F) \tag{1.29}$$

then we can write ΔE_C as

$$\Delta E_C = -U(n_\uparrow - n_\downarrow)D(E_F) \times \delta E = -UD(E_F)^2\delta E^2 \tag{1.30}$$

If the decrease in electron pairing energy due to splitting the spin up and spin down bands is greater than the corresponding increase in kinetic energy a stable ferromagnetic state results. Thus the condition for itinerant ferromagnetism, known as the Stoner criterion, is written as shown below:

$$UD(E_F)^2\delta E^2 > D(E_F)\delta E^2 \rightarrow UD(E_F) \geq 1 \tag{1.31}$$

1.4.5 Magnetic Anisotropy

Despite extensive discussions on symmetry, bonding, and the crystal field in perovskite systems, we have thus far largely ignored the effects of the crystal symmetry on the magnetism. It is, however, not necessarily reasonable to assume that something as anisotropic as a crystal system will behave completely isotropically magnetically. In fact, the crystal anisotropy has profound effects on the behavior of the final magnetic state. Therefore, we will conclude this section with a brief discussion on the origins of magnetocrystalline anisotropy, referring once more to the textbooks of Stohr and Coey.[23, 141] In order for a crystal lattice to impose anisotropy on the spin moments of the system, there must be an interaction linking the two parameters. We find this link in the coupling between the spin magnetic moment of the atoms, which are not tied to the lattice, and the orbital magnetic moments, which are stronly tied to the lattice.

A cursory examination of the bonded d-orbital wave functions reveals that they are entirely real. The angular momentum operator, however, is a complex function. This requires, therefore, that bonded orbitals carry no orbital angular momentum, and the orbital magnetic moment of the system is said to be quenched. How then can a spin-orbit action be realized in such a system? The Bruno model of magnetocrystalline anisotropy describes the spin orbit action as:

$$H_{Spin-Orbit} = \delta(\overrightarrow{L} \bullet \overrightarrow{S}) \tag{1.32}$$

where L is the orbital angular momentum and S is the spin angular momentum, and δ represents the strength of the interaction. We may divine a clue to the sign of the parameter δ by consulting the well known Hund's rules, which govern the electron configuration of an atom and say that the lowest energy configuration will:
1. Maximize the spin quantum number S
2. Secondarily will maximize the orbital angular momentum L
3a. If the electron energy levels are less than half full, minimize the total angular momentum J. This requires that S and L be antiparallel.
3b. If the electron energy levels are more than half full, maximize the total angular momentum J. This requires that S and L be parallel.

With a shell that is less than half filled, δ is positive so that

$$\begin{aligned} \overrightarrow{L} \bullet \overrightarrow{S} &< 0 \\ H_{Spin-Orbit} = \delta(\overrightarrow{L} \bullet \overrightarrow{S}) &< 0 \end{aligned} \tag{1.33}$$

However in a system with a shell that is more than half filled, δ is negative so that

$$\begin{aligned} \overrightarrow{L} \bullet \overrightarrow{S} &> 0 \\ H_{Spin-Orbit} = \delta(\overrightarrow{L} \bullet \overrightarrow{S}) &< 0 \end{aligned} \tag{1.34}$$

Finally, it is known that the total magnetic moment of an atom may be expressed as

$$\overrightarrow{m} = -\frac{\mu_B}{\hbar}(\overrightarrow{L} + 2\overrightarrow{S}) \tag{1.35}$$

so that the magnetic moment associated with either L or S points in the opposite direction of their respective quantum numbers. Thus the energy of a less than half-filled system may be reduced by the introduction of an orbital magnetic moment aligned antiparallel to the spin magnetic moment. The energy of a more than half-filled system may be reduced by the introduction of an orbital magnetic moment aligned parallel to the spin magnetic moment. The spin moment in a magnetic system therefore perturbs the bonding orbitals so that the orbital angular moment is not entirely quenched. Due to the anisotropic nature of bonded d-orbitals, however, the magnitude of the resulting angular momentum will itself be anisotropic. Thus magnetocrystalline anisotropy emerges because the system has a lower energy when magnetized along axes with larger L. Of course, the model becomes significantly more complex when dealing with energy shells which are split by a crystal field, but the general principles may still be applied.

The strength of magnetocrystalline anisotropy scales with the strength of the spin-orbit interaction. Spin-orbit interaction is a result of the motion of the electrons about the nuclei. In the electron reference frame, the nuclei are moving charges which create a magnetic field, which interact with the electron spin. Because a larger nuclear charge will create a larger apparent magnetic field in the electron frame of reference, the strength of the interaction increases with Z, the nuclear charge. In fact, the spin orbit splitting energy generally scales as Z^4. Thus, spin-orbit effects are far more pronounced in $4d$, $5d$, $4f$, and $5f$ systems than in the $3d$.

1.5 Controlling Magnetism in Transition Metal Oxide Thin Films

As demonstrated in the preceding sections, transition metal oxides based on the perovskite structure exhibit a vast array of magnetic and electron ground states. The flexibility of these materials in terms of structure, valence, and bonding makes them excellent candidates for the stabilization of novel magnetic ground states as well as ideal model systems for the exploration of the interrelationship between magnetism, stoichiometry, defect, and distortions. Growing transition metal oxides in thin film form yields a number of ways by which we can tune these parameters, and in this dissertation we will focus on strain, interfacial electronic reconstruction, and, to a lesser degree, defects.

Strain, or substrate induced lattice distortions are perhaps the simplest and most direct method by which we may tune the properties of thin films. At its most basic, strain may

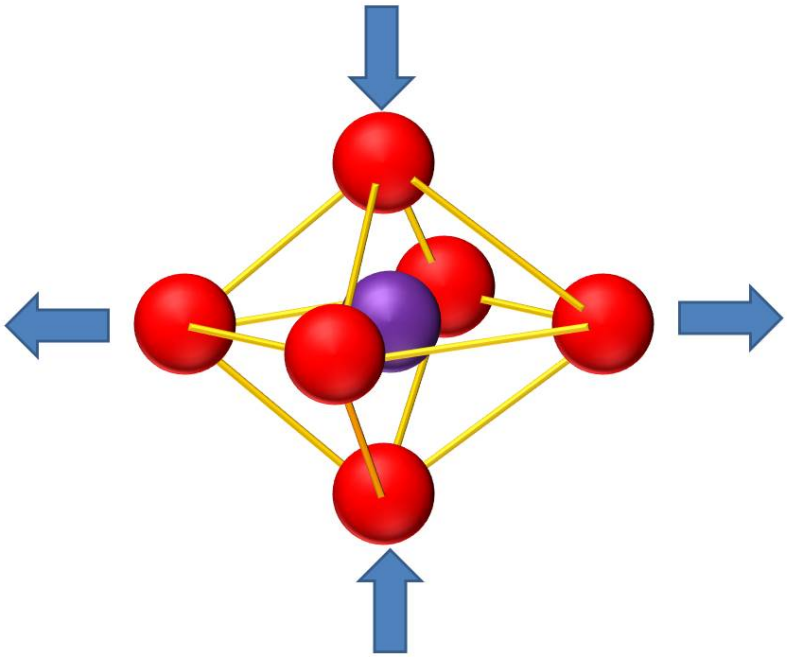

Figure 1.7: A simple picture of a strain distorted perovskite structure

be thought of as a competition between coherent epitaxial growth, where, bonding occurs across the film-substrate interface, and the energetic favorability of the film's natural crystal structure. In a coherently strained film, it costs more energy to have dangling bonds at the interface than to distort the crystal structure of the film to match that of the substrate along the growth direction. In fact, the energetic favorability of epitaxy is often so strong that it often contributes to the stabilization of crystal structures which would otherwise the thermodynamically unstable.

Although the most naive picture of strain accommodation can be found in Figure 1.7, in which the bonds simply stretch and contract to accommodate the imposed lattice parameter, it is often much easier to bend a spring than to stretch it. Similarly, strain may result in higher order alterations to a perovskite system such as rotation of the oxygen octahedral. Similarly, the introduction of oxygen or cation vacancies can shrink or expand the film unit cell to relieve strain. In extreme cases microstructural effects such as roughening of the film surface or even cracking can also occur. As film thickness increases, the energy associated with the structural distortion grows rapidly while the energy associated with dangling bonds at the interface remains constant. Thus, at some thickness relaxation will begin, frequently (but not always) in the form of misfit dislocations at the film-substrate interface. Commonly, there is a thickness regime of partial relaxation which may take the form of a strain gradient throughout the film or an intermediate number of interfacial defects which are not sufficient to completely relax the film.

Strain may have a significant effect on magnetic properties either through the alteration of stoichiometry, the introduction of defects, or through the alteration of bonding. It is this last mechanism which is most commonly cited and easiest to control. Lattice distortions, either through the alterations of bond lengths or angles, can significantly affect the orbital

overlap in the system, which has profound implications for the exchange interactions.

It has also been demonstrated that electronic interactions or reconstruction across interfaces may result in the stabilization of magnetic and electronic states not present in bulk systems. This may take the form of a simple exchange interaction as in the case of $LaFeO_3/LaCrO_3$ superlattices where the Goodenough-Kanamori rules predict ferromagnetic exchange. However, electronic reconstruction may also be driven by polar interfaces as in $LaAlO_3/SrTiO_3$ thin films where a highly conductive layer manifests at the interface. As will be discussed in chapters 6 and 7, electron leakage from a metal into an insulator may allow an interfacial double exchange interaction to stabilize ferromagnetism in a bulk antiferromagnet.

Interfacial electronic interactions are among the most difficult to describe theoretically, often requiring extensive density functional theory calculations to develop an understanding of the underlying band structure. It is also often difficult to separate such effects from those of defects or intermixing at the interface. These defects arise concurrently with both heteroepitaxy and epitaxial strain, and throughout this work we will endeavor to isolate the contributions of strain, interfaces, and defects to better understand the magnetic interactions in thin films and superlattices of transition metal oxides.

1.6 Thesis Goals and Chapter Summary

Chapter 1 has focused on the introduction of transition metal perovskite oxides. Throughout this chapter, we have seen the basic reasons, both structural and compositional, for the variety and tunability of electronic and magnetic properties in these systems. Chapter 1 also laid the groundwork for understanding magnetic coupling of these systems in terms of superexchange, double exchange, and itinerant ferromagnetism. Finally, chapter 1 discussed methods by which the magnetism in these systems may be tuned. Chapter 2 will continue to build a framework for probing magnetism in transition metal oxide thin films by discussing the experimental techniques used throughout the work. The experimental methods will be broadly divided into four sections: growth, structural characterization, magnetic characterization, and electron transport. Particular emphasis will be devoted, both in chapter 2 and the appendices, to a detailed description of the more exotic magnetic characterization techniques of X-ray magnetic circular dichroism, neutron diffraction, and neutron reflectometry. When combined with SQUID magnetometry, these three techniques allow for a characterization of the magnetic properties of the film as a whole, of individual elements, and a complete construction of the magnetic depth profile. Thus, a complete picture of the magnetic properties can be formed.

The next section comprises chapters 3-5 and uses $SrRuO_3$, a unique example of $4d$ itinerant ferromagnetism in the transition metal oxides, as a model system in which to isolate the effects of strain on the magnetic properties due to the increased sensitivity of a $4d$ to changes in bonding. Chapter 3 introduces $SrRuO_3$ in general and discusses the growth and characterization of the simplest case of $SrRuO_3$ films on (100) oriented substrates. The effects of strain on the magnetic properties will be investigated for a wide variety of strain magnitudes. Specific emphasis will be placed on separating the effects of substrate induced lattice distortions from those of stoichiometric variations, structural variations, and surface effects. We will see that strain can significantly affect both the saturated magnetic moment

and Curie temperature of $SrRuO_3$ thin films. Chapter 4 will explore other distortion symmetries. While chapter 3 focused on the (largely) tetragonal distortion on (100) films, chapter 4 will concentrate on films in the (110) and (111) orientation, which induce orthorhombic and trigonal distortions, respectively. We will see that the *symmetry* of an applied distortion is sometimes even more important than the magnitude of the resulting strain. On (111) oriented films, a spin transition will be reported for the first time in $SrRuO_3$. Chapter 5 will complete the discussion of $SrRuO_3$ by examining the effects of strain on the film anisotropy in all orientations. We will see that a very strong uniaxial magnetic easy axis may be induced along in-plane or growth axes of all films, regardless of crystallographic orientation. Finally, we will establish a coherent framework by which all of these different effects may be understood.

The final section will discuss interfacial ferromagnetism in $CaMnO_3$-based superlattices. Chapter 6 will introduce the physics of $CaRuO_3/CaMnO_3$ based superlattices, in which a ferromagnetic moment has been reported at the interface between paramagnetic $CaRuO_3$ and antiferromagnetic $CaMnO_3$. Current roadblocks to the understanding of the "interfacial" ferromagnetism, primarily the potential for intermixing and the difficulty of decisively locating the magnetism at the interface, will be discussed and approached through neutron scattering measurements. By applying neutron reflectometry, the precise magnetic depth profile of the films will be elucidated. Interlayer coupling will also be examined by using neutron diffraction to probe some very interesting magnetic phenomena recently reported. In chapter 7, an alternative candidate system for the stabilization of interfacial ferromagnetism in $LaNiO_3/CaMnO_3$ superlattices, will be studied. Utilizing the thickness dependent metal insulator transition of $LaNiO_3$, the electronic structure of the interface can be changed independently of intermixing and other factors. Consequently, it will be decisively demonstrated that the observed ferromagnetic signal is due to interfacial electronic effects.

As a whole, this work demonstrates two different methods by which complex oxide heterostructures can be used to generate phenomena not observed in bulk: epitaxial strain and interface reconstruction. We also isolate the contributions of strain and reconstruction from those of defects, off-stoichiometry, and alloying. We will demonstrate unprecedented control over the magnetic ground state of $SrRuO_3$ using strain, yielding a completely tunable uniaxial magnetic anisotropy and saturated magnetic moment. We will present the first ever reported transitions to high-spin and zero-spin states in Ru. For the first time, we will definitively isolate the interfacial ferromagnetism reported in $CaRuO_3/CaMnO_3$ superlattices to a single unit cell at the interface. We find surprising new mechanisms for the oscillatory magnetic moment also recently reported in this system, including remarkable differences in the structural half-order and long range antiferromagnetic order which passes through intervening paramagnetic superlattice layers. Finally, we show, for the first time, interfacial ferromagnetism in $LaNiO_3/CaMnO_3$ superlattices. This interfacial ferromagnetism is demonstrated to be inextricably linked to the conducting state of $LaNiO_3$ through the use of a thickness dependent metal insulator transition, conclusively eliminating intermixing as a possible explanation for the ferromagnetic signal. These observations represent a significant advance in our ability to tune magnetic properties at the nanoscale.

Chapter 2

Experimental Methods

Having established much of the underlying physics behind magnetic ordering in the transition metal complex oxides in chapter 1, we must now discuss the various techniques used to explore these materials. These techniques fall into five broad categories - thin film growth, structural characterization, stoichiometry and valence, and magnetic characterization. We will explain how these techniques are used to deposit our thin films, extract their crystal structure and strain state, ensure correct stoichiometry and oxygen content. We will describe a wealth of techniques for magnetic characterization that allow us to probe the magnetic properties of an entire film or a single element and reconstruct the magnetic depth profile. Finally, we will discuss various electrical characterization techniques before moving on to the first of our model systems in chapter 3.

2.1 Thin Film Growth

2.1.1 Pulsed Laser Deposition

Since first used for the fabrication of thin films of high temperature superconductors in 1987, in which precise stoichiometric control of complex alloys is highly desirable, pulsed laser deposition has become one of the most popular techniques used to fabricate high quality epitaxial thin films of transition metal oxides, including many perovskites.[155, 135] The reason for the rapid popularization of the technique is primarily the ability to precisely obtain complex stoichiometries.[155, 135, 22, 112] For such precision, pulsed laser deposition relies on the highly stoichiometric transfer to the substrate from ceramic targets containing precisely the composition of elements desired in the final sample.[135] These targets are typically composed of finely ground oxides of the desired elements sintered together through the application of high temperature and pressure. Ideally, the targets should be as uniform and dense as possible, containing no air pockets. The target is then placed in a vacuum chamber and illuminated with short pulses high intensity pulses of ultraviolet light from an excimer laser. Films are typically deposited using an ultraviolet laser with a pulse duration of 25-40 ns at a fluence between 1.0-2.0 J/cm^2, resulting in applied power densities of 40-80 MW/cm^2 on the surface of the target.[22] This immense power application results in bond dissociation and the formation of a high temperature plasma at the region of absorption. This plasma forms a highly directional "plume" of material which, to first order, travels

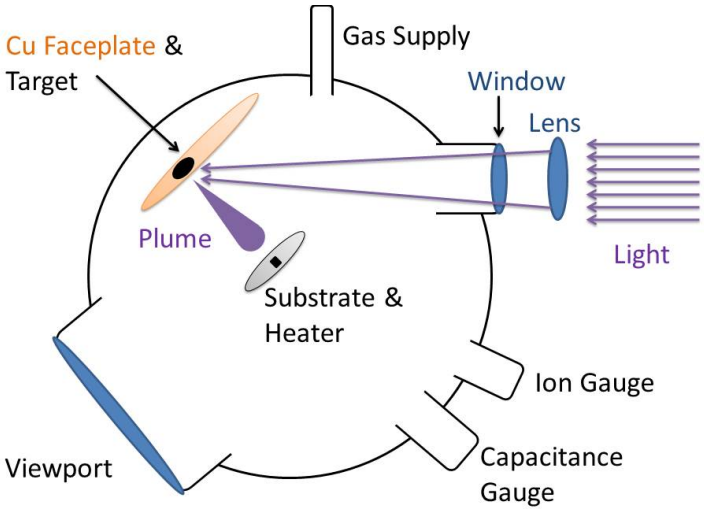

Figure 2.1: Schematic of one pulsed laser deposition chamber used to fabricate samples for this work

perpendicular to the target surface. More precisely, the plume deposition density takes the form

$$Density \sim cos^n(\theta) \tag{2.1}$$

where n may vary over a wide range from 4-30.[112]. Such a strong directionality requires that a substrate be placed precisely in the center of the plume's path to capture the material for deposition. Any deviation may result in nonuniform deposition deviation from the desired stoichiometry. An additional limitation imposed by the directionality of the plume is the limited size of the sample produced. Across substrates larger than 1 cm^2 significant variations in film thickness may be produced.[112] There are geometries that may allow this limitation to be circumvented, but they require specialized equipment and are difficult to achieve consistently.[112]

If a number of conditions are met, the extreme power density represented by the laser pulse results in a highly stoichiometric transfer of material from target to substrate. First, the target material must be able to absorb all of the pulse energy in a very shallow area at the surface. That is, the material absorption at the laser wavelength must be relatively high.[112] Thus, materials with a band gap in excess of 5 eV generally cannot be ablated using a 248nm UV laser. At the other end of the spectrum, metals with a sufficiently high plasma frequency may reflect the light rather than absorb it. In addition, low thermal conductivity is highly desirable to concentrate the thermal energy at the surface of the target. Finally, stoichiometry may not be effectively transferred if the substrate is not in the center of the plume, as off-axis components may contain slightly different elemental ratios.

A final consideration in pulsed laser deposition is the control of oxygen content in the films. Even if the target begins with the desired oxygen content, the high energy deposition process and volatile nature of oxygen make oxygen loss common. In order to return the

oxygen content to the desired value, films are frequently deposited in an ambient oxygen atmosphere. In some cases, annealing in atmospheric oxygen pressure is necessary to capture the desired stoichiometry. Oxygen pressure, or even growth in more reactive atmospheres such as ozone, can also be used as a tool for controlling valence states.[112] The addition of such a background gas offers the additional advantage of interacting with and reducing the velocity of incoming atomic species. Without a background gas, the high energy plume may sputter and reduce the newly deposited surface of the film, but the dissipation of kinetic energy by a background gas significantly alleviates this concern.[135, 112]

Thus, all samples discussed in this work were deposited using pulsed laser deposition with a 248 nm KrF excimer laser illuminating sintered polycrystalline targets. The laser pulse rate was varied between 1-3 Hz with a pulse length of 25 ns and a per-pulse energy of 130-175 mJ. The laser beam was focused to a spot size of 10-12 mm^2, resulting in a fluence of 1.2-1.5 J/cm^2. The ambient oxygen pressure was varied between 30-60 mtorr. Films were affixed to a heater and maintained at a temperature of 700 °C throughout growth.

2.1.2 Reflection High Energy Electron Diffraction

We use reflection high energy electron diffraction for in-situ monitoring of film growth rates and surface quality.[91] Formerly limited to extremely low-pressure deposition techniques such as molecular beam epitaxy, reflection high energy electron diffraction (RHEED) has been increasingly incorporated into higher pressure applications through the application of differential pumping techniques to create a localized low pressure environment around the filament of the electron gun.[126] The RHEED system used is operated at 2.2 A and 20 keV and directs an electron beam at grazing incidence (approx. 3°) to the sample. The electron beam diffracts off the sample surface onto a phosphor screen, as shown in Figure 2.2(a). Maintaining a very shallow grazing angle results in a surface sensitive, essentially two dimensional, diffraction pattern. As demonstrated by the shape of the diffraction spots in Figure 2.2(b), this results in "rods" in reciprocal space, rather than points. The intensity of the diffraction pattern is extremely sensitive to changes in the surface quality, and it is consequently possible to observe oscillations in the peak brightness during layer by layer growth of many oxides, as shown in Figure 2.2(c). The slight roughening of the surface as an atomic layer is deposited and the reduction in roughness as it is completed are accompanied by an oscillation in the RHEED intensity. Thus we can determine the precise thickness of a given layer in real time.

It is important to note that this technique is useful only in the case of layer-by-layer growth. Step-flow growth is typically manifested only as steady or slowly decreasing signal intensity while island growth will typically destroy the diffraction pattern very rapidly due to the extreme sensitivity to surface roughness. In fact, RHEED systems will generally not produce diffraction patterns from films or superlattices with root-mean-square roughnesses significantly greater than a single perovskite unit cell (4 Å). In this dissertation, all deposited superlattices of $CaRuO_3/CaMnO_3$ and $LaNiO_3/CaMnO_3$ were monitored using the RHEED while single films of $CaRuO_3$ and $SrRuO_3$ were not.

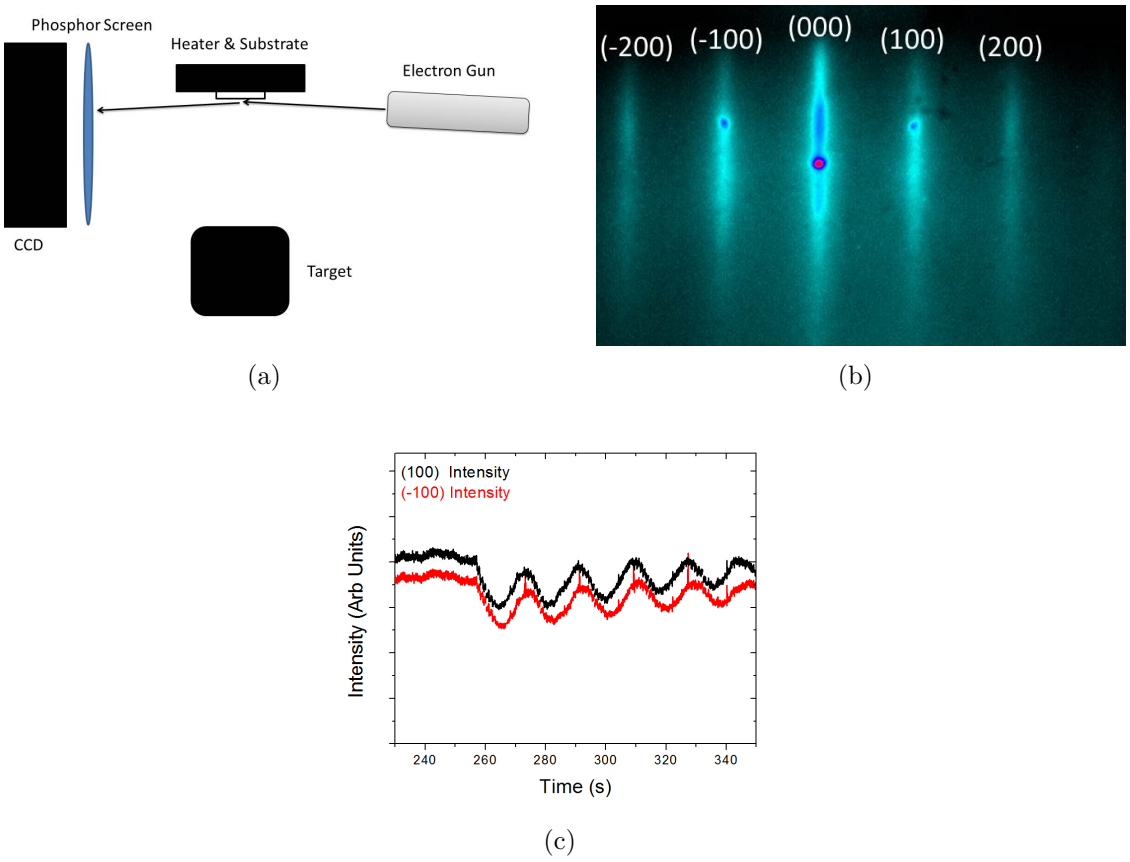

(a) (b)

(c)

Figure 2.2: a) Schematic RHEED setup. b) Typical RHEED diffraction pattern from a film during deposition. c) Oscillation of the intensity of the $(\bar{1}00)$ and (100) reflections for a typical $LaAlO_3/LaNiO_3$ superlattice during deposition.

2.2 Structural Characterization

All of the fabricated films were characterized using a variety of techniques in order to ensure epitaxial, high quality crystal growth of the desired thin film material, as summarized below. We used atomic force microscopy to determine surface morphology and microstructure of the films. Structural information such as film quality, mosaicity, strain state, and lattice parameters were obtained through X-ray diffraction. Film thickness was obtained through X-ray reflectometry. Finally, in some cases, scanning transmission electron microscopy was utilized to confirm crystal registry across interfaces.

2.2.1 Atomic Force Microscopy

Atomic force microscopy is a technique which uses an extremely sharp Si probe scanned across the film surface to make a topographical map of the surface. To probe our sample surface morphology, we used a Dimension 3100 atomic force microscope (AFM) operating in tapping mode. In tapping mode AFM, a long, narrow tip mounted on a vertically oscillating Si cantilever is lowered into close proximity with the sample surface using a piezoelectric scanning crystal for precision motion control.[58] Before being lowered, the cantilever and tip are tuned and driven to oscillate near their resonant frequency. As the tip approaches the surface, contact between the tip and the surface begins to damp the oscillation of the cantilever. The tip continues to approach the sample surface until the amplitude of the oscillation has been reduced to a pre-defined value selected for good surface contact. At this point, the tip is scanned across the surface of the sample, and the cantilever is raised and lowered to maintain the oscillation amplitude at a constant value. By tracking the vertical position of the cantilever, the AFM forms a topographical map of the sample surface. By operating in tapping mode, rather than contact mode, we avoid exerting potentially damaging lateral forces on the tip and sample as the probe moves across the surface. A basic schematic of this mode of operation can be seen in Figure 2.3.

For characterization throughout this dissertation, cantilevers were tuned to find their resonant frequency and then driven at a frequency which results in a 5% reduction relative to the amplitude precisely on-resonance, typically 250-350 kHz. Cantilever oscillations were then driven such that the undamped amplitude registered 2.5 V on the detector. Contact was generally achieved once the amplitude was reduced to 1.7-1.9 V, at which point the setpoint was usually reduced manually to 1.5-1.7 V to ensure the tip would not lose contact as it scanned across the surface.

2.2.2 X-Ray Diffraction

We used X-ray diffraction iin a veriety of geometries to probe the crystal structure, crystal quality, and strain state of our thin films and superlattices. The X-ray diffraction scans utilized to accomplish this in this dissertation generally fall into one of three categories: θ-2θ scans, ω rocking curves, and reciprocal lattice maps. Before each of these techniques is described in detail, it is necessary to review the fundamentals of diffraction in thin films. Although not intended to be a comprehensive guide, this work will often follow the method of B.D. Cullity, which the reader may find to be an excellent reference for the basics of X-ray

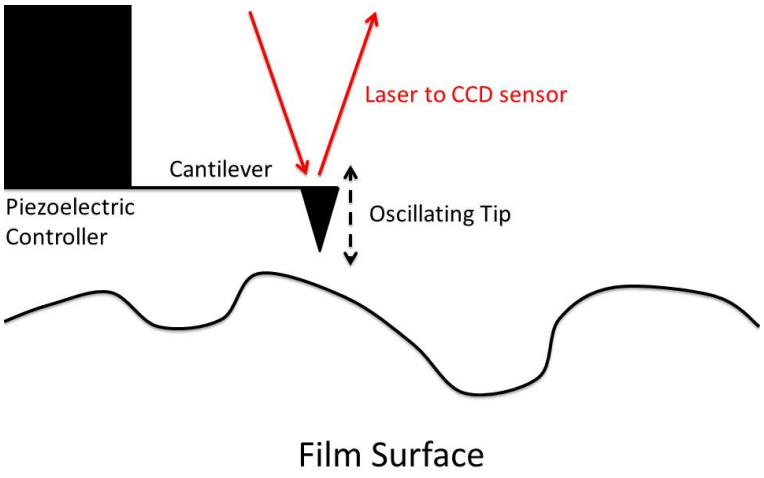

Figure 2.3: Tapping mode atomic force microscopy

diffraction.[24] The diffraction condition is most simply described by Bragg's Law, which treats the problem as one of interference and reflection off atomic planes.

$$n\lambda = 2d\sin\theta \tag{2.2}$$

where n is any positive integer, λ is the wavelength of the incoming light, d is the spacing of the diffracting atomic planes, and θ is the angle that the direction of photon propagation makes with the "reflecting" planes of atoms. Despite the usefulness of Bragg's Law, it is often more useful to treat the problem in directly in reciprocal space and phrase the diffraction condition as:

$$\overrightarrow{G}_{hkl} = \frac{2\pi}{\lambda}(\overrightarrow{k}' - \overrightarrow{k}) \tag{2.3}$$

where $\overrightarrow{G}_{hkl}$ is the reciprocal lattice vector associated with the hkl reflection, $\overrightarrow{k}'$ is the wave vector of the diffracted photon, and $\overrightarrow{k}$ is the wave vector of the incoming light. Thus, the diffraction process can be represented using the Ewald sphere construction as demonstrated in Figure 2.4, which shows diffraction from the (200) planes. In Figure 2.4, we can see other features of note in thin film diffraction; the reciprocal lattice points are narrow along the film in-plane direction but elongated along the growth axis. This is a result of the reduced dimensionality of thin films along the growth axis. Additionally, in thin film diffraction one will frequently vary the angle of the incoming beam relative to the film axis, hereafter referred to as ω, independently from the diffraction angle 2θ.

However, we will first consider the simplest case of a $\theta - 2\theta$ or $\omega - 2\theta$ scan in which ω is always defined to be equal to θ. In this case one scans across a line in reciprocal lattice space which encompasses all reciprocal lattice points along the film growth axis i.e. (100), (200), (300),... in the case of a (100) oriented film. Scans of this type are used throughout this dissertation to determine the film lattice parameter along the growth axis, to demonstrate

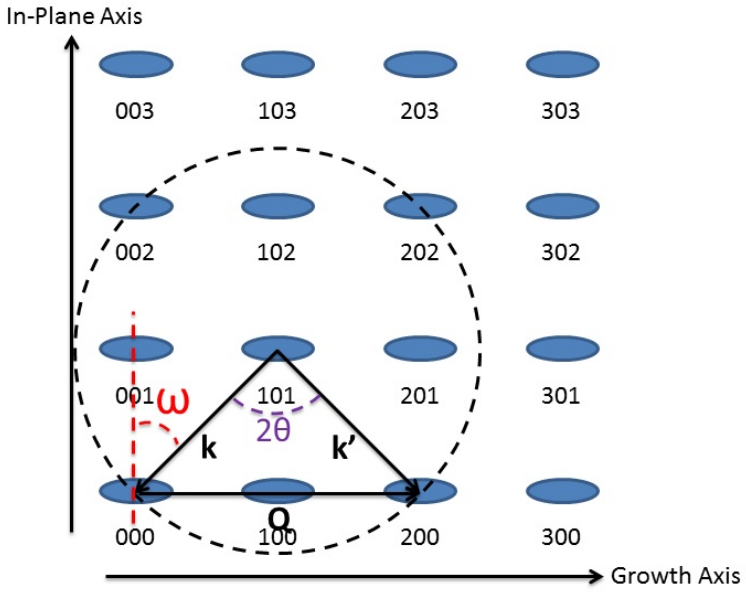

Figure 2.4: Ewald sphere construction of thin film X-ray diffraction

that the films are epitaxial and have a preferential growth axis, and to search for undesired phases of the deposited material.

The second type of XRD scan commonly performed on the prepared samples was an ω-rocking curve. In a rocking curve, a single parameter is changed while all others are held constant. In this case, the diffracted beam detector is set for diffraction from a given peak while ω is rocked around a small range passing through the ideal diffraction condition. This allows us to measure the mosaic spread of our films - a measure of the uniformity of alignment of the diffracting planes. More defective films typically have a greater degree of misalignment and consequently a larger mosaic spread.

Information about the in-plane and out-of-plane strain state was obtained using a reciprocal lattice map obtained by performing a series of ω rocking curves at different θ values near the diffraction condition for a reciprocal lattice point. Reciprocal lattice points containing information on both the in-plane and growth axis lattice parameters were chosen such that by mapping out the entire reciprocal lattice point both the in-plane and out-of-plane lattice parameters could be extracted. In order to present such a plane for diffraction it is generally necessary to introduce a significant ω offset prior to film measurement. The real and reciprocal space constructions for such a reciprocal lattice map are shown in Figure 2.5a and 2.5b, respectively.

All X-ray diffraction measurements were taken using Cu K_α radiation from an X'Pert Materials Research Diffractometer (MRD) operating at 45 kV and 40 mA. The MRD is a four circle diffractometer, with the ability to independently vary the four angular parameters ω, θ, ϕ, and ψ. These parameters are shown and geometrically defined below in Figure 2.6. In this work, however, the primary parameters of interest will continue to be ω and θ, as described above, with ϕ and ψ utilized primary for alignment purposes and correcting sample offsets.

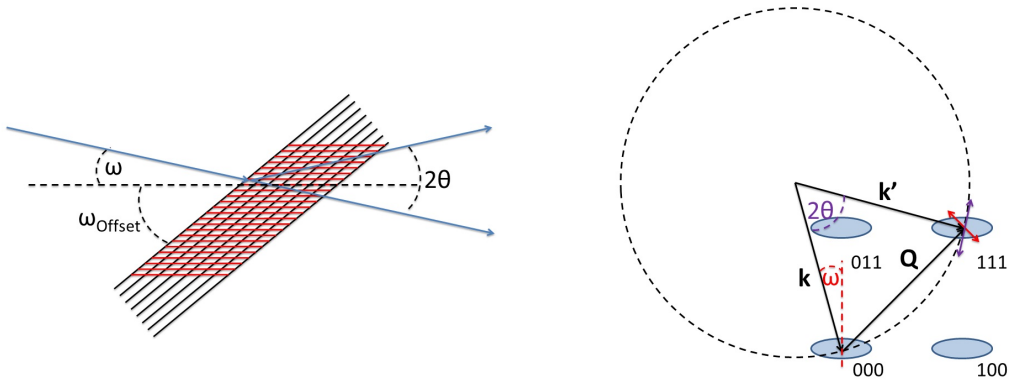

(a) (b)

Figure 2.5: a) Real and b) reciprocal space construction of reciprocal space mapping with component along the growth and film axes

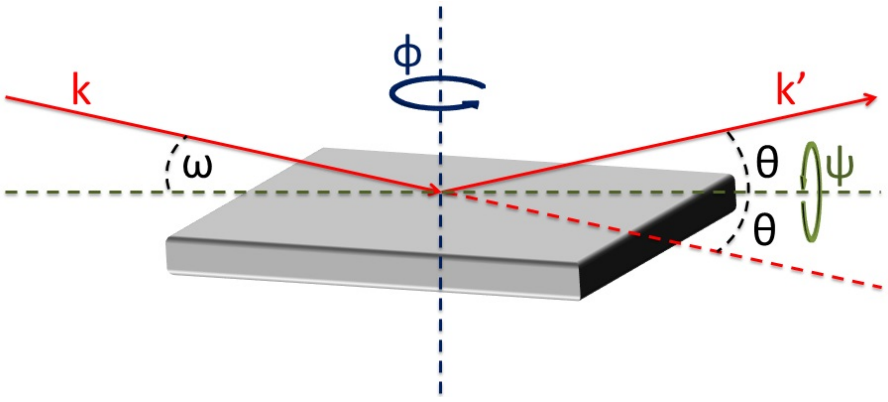

Figure 2.6: X-Ray diffraction geometry

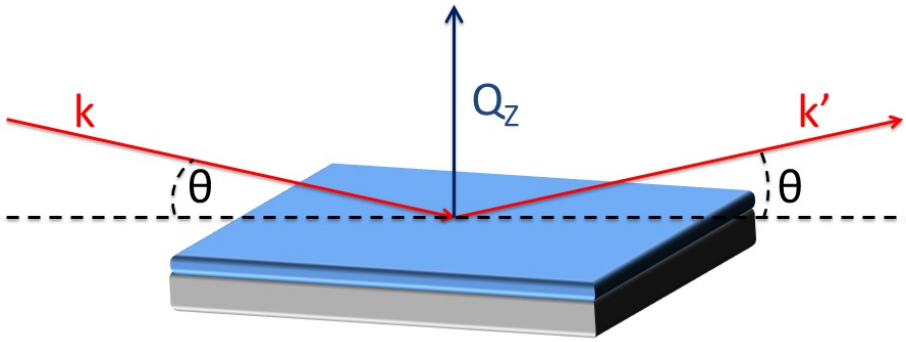

Figure 2.7: X-Ray reflectometry geometry

Finally, in some cases additional intensity was required to resolve diffraction peaks from ultrathin layers, orthorhombic distortions, or other fine structure. In these cases, X-ray diffraction was performed at beamline 2-1 of the Stanford Synchrotron Radiation Laboratory (SSRL) at the SLAC National Accelerator Laboratory. The much higher internsity available at SSRL allows the resolution of features normally inacessible using a traditional X-ray diffractometer. All measurements at SSRL, as well a several of the reciprocal lattice maps, were taken by Dr. Arturas Vailionis of Stanford University and the SLAC National Accelerator Laboratory.

2.2.3 X-Ray Reflectometry

X-ray reflectometry (XRR) is a low angle of incidence X-ray scattering technique which enables us to reconstruct a depth profile of the photon scattering length density in a thin film.[20] An X-ray beam incident on any interface above the critical angle will be partially reflected and partially transmitted. In this condition an X-ray beam reflected from a thin film or superlattice with multiple interfaces (air/film, film/substrate, etc.) will exhibit interference from reflections at the various interfaces. X-ray reflectometry measures total film reflectivity as a function of incident angle and uses the resulting interference patterns to probe the film depth profile. In this section, we will draw from a number of sources and attempt to describe the basic physics of X-ray reflectometry. For a more complete description of the technique, the reader is encouraged to consult the associated references.[20, 68, 27, 164]

X-ray reflectometry scans must be performed at angles very near the critical angle, as the total reflectivity falls rapidly with increasing angle and is proportional to Q_Z^{-4}, where Q_Z is the scattering vector. In this work we are concerned only with specular reflectivity in which the incident and final angle are equal and all of the momentum transfer occurs in the direction of the film normal. In this condition the momentum transfer for a given wavelength is

$$Q_Z = \frac{4\pi}{\lambda} \sin\theta \tag{2.4}$$

where λ is the photon wavelength and θ is the incident angle. This geometry can be seen in Figure 2.7.

X-ray reflection occurs at interfaces, which appear as a discontinuity in the film depth profile. When we say depth profile, of course, we are referring to the depth profile of the film index of refraction, which is itself almost entirely determined by the electron density, as shown below:

$$n = 1 - \delta - i\beta \tag{2.5}$$

where n is the index of refraction, δ is a real number defined below, and β is the complex portion of the index of refraction, which represents the absorption of a material and is also defined below.

$$\delta = \frac{\rho_e r_e \lambda^2}{2\pi} \tag{2.6}$$

$$\beta = \frac{\mu\lambda}{4\pi} \tag{2.7}$$

where ρ_e is the electron volume density, r_e is the classical electron radius, λ is the photon wavelength, and μ is the linear absorption coefficient of the material. In general, we would like to neglect absorption effects, but before we may do so we must first show that the skin depth, the distance a photon beam must travel in a material in order to reduce its intensity by a factor of e, is much greater than the thickness of the film. For all materials examined in this work, the skin depth of the Cu K_α radiation used is expected to be on the order of 7-30 microns.[56] Obviously this is several orders of magnitude larger than the thickness of our films, which in general range from 10-120 nm thick in this dissertation. However, the actual distance traveled in the film is a function of the very shallow incoming angle and may be calculated as

$$d = \frac{l \times Sin(\theta)}{2} \tag{2.8}$$

where d is the depth at which the intensity of a subsurface is reduced by e and l is the skin depth of the material. The factor of two is introduced because a photon must travel into the film, reflect off a buried interface, and then exit the film. For a typical critical edge appearing around 0.3°, d is between 25-75 nm. At this angle, we clearly may not ignore the effects of absorption for most films. However, the issue improves significantly with increasing angle of incidence, and for a scan that goes out to 6 degrees, d reaches a value of 130-390 nm. Thus, for a significant majority of a typical spectrum, absorption plays only a minor role. However, features near the critical edge probe subsurface interfaces much more weakly and it is therefore unsurprising that interference features near the critical edge are much weaker than those at higher angles. Fortunately, analysis software exists which can easily take these effects into account in simulations and we will not address absorption effects further.

We now turn to the physics of reflection itself. The simplest method for representing reflections is through a plane wave model. Thus, in the air above the sample, the photons may be represented as

$$\Psi_0 = e^{ik_0 z} + re^{-ik_0 z} \tag{2.9}$$

where k_0 is the wavevector in air and r is the magnitude of the reflected plane wave. Thus we have represented the wave vector in the air as an incoming plane with with amplitude 1 and a reflected plane wave with amplitude r. Inside the film, the transmitted portion of the plane wave is written

$$\Psi_1 = te^{ik_1 z} \tag{2.10}$$

where $k_1 = n_1 k_0$ is the wave vector in medium 1. Now, simply by enforcing continuity of the wave function and its derivative at the interface (z = 0) we may find the magnitude of the reflected wave.

$$\Psi_0(0) = \Psi_1(0) \rightarrow 1 + r = t \tag{2.11}$$

and

$$\frac{\partial \Psi_0}{\partial t} = \partial \Psi_1 \partial t \rightarrow ik_0(1 - r) = ik_1 t \tag{2.12}$$

thus

$$r = \frac{k_0 - k_1}{k_0 + k_1} \tag{2.13}$$

The reflectivity of a single interface is

$$R = r^* r = \left(\frac{k_0 - k_1}{k_0 + k_1}\right)^* \left(\frac{k_0 - k_1}{k_0 + k_1}\right) = \left(\frac{n_0 - n_1}{n_0 + n_1}\right)^* \left(\frac{n_0 - n_1}{n_0 + n_1}\right) \tag{2.14}$$

Thus we have an expression for the intensity of a reflection from the surface of a film. This, however, gives us very little information about the film. To do that, we must add a reflection from an interface - that of the film and substrate. Clearly, the reflection from this interface may be treated identically to that of the air-film interface, with four major exceptions. First, the intensity of the beam is reduced by the surface reflection. Near the critical angle this is a large factor, while at higher angles it is almost completely negligible. Second, the transmitted beam is attenuated by passing through the film. Again, this is much more significant near the critical edge. Third, the difference in refractive indices for an oxide-oxide interface is much smaller than that of an air-oxide interface. This will reduce the magnitude of the reflection globally. Fourth, there may be additional reflection at the oxide air interface as the X-ray beam makes it's way out of the film. We will generally ignore this second order effect (and the infinite higher order effects propagating from it). In the end, the film/substrate contribution may be written as

$$(1 - R)\left(\frac{n_{film} - n_{sub}}{n_{film} + n_{sub}}\right) e^{-ik_0(z+\phi)} A(\theta) \tag{2.15}$$

where ϕ is the phase difference associated with travel through the film to the substrate and back to the surface. ϕ is given by

$$\phi = 2tSin(\theta) \tag{2.16}$$

thus it is clear that in a single layer thin film sample the interference takes the form of Kiessig fringes, oscillations in the total reflectivity with a frequency in Q_Z which is related to the layer thickness (t) by a factor of $2\pi/t$. In a bilayer film, several oscillations will be superimposed, each corresponding to the thickness of one of the layers or the total thickness of the film. Finally, superlattices will exhibit thickness fringes corresponding to total thickness in addition to a series of Bragg peaks at Q_Z values corresponding to the superlattice period. These superlattice reflections are referred to as Bragg peaks because they share an important property with diffraction peaks. Because of the large number of superlattice periods in a given sample, the reflections from all superlattice interfaces tend to cancel out unless the transferred reciprocal lattice vector is precisely associated with the superlattice period. The intensity of these Bragg peaks is proportional to the square of the number of superlattice repetitions, and the more reflections there are, the sharper the peaks will be.

Many factors other than thickness influence the observed reflectivity spectra. Among the most important of these is the nonuniformity of the interface, which can take the form of surface roughness, thickness variations across the substrate, or interdiffusion. Whatever the mechanism, a decrease in the sharpness of an interface will reduce the intensity of the Kiessig fringes and superlattice peaks as well as the intensity of the reflectivity spectrum as a whole. Thus we can use XRR to determine the thickness or periodicity of thin films and superlattices. The reflectivity of a rough interface may be related to that of a perfectly sharp interface by

$$R = R_{Sharp} e^{(-2k_Z k'_Z \sigma^2)} \tag{2.17}$$

where k_Z and k_Z' are the photon wave vector above and below the interface and σ is the RMS roughness of the interface.

Thus, we have seen that although X-ray reflectivity is extremely simple in theory, there are many, many complicating factors ranging from absorption to large numbers of interfaces to higher order reflections. Although these factors are easily understood individually, when combined they result in spectra which are very complex to analyze and simulate. Fortunately, there are many excellent programs available for this purpose and by fitting the XRR spectrum of a given sample, we can generally extract its thickness, superlattice period, and average interfacial roughness. All XRR measurements in this dissertation were performed using Cu Kα radiation from an X'Pert Materials Research Diffractometer (MRD) operating at 45 kV and 40 mA. The incident angle θ ranged from 0.1°-3°.

2.2.4 Scanning Transmission Electron Microscopy

To confirm epitaxial growth and determine the extent of intermixing at layer interfaces in our $LaNiO_3/CaMnO_3$ superlattices, scanning transmission electron microscopy (STEM) was performed. STEM is a derivative of conventional transmission electron microscopy (TEM) in which a high energy beam of electrons (100-400 keV) is transmitted through a thinned sample to obtain images with atomic-position level resolution.[143] Unlike conventional TEM, STEM utilizes a highly focused, confined electron beam which is scanned across the sample to create a complete image. This has the advantage that the electron beam passes through only a very small sample area at any given time, allowing for measurements such as energy dispersive X-

ray spectroscopy and electron energy loss spectroscopy (described later) to be performed with equally precise position resolution. Thus, samples were prepared in a cross sectional geometry and thinned first using abrasive materials and then using a focused ion beam to mill through the final 10-20 microns, leaving a region of the sample sufficiently thin for an electron beam to be transmitted through. Through alignment of the sample precisely along crystallographic axes, sample atomic columns were imaged of with sub-Angstrom resolution. Z-contrast images were obtained showing the epitaxial registry and sharpness of the interfaces. All STEM in this work was performed at Pacific Northwest National Lab by Hao Yang of the University of California, Davis.

2.3 Stoichiometry and Valence

2.3.1 Rutherford Backscattering Spectrometry

To probe film thickness and stoichiometry, we extracted the film nuclear depth profile using Rutherford backscattering spectrometry (RBS). RBS is derived from the Rutherford gold foil experiment and uses collisions between sample nuclei and high energy alpha particles to determine the depth profile. This description of RBS will largely follow that of E. Haller.[52] Helium atoms are first ionized and then accelerated to approximately 3 MeV. The thin film sample is then bombarded by these high energy alpha particles, resulting in backscattering as the helium ions encounter atomic nuclei. The energy deposited and retained by a scattered particle during RBS can largely be described through the application of "bowling ball physics".

$$K_m = \left(\frac{\sqrt{M^2 - m^2(\sin\theta)^2} + m\cos\theta}{M+m} \right)^2 \tag{2.18}$$

where K_m is the fraction of the initial kinetic energy retained by the alpha particle and consequently (1-K_m) is the fraction of the kinetic energy transferred to the impacted particle. M is the mass of the impacted particle, m is the alpha particle mass, and θ is the scattering angle ($\theta = \pi$ for perfect backscattering). In general, θ is selected to be very near total backscattering and for all of the experiments in this work $\theta \approx 168°$. Thus, the energy transferred from one particle to another in an inelastic collision can be easily calculated and is only a function of the particle masses and the scattering angle. Knowing the incoming energy and measuring the energy deposited by the backscattered ion in the detector allows the determination of the scattering particle. Combined with a knowledge of the elemental scattering cross sections (proportional to Z^2), RBS allows the determination of film stoichiometry within 3-5%. It must be noted, however, that the interaction cross sections for very low-Z elements such as oxygen are weak enough to prevent determination of the oxygen content with any significant accuracy. Heavier elements studied in this work such as Ru, Sr, La, Ni, and even Ti pose no such difficulty.

In addition to the large energy loss encountered during backscattering, the incoming alpha particles experience small continuous energy losses, primarily due to electron interactions, as they pass through the film. The change in the detected energy as the alpha particle passes through a section of film thickness δx can be written as:

$$\frac{\partial E_m}{\partial x} = \left(K_M \frac{\partial E}{\partial x} + \frac{\partial E}{\partial x} \right) = S \tag{2.19}$$

where E_m is the energy deposited by a backscattered alpha particle in the detector and S is the energy loss factor. Due to these smaller incremental losses, alpha particles scattered from deeper in the film are less energetic when they reach the detector and consequently a plot of the number of backscattered particles energy deposited in the detector appears as a wide plateau rather than a sharp peak. The thickness of a region of material containing a given element can be extracted from the width of the elemental peak.

Finally, to partially address the insensitivity of RBS measurements to oxygen, it is possible to tune the energy of the incoming particle beam to precisely 3.045 eV, exciting an oxygen interaction resonance. This results in a significantly enhanced oxygen peak from which the oxygen content can usually be determined within 10-20% accuracy. However, this technique is only effective at the film surface as the energy loss factor generally causes the particle beam to be off-resonance within 20 nm of entering the sample. Additionally, very small instabilities in the beam energy can cause large changes in the detected signal, further reducing accuracy. All RBS measurements in this work were performed at Lawrence Berkeley National Lab and analyzed using either the RUMP software package developed by Michael Thompson, Cornell University or the SIMNRA program developed by Matej Mayer of the Max Plank Institute. A significant fraction of the RBS measurements themselves were taken by Dr. Kin Man Yu of Lawrence Berkeley National Laboratory.

2.3.2 X-Ray Absorption Spectroscopy

X-ray absorption spectroscopy (XAS) is a highly sensitive synchrotron radiation technique capable of determining elemental valence states and detecting low-level impurities. XAS measurements in this work expose a sample to high intensity soft X-rays with energies from 400-2100 eV. Sample X-ray absorption is measured as a function of incoming photon energy as the energy is scanned through elemental core-valence electronic transition energies. The presence of a given element is marked by an absorption peak at the expected transition energy. A schematic of a typical absorption process is shown in Figure 2.8(a), where an electron is excited from the $2p$ band to the $3d$ band. High energy resolution and fingerprinting of the different absorption spectra allows the identification of the valence states of certain elements through XAS.

XAS may be measured using a number of different techniques, most commonly luminescence, fluorescence, and total electron yield. X-ray luminescense is a transmission technique which relies on a luminescent substrate. As X-rays are transmitted through a thin film into the substrate, the substrate emits light, which is then captured by a photodiode. As the absorption of the film changes with the incident photon energy, so too does the intensity of the luminescence and an absorption profile is created. X-ray fluorescence relies on a different mechanism which can be seen in Figure 2.8(b). From the excited state in 2.8(a), a valence electron falls down into to now unoccupied core level, emitting an X-ray photon corresponding to the transition energy. This emitted X-ray may then be detected and used to extract the X-ray absorption spectrum. Because of the long X-ray mean free path, both luminescence and fluorescence typically yield an absorption signal from the entire thin film

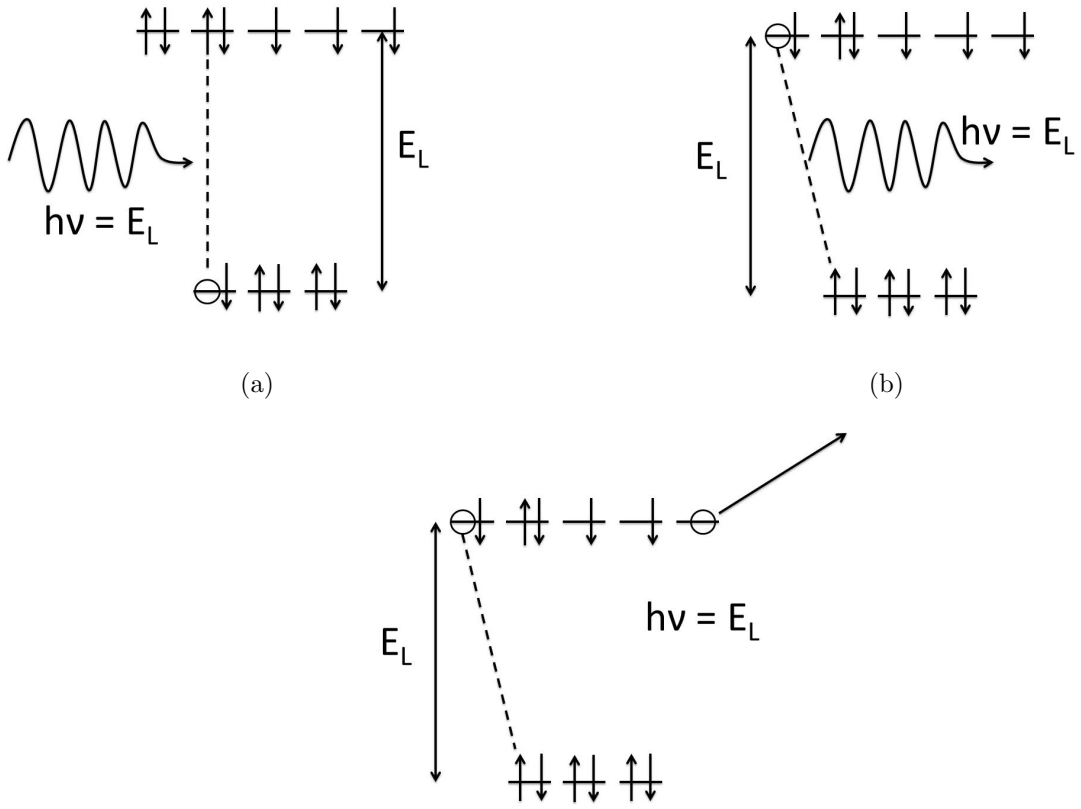

Figure 2.8: a)X-ray absorption mechanism b) X-ray fluorescense interaction c) Auger electron emission

sample. Although this is an advantage in some experiments, it also results in a significant "saturation effect" that blurs the spectra. As the X-rays pass through many nm of material, the X-rays at the absorption edge are preferentially absorbed. When the number of photons near the absorption edge is significantly decreased, this appears as a significant increase in the signal to noise ratio and a marked decrease in energy resolution.

For applications requiring high energy resolution such as spectral fingerprinting it is most common to measure XAS in total electron yield mode. Total electron yield mode is a surface sensitive technique which detects absorption through the collection of electrons ejected from the sample. As shown in Figure 2.8(c), rather than emitting an X-ray when it drops to the unoccupied core state, an electron may instead emit an Auger electron. These electrons interact very strongly with the surrounding material and consequently have a highly energy dependent escape depth of less than 5 nm, limiting the source of the detected signal to the sample surface. Figure 2.9, produced using the NIST inelastic mean free path database and confirmed by Seah and Dench, shows the mean scattering length for an Auger

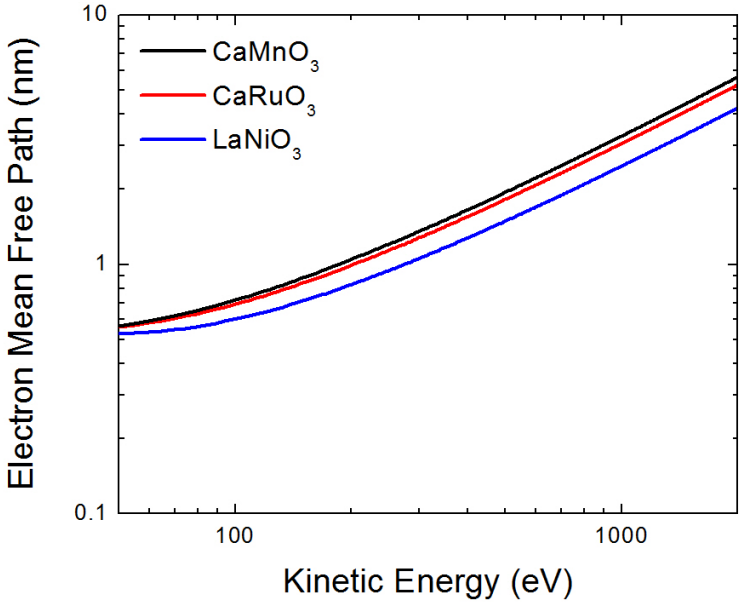

Figure 2.9: Electron mean free path as a function of kinetic energy, produced using theoretical calculations by the NIST inelastic mean free path database and confirmed Seah and Dench.[119, 136] Electron mean free path has been calculated as a function of energy for three important materials used in the thesis: $CaMnO_3$, $CaRuO_3$, and $LaNiO_3$. Note the very similar of all three systems.

or photoelectron as a function of kinetic energy.[119, 136] Although for the energies we are interested in (400-700 eV) the escape depth is predicted to be as low as 7 Å, in practice total electron yield captures a number of secondary electron channels excited by the Auger electron, raising the expected escape depth to 2-3 nm.[86] We can see, therefore, that X-ray absorption measurements performed in total electron yield mode are very surface sensitive. As the electron escape depth is much lower than the X-ray penetration depth, saturation effects may be neglected and very high energy resolution ($\leq$ 0.1 eV) is achievable)

A final concern is that the escape of Auger electrons may be impeded by charge buildup if ejected electrons are not replaced. This effect can significantly distort the absorption spectrum but can be alleviated by grounding the sample to a copper rod through carbon tape and silver paint. In some cases, this is insufficient and attaching a copper electron collector mesh biased at 1 kV was necessary to remove the electrons. Insulating samples often experienced significant charging despite both of these additions.

All XAS in this work was performed in total electron yield mode at the Advanced Light Source, Lawrence Berkeley National Lab on beamlines 6.3.1 and 4.0.2. Beamline 6.3.1 is a bending beamline with the capability of applying magnetic fields of $\pm$ 2T along the direction of x-ray propagation. Beamline 4.0.2 is an elliptically polarizing undulator offering higher energy resolution and a quadrapole magnet limited to 700 mT but capable of applying magnetic field in any direction. Films were measured at temperatures ranging from 10-300

K, and the primary absorption edges studied were the Ru $M^{5,4}$, Mn $L^{3,2}$, Ni $L^{3,2}$, and O K, in addition to scans for common magnetic impurities such as Fe.

2.3.3 Electron Energy Loss Spectroscopy

Electron energy loss spectroscopy (EELS) is theoretically very similar to XAS in that it relies on exciting core to valence electronic transition to extract stoichiometry and valence information. Rather than synchrotron radiation, EELS utilizes a high energy electron beam for excitation and is performed using a transmitted electron beam in a scanning transmission electron microscope (STEM). The confined electron beam of a STEM is rastered across the sample, allowing atomic site-resolved measurements to be performed. By exposing the sample to electrons of a known kinetic energy high enough to excite a transition (in this work the Mn $L^{3,2}$ edge and La $M^{5,4}$ edge) and searching for an energy absorption peak, the elemental composition of individual atomic columns may be resolved. By only counting electrons in a single energy loss band corresponding to an elemental absorption peak, we obtained the distribution profile of a single element rather than a simple Z-contrast image. Such a measurement technique also allows the ratios of a given set of elemental concentrations to be determined with atomic-site resolution. A typical EELS measurement on thin films or superlattices will utilize a cross sectional STEM sample to examine interfacial quality and determine the extent of intermixing between layers. By creating a depth profile of the elemental composition, the amount of interdiffusion can be precisely determined. Additionally, measurement of a number of energy loss bands across an entire absorption edge will reveal the entire absorption spectra and allow us to employ spectral fingerprinting similar to that extant in XAS spectra, yielding site-specific valence information. All EELS measurements were performed at Pacific Northwest National Lab by Hao Yang, UC Davis.

2.4 Magnetic Characterization

2.4.1 SQUID Magnetometry

To probe the magnetic response of an entire film or superlattice under an applied magnetic field, we used a superconducting quantum interference device (SQUID) magnetometer. Potentially the most sensitive instrument ever constructed, a SQUID magnetometer is composed of a pickup coil with two Josephson junctions in parallel and allows the detection of changes in magnetic flux as small as a single magnetic flux quanta.[48] Although, in practice, external noise limits actual sensitivity significantly, we are able to easily resolve magnetic signals as small as 1×10^{-7} emu. Bulk magnetometry measurements were performed in a Quantum Design Magnetic Property Measurement System (MPMS) incorporating a SQUID magnetometer. The MPMS systems varied the applied field up to 7 T and varied temperature from 2-300K. Measured magnetization values were normalized to film volume using the substrate surface area and thicknesses obtained through XRR and RBS. Magnetization in this work will generally be discussed in terms of Bohr magnetons ($\mu_B = 9.27\times10^{-21}$ emu) per atom of the present magnetic element.

Two types of magnetometry measurements occur frequently throughout this work. The

first is measurement of magnetization as a function of temperature, which generally serves to identify the transition temperature of magnetic phases. Ferromagnetic films are typically cooled through the transition temperature in a large field (5 T) and then magnetization is measured while temperature is swept from 10-300 K with a significantly lower field (on the order of 100 Oe). A lower field must be applied during the measurement as a large field tends to smear out the magnetic transition.

The second type of scan commonly employed is measurement of film magnetization as a function of applied field. Such measurements may be done with or without field cooling (the application of a field as it is cooled through its magnetic transition temperature). In this dissertation, field cooling is generally not employed in order to preserve the virgin magnetization curve, but is utilized to probe exchange bias effects in systems with a ferromagnetic and antiferromagnetic component. In both cases, a linear diamagnetic background contributed by the substrate must generally be subtracted to reveal the true shape and magnitude of the film magnetic hysteresis loop. As will be shown in chapter 5, the orientation of the thin film relative to the applied field is important, and measurements were performed with the magnetic field applied along the growth axis as well as several in-plane directions.

In magnetometry measurements of thin films, particularly magnetization vs. applied field measurements, there are a number of extrinsic factors which may contribute to the measured magnetic moment and must be carefully examined. As the SQUID magnetometer simply measures a voltage induced as the sample is transported through a set of pickup coils, everything which is moved through the coils contributes to the signal. The largest contributions are diamagnetic and primarily originate in the sample holder (a plastic straw) and the substrate upon which the film is deposited. The contribution of the straw is generally not observed in the SQUID data, as the total mass of the long straw passing through the pickup coil is constant throughout the measurement. The magnetic moment of the substrate, however, does appear as a very large diamagnetic background at the same location as the film. Although often much larger than the actual film background, this extrinsic effect is easily dealt with through the subtraction of a straight line from the magnetic moment vs. applied field data.

Much more difficult to remove are paramagnetic and ferromagnetic contributions that do not originate in the film. The first is often caused by paramagnetic iron oxide impurities introduced into the substrate during growth. Although the significant majority of the paramagnetic signal from paramagnetic iron oxide impurities in substrates is linear and may be subtracted in the same way, slight nonlinearities may be introduced at high fields which will affect the background subtraction and shape of the hysteresis loop. As the magnetic moment of these paramagnetic impurities is expected to exhibit a 1/T dependence, we may estimate the significance of this effect through the size of the observed paramagnetic "tail" (if any) observed in high field (10 kOe) magnetization vs. temperature measurements of films and substrates. In general, we find negligibly small contributions of at most 1×10^{-6} emu for all substrates except $LaAlO_3$. In fact, in most substrates the paramagnetic contribution is so weak that it is not observable in magnetization vs. temperature measurements of our films. The lone exception, $LaAlO_3$, shows nonlinear paramagnetic contributions on the order of 2×10^{-6} emu at field of 1 T and may reach values as high as 1×10^{-5} emu at fields of 5 T. Of course, these contributions are negligibly small in the case of large magnetic moments between 1×10^{-4} and 6×10^{-6} emu, but become much more significant in interfacial magnetic

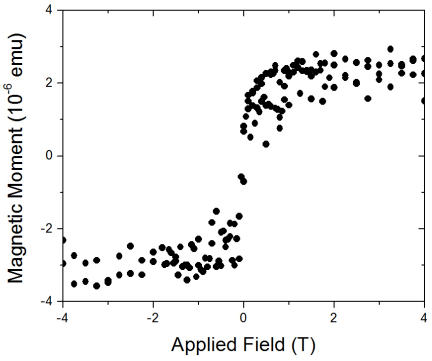

Figure 2.10: Magnetization vs. applied field measurement of a blank $SrTiO_3$ substrate contaminated with ferromagnetic iron oxide. The measurement was taken using SQUID magnetometry at 10 K, and a linear diamagnetic background was subtracted.

systems where magnetic moments are on the order of 6×10^{-6} to 1×10^{-5} emu. In this case, it is important to carefully characterize the response of the paramagnetic impurities to an applied field and subtract this from the final signal, normalizing for substrate volume.

The final category of extrinsic signals that are of concern is ferromagnetic contributions, which typically originate in one of two ways. First, a small amount of ferromagnetic iton oxide dust may adhere to the sample. This contribution is extremely pervasive but unlikely to exceed 2-4 μemu (often significantly less).[40] It has been shown that the occurence of this type of contamination may be significantly reduced through storing samples in clean, sealed containers and avoiding the use of sticky surfaces such as Kapton tape in the sample mounting process.[40] The second major source of iron oxide contamination is the use of magnetic steel tools in sample preparation and manipulation. Samples contaminated in this manner are shown to exhibit extrinsic ferromagnetic moments as high as 1×10^{-4} emu. In the case of such severe contamination, it may still be theoretically possible to extract an accurate hysteresis loop through subtraction of a magnetization vs. applied field measurement significantly above the film transition temperature. However, because of the inexact nature of such a subtraction samples in which such contamination is suspected are not included in the analysis of this thesis.

Thus, the most concerning type of background signal in SQUID magnetometry originates in the ferromagnetic particles which may be introduced through either dust or steel tools. All of the samples in this thesis are consequently stored in sealed containers immediately after deposition and no magnetic tools are used to manipulate them. Rather, nonmagnetic tweezers are employed immediately after being cleaned with organic solvents and all sample manipulation take place on fresh cleanroom wipes. Finally, no SQUID magnetometry measurements are taken using Kapton tape to secure the sample unless all taking and sample manipulation takes place in a clean room. It has been demonstrated that such precautions will eliminate the significant majority of ferromagnetic contamination issues, and samples on with magnetic moments on the order of 1×10^{-4} emu or higher may generally neglect these contributions.[40] In systems with much smaller ferromagnetic signals care must be taken in identifying samples with ferromagnetic contamination, as exemplified by Figure 2.10. Figure

2.10 shows an example of typical contamination with ferromagnetic iron oxide. As expected, it is very small and shows very little hysteresis due to the extremely soft nature of iron oxide. Finally, cases of extremely small ferromagnetic moments must always be verified through alternative techniques which allow elemental sensitivity or spatial resolution. Two such techniques that allow us to separate film properties from extrinsic factors are X-ray magnetic circular dichroism and polarized neutron reflectometry, described below.

2.4.2 X-Ray Magnetic Circular Dichroism

A synchrotron radiation technique derived from X-ray absorption spectroscopy, X-ray magnetic circular dichroism (XMCD) probes the magnetic properties of a system with elemental specificity. To perform XMCD, samples are illuminated by a beam of circularly polarized x-rays while magnetized alternatively parallel and antiparallel to the axis of photon polarization. Although this can be achieved either by placing a sample in an alternating magnetic field or by changing the X-ray polarization from left to right handed, the former technique is much more commonly employed. In the most common XMCD measurements in this thesis, the energy of the incoming photons is swept through an elemental absorption edge and an absorption spectrum is taken for both the parallel and antiparallel magnetization state. From the difference between the two spectra, we extract element specific magnetic information such as which elements and energy levels are ordering magnetically, relative magnitude of a ferromagnetic signal and, through application of the XMCD sum rules, the ratio of orbital magnetic moment to spin magnetic moment. In some systems XMCD fingerprinting even enables us to distinguish magnetism arising from different oxidation states of a given element.[6] An alternative measurement exploiting the XMCD effect sets the X-ray energy to the point of maximum positive and negative dichroism and slowly scans the magnetic field to trace out the magnetic hysteresis loop of a given element in a sample.

The specific details of the XCMD effect and its analysis are very involved, and the reader is encouraged to consult appendix A and the textbook by Stohr for a rigorous treatment.[141] However, the reader may gain a basic understanding of XMCD by examining Figure 2.11. In this figure, we see a typical magnetic L-edge transition in which the $2p$ band is split by spin orbit coupling and the $3d$ band is exchange split into spin-up and spin down bands. Clearly, the density of states of the $3d$ band is different for spin-up and spin-down electrons, resulting in a different transition probability for different spin states, as required by Fermi's Golden Rule. Thus, the $3d$ band may act as a detector of spin states. However, this alone is insufficient to probe the magnetism of this element.

XMCD operates by additionally exploiting the selection rules for atomic transitions. The two $2p$ subbands have opposite spin-orbit coupling, and the state mixing which occurs in these core levels results in one of the levels being more likely to excite a spin-up electron while the other is more likely to excite a spin-down electron. It is this polarization of the excitation that combines with the spin sensitivity of the $3d$ band to yield magnetic information. By switching the direction of the magnetization, the majority and minority $3d$ spin bands will switch, causing the intensity of one L-edge to rise and the other to fall. In a nonmagnetic system, the intensity would remain constant, as there would be more majority or minority spin band. Similarly, in a system without spin-orbit coupling (a K-edge for example), the L_3 and L_2 edge would each excite equal numbers of spin-up and spin-down electrons, and

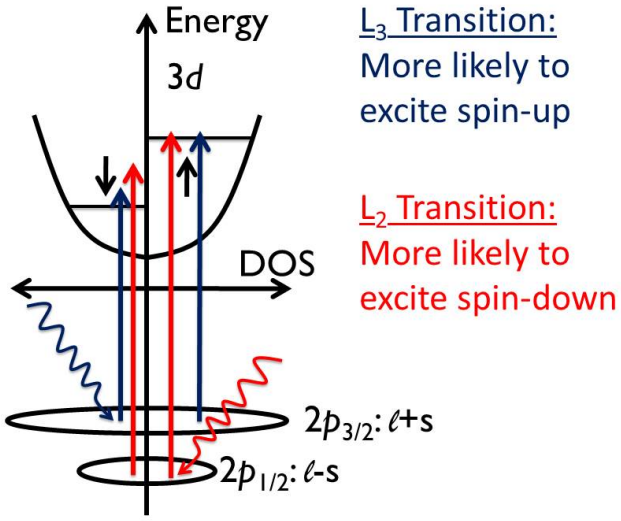

Figure 2.11: Schematic of L-edge X-ray absorption in a system with a ferromagnetically ordered d band, showcasing the requirements for observing X-ray magnetic circular dichroism

switching the magnetization would have no observable effect. Both factors are required, and when present they result in significant dichroism of the X-ray absorption signal as the magnetization of the sample reverses direction. The XMCD spectra in this dissertation were of the Ru $M^{5,4}$, Ni $L^{3,2}$ and Mn $L^{3,2}$ edge at beamlines 6.3.1 and 4.0.2 of the advanced light source. Magnetic fields were varied between $\pm$ 1.7 T and sample temperatures ranged from 10-300 K.

2.4.3 Polarized Neutron Reflectometry

We used polarized neutron reflectometry to extract the nuclear and magnetic depth profile of our thin films and superlattices. The theory and treatment of neutron reflectometry is essentially identical to that of X-ray reflectometry, except that, as an uncharged particle possessing a magnetic moment, the neutron beam is not significantly attenuated when passing through the sample and magnetic information may be extracted through the use of a spin-polarized neutron beam. In this discussion of neutron reflectometry, we will largely follow the pair of excellent primers published by Los Alamos National Lab and the NIST Center for Neutron Research.[94, 33] The neutron, unlike the X-ray photon, will be scattered by the nuclei of whatever medium it passes through rather than the electron cloud. In this case, the wave equation is typically written

$$\left(\frac{\hbar^2}{2m_n}\frac{\partial^2}{\partial z^2} + V(z)\right)\Psi(z) = E\Psi(z) \tag{2.20}$$

where z is the vertical coordinate, m_n is the neutron mass, and V(z) is the nuclear scattering potential, which is (hopefully) only a function of depth in the film. In general

$$V(z) = \frac{2\pi\hbar^2}{m_h}\rho(z) \tag{2.21}$$

where ρ is the nuclear scattering length density. Thus we may write the neutron index of refraction for a given material as

$$n = \sqrt{1 - \frac{4\pi\rho}{k_0^2}} \tag{2.22}$$

where k_0 is the wave vector of the neutrons. In a non-air medium, $k_1 = nk_{air}$. If the beam of neutrons is magnetically unpolarized, this is the only portion of the scattering that we need concern ourselves with. Neutron reflectometry performed with a neutron beam which is not spin polarized will yield structural information but cannot be used to reconstruct the magnetic depth profile. However, when taking reflectometry spectra with a spin-up and spin-down polarized beam, the magnetic scattering of the spin-$^1/_2$ becomes important. In this case, we must modify the scattering potential to be

$$V(z) = V_n(z) + V_m(z) \tag{2.23}$$

where the nuclear and magnetic contributions to the scattering potential are both included. Specifically, we write the magnetic scattering length density as

$$V_m = \mp\mu \bullet \overrightarrow{B} \tag{2.24}$$

where the invered plus/minus sign accounts for the fact that the neutron g-factor is negative i.e. the neutron magnetic moment is antiparallel to its spin. Since

$$B = \mu_0\overrightarrow{H} + \overrightarrow{M} \tag{2.25}$$

where H is the applied field and M is the magnetization, it is clear that a change in the magnetization at an interface will result in scattering. Most importantly, the scattering length density is determined by the dot product of two vectors! As shown below, at an interface between a nonmagnetic material with nuclear scattering length density ρ_{nm} and a ferromagnetic material with nuclear scattering length density ρ_{nm} and magnetization M, a spin-up and spin-down neutron will observe different indices of refraction, due to a scattering potential difference of $2\mu \times M$.

$$n_\pm = \sqrt{1 - 4\pi(\rho_n \pm \rho_m)/k_0^2} \tag{2.26}$$

This equation assumes, of course, that the neutron spins are parallel or antiparallel to the magnetization. In an unpolarized neutron beam, of course, the neutrons will simply see an average index of refraction halfway between the spin-up and spin-down cases. However, by taking a spectrum with a beam in which the neutron spins are polarized parallel and antiparallel to the magnetization, we can use the difference between a spin-up polarized and a spin-down polarized spectra to obtain a depth-dependent picture of the magnetization of either a thin film or superlattice. One final noteworthy issue in neutron diffraction is that only the component of the magnetization that is perpendicular to the scattering vector

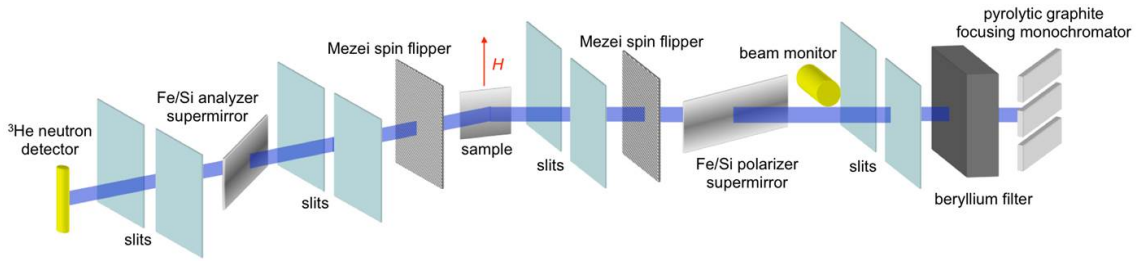

Figure 2.12: Schematic of the Polarized Beam Reflectometer and the NIST Center for Neutron Research.[10]

contributes to the magnetic scattering. Consequently, in a typical setup the magnetization and beam polarization will be perpendicular to the scattering vector and the films must be magnetized in-plane.

Polarized neutron reflectometry measurements for this dissertation were performed at the Asterix beamline at the Lujan Neutron Scattering Center at Los Alamos National Lab and at the Polarized Beam Reflectometer at the NIST Center for Neutron Research. A schematic of the Polarized Beam Reflectometer is shown in Figure 2.12, reproduced with permission from the NIST Center for Neutron Research website.[10] In it, we can see the supermirrors and spin flippers used to control and analyze the neutron spins as well as the ^{3}He neutron detectors used for monitoring both sample reflectometry and beam intensity. Samples were cooled to 5K in fields of up to 800 mT prior to measurement. All reflectometry spectra were analyzed using the Refl1d package developed by Paul Kienzle, Nikunj Patel and James Krycka of the NIST Center for Neutron Research.

2.4.4 Neutron Diffraction

To probe the antiferromagnetic structure of our samples, we turned to neutron diffraction. As with neutron reflectometry, neutron diffraction takes advantage of the magnetic scattering inherent in diffraction with a spin $^1/_2$ particle to observe diffraction peaks associated with magnetic order. This neutron diffraction may be treated almost identically to its X-ray analog, with two notable exceptions. First the weakly interacting nature of the neutron beam results in very little attenuation as the beam passes through the sample. More importantly, as we have just explored in detail, the magnetic moment of a neutron renders it sensitive to scattering from magnetic structures as well as nuclear structures. This magnetic sensitivity means that neutron diffraction can be used to examine antiferromagnetic structures in which the magnetic order results in a diffraction peak. Even more remarkably, the magnitude of the magnetic scattering length density is well matched to those of the nuclei, resulting in peaks of similar magnitude for both magnetic and structural peaks. If the width of the antiferromagnetic peak is not instrumentally limited we can extract the antiferromagnetic correlation length very simply:

$$l = \frac{1}{FWHM} \tag{2.27}$$

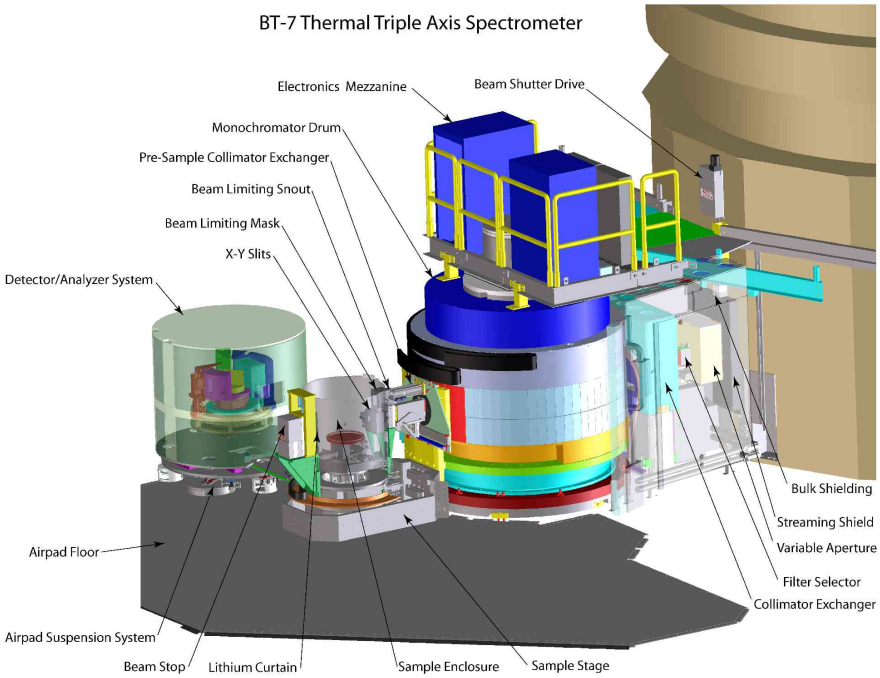

Figure 2.13: Schematic of the BT7 triple axis diffractometer, reproduced from Lynn et al..[87]

The correlation length is simply the inverse of the peak width. We will explore the implications of this further in chapter 6. A schematic of one neutron diffractometer used in this thesis, the BT7 triple axis diffractometer at the NIST Center for Neutron Reseach, is reproduced from Lynn et al. in Figure 2.13.[87]

2.5 Electron Transport

We characterized the electron transport of samples using resistance measurements in the van der Pauw and Hall geometries. Samples were placed in a Quantum Design Physical Property Measurement System (PPMS) varying temperature from 2-380K and the applied field from 0-7 T. As the samples were either square or rectangular, contacts were placed as close to the corners of the films as possible. In the van der Pauw geometry, defined in Figure 2.14, current is passed through leads 1-2 while voltage is measured across leads 3-4. The measured voltage across leads 3-4 at a preset current level is defined as V_{34}. Current is then passed through leads 1-3 while voltage, defined as V_{24}, is measured across leads 2-4. With these voltages and currents we can then define two resistances - R_A and R_B. We can then solve for the sample sheet resistance (R_S) by numerically solving the equation below:

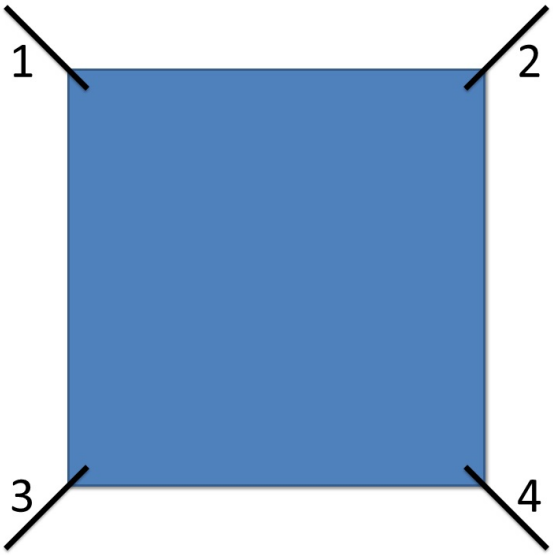

Figure 2.14: van der Pauw geometry for electrical characterization

$$e^{\left(-\frac{\pi R_A}{R_S}\right)} + e^{\left(-\frac{\pi R_B}{R_S}\right)} = 1 \tag{2.28}$$

We can then combine measurements of the sheet resistance with thickness measurements to extract the resistivity. An additional measurement frequently performed in the van der Pauw geometry was that of magnetoresistance. In this work, we measured sample resistivity as a function of temperature in no magnetic field and at a magnetic field in excess of what was required to saturate the sample, usually 5 T. We then calculated the magnetoresistance to be

$$MR(\%) = \frac{\rho(5T) - \rho(0T)}{\rho(0T)} 100 \tag{2.29}$$

In this dissertation, we occasionally use peaks in magnetoresistance vs. temperature measurements to confirm the magnetic transition temperature measured through SQUID magnetometry.

We can also combine resistivity measurements with Hall effect measurements to calculate the carrier concentration and resistivity. The relationship between sheet resistance and resistivity is simply $\rho = \mathrm{R}_{sheet} \times$ thickness. Referring again to Figure 2.14, we make Hall effect measurements by passing current through leads 1-4 and measuring voltage between leads 2-3 and then by passing current through leads 2-3 and measuring voltage between leads 1-4. This again defines voltages V_{14} and V_{23}. We may then write the Hall voltage as

$$V_H = \frac{V_{14} - V_{23}}{2} \tag{2.30}$$

and the Hall Resistance as

$$R_H = \frac{V_H t}{IB} = -\frac{1}{ne} \tag{2.31}$$

where t is the sample thickness, I is the sourced current, B is the applied magnetic field, n is the carrier density, and e is the charge of an electron. Because the Hall resistance is a constant along with n, t, and I, this equation requires that the Hall voltage vary linearly with the magnetic field. In practice, however, this is not the case for ferromagnetic samples as the "extraordinary" or anomalous Hall effect introduces an additional component to the Hall resistivity. The orbinary Hall effect is a simple magnetoresistance effect observed as a transverse current and voltage as electrons trend in one direction perpendicular to the electric field when moving in a magnetic field perpendicular to both the electric field and current. In contrast, the anomalous Hall effect is a contribution to the Hall resistivity which is directly proportional to the magnetization of the conducting material. Despite decades of investigation, the anomalous Hall effect is still not well understood, but is generally considered to be attributable to three different contributing effects.[108] Two, skew scattering and side-jump scattering are related to impurity scattering while the third is an intrinsic contribution related to the Berry's phase, a geometric interference effect induced by the breaking of time reversal symmetry in a ferromagnet.[108] For further reading on the anomalous Hall effect, the reader is encouraged to consult the excellent review article referenced here.[108] In non-ferromagnetic systems it is generally a negligibly small linear contribution, but in ferromagnetic systems will result in a strong nonlinearity at lower fields until the system is saturated. Thus, only data past the saturation point will be linear and can be used to determine the Hall resistivity. Therefore it is important to take Hall measurements at a large number of magnetic field points until the magnetization of the ferromagnetic sample has completely saturated. We then perform a linear fit of all field points after magnetic saturation to precisely determine R_H using the equation below:

$$R_H = \frac{\partial \rho_{xy}}{\partial B} \tag{2.32}$$

So that the slope of the linear region of the transverse resistivity as a function of the applied magnetic field B is the Hall coefficient. We may then calculate the carrier concentration:

$$n = -\frac{1}{eR_H} \tag{2.33}$$

This result can be combined with our earlier measurement of the resistivity to calculate the carrier mobility of the sample as shown below:

$$n = \frac{1}{\rho e \mu} \tag{2.34}$$

It should be noted here that we have assumed all conductivity comes either from a single electron band or a single hole band. In practice this may not be the case. If conductivity arises from a combination of electron and hole bands, it becomes much more difficult to extract the number of carriers.[78] If, for example, there is a hole contribution to the conductivity, each carrier will have it's own hall coefficient, and the net Hall coefficient may be expressed as

$$R_H = \left(\left(\frac{1}{\rho_e}\right)^2 R_e + \left(\frac{1}{\rho_h}\right)^2 R_h\right) \frac{\rho_e \rho_h}{\rho_e + \rho_h} = \left(\left(\frac{\rho_h}{\rho_e}\right) R_e + \left(\frac{\rho_e}{\rho_h}\right) R_h\right) \frac{1}{\rho_e + \rho_h} \tag{2.35}$$

where

$$\begin{aligned} \rho_e &= \frac{1}{n_e e \mu_e} \\ \rho_h &= \frac{1}{n_h e \mu_h} \end{aligned} \tag{2.36}$$

and in the end we find

$$R_H = \frac{1}{e} \frac{n_e \mu_e^2 - n_h \mu_h^2}{(n_e \mu_e + n_h \mu_h)^2} \tag{2.37}$$

Clearly, simply measuring the net Hall coefficient and resistivity in this case does not provide sufficient information to extract either carrier concentration. Hole and electron mobility will be similarly inaccurate. The single band approximation, however, may still be effective in providing a qualitative comparison of several samples of the same material, even if they are governed by the two-band model. Even in a system with multiple bands contributing carriers, changes in carrier concentration in one of the bands will produce the same general trends in R_H that are expected in the single band picture. Therefore they may be used as a qualitative comparison between similar samples, although the actual carrier concentration values extracted may not be accurate.

Part II

Strain Tuning Magnetism in $SrRuO_3$

Chapter 3

Tuning Ferromagnetism in $SrRuO_3$ Films Using Epitaxial Strain

With our grounding in complex oxide physics and the requisite experimental methods finally complete, chapter 3 will introduce the first of our model systems. $SrRuO_3$ is, for a variety of reasons that will be discussed, an excellent candidate for tuning magnetic order as well as a technologically interesting system. We will first explore the simplest case of strain-altered magnetic properties - that of films under (100) oriented epitaxial strain. We will demonstrate high quality film growth and show an alteration of the saturated magnetic moment and transition temperature through strain tuning of the crystal field and density of states.

3.1 An Introduction to $SrRuO_3$

The growth and study of $SrRuO_3$ thin films was originally driven by its excellent (for an oxide system) metallicity and high quality growth in heteroepitaxial structures, which make it ideal for device applications. Because of these properties, $SrRuO_3$ is commonly integrated into oxide heterostructures and devices at a contact electrode or buffer layer.[95, 122, 163, 80, 165] However, the emergence of significant deviations from bulk properties in $SrRuO_3$ thin films resulted in significant interest in behavior of $SrRuO_3$ itself. In the bulk, $SrRuO_3$ is an itinerant ferromagnetic metal with a Curie temperature of 160 K and a saturation magnetization ranging from 1.1-1.6 μ_B per formula unit.[2, 76, 66, 16] In thin films, $SrRuO_3$ has been reported to exhibit properties ranging from a metal-insulator transition to competition between ferromagnetic and antiferromagnetic states and spin-glass behavior.[149, 90, 116] It has also been reported that $SrRuO_3$ films grown on (100) and (110) $SrTiO_3$ show uniaxial anisotropic behavior independent of crystallographic orientation, a topic which will be discussed in detail in chapter 5.[116, 152]

To understand the origins of non-bulk-like behavior in $SrRuO_3$ thin films, it is critical to first examine the remarkable underlying physics present in the bulk system. From the bulk system we can see that as the lone $4d$ itinerant ferromagnet among the transition metal oxides, $SrRuO_3$ offers a unique opportunity to probe magnetic exchange interactions in a system which is particularly sensitive to perturbations. This sensitivity originates in the fact that

Ru is a $4d$ system as opposed to the more common $3d$ ferromagnets. The extended nature of the $4d$ orbitals leads to unusually strong bonding interactions with neighboring oxygen atoms and correspondingly strong responses to any alteration of these interactions.[93]

It is also the extended nature of the orbitals which precludes ferromagnetism in the vast majority of other $4d$ systems. As discussed in Chapter 1, an itinerant system must have some critical density of states at the Fermi level for ferromagnetism to be stabilized. This requirement is known as Stoner's criterion. However, the large orbital overlap in $4d$ systems generally results in strong crystal field splitting, wide bands, and a correspondingly low density of states. $SrRuO_3$ is highly unusual in that the Ru-O orbitals are strongly hybridized, with bonds which are very covalent in character. Electrons are free to flow across a network of Ru-O octahedral cages and create an itinerant metal with a strong enhancement to the density of states at the Fermi level originating in hybridized orbitals with mostly O-character. This enhancement of the density of states satisfies Stoner's criterion, and the magnetic ground state of $SrRuO_3$ is a ferromagnetic metal.

The importance of the Ru-O hybridization is demonstrated by the contrast between the otherwise similar systems $CaRuO_3$ and $SrRuO_3$. As shown in Chapter 1, the tolerance factor of $SrRuO_3$ is very close to one - 0.99.[124] Despite the nearly ideal cation sizes, there is a slight orthorhombic distortion to the unit cell which can be seen in Figure 3.1(a). The two Ru-O-Ru bond angles are approximately 167° 159° respectively.[127, 93] In $CaRuO_3$, with a tolerance factor of 0.96, a larger orthorhombic distortion is induced and the Ru-O-Ru bond angles are decreased to 150.6° and 151.2°.[75] As a result of the increased octahedral rotation and tilting in $CaRuO_3$, the electron hopping interaction, which is expected to be strongest for a Ru-O-Ru bond angle of 180°, is much weaker in $CaRuO_3$.[93] Correspondingly, the relative strength of electron correlation effects is higher in $CaRuO_3$ than in $SrRuO_3$ and long range magnetic ordering is suppressed in $CaRuO_3$. Thus we can see that the magnetic ordering in perovskite ruthenates is likely to exhibit sensitivity to structural alterations.

Despite this potential for tuning of the magnetic ground state, the vast majority of the literature remains focused on films grown on $SrTiO_3$ in the (100) orientation.[151, 60, 39, 31] Although there has been more recent interest in growth on alternative substrates of varying orientation, a systematic investigation of the range of accessible magnetic ground states has yet to be experimentally realized. Therefore, we have grown $SrRuO_3$ thin films with a wide range of thicknesses on a wide variety of different substrates. In this chapter, we will focus on the effects of varying the sign and magnitude of substrate induced strain on the magnetism in (100) oriented films.[50] Chapter 4 will examine the consequences of altering the symmetry of the substrate induced lattice distortion by investigating films grown on substrates with a variety of crystallographic orientations. We will conclude our discussion of $SrRuO_3$ films in chapter 5 with an examination of our ability to control magnetic anisotropy $SrRuO_3$ thin films through induced structural distortions.

3.2 Sample Growth and Structure

In order to vary the epitaxial strain applied to the $SrRuO_3$ films, samples were grown on $LaAlO_3$, $(LaAlO_3)_{0.3}(Sr_2AlTaO_6)_{0.7}$ (LSAT), $SrTiO_3$, and $KTaO_3$ substrates, which have lattice parameters of 3.79 Å, 3.86 Å, 3.905 Å, and 3.988 Årespectively and are all ideal

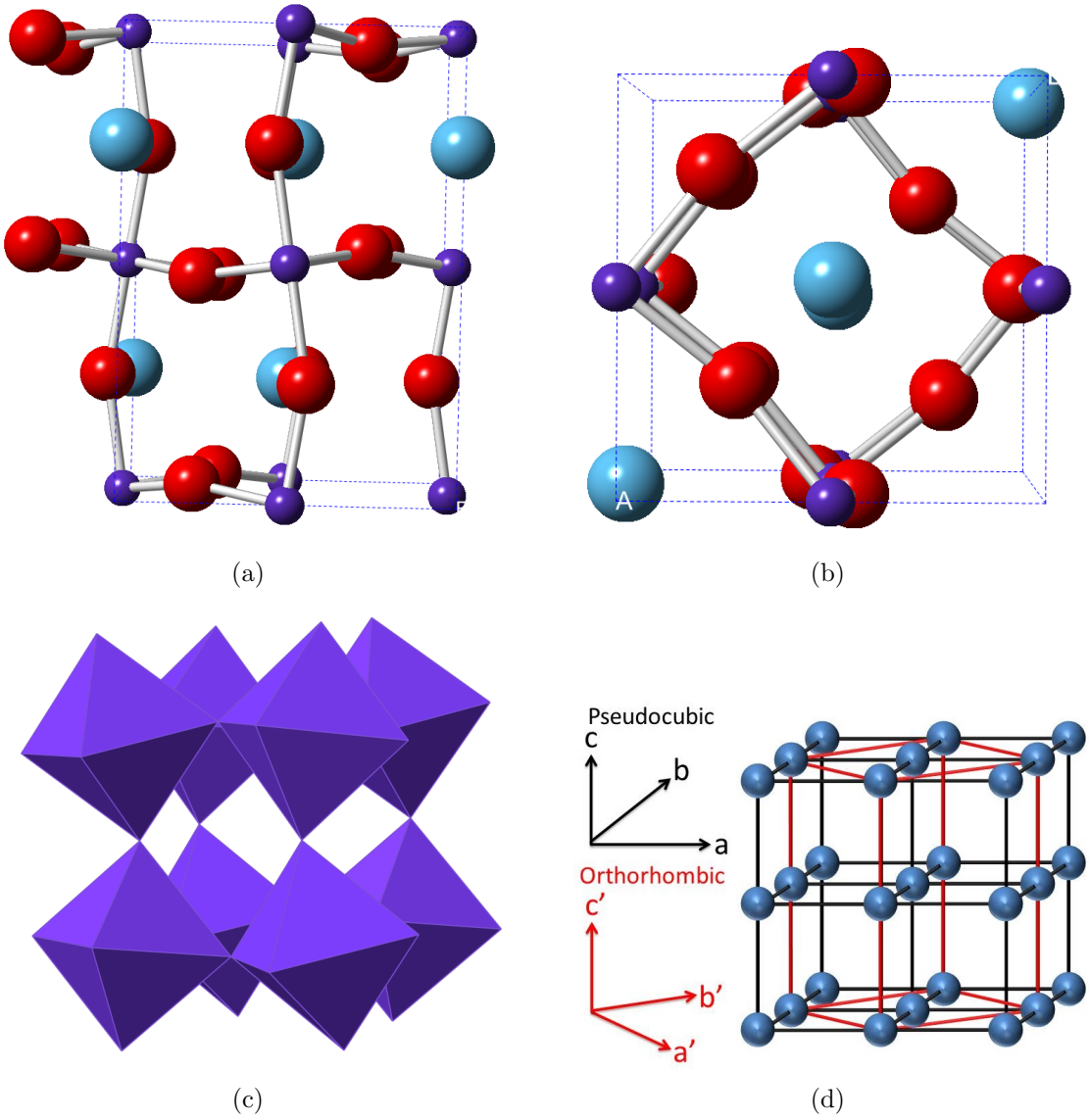

(a) (b) (c) (d)

Figure 3.1: Schematic of the crystal structure of $SrRuO_3$ at 300 K, as determined through neutron powder diffraction by Gardner et al.[43] the rotation of the Ru-O octahedra can be clearly seen. Structure is shown along a) the $(110)_{pc}$ or $(100)_O$ axis and b) $(001)_{pc}$ or $(001)_O$ axis. These two views show the rotation of the RuO_6 octahedra. c) Schematic of the $SrRuO_3$ crystal structure showing only the RuO_6 octahedra. d) Schematic showing the relationship between the pseudocubic (black) and orthorhombic (red) unit cells for perovskite systems with octahedral rotations as those found in $SrRuO_3$, $CaMnO_3$, and many others. Note that the a and b axes are at a 45° angle to the a' and b' axes while the c and c' axes are parallel.

or nearly ideal cubic perovskites. As already discussed, $SrRuO_3$ has an orthorhombically distorted perovskite crystal structure with bulk lattice parameters a = 5.57 Å, b = 5.53 Å, c = 7.84 Å; however, the distortion is minor enough that, especially in thin film form, it can be well represented as a pseudocubic perovskite with a = 3.93 Å.[62, 31, 39] Thus, to avoid confusion when comparing crystallographic directions of substrates and films, we will describe the orientation of $SrRuO_3$ films using the pseudocubic system unless otherwise noted. A reference to the orthorhombic system will be denoted by the subscript *O*. In this way, (100) growth on a (100) substrate represents a (100) pseudocubic type axis, which corresponds to either a $[110]_O$ or $(001)_O$ orthorhombic growth direction, as can be seen in Figure 3.1(b). In an ideal cubic perovskite the epitaxial strain induced by growth on a (100) substrate induces a tetragonal distortion in which the RuO_6 octahedra is compressed in-plane and expanded along the growth axis. Such a distortion, in which bond angles are preserved while bond lengths are modified, would be volume preserving. However, even the ideal case is likely to induce rotation and tilting of the RuO_6 octahedra, breaking the tetragonal symmetry and inducing a volume expansion or contraction. An orthorhombically distorted structure such as $SrRuO_3$ is even more prone to breaking the tetragonal symmetry in this way, although it may still remain confined to the substrate. For a more comprehensive discussion of symmetry and substrate induced strain, please refer to appendix B.

Comparison of substrate lattice parameters with the bulk pseudocubic lattice parameter of $SrRuO_3$ yields mismatches of -3.56%, -1.53%, -0.64%, and +1.47% when grown on $LaAlO_3$, LSAT, $SrTiO_3$, and $KTaO_3$. These substrates were selected to provide a large range of both compressive and tensile strains. To more fully probe the range of strains, sample thickness was also varied from 15 nm to 120 nm, inducing partial or complete relaxation in some samples. Samples were grown on (100) oriented substrates using pulsed laser deposition in 60 mtorr O_2 at a temperature of 700 °C and a laser fluence of approximately 1.3 J/cm^2. They were then post-annealed in 100 torr O_2 at 600 °C for 7 minutes to reduce the number of oxygen vacancies. To determine film thickness and confirm stoichiometric transfer of material from target to substrate, we performed Rutherford backscattering spectrometry measurements. The backscattering spectra of films on all samples were consistent with $SrRuO_3$, showing a 1:1 ratio of Sr and Ru. It is much more difficult to accurately determine O content; all measurements of the oxygen content are consistent to within experimental error (10-20%) with the expected stoichiometry.

Atomic force microscopy on (100) oriented films on $SrTiO_3$ and LSAT showed extremely flat surfaces with characteristic atomic terraces while those on $LaAlO_3$ and $KTaO_3$ showed significantly rougher surfaces. In the majority of the thickness range (20-100 nm), root-mean-square surface roughness values were fairly consistent and increased with film-substrate mismatch. Typical values ranged between 0.25-0.55 nm in $SrRuO_3$ on $SrTiO_3$, 0.6-0.8 nm on $KTaO_3$, 0.7-1.2 nm on LSAT, and approximately 2 nm on $LaAlO_3$. At either extreme of the probed thickness range, less than 20 nm or greater than 100 nm, a significant increase in surface roughness is observed, with very thick and very thin films on $SrTiO_3$ exhibiting roughnesses on the order of 1 nm.

θ-2θ X-ray diffraction measurements confirmed that all $SrRuO_3$ films exhibited excellent epitaxy, showing only diffraction peaks corresponding to the substrate orientation. Figure 3.3(a) shows representative θ-2θ scans through the film and substrate (200) peaks. We can see that the film peak moves progressively to higher θ as mismatch changes the strain

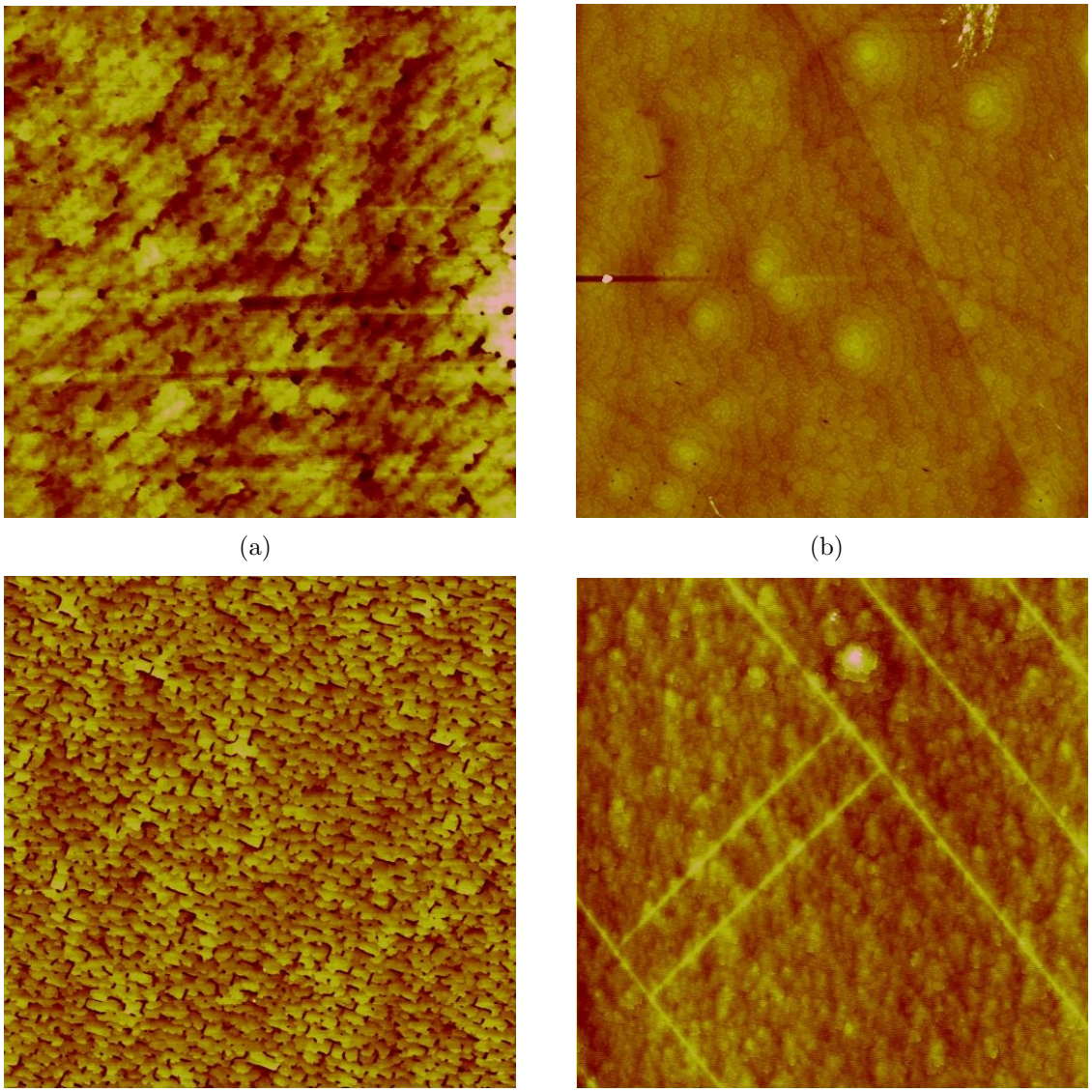

(a) (b)

(c) (d)

Figure 3.2: Atomic force micrographs of $SrRuO_3$ on a) LSAT, b) $SrTiO_3$, c) $LaAlO_3$, d) $KTaO_3$

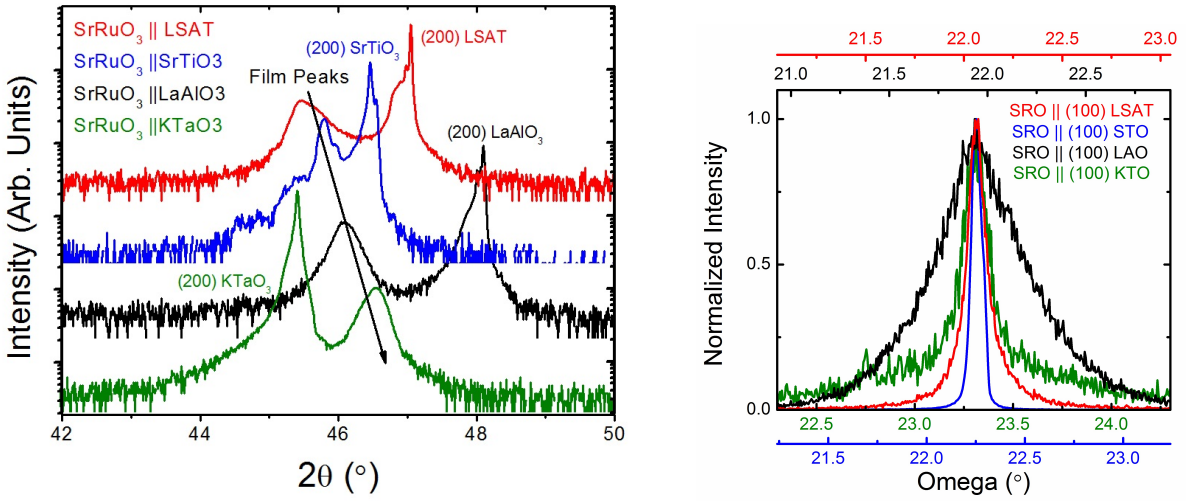

(a) (b)

Figure 3.3: a) Representative x-ray diffraction θ-2θ scans and b) ω rocking curves for films on all (100) substrates

from compression to tension, illustrating the expected modulation of the out-of-plane lattice parameter. Additionally, weak thickness oscillations are exhibited in the films grown on ($SrTiO_3$). These are only observable in the smoother films on $SrTiO_3$, not rougher films on other substrates. Mosaic spreads of film peaks in $\Delta\omega$ scans, shown in Figure 3.3(b), demonstrate film quality to be inversely related to lattice mismatch, with typical $\Delta\omega$ values of 0.06° on (001) $SrTiO_3$, 0.11° on (001) LSAT, 0.45° on (001) $LaAlO_3$, and 0.17° on $KTaO_3$. When comparing these values, it should be noted that $LaAlO_3$ substrates are commonly twinned, and the underlying structure of the substrate may be artificially enhancing the film rocking curve width.

Although extraction of the growth-axis lattice parameter from θ-2θ measurements provides some strain state information, a complete picture requires mapping of the film and substrate reciprocal lattice. To probe the film in-plane and out-of-plane lattice parameters we mapped an area of reciprocal space encompassing the film and substrate (103) peaks. This combination of the (100) and (003) planes contains information about the structural periodicity of the system along the growth and film axes. In a coherently strained tetragonal system, this information is sufficient to completely describe the structure and we may extract both the in-plane and out-of-plane lattice parameters. Because more extensive lattice mapping is prohibitively expensive with regards to diffractometer time, we will proceed under the assumption that the cubic substrate induces tetragonal order in all of our (100) oriented films. In any case, the in-plane lattice parameter, which is the primary parameter of interest in this chapter, varies only slightly in films which retain a small orthorhombic distortion.

A comparison of reciprocal lattice maps of SRO films grown on different substrates revealed a wide range of strain states. By varying lattice mismatch from -0.64% to -3.8% and thickness from 15 to 120 nm we grew films that were coherently strained, partially relaxed, and fully relaxed. We find that films grown on (100) $SrTiO_3$ show that films are strained

up to thicknesses of 80 nm, but begin to show partial relaxation by 120 nm. Films on LSAT begin to relax partially at thicknesses above 60 nm. Films grown on $KTaO_3$ begin to relax past thicknesses of 50 nm but relax slowly with 80 nm thick films showing in-plane strain values as high as 1%. On $LaAlO_3$, films are difficult to grow fully strained; 40-50 nm thick films show significant partial relaxation and full relaxation occurs by 80 nm. These fully relaxed films on $LaAlO_3$, as well as the thicker partially relaxed films on $SrTiO_3$, can serve as important reference samples. If lattice distortions are controlling the film properties, these films should show much more bulk-like behavior. From reciprocal space map data, volume-preserving and non-volume-preserving contributions to the strain can be easily calculated on $SrRuO_3/SrTiO_3$ and $SrRuO_3$/LSAT samples. These results indicate that in compressively strained films there is a significant volume-preserving tetragonal distortion with a smaller volume contraction. In films under tensile strain, there is a significant volume-preserving tetragonal distortion with a small volume expansion. Figure 3.4 shows reciprocal space maps of $SrRuO_3$/STO, $SrRuO_3$/LSAT for films 50-60nm thick, a 70 nm thick $SrRuO_3/KTaO_3$ film, and for 75 nm thick $SrRuO_3/LaAlO_3$ films. Coherently strained growth is indicated when the film and substrate peaks line up along the in-plane reciprocal lattice direction (QIP).

An alternative method of estimating film crystal quality is to perform electron transport measurements and extract film residual resistivity ratios (RRRs), defined as the resistivity at 300 K divided by the resistivity at 10 K. At the same time, transport and magnetoresistance measurement reveal film magnetic transition temperatures, carrier density, and carrier mobility. Although the absolute determination of carrier density and mobility in $SrRuO_3$ is subject to interpretation due to the involvement of hole-like conduction bands with high oxygen $2p$ character (see chapter 2 for a complete discussion), it is still useful as a comparison between films.[108, 44, 67] Figure 3.5 shows transport dependent resistivity measurements for representative $SrRuO_3$ films on (100) $SrTiO_3$, LSAT, and $LaAlO_3$. All SRO films exhibit metallic behavior with a kink corresponding to the magnetic ordering transition. Additionally, for films on a given substrate resistivity was only weakly thickness dependent. On $SrTiO_3$ substrates, resistivity varied by only 14% across a range of film thicknesses from 20-120 nm and temperatures from 2-300 K. On LSAT and $LaAlO_3$ substrates the range of variation was 18% and 9% across the same thickness and temperature regime. In all cases, a slight increase in resistivity is noted with increasing thickness, most likely reflecting the increase in defect concentration as a result of relaxation and strain accommodation. Film RRRs ranged in value from 3.1 to 4.2, and we find surprising disagreement between the crystal quality estimates based on ω rocking curves. The lowest RRRs are found for films grown on $SrTiO_3$ while the highest are found on $LaAlO_3$ substrates and films grown on LSAT fall in between. This may indicate that the rocking curves in the case of films on $LaAlO_3$ are a poor method by which to measure film quality, as the wide rocking curve of $LaAlO_3$ itself may artificially increase the apparent mosaicity. In any case, all RRR values fall well within the typical range for previous high-quality epitaxial SRO films.[59, 69, 73] In addition, there is significantly more microstructural disorder in the $LaAlO_3$ samples as observed in the mosaic spread of the XRD peaks and surface morphology; this increased disorder further increases the total resistivity of the $LaAlO_3$ samples relative to the $SrTiO_3$ and LSAT ones. Thus, through a combination of AFM, X-ray diffraction, electrical transport, and RBS measurements, we conclude that we have grown high-quality stoichiometric films of SRO in a wide

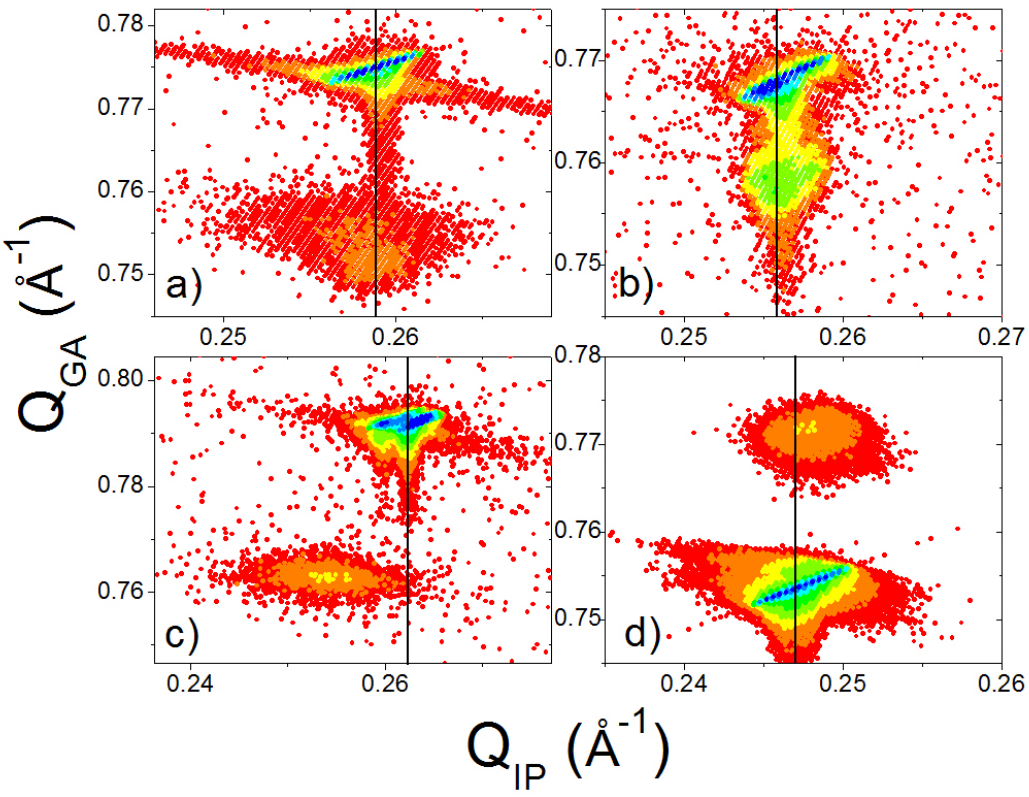

Figure 3.4: (103) Reflection reciprocal lattice maps of typical $SrRuO_3$ films grown on a) 100 LSAT, b) (100) $SrTiO_3$, c) (100) $LaAlO_3$, and d) (100) $KTaO_3$. All films shown are between 50-70 nm thick.

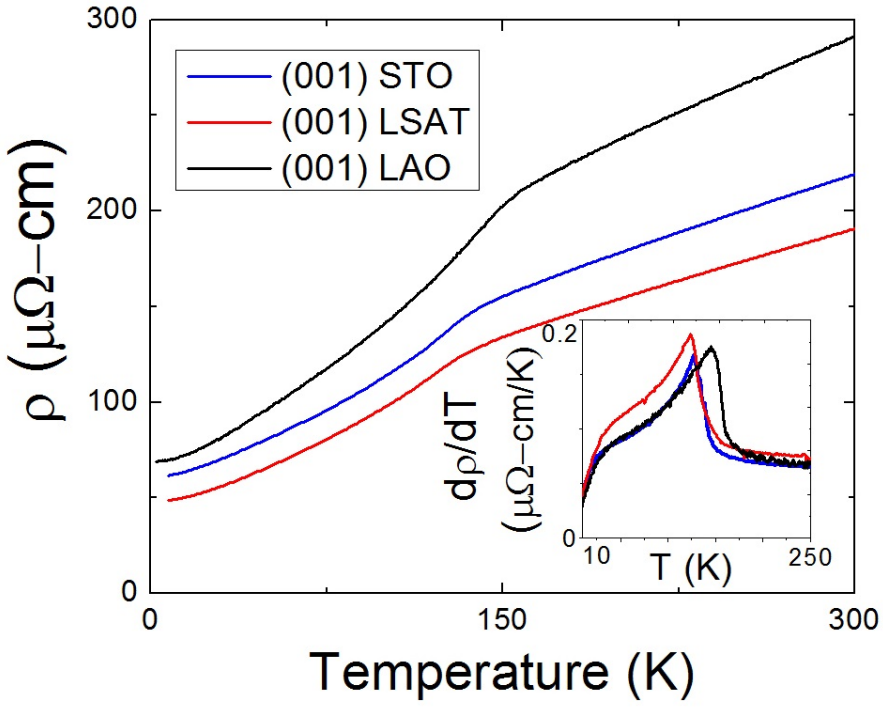

Figure 3.5: Resistivity vs. Temperature measurements for representative 70-80 nm thick films on $SrTiO_3$, LSAT, and $LaAlO_3$ substrates (Inset) dρ/dT showing a peak at the T_C

variety of strain states.

3.3 Relationship Between Thin Film Magnetism and Structure

Magnetic characterization revealed a strong relationship between the magnetic transition temperature of the films and the applied epitaxial strain. The film Curie temperatures were probed using magnetization vs. temperature measurements in a SQUID magnetometer and confirmed using ρ vs. T and magnetoresistance measurements. The Curie temperature is defined in terms of these techniques as the peaks in $^{\partial M}/_{\partial T}$, $^{\partial \rho}/_{\partial}$T, and magnetoresistance vs. temperature plots, respectively. All techniques generally agree within 1-2K and show that all compressively strained films, have Curie temperatures lower than bulk. This is not unexpected, as studies have shown that both compressive strain and off-stoichiometry can suppress the Curie temperature in $SrRuO_3$ thin films.[26, 28, 19] Strained films grown on LSAT had typical T_Cs of 122-126 K while those on $SrTiO_3$ were slightly higher with T_Cs between 128-138 K. T_C of fully relaxed SRO/LAO films were consistently higher than both and typically 140-148K. Finally, films under tensile strain on $KTaO_3$ exhibited very bulk-like transition temperatures on the order of 160-165 K. This difference in transition temperature is illustrated in Figure 3.6(a). The strong substrate dependence, and particularly the bulk-like values in the case of tensile strain, suggests strongly that strain rather than off-stoichiometry is altering the T_C. In fact, a direct comparison of T_Cs with in and out-of-plane lattice

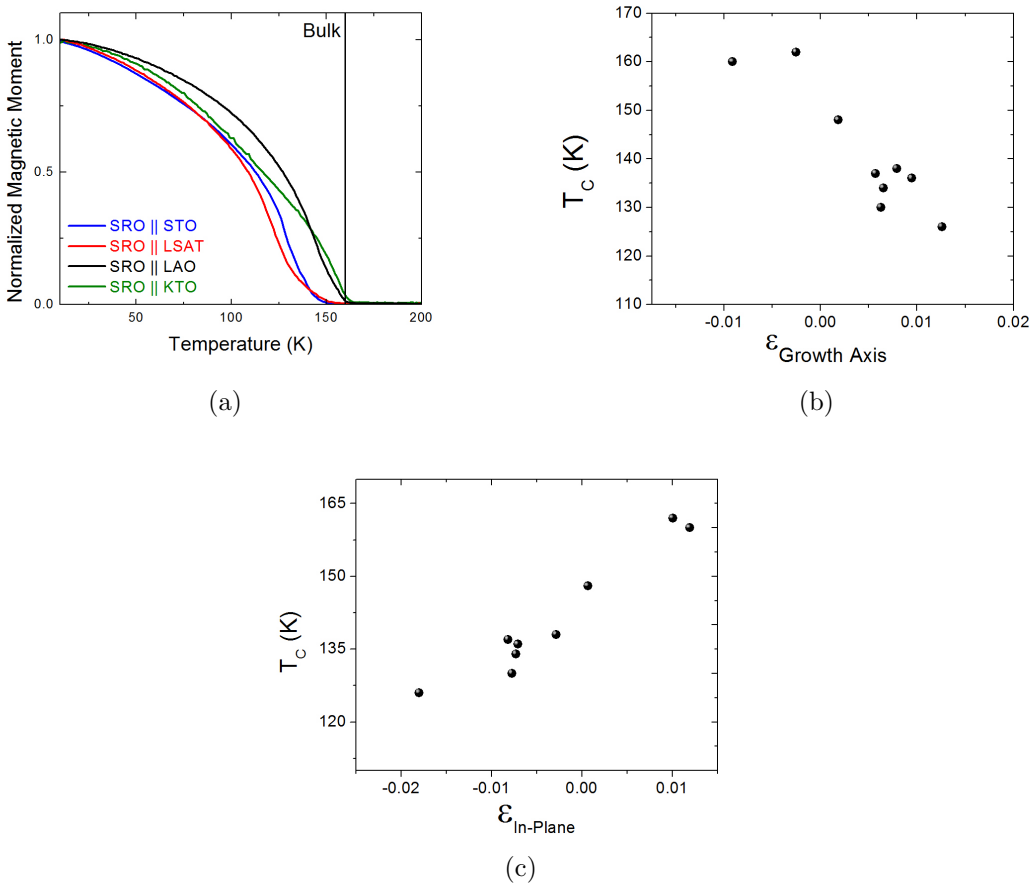

Figure 3.6: a) Magnetization vs. temperature, b) T_C vs. growth axis strain, and c) T_C vs. in-plane strain for films on all (100) substrates. The thicknesses of the films shown here range from 50-120 nm.

parameters extracted from reciprocal lattice maps of films across all substrates reveals that the Curie temperature varies monotonically with applied epitaxial strain. Figure 3.6 (b) and (c) plot T_C vs. in-plane and out-of-plane lattice parameters respectively.

Even more surprising is the dependence of the film saturated magnetic moment on the substrate, as illustrated by magnetization vs. applied field measurements. Figure 3.7(a) shows these measurements for a typical series of films between 60-80 nm thick on (100) oriented LSAT, $SrTiO_3$, $LaAlO_3$, and $KTaO_3$. Fully relaxed 75 nm thick films on $LaAlO_3$ exhibited moments of 1.2-1.3 μ_B/Ru, in agreement with bulk measurements, while thinner, partially relaxed films on $LaAlO_3$ exhibited moments as high as 1.8 μ_B/Ru. In contrast, films on (001) $SrTiO_3$ and LSAT exhibited moments of about 1.7 and 1.9 B/Ru, respectively. Compressively strained films of all orientations exhibited these enhanced saturated magnetic moments compared to previous bulk and thin film values of 1.1-1.6 μ_B/Ru^{4+} from the literature regardless of film thickness. Our completely relaxed films on (100) $LaAlO_3$ showed much more bulk-like behavior, saturating at a magnetic moment of 1.2 μ_B/Ru^{4+},

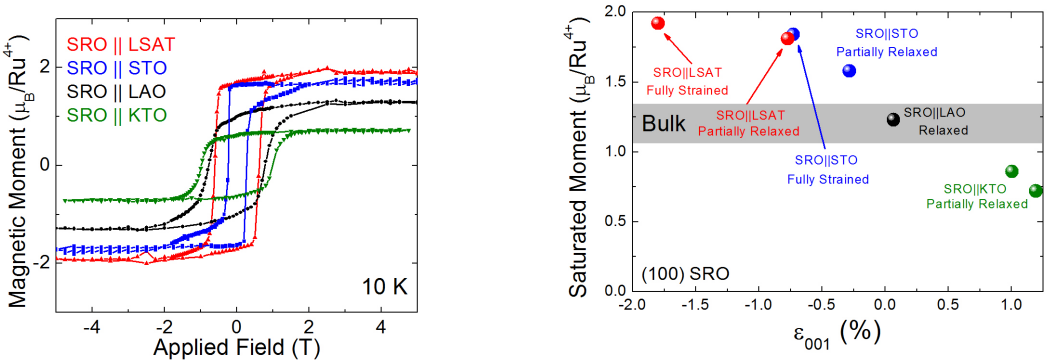

(a) (b)

Figure 3.7: a) Easy axis magnetic hysteresis loops and b) relationship between saturated moment and in-plane strain for films on all (100) substrates. Samples shown are representative films between 60-80 nm thick.

while the thickest, partially relaxed films on (100) $SrTiO_3$ had saturated moments of 1.44 μ_B/Ru^{4+}. Films under tensile stress on $KTaO_3$ exhibited a reduction of the saturated magnetic moment from bulk values, with saturated moments ranging between 0.5-1.0 μ_B/Ru^{4+}. This information points strongly towards a strain dependence of the saturated magnetic moment on the applied epitaxial strain, as can be seen in Figure 3.7(b). Here we extract the in-plane lattice parameter for a series of films on different substrates and plot it against the saturated magnetic moment. Some are completely relaxed, some are partly relaxed, and some are coherently strained, but all fall onto the same monotonic curve that decreases saturated magnetic moment as we move from compressive to tensile strain. A particularly telling example can be seen in a partially relaxed film on (100) LSAT whose in-plane lattice parameter is nominally 0.7% smaller than bulk. Its saturated moment is nearly identical to that of a coherently strained film on (100) $SrTiO_3$, which is under 0.7% compressive strain. Both films exhibit saturated moments of 1.8 μ_B/Ru^{4+}. Alternatively, we can use the example of a fully relaxed and partially relaxed pair of films on (100) $LaAlO_3$ which saturate at 1.3 and 1.8 μ_B per formula unit, respectively.

To understand the origins of the magnetism in our samples, we performed X-ray absorption (XA) and X-Ray Magnetic Circular Dichroism (XMCD) at beamline 6.3.1 and 4.0.2 of the Advanced Light Source. Typical examples of Ru and O XA spectra taken at beamline 4.0.2 can be seen in Figure 3.8. The spectra are consistent with previously reported examples of Ru^{4+} in an octahedral environment.[115] Also shown in Figure 3.8 are typical XMCD measurements taken with an alternating $\pm$ 0.5 T applied field normal (90°) to the film surface. Because magnetic hysteresis loops show that 0.5 T is not generally sufficient to saturate the film magnetic moments at 10 K, the spectra were taken at 75 K. At this temperature the width of the hysteresis loop is decreased enough for the magnetic moment to completely switch in 0.5 T. Additionally, the results were confirmed using the larger electromagnet at beamline 6.3.1 with an alternating field of $\pm$ 1.7 T.

In order to show the salient features of the XA and XMCD spectra, we show here the results from beamline 4.0.2 with much higher resolution and intensity associated with the elliptically polarizing undulator present at 4.0.2 relative to the bending magnet source at 6.3.1. The obtained spectra showed the samples to be free of magnetic impurities such as Fe, Ni, and Co to within the sensitivity of the measurements. As these contaminants may be easily detected in concentrations as low as 0.1 at%, these results confirmed that the magnetism originates primarily on the Ru^{4+}, with a contribution from O^{2-} ions. It is interesting to note that the magnetic polarization and anisotropy is present in the O spectra, rather than the Ru alone. This is likely the result of strong Ru $4d$ - O $2p$ hybridization. Although there is no mehtod by which we can estimate the O contribution, it is suspected to be small.[115] We then calculated the ratio between spin and orbital moment of films in a variety of strain states. The details of the XMCD sum rules can be found in appendix 1 but in general show the spin and orbital moments to be:

$$\frac{m_l}{m_s} = \frac{3}{2}\frac{A_{M5} - A_{M4}}{A_{M5} + 2A_{M4}} \tag{3.1}$$

where A_{M5} is the area of the XMCD signal under the M^5 edge and A_{M4} is the area under the M^4 edge. Thus we can clearly see that the larger the difference between the area of the two peaks, the larger the orbital contribution to the magnetic moment. Careful application of the XMCD sum rules to the spectra is necessary to ensure that spectra from different samples have been properly normalized to the X-ray absorption spectra before extracting the ratio. Once obtained, the ratio m_l/m_s was then calibrated to saturated moments measured in the SQUID to yield the estimated magnitude of the orbital moment. Measurements on strained samples show that both the ratio m_l/m_s and the absolute value of the orbital moment are significantly larger for strained films on $SrTiO_3$ than for relaxed films on $LaAlO_3$. The strained films had ratios between 8-15%, corresponding to orbital moments between 0.14-0.32 μ_B/Ru^{4+} while relaxed films on $LaAlO_3$ had much lower values of $m_l/m_s < 5\%$ and $m_l < 0.06$ μ_B/Ru^{4+}.

3.4 Understanding the Mechanism for Tuning the Saturated Magnetic Moment

From the magnetic and structural results, it is clear that a strong correlation exists between the strain state and magnetic properties of $SrRuO_3$ thin films. The mechanism behind this correlation, however, remains unclear, but the most obvious ways in which strain can modify the ground state of a system fall into three general categories - changing the shape, connectivity, or size of the RuO_6 octahedra in which the magnetism originates.[128] A change in shape refers to the volume change and tetragonal distortion imposed on the system in the ideal case of a $SrRuO_3$ film epitaxially strained to the (100) substrate. In this case bond lengths are expanded or contracted based on the symmetry of the distortion, and it has been shown through density functional theory calculations that such an effect may lead to a modification of the magnetic state in $SrRuO_3$.[128, 162] Modifying the connectivity of the RuO_6 octahedra refers to altering the Ru-O-Ru bond angles shown in Figure 3.1 through tilting and rotation of the RuO_6 octahedra. Such a modification will affect the Ru $4d$ O $2p$ orbital

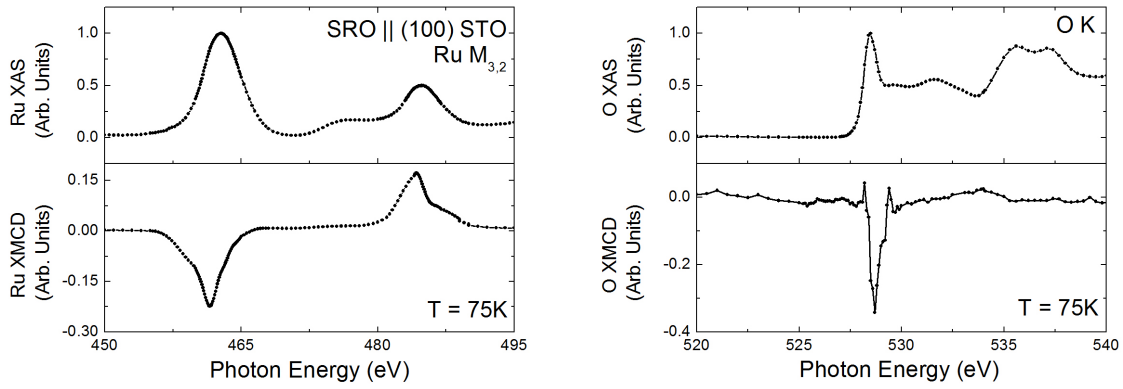

(a) (b)

Figure 3.8: a) Ru $M^{3,2}$ edge and b) O K edge X-ray absorption and X-ray magnetic circular dichroism

overlap and, consequently, the crystal field, bandwidth and exchange interactions. A change in the size of the RuO_6 octahedra is most likely to be induced through an off-stoichiometry which may be induced either as a means of strain accommodation or as a byproduct of the deposition process. Determining whether such a volume expansion or contraction is an intrinsic strain effect is problematic. Clearly, before we can begin to address the possibility that strain effects are enhancing or suppressing the saturated magnetic moments and magnetic transition temperatures of our films, we must first assess likely alternative causes of our observations. The case of a suppressed saturated magnetic moment may be ascribed to the reduction to a reduction crystallographic quality. An increased saturated moment, in contrast, may be caused by contamination of the sample with ferromagnetic particles such as iron or nickel. Doping or changes in stoichiometry may also be expected to significantly alter the saturated magnetic moment. We will examine these three possibilities before turning to a discussion of strain effects and their consequences.

Of the measurements taken, the two best indicators of film quality are the ω rocking curves through the (200) X-ray diffraction peaks and the film residual resistivity ratios. At already discussed, although the suppressed magnetic moment is exhibited by $SrRuO_3$ films deposited on $KTaO_3$, films on $LaAlO_3$ have by far the widest ω scan peaks. The rocking curves of films on $KTaO_3$ are in fact most comparable to films on LSAT, which exhibits the highest saturated magnetic moment of the compressively strained films. In fact, films deposited on $SrTiO_3$ have the narrowest rocking curves but show lower saturated magnetic moments than those on LSAT. Thus, there does not appear to be any significant correlation between the saturated magnetic moment and film quality as measured by the width of the ω rocking curve. Reduced crystalline quality that suppresses the saturated magnetic moment might also be expected to suppress film T_C, but we observe no such consistent trend and it is the films with the widest rocking curves that exhibit the highest and most bulk-like T_Cs while the T_C of films on $SrTiO_3$ and LSAT are in fact suppressed. It must be noted, however, that examining the rocking curve width along may not be an ideal measure of crystallographic

quality. It is well known that $LaAlO_3$ substrates are prone to twinning which may result in a very wide ω rocking curve. This increased width is then transferred to the film and may artificially inflate the estimate of rocking curve width. That is, it is possible for a film to exhibit significant mosaic spread across the entire film while maintaining excellent local crystallinity. Therefore we must renormalize the rocking curve width of the film to that of the substrate. When we do this we find ratios of 4.4, 3.16, 2.25, and 3.95 for films on LSAT, $SrTiO_3$, $LaAlO_3$, and $KTaO_3$ respectively. We conclude, therefore, that the films on $LaAlO_3$ are of comparable quality to those on LSAT and $LaAlO_3$.

The RRRs extracted from the ρ vs. temperature measurements follow the same trends. A suppressed T_C is associated with the lowest RRRs in films grown on $SrTiO_3$ and LSAT while the highest RRR on $LaAlO_3$ is much more bulk-like. The RRRs of films with suppressed moment on $KTaO_3$ are on the order of 2-2.5, while the T_C of these films is very bulk like. Additionally, the films on LSAT which have the highest saturated magnetic moments have RRRs in the middle of the spectrum, flanked on one side by films on $SrTiO_3$ and on the other by $LaAlO_3$. Finally, although films on $SrTiO_3$ with saturated moments ranged from 1.44-1.95 μ_B/Ru^{4+}, no significant variation in their RRRs was observed. Thus, there is no clear correlation between film RRR and either T_C or saturated magnetic moment. These results agree with those from the ω rocking curves and demonstrate that a parameter other than crystal quality must be responsible for both the increased saturated moment in compressively strained films and the suppressed saturated moment in films under tensile strain.

Doping, contamination, and off-stoichiometry are all best probed through the X-ray absorption and Rutherford backscattering spectra we obtained. As already discussed, no ferromagnetic impurities were found to be present either incorporated into the films or on the surface. There is, however, evidence in the X-ray absorption spectra for trace contamination of the A-site by Barium impurities, which most likely originate in the sintered laser ablation target. The impurity levels are so low that it is not possible to obtain an accurate estimate of the Barium content through fitting of the Rutherford backscattering spectra, although we can establish an upper limit of 2%. In any case, Ba is expected to be an A-site impurity with little impact on the magnetic properties except potentially through a slight increase in unit cell volume. However, as little to no such volume expansion is observed in the relaxed films on $LaAlO_3$, it is very unlikely that the contamination is related to the non-bulk-like magnetic behavior.

The issue of slight off-stoichiometry is much more difficult to resolve, in part because of highly contradictory results in the literature. Although energy-dispersive X-ray spectrometry measurements have indicated that reductions in the Ru content as small as 6% may reduce the Curie temperature to 120 K, site occupation measurements performed using neutron diffraction suggest that the T_C may be bulk-like even for a Ru-deficiency as high as 5%.[25] Others have fabricated slightly (less than 2%) Ru-poor films using both molecular beam epitaxy and pulsed laser deposition without significant T_C variation.[138] A Ru-content variation of 6% in our films is easily eliminated by Rutherford backscattering measurements, but variations on the order of 2-3% cannot be fitted with complete confidence. The effect of such a small variation in Ru-content on the transition temperature is not clear from the literature. In the most extreme case, such a variation might reduce the transition temperature by as much a 15-20K, accounting for nearly half of the observed T_C variation, while less extreme predictions expect little to no effect on. It is critical to note that a decrease in

the transition temperature associated with Ru-deficiency is expected to be accompanied by significant volume expansion, while Figure 3.9(b) shows precisely the *opposite* trend. This suggests very strongly that the observed suppression and variation of T_C is not the result of varying Ru content. In any case, growth studies have shown that an oxygen pressure between 50-100 mtorr during film deposition, as used to prepare our samples, is ideal for obtaining bulk-like Sr and Ru content.[167]. Consequently, it is very unlikely that any deviation from the expected Ru content in our films is significant enough to affect the magnetic properties. Neither is there any proposed mechanism by which Ru-deficiency may enhance the magnetic moment nor any observation of such an effect experimentally despite many studies of Ru poor $SrRuO_3$ films.

Alternatively, Oxygen vacancies or compressive strain resulting in an expansion of the c-axis have also been suggested as factors which may reduce the film transition temperature.[19] However, the literature again shows no clear conclusion on the relationship between Oxygen vacancy formation and the Curie temperature of $SrRuO_3$. It has been demonstrated that a large variation in Curie temperature (40-165 K) may be achieved with no statistically significant variation in oxygen site vacancy across the entire range.[25] The lack of clear results on this topic may be related to the ease of achieving fully oxygenated $SrRuO_3$. It is generally agreed that adding a short annealing stage to the deposition process, as in the case of our films, will result in homogenous, fully oxygenated films.[156] Unfortunately, Oxygen content may be determined with much less confidence than that of Sr or Ru, and off-stoichiometry as high as 20% may not be detected through Rutherford backscattering. Thus, we rely primarily on the literature for a more complete analysis of growth conditions leading to full oxygen content and although Rutherford backscattering spectrometry shows no evidence of off-stoichiometry in the films, it is possible that some may be present.

Since off-stoichiometry is almost universally accompanied by either volume contraction or expansion, we may use this as a further proxy for off stoichiometry. Figure 3.9 shows the relationship between unit cell volume and (a) saturated magnetic moment and (b) Curie temperature. Although a general trend may be observed, with volume contraction associated with high saturated moment and lower Curie temperatures while volume expansion is associated with low saturated moment and high Curie temperature, films on both $LaAlO_3$ and $SrTiO_3$ exhibit very little lattice expansion or contraction ($\leq 0.8\%$) while showing both bulk-like and enhanced saturated moments, respectively. Other enhanced films on LSAT are accompanied by a volume contraction. Since the enhancement of the saturated magnetic moment appears without any significant deviation from the bulk unit cell volume, it is very unlikely that stoichiometric effects are responsible for enhancing the saturated magnetic moment. As has already been discussed, Ru-deficiency resulting in supression of T_C is coincident with significant volume expansion. Similarly, growth of $SrRuO_3$ in very low oxygen pressure was studied by Yoo et al. and Zou et al., who showed that for oxygen deposition pressures below 50 mtorr a sharp rise in unit cell volume occurs with volume expansions in excess of 3%.[160, 167] Films grown at 60 mtorr, as in this study, are structurally very bulk-like.[160, 167] Once again we conclude that the reduction in T_C shows a dependence opposite what is expected from an effect originating in off-stoichiometry. Finally, volume expansion and contraction observed in our films almost exactly matches not only the volume modulation predicted for the case of pure epitaxial strain in perfectly stoichiometric $SrRuO_3$, but also the relationship between T_C and the c/a axis ratio found by Wissinger et

al.[156, 161]

We may gain some additional insight into the effects of any slight off-stoichiometry by examining the relaxed films on $LaAlO_3$, which exhibit bulk-like saturated magnetic moment but reduced Curie temperatures of 148-150 K. Since we may neglect strain effects in this case, it is possible to estimate the maximum possible reduction in T_C due only to stoichiometric effects. Since the T_C is reduced by only 11-13 K in this case, the effects of Ru or O vacancies would appear to be minimal. In fact, a suppression of this magnitude, if caused *only* by Ru vacancies, would correspond to off-stoichiometry of approximately 0-3%, in agreement with the limits of the Rutherford backscattering measurements.[25] It is equally likely that the slight T_C reduction of films on $LaAlO_3$ substrates may be simply explained by lower crystal quality originating in the higher roughness, lower crystal quality, and significant relaxation exhibited by these films. Although the application of epitaxial strain may cause the stabilization of additional Ru or O vacancies in films on $SrTiO_3$, LSAT, or $KTaO_3$, many examples of stoichiometric $SrRuO_3$ films on $SrTiO_3$ and LSAT substrates deposited in similar conditions exist in the literature.[25, 60, 138, 156] Finally, films on $KTaO_3$ have precisely bulk-like transition temperatures. In these samples, therefore, either tensile strain must stabilize the ferromagnetic state and increase the T_C to compensate for the off-stoichiometry, or the films on $KTaO_3$ must be perfectly stoichiometric.

In particular, the stabilization of oxygen vacancies in the film is a very poor candidate given that its two primary effects are likely to weaken the magnetic coupling rather than strengthen it. First, the stabilization of Ru^{3+} which, with a t_{2g}^5, $S={}^1/_2$ electron configuration, is expected likely to reduce the saturated magnetic moment rather than increase it. Second, O vacancies are likely to produce a volume expansion.[167, 160] Such an expansion is also likely to reduce the Ru-O orbital overlap and weaken the strong hybridization which stabilizes ferromagnetism in bulk $SrRuO_3$. It is now clear that strain effects are the best candidate for explaining the observed modulation of film saturated magnetic moment as well as the majority of the variation in Curie temperature. In addition to a strong correlation between the in-plane strain and saturated magnetic moment, the films saturate to bulk values when relaxed. Even samples on different substrates with the same strain saturate to the same value. These are very strong indicators that strain is the parameter controlling the saturated magnetic moment. There is also strong evidence that off-stoichiometric effects play at most a very small role in the variation of film transition temperatures. Rather, the final Curie temperature is most likely dominated by strain effects, although a lack of a bulk T_C in relaxed films suggests additional relevant parameters.

As has already been stated, Zayak et al. predicted that the introduction of epitaxial strain would modify the saturated moment of $SrRuO_3$.[162, 161] They additionally show that the epitaxial changes in bond angle induced by epitaxial strain will be accompanied by significant distortions in the octahedral shape.[162, 161]. In their work, which accounts for both compressive and tensile distortions, they predict an increase in the saturated magnetic moment under *tensile* epitaxial strain and a suppression under compressive strain! The schematic shown in Figure 3.10, shows a distorted octahedra resulting from compressive strain along with the predicted splitting which may be induced in the t_{2g} orbitals.[162] From this splitting, it is possible to understand the predicted trends. Neglecting the unoccupied e_g orbitals, we can see that the distortion splits the t_{2g} orbitals such that a spin zero configuration is stabilized.[162] This splitting is not one which is immediately expected from a

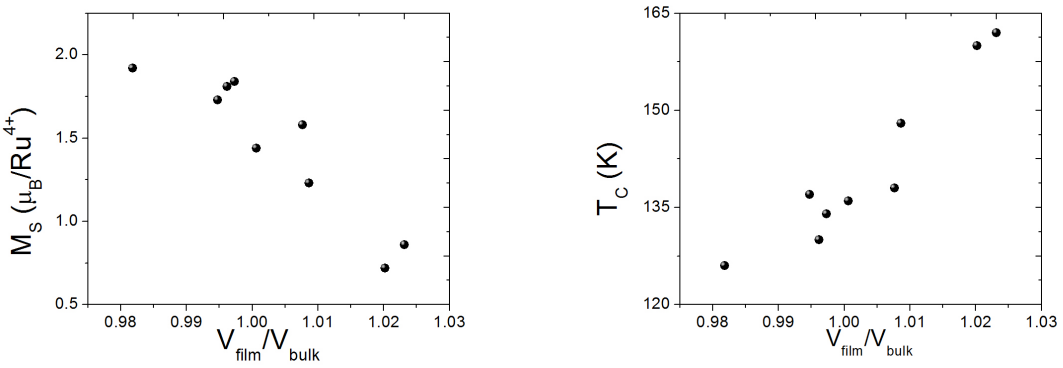

(a) (b)

Figure 3.9: Film unit cell volume vs. a) saturated magnetic moment and b) Curie temperature for films on all (100) substrates

distortion which lengthens the in-plane bonds and compresses the bonds along the growth axis (z), but is the result of both changes to bond length and bond angle.[161] As the compressive strain is increased, a mixture of the low (S = 0) and intermediate (S = 1) spin states is stabilized and the saturated magnetic moment is gradually suppressed. The origins of the predicted enhancement of the saturated magnetic moment with tensile strain are less clear. In any case, it is clear that the predictions are directly in conflict with the results presented in this work.

However, these predictions were made assuming that the final symmetry of the system would fall into the orthorhombic Pbnm symmetry. Zayak et al. also performed calculations for the case of tensile strainwith the assumption that additional rotation of the RuO_6 octahedra will be limited and the final structure falls into the tetragonal P4/mmm structure. In this case, Zayak et al., predicts a sharp decrease in the saturated magnetic moment with increasing compressive strain as a nonmangetic spin-zero state is stabilized in the Ru ions.[162, 161] In this case, we find excellent agreement between the predictions and our experimental results. Even the magnitude of the moment suppression for a given strain value is well matched to the theoretical values.[162, 161]. Therefore we have performed a series of ϕ dependent reciprocal space maps of the (301), (310), (30$\bar{1}$), and (3$\bar{1}$0) reflections for compressively strained films. As shown in Figure 3.11, we find that all four peaks show precisely the same lattice parameters, indicating a tetragonal system. Therefore it is highly likely that we have stabilized the nonmagnetic Ru spin configuration predicted by Zayak et al..

Finally, it is worth noting that the theoretical work by Zayak et al. predicts a strain induced volume contraction of 2% at 2% compressive strain with a linearly increasing volume that reaches 2% expansion at 2% tensile strain.[161] These predictions are in excellent agreement with the variation shown in Figure 3.9, although the expected unit cell volumes are approximately 3% lower than those which are experimentally realized.[161] This difference may be responsible in part for the disagreement between experiment and the theoretical predictions made assuming an orthorhombic unit cell in the case of compressive strain. The

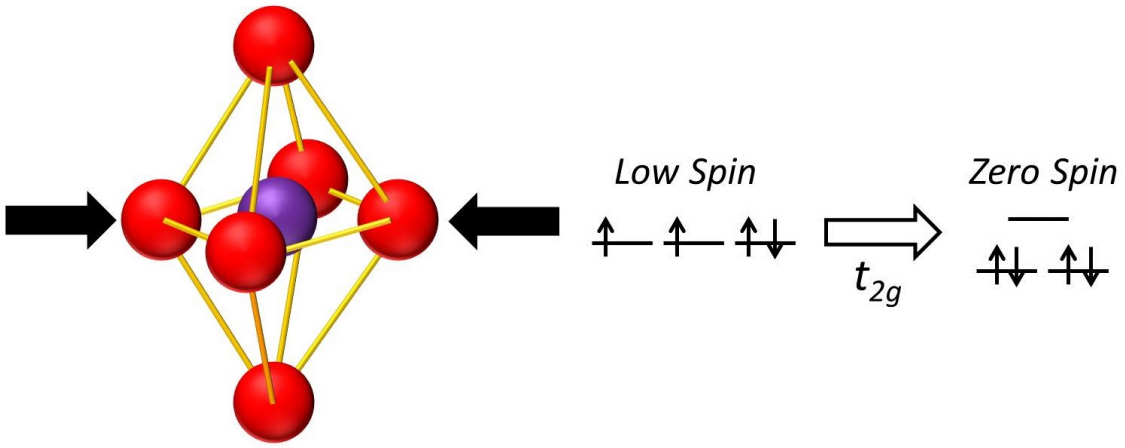

Figure 3.10: a) Octahedra distorted by compressive strain and b) Example splitting of the t_{2g} orbitals which may result in a reduced moment

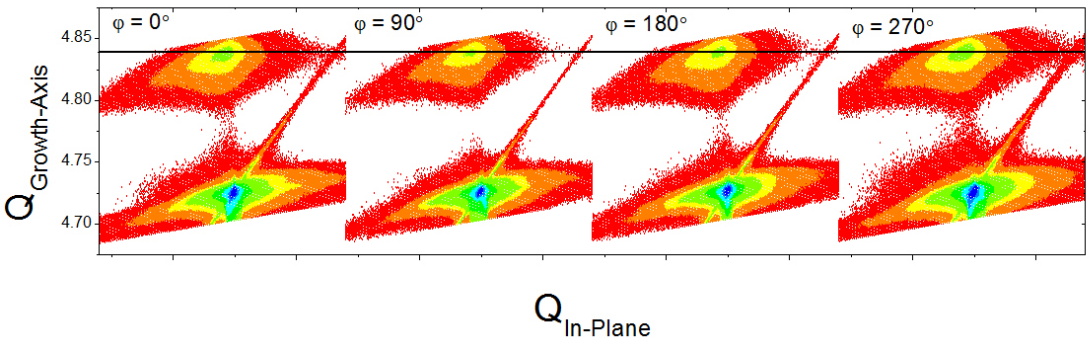

Figure 3.11: a) Reciprocal lattice maps of a series of (301) type reflections taken at 90° ϕ intervals for a representative $SrRuO_3$ film on (100) $KTaO_3$

difference in unit cell volume likely represents a significant variation in the induced tilt and rotation of the RuO_6 octahedra.

An alternative explanation for the discrepancy in the case of compressive strain is the neglect of the orbital contribution to the magnetic moment. We have decoupled the orbital and spin contributions of the saturated magnetic moment using the sum rules for X-ray magnetic circular dichroism. As discussed in section 1.4.5, the quenching of the orbital magnetic moment is a competition between bonding, which favors standing waves without imaginary wavefunction components, and the spin-orbit interaction, which favors an increase in the orbital magnetic moment. Thus, the spin moment in a ferromagnetic compound perturbs the bonded wavefunction and causes the otherwise quenched orbital moment to be "recreated". A weakening of the Ru-O bonding along the expanded axis will result in a relatively stronger perturbation and consequently a larger orbital magnetic moment in that direction. This is precisely what we observe in the compressively strained samples, with fully relaxed films exhibiting orbital moments less than 0.06 μ_B/Ru^{4+} while the out of plane orbital moments of compressively strained films reach as high as 0.32 μ_B/Ru^{4+}. Given a bulk magnetic moment between 1.2-1.4 μ_B/Ru^{4+}, this increase is sufficient to explain moments as high as 1.7 μ_B/Ru^{4+} in compressively strained films, but not the entire observed range. The orbital magnetic moment of films under tensile strain is also increased along the in-plane axis to 0.1-0.16 μ_B/Ru^{4+} despite the suppressed saturated magnetic moment. We conclude, therefore, that additional effects must play a role.

The final explanation we will consider is that the epitaxial strain has, through a combination of octahedral rotations and distortions, changed the Ru-O orbital overlap. This will alter the hopping parameter t in the Hubbard Hamiltonian, which may be roughly equated to W, the bandwidth. A change in the bandwidth must be accompanied by a modulation of the density of states near the Fermi level. Such a modulation can be expected to increase or decrease the saturated magnetic moment for a given exchange energy. Therefore we may construct a model in which the density of states at the Fermi level is increased by compressive strain, resulting in a larger saturated magnetic moment, and decreased by tensile strain, resulting in a smaller saturated moment. This effect, combined with the variation of the orbital magnetic moment, can explain all of the observed effects.

3.5 Outlook and Concluding Remarks

Having demonstrated the important of epitaxial strain, we now turn to unanswered questions and future experimentation. Among the most pressing issues is the precise nature of the distortion which causes the enhancement or suppression of the saturated magnetic moment. In order to describe and model the observed behavior, a thorough understanding of the structure is necessary. Although it is well known that the measurement of bond distances and angles in thin films via the Rietveld method is both difficult and unreliable, alternative techniques may offer additional insight. The most promising avenue is that of extensive reciprocal lattice mapping, including scans of reciprocal lattice points at many different ϕ values. Such measurements may allow the precise nature of the distortion to be probed systematically. Such an endeavor requires extensive mapping of samples in all strain states, however. Other issues include the possibility of a strain gradient present in the films.

Thicker films which are partially or completely relaxed are of particular interest here, as the non-bulk T_C observed in relaxed samples may be partially explained by a strain gradient. Such a phenomenon could be probed through polarized neutron reflectometry, as a strain gradient might also be expected to induce a magnetization gradient. Finally, the surprising relationship between saturated moment and T_C merits further investigation, as the typical direct relationship between the two parameters becomes an inverse one in our $SrRuO_3$ films.

These issues notwithstanding, this work demonstrates the opportunity for tuning the magnetism in complex oxide thin films using epitaxial strain. Even in the simplest case of (100) oriented films we find sweeping changes to the magnetic ground state manifested as modifications in saturated magnetic moment and Curie temperatures. This work shows that the non-bulk behavior originates in an extreme sensitivity of the crystal field to changes in bonding. Having established $SrRuO_3$ as an excellent model system, we now turn our attention to alternative distortion symmetries in Chapter 4.

Chapter 4

Stabilizing High Spin Ru^{4+} in $SrRuO_3$

In chapter 3, the simplest case of strain modifying the magnetic ground state of $SrRuO_3$ was addressed through growth on (100) oriented substrates. Although this work reports some surprising results, the (100) orientation has historically been the focus of most investigations into the growth and properties of $SrRuO_3$ thin films. With a few exceptions, growth on (110), (111), and other substrate orientations remains relatively unexplored. This chapter will focus on the effects of alternative distortion symmetries by probing magnetism in $SrRuO_3$ films grown on (110) and (111) oriented substrates. This study will show a remarkable dependence of the magnetic and electron transport properties on the substrate orientations. A spin transition from low to high-spin Ru^{4+} is observed, only the second reported instance of this spin configuration, and the mechanisms behind the spin transition are explored.

4.1 $SrRuO_3$ on (110) and (111) Substrates

As the bulk structure and properties of $SrRuO_3$ have already been discussed in Chapter 3, this discussion will be omitted here and the reader is encouraged to refer back for such details. For this work, a series of $SrRuO_3$ thin films were grown on (110) LSAT, $SrTiO_3$, $LaAlO_3$, and $KTaO_3$ substrates along with (111) oriented $SrTiO_3$ and $KTaO_3$ substrates using pulsed laser deposition as described in chapter 3. Films were not grown on (111) LSAT or $LaAlO_3$ due to the difficulty of achieving high quality epitaxy on (111) substrates with large mismatches. As in chapter 3, film thicknesses were varied from 15-120 nm to probe a variety of strained, relaxed, and partially relaxed states. In the ideal case of a cubic perovskite grown on (110) and (111) oriented substrates, distortions with monoclinic and trigonal distortions are expected to be induced respectively. Although $SrRuO_3$ is slightly orthorhombically distorted, this model represents an excellent starting point for understanding the distortions in the films. Figure 4.1(a) and (b) illustrate the stress direction exerted on the film in the case of compressive mismatch with (110) and (111) oriented substrates, respectively. If $SrRuO_3$ is approximated to have cubic symmetry, the resulting distortions will have strain tensors of the form:

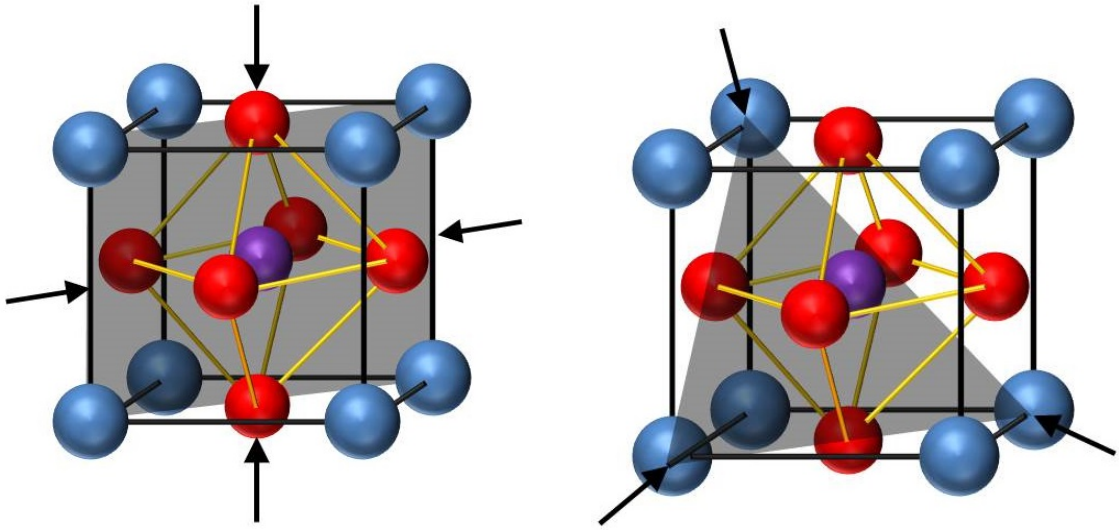

(a) (b)

Figure 4.1: Compressive stresses applied to a cubic system by a) (110) and b) (111) oriented substrates

$$\epsilon_{110} = \begin{pmatrix} \epsilon_{11} & \epsilon_{12} & 0 \\ \epsilon_{12} & \epsilon_{11} & 0 \\ 0 & 0 & \epsilon_{33} \end{pmatrix} \tag{4.1}$$

$$\epsilon_{111} = \begin{pmatrix} \epsilon_{11} & \epsilon_{12} & \epsilon_{12} \\ \epsilon_{21} & \epsilon_{11} & \epsilon_{12} \\ \epsilon_{12} & \epsilon_{12} & \epsilon_{11} \end{pmatrix} \tag{4.2}$$

From this it can be seen that a (110) oriented film may be expected to experience a volume change, a tetragonal distortion, and a shear strain while a (111) oriented film will undergo a volume change and shear strain. For a full treatment of epitaxial strain of a cubic system on (110), and (111) substrates, see Appendix B or the following references.[157, 113] These strain states differ from those presented in Chapter 3 in the addition of a shear strain in both orientations and the lack of a tetragonal strain component in the (111) orientation.

4.2 Structure and Film Quality

A systematic study of the effect of lattice distortions requires a set of consistently high quality samples and accurate characterization of the magnitude of the applied strain. To that end, structural and surface characterization techniques were once again employed and indicate that the SRO films are epitaxial, highly crystalline, stoichiometric, and smooth. Figure 4.2a) shows a series of $\theta - 2\theta$ X-ray diffraction scans on all (110) oriented substrates that indicate high quality films with peaks corresponding exclusively to $SrRuO_3$ and the substrates in the expected crystallographic orientations. Films on (110) substrates are of

very high quality relative to those in the (100) and (111) orientation, as is evident from the strong interference fringes displayed by the film on (110) $SrTiO_3$ in Figure 4.2. θ-2θ scans of (111) films ω illustrate the difficulty of achieving high film quality on (111) substrates. Both films in Figure 4.2(b) are 70-80 nm thick, but the strength of the film peak is significantly degraded on $KTaO_3$ relative to $SrTiO_3$. As the mismatch increases, the crystallinity of the (111) oriented film rapidly decreases. Thus, with the exception of using films on (111) $KTaO_3$ as a control for very low-quality material, discussion of (111) oriented films is confined to $SrTiO_3$ substrates. Rocking curves of the film peaks on $SrTiO_3$ showed excellent epitaxy with mosaic spreads as low as 0.038° in the (110) orientation and as high as 0.23° in the (111) orientation, as shown in Figure 4.3(a), with a (100) oriented film for comparison. Among films on (111) $KTaO_3$ the mosaic spread may reach as high as 1.3°. Finally, for films of any orientation, mosaicity is inversely related to lattice mismatch, with films on STO showing smaller mosaic spread than films on LSAT and LAO, which show increasing mosaicity.

A comparison of reciprocal lattice maps of SRO films grown on different substrates and in different orientations revealed a variety of strain states. Due to the inherent anisotropy of mechanical properties in the (110) plane (see Appendix B), it was necessary to probe two distinct in-plane directions - [001] and $[1\bar{1}0]$ - in order to characterize the strain state of (110) oriented films. This was accomplished through reciprocal lattice maps of the film and substrate (310) and (221) peaks. In contrast, the threefold symmetric (111) oriented films required only a single map to characterize - the (321) peak. By varying lattice mismatch from -1.53% to +1.47% and thickness from 15 to 120 nm, strain states ranging from coherently strained to partially or fully relaxed were achieved. Reciprocal lattice maps of the films on (110) STO show that films are strained up to thicknesses of 80 nm, but begin to show partial relaxation by 120 nm. (110) films on LSAT begin to relax partially at thicknesses above 60 nm. The strain state of partially relaxed films on LSAT is particularly difficult to understand systematically as they do not relax at the same rate along the [001] and $[1\bar{1}0]$ directions. As in the (100) orientation on $LaAlO_3$, films are difficult to grow fully strained, beginning to relax by 40 nm in thickness. It is more difficult to stabilize coherently strained films in the (111) orientation. Reciprocal lattice maps of films on (111) STO show greater relaxation than films of comparable thickness in other orientations. For SRO films on (111) STO, coherent strain can be maintained only for films less than 30nm thick. In these films on (111) STO, a variety of different strain states were obtained ranging from coherently strained to partially relaxed as film thickness was increased from 15 to 120 nm.

Film quality was additionally confirmed through characterization of surface morphology using AFM and film stoichiometry using RBS. AFM measurements reveal that (110) and (111) oriented films grow with a columnar or island morphology with root-mean-square surface roughnesses ranging from 0.5-1.8 nm on $SrTiO_3$ (depending on thickness) and as high as 4.9 nm on (110) $LaAlO_3$. Even the roughest films on LAO had roughnesses more than an order of magnitude lower than the film thickness. Rutherford backscattering spectra were consistent with those of (100) $SrRuO_3$ discussed in chapter 3, showing a 1:1 ratio of Sr and Ru. Again, it is much more difficult to accurately determine O content; all measurements are consistent to within experimental error with the expected stoichiometry. The reader is referred to an extensive discussion on films stoichiometry in chapter 3 for further information. Thus, through a combination of AFM, X-ray diffraction, and RBS, it is concluded that high-quality stoichiometric films of $SrRuO_3$ have been grown in a wide variety of strain states on

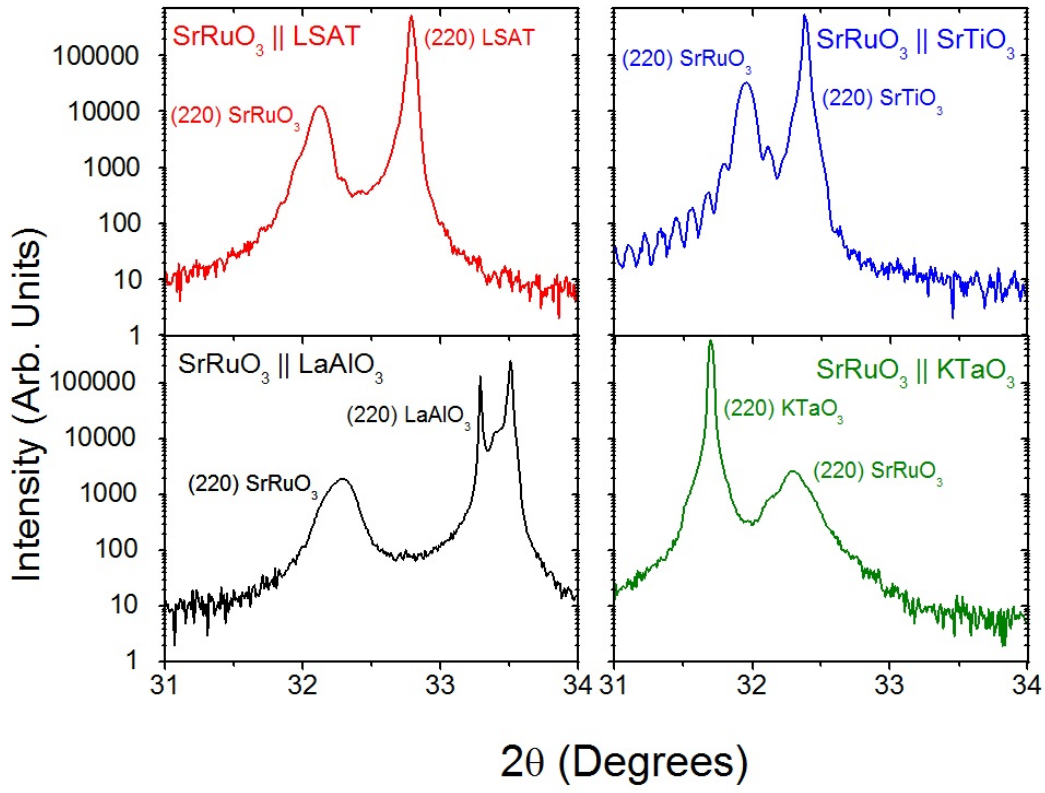

(a)

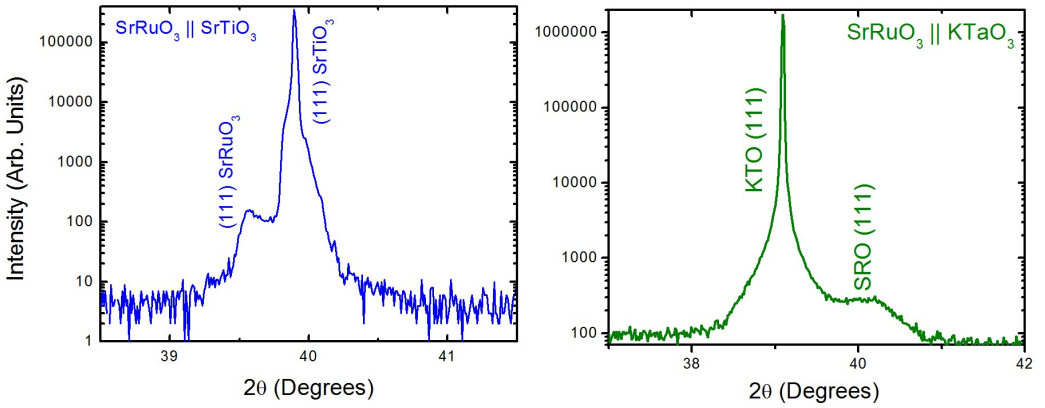

(b)

Figure 4.2: θ-2θ X-ray diffraction scans of $SrRuO_3$ films on a) (110) and b) (111) oriented substrates. The reader may take note of the substrate peaks, which occasionally exhibit small shoulders or, in the case of $LaAlO_3$, multiple peaks. This is common in commercially produced oxide substrates and is typically the result of twinning in the sample. All samples shown are representative films between 50-80 nm in thickness.

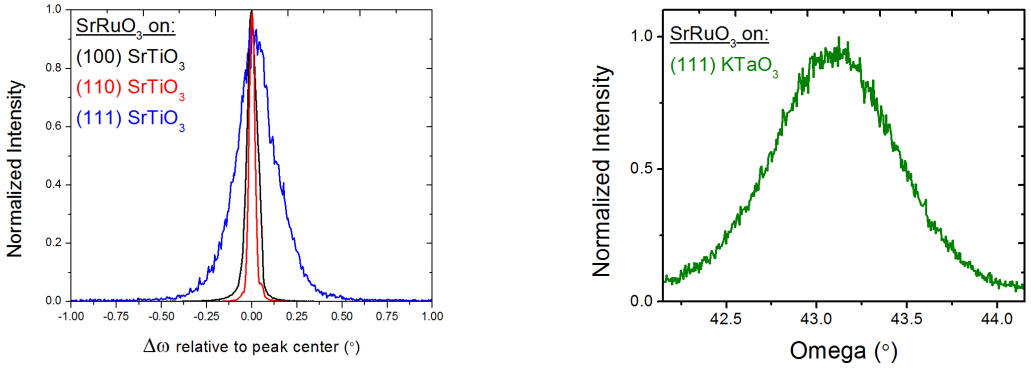

(a) (b)

Figure 4.3: ω X-ray diffraction rocking curves of $SrRuO_3$ films on a) $SrTiO_3$ and b) (111) $KTaO_3$ substrates. All samples shown are representative films between 50-80 nm in thickness.

(110) and (111) substrates.

4.3 Strain and Magnetism

Having grown high quality $SrRuO_3$ films in a variety of strain states, we examined the magnetic behavior of the films and correlated it with the structure. To examine the relationship between epitaxial strain, Curie temperature, and magnetic moment, we used SQUID magnetometry to probe the saturated magnetic moment with the field applied along the film growth axis at 10 K. These measurements revealed a strong dependence of the saturated moment and Curie temperature on substrate orientation. This work will first discuss films grown on $SrTiO_3$ substrates before turning to those on LSAT, $LaAlO_3$, and $KTaO_3$. The orientation dependence of the saturated magnetic moment and Curie temperature is illustrated by Figure 4.5, which shows magnetic hysteresis loops and magnetization vs. temperature scans for a typical series of films between 60-70nm thick on (100), (110), and (111) oriented $SrTiO_3$. Films on all orientations of $SrTiO_3$ exhibited enhanced saturated magnetic moments compared to previous bulk and thin film values of 1.1-1.6 μ_B/Ru^{4+} regardless of film thickness. (110)-oriented films generally had higher saturated moments than those of (100) oriented films reported in chapter 3, but as with (100) oriented films, all (110) films on $SrTiO_3$ saturate at or below 2.35 μ_B/Ru^{4+} and can be explained in terms of a low spin moment of 2 μ_B/Ru^{4+} ions combined with a 10-15% orbital contribution. In contrast, SQUID magnetometry of $SrRuO_3$ in the (111) orientation revealed saturated moments which are far in excess of 2 μ_B/Ru^{4+}. Numerous films on (111) STO exhibit values in excess of 2.4 μ_B/Ru^{4+}, with some as high as 3.5 μ_B/Ru^{4+}. Such large moments cannot be explained in terms of a low spin Ru state. A remarkable feature of (111) hysteresis loops may be seen in Figure 4.5(a), in which the hysteresis loop exhibits characteristics of multiple switching fields. The (111) loops had lower remnant magnetizations, frequently appeared "pinched" in the center, and saturate at higher applied fields. These features may be indicators of

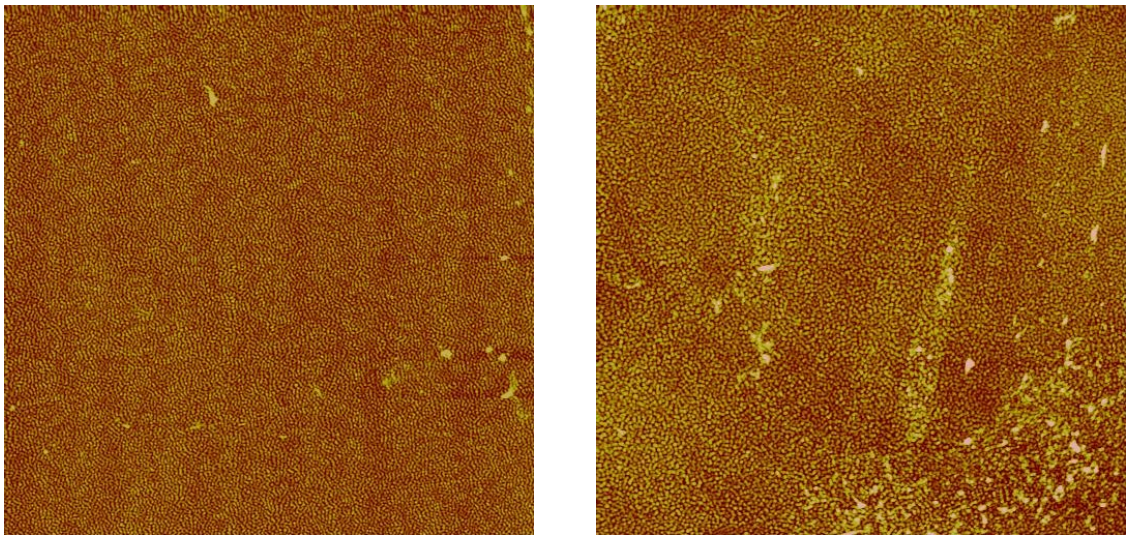

(a) (b)

Figure 4.4: 10 μm atomic force micrographs of films on (110) and (111) $SrTiO_3$

either two distinct, but coupled, magnetic states within the film or inhomogeneity within the film. The Curie temperatures of films on $SrTiO_3$ was also strongly orientation-dependent and followed the same trends as saturated moment. (110) oriented films had Curie temperatures ranging from 142-148 K while (111) oriented films ranged from 147-154 K. Despite evidence for multiple coercive fields in the hysteresis loops of (111) films, only a single Curie temperature is observed.

The rapid relaxation of $SrRuO_3$ on (111) $SrTiO_3$ is well illustrated through changes in the saturated magnetic moment in Figure 4.6(a), which plots the saturated magnetic moment of films on (100), (110), and (111) $SrTiO_3$ as a function of thickness. As shown, the saturated moments of (111) films are a strong function of thickness while (100) and (110) films change much more slowly. This is because (111) films are already partially relaxed at a thickness of 40 nm. As shown in Figure 4.6(b), which plots the in-plane strain against the saturated magnetic moment of (111) $SrRuO_3$ on $SrTiO_3$, a very small change in the epitaxial strain produces a large response in the magnetic properties. Thus, the (111) films relax more quickly and are more sensitive to relaxation, producing the strong thickness dependence evident in Figure 4.6(a) while (110) and (100) oriented films relax more slowly and are less sensitive to strain, producing a weak thickness variation.

As in the case of (100) oriented film, (110) and (111) samples were probed with X-ray absorption spectroscopy and X-ray magnetic circular dichroism of the Ru $M^{4,5}$ edge and the O K edge. As in chapter 3, X-ray absorption measurements show the samples to be free of magnetic contamination and are consistent with Ru^{4+} in an octahedral oxygen cage. X-ray magnetic circular dichroism showed that the ferromagnetism in both (110) and (111) oriented films originates primarily in the Ru with a smaller contribution from states with O $2p$ character due to the strong mixing between the Ru $4d$ and O $2p$ states. Extracting the spin and orbital contributions of the magnetic moment using the sum rules for X-ray magnetic

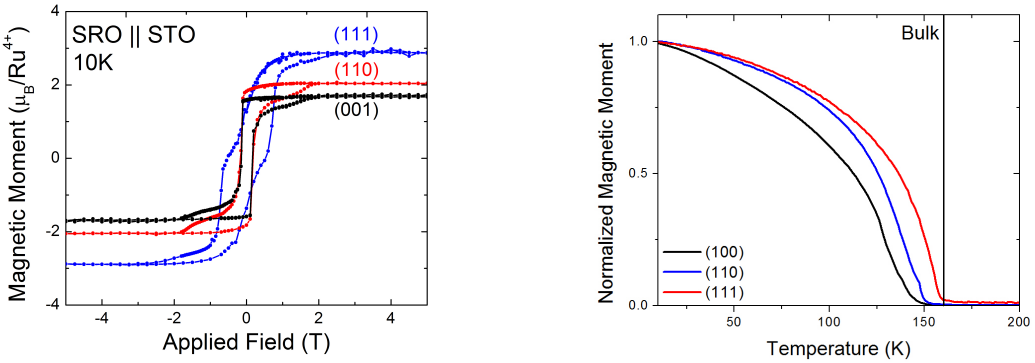

(a) (b)

Figure 4.5: a) Magnetic hysteresis loops and b) magnetization vs. temperature plots of representative films on (100), (110), and (111) $SrTiO_3$

circular dichroism, which may be found in Appendix A reveals an orbital contribution between 8-13% of the total moment in both (110) and (111) oriented $SrRuO_3$. In (110) samples, this corresponds to a contribution of up to 0.3 μ_B/Ru^{4+} and the total saturated moment of all (110) films may thus easily be explained in terms of a more complete alignments of spins in a low-spin Ru^{4+} configuration plus an orbital contribution. In (111) samples, the orbital contribution is somewhat larger and may reach as high as 0.3-0.4 μ_B/Ru^{4+}. However, the orbital contribution to the magnetic moment in (111) films cannot explain the greatly increased saturated moments they exhibit.

Despite the clear dependence of the saturated moment in (111) $SrRuO_3$ on strain, it may be argued based on the thickness dependence of the saturated moment shown by Figure 4.6(a) that some uniform ferromagnetic contamination is present in all (111) oriented samples. Such contamination, if fairly uniform in magnitude across samples, would also be expected to yield an increased saturated moment with decreasing film thickness as the magnetic moments shown are normalized by film volume. In such a case, it may be expected that the observed trends in Figure 4.6(a) may be fitted by a function with the form

$$M_{Observed} = M_{Film} + \frac{M_{Contamination}}{FilmThickness} \tag{4.3}$$

where M_{Film} is a constant corresponding to the bulk magnetization of $SrRuO_3$. As shown in Figure 4.6(c), which plots the thickness dependent magnetization shown in part (a) against a model which models the thickness dependence using equation 4.3, any attempt to use this function to describe the data shows a markedly inadequate rate of increase in the saturated moment with decreasing thickness and in fact argues against such a model. That is, the enhanced magnetization of thicker films is sufficiently large relative to bulk that a contamination based model expects very large magnetic moments at lower thickness, on the order of 5-8 μ_B per Ru ion. Such large moments are not observed at lower thicknesses, demonstrating that any contamination present cannot explain more than a small fraction of the total increase in saturated magnetic moment. We may gain additional insight through the

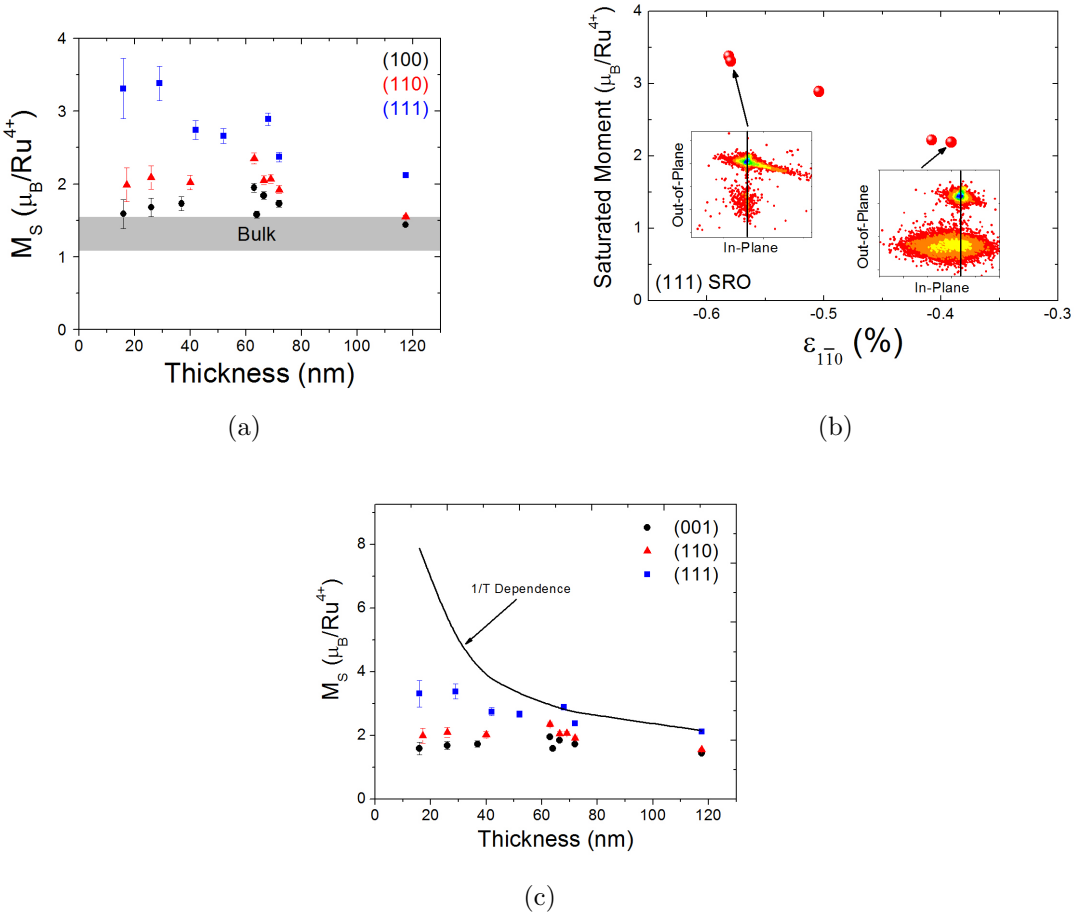

Figure 4.6: a) Saturated magnetic moment vs. thickness of representative films on (100), (110), and (111) $SrTiO_3$. b) Saturated magnetic moment vs. in-plane strain for films on (111) $SrTiO_3$ along with (Insets) (321) reciprocal lattice maps associated with representative films. c) Data shown in plot (a) against a model which describes the (111) oriented films as a contamination effect using equation 4.3. As can be seen, the (111) oriented films do not show a 1/T dependence.

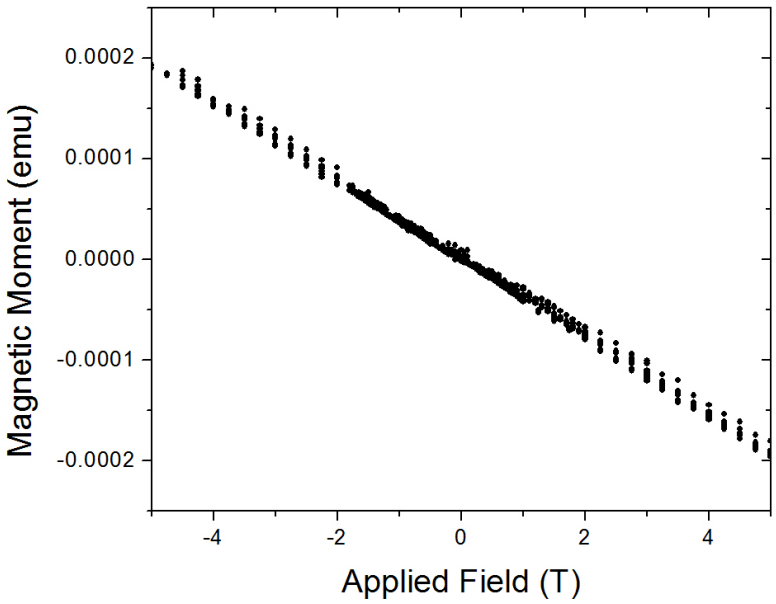

Figure 4.7: Magnetization vs. applied field of a typical (111) oriented $SrTiO_3$ substrate from the same batch as those used for $SrRuO_3$ film depositions

examination of an outlier film not included in Figure 4.6(a). This 40-nm thick, (111) oriented film relaxed much more quickly than expected, with an in-plane strain of approximately 0.39%. In contrast, all other (111) oriented sample with a thickness of 70 nm or less exhibited in-plane strains greater than 0.5%. This lone, highly relaxed film had a saturated magnetic moment of 2.19 μ_B per Ru ion. This is in almost perfect agreement with a highly relaxed 120 nm thick film which exhibited a saturated moment of 2.22 μ_B per Ru ion and an in-plane strain of 0.41%. Although the reason for such extensive relaxation in this sample is unknown, the excellent agreement between the strain state and the magnetic state strongly argue that the enhancement of the saturated magnetic moment is a strain effect rather than contamination.

In addition, such contamination was not observed in either the X-ray absorption spectra, a surface sensitive technique, or Rutherford backscattering spectra, which penetrate past the $SrRuO_3/SrTiO_3$ interface. The only remaining method of explaining the data through contamination, then, is a bulk ferromagnetic contamination of the $SrTiO_3$ substrates which is too dilute to be observed through Rutherford backscattering. To address this final possibility, (111) $SrTiO_3$ substrates were prepared in the same way as the films and characterized magnetically. The observations, shown in Figure 4.7, are in precise agreement with the expected pure diamagnetic signal from $SrTiO_3$ with no evidence of a ferromagnetic component. Therefore it is clear that the enhancement of the saturated magnetic moment is an effect intrinsic to the $SrRuO_3$ film.

As in the case of (100) oriented films in Chapter 3, there also is no evidence of either significant doping or off-stoichiometry to explain the observed enhancements of saturation

magnetization in (110) or (111) oriented $SrRuO_3$ films. This work has also ruled out the possibility that all of the increase originates in the orbital contribution to the magnetic moment. Given these constraints and the observed strain dependence, it is very likely that the distortions imposed by the substrate have altered the density of states at the Fermi level such that, for a given exchange energy, a significant increase in spin splitting occurs. Such a modifcation of the band structure would likely result due to a combination of altered Ru-O bond length and Ru-O-Ru bond angles anisotropically changing the crystal field splitting and bandwidth. These concepts will be addressed in the next section through characterization of the electron transport properties of films on $SrTiO_3$ on all orientations.

Other films under compressive strain on (110) LSAT and $LaAlO_3$ behaved similarly relative to the (100) oriented counterparts. Films on (110) LSAT and (110) $LaAlO_3$ had higher saturated magnetic moments than on (100) oriented substrates, with values ranging as high as 3.3 μ_B/Ru^{4+} and 1.91 μ_B/Ru^{4+}, respectively. (110) oriented films on LSAT had Curie temperatures between 150-152 K while films on LAO had T_Cs between 151-152 K. Thus, although the expected trend of higher saturated moments being coincident with higher transition temperatures is not seen across different substrate materials, as discussed in Chapter 3, higher saturated moments are definitely coincident with higher transition temperatures when considering different orientations of a given substrate material. Although the films on (110) oriented LSAT and $LaAlO_3$ reinforce the dependence of the magnetic ground state on the symmetry of lattice distortions, the rapid relaxation of (110) films coupled with the different relaxation rates along the [001] and $[1\bar{1}0]$ axes makes a consistent description of the strain states in these samples unachievable. Thus, this work will not focus on further analysis of results based on them. Films under tension on $KTaO_3$ exhibited little dependence of the saturated moment on film orientation, with (110) and (111) oriented films saturating between 0.6-1.0 μ_B/Ru^{4+} and 0.5-0.9 μ_B/Ru^{4+}, respectively. Both ranges agree well with that of (100) oriented films on $KTaO_3$. Similarly, the Curie temperatures of films on $KTaO_3$ showed little orientation dependence, with (100) oriented films in the range of 160-162 K while (110) and (111) oriented films were in the range of 162-164 K and 162-166 K, respectively.

4.4 Probing the Density of States

Both resistivity vs. temperature measurements and Hall effect measurements in the van der Pauw configuration were used to extract the residual resistivity ratio, carrier type and density, and carrier mobility of the $SrRuO_3$ films. The location of the "kink" in ρ vs. temperature measurements was also used to confirm the Curie temperature as determined from $\partial M/\partial T$ scans. As can be seen in Figure 4.8, which shows ρ vs. temperature for typical films of all orientations on $SrTiO_3$, the resistivity of (110) $SrRuO_3$ was lower than that of (100) films. This lower resistivity occurs despite the microstructural effects associated with the rougher columnar growth (110) $SrTiO_3$ and is a testament to the high crystal quality of (110) type films. The resistivity of (111) films, by contrast, is significantly higher, reflecting the rougher growth, columnar microstructure, and lower crystal quality present in these films. In Figure 4.8, the residual resistivity ratios were 4.67 for (110) $SrRuO_3$, 3.51 for (100) $SrTiO_3$, and 3.2 in (111) $SrRuO_3$. These results are within the expected range for $SrRuO_3$ films on $SrTiO_3$ and confirm earlier estimates of relative crystal quality. In particular, they

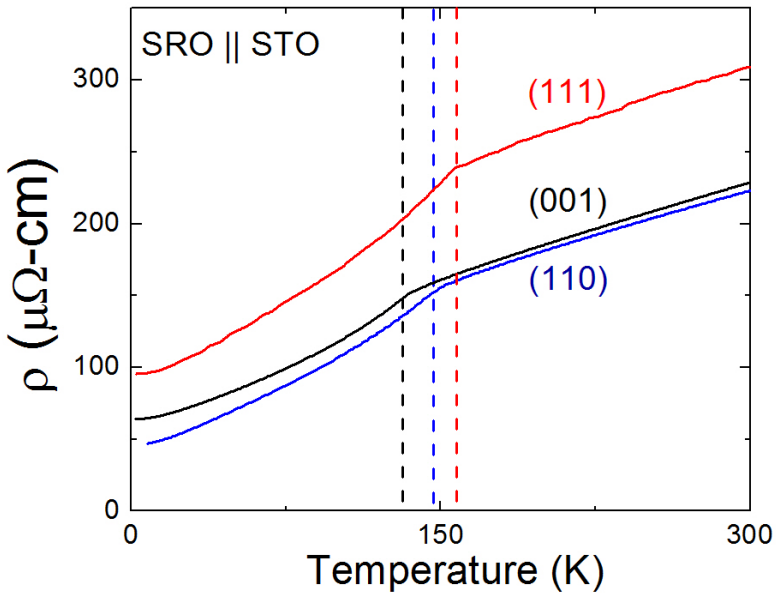

Figure 4.8: Resistivity vs. temperature for a series of 70-80 nm thick films on (001), (110), and (111) $SrTiO_3$

indicate that the (111) films are of lower crystallographic quality than either (110) or (100) films.

Having established the basic transport behavior of the films, we will now discuss the carrier density and mobility of our samples. The carrier density is of particular interest because it reflects the density of states at the Fermi level. In the itinerant picture of $SrRuO_3$, the saturated magnetic moment may be roughly represented as

$$M_{Sat} = \mu_B E_{ex} D(E_F) \tag{4.4}$$

where E_{ex} is the exchange energy and $D(E_F)$ is the density of states at the Fermi level. In this model, the field applied to the ferromagnet is treated as negligible relative to the exchange energy such that the applied field is only responsible for the movement of domain walls rather than appreciably changing the splitting between the "spin-up" and "spin-down" bands. This condition is generally considered to be valid and it is therefore expected that an increase in the carrier concentration will be highly correlated with an increase in saturation magnetization. However, the extraction of carrier concentrations from $SrRuO_3$ is a complex topic, as the Hall effect measurements and calculations assume conduction occurs in a single band. Although the validity of this model is debated in many systems, $SrRuO_3$ is a system in which it clearly does not apply.[44, 70, 67] Temperature dependent measurements of $SrRuO_3$ thin films have observed a crossover from electron to hole type conduction as the temperature is raised from low to high.[44, 70, 67] This evolution is highly suggestive of, and usually attributed to, a significant temperature dependent contribution to the conductivity by an O $2p$ band with hole character.[44, 70, 67] Absolute values of the carrier concentration

are consequently highly suspect and this work will instead use the relative values obtained at a fixed temperature. A temperature of 50 K was chosen for comparison as a point at which the contribution from the Ru $4d$ bands to the conductivity is still very dominant while allowing probing a larger energy region near the Fermi level. A number of other temperatures (10K, 75K) were probed for additional confirmation of the results and general agreement was found.

The Hall resistivity and carrier concentrations are therefore extracted from ρ vs. temperature and ρ vs. applied magnetic field measurements. A typical example of ρ vs. applied field may be seen in Figure 4.9(a) and shows both the anomalous and ordinary Hall effect. The anomalous or "extraordinary" Hall effect is a contribution to the Hall resistivity which is directly proportional to the magnetization of the conducting material. Despite decades of investigation, the anomalous Hall effect is still not well understood, but is generally considered to be attributable to three different contributing effects.[108] Two of these effects, skew scattering and side-jump scattering, are related to impurity scattering while the third is an intrinsic contribution related to the Berry's phase, a geometric interference effect induced by the breaking of time reversal symmetry in a ferromagnet.[108] For further reading on the anomalous Hall effect, the reader is encouraged to consult the excellent review article referenced here.[108] In non-ferromagnetic systems it is generally a negligibly small linear contribution, but in ferromagnetic systems will result in a strong nonlinearity at lower fields until the system is saturated. Thus, only data past the saturation point will be linear and can be used to determine the Hall resistivity.

Once the carrier concentration has been extracted, it is clear that (111) films have higher carrier concentrations than (110) films, which in turn have higher carrier concentrations that (100) films. The carrier concentrations of most films fall into the range typical of the literature for $SrRuO_3$ thin films, although some of the highest (111) oriented films appear significantly enhanced from typical reported values.[1] It is at first surprising that the films with the highest resistivity also have the highest carrier concentration. However, (111) films also exhibit significantly decreased mobility which are likely associated with a higher incidence of defects and increased mosaic spread, as observed in residual resistivity and X-ray diffraction measurements respectively. Figure 4.9b shows the relationship between saturated Ru moments and the carrier concentrations extracted from Hall effect measurements for 30-60nm thick SRO films on STO of various orientations. Across a variety of orientations of STO with similar thickness, we find that the saturated Ru moment scales with carrier concentration, indicating an enhancement of the density of states at the Fermi level with increasing saturated moment.

The extent of the increase in carrier concentration in $SrRuO_3$ films with the highest saturated moments is remarkable, reaching a factor as high as 2.8. Although these values represent only the nominal number of carriers based on the clearly inapplicable single band picture, if taken as a direct representation of the density of states near the Fermi level the data would suggest that the density of states has more than doubled. The preponderance of evidence, therefore, suggests a significant modification of the band structure through strain.

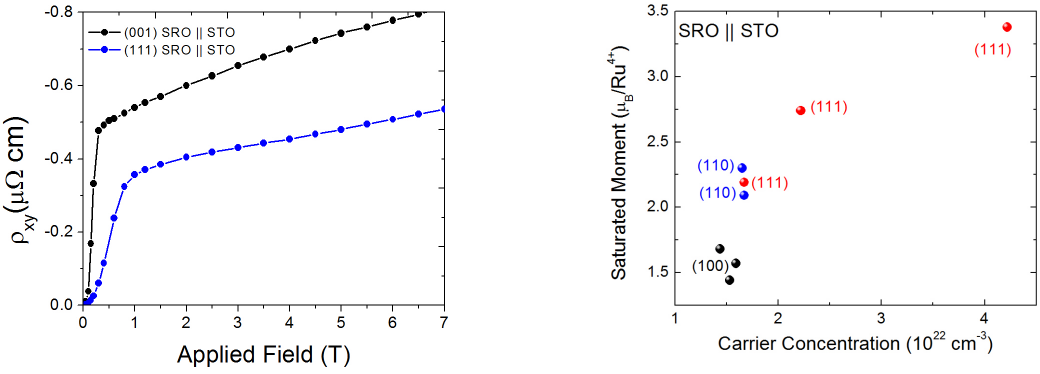

(a) (b)

Figure 4.9: a) ρ_{xy} as a function of applied field for representative (100) and (110) oriented films on $SrTiO_3$. b) Saturated magnetic moment vs. nominal carrier concentration for films on $SrTiO_3$. The films shows represent a wide range of thicknesses from 30-120 nm for all substrate orientations. As described in the text, the data displayed was taken at 50 K, and general agreement was found below the Curie temperature.

4.5 Discussion and Conclusions

This work has demonstrated the ability to significantly modify the magnetic and electronic ground state of $SrRuO_3$ thin films by varying the symmetry of substrate imposed lattice distortions. A clear dependence of the saturated magnetic moment and Curie temperature on substrate orientation is shown, with the saturated magnetic moment and Curie temperatures of both (110) and (111) oriented films significantly greater than in the (100) orientation. Through reciprocal lattice mapping of partially relaxed films, it has been demonstrated that the saturated moment of these films is a monotonic function of increased strain. Although, as in the case of the (100) orientation, (110) films may be described in terms of an increased orbital magnetic moment and better alignment of electron spins, the saturated magnetic moments of (111) oriented films are found to be far in excess of the 2 μ_B/Ru^{4+} which may be expected as the maximum moment expected from Ru^{4+} in the low-spin t_{2g}^4 configuration. It has also been shown that alternative interpretations such as crystal quality, off-stoichiometry, or contamination do not well explain the observed enhancement. In fact, since our initial publication of these results, multiple other experimental groups have reported similarly enhanced magnetic moments in excess of 2 μ_B per Ru.[9, 51, 49, 152] It is therefore theorized that the strain in $SrRuO_3$ thin films on (111) $SrTiO_3$ has induced a spin transition to the $t_{2g}^3 e_g^1$ state, only the second instance of a high-spin Ru^{4+} configuration ever reported, and the only such transition in Ru reported to be induced through strain.[57] Such a spin is thought to be difficult to stabilize because of the strong crystal field splitting associated with the extended $4d$ orbitals and strong Ru-O bonding. The proposed spin transition would bring saturated magnetic moments as high as 4 μ_B/Ru^{4+} within reach, and this work notes several indicators of its manifestation.

The most significant evidence is in the strain dependence of the saturated moment it-

self. It reaches values which are difficult to explain without involving the e_g orbitals in the magnetism, the smooth variation of the saturated moment with both thickness and in-plane strain suggests a competition between two states which are close in energy. The high-spin state becomes more and more preferentially occupied as the distortion increases. It is unclear at this time whether the coexistence of low- and high-spin states suggests a strain gradient present in the film or a homogenous mixture of the two states. Polarized neutron reflectometry of the films may allow the two cases to be distinguished. The second key piece of evidence may be found in the shape of the (111) oriented hysteresis loops. The "pinched" shape of the loops as well as the reduced remnant magnetization is indicative of two distinct magnetic states with different coercive fields and magnetocrystalline anisotropy. The third indicator is that of the interdependence and strong variation of the film carrier concentration. An expected consequence of enhancing the density of states at the Fermi level with e_g levels is a sharp increase in the density of states and consequently the carrier concentration. Therefore, it is very likely that the application of a compressive trigonal distortion to $SrRuO_3$ thin films anisotropically reduces the crystal field such that the e_g band enhances the density of states at the Fermi level.

A final point of interest is found in the case of (100), (110), and (110) oriented films on $KTaO_3$. Despite the extreme variation in crystal quality , all three saturate in the same range of 0.5-1 μ_B/Ru^{4+} and have similar bulk-like Curie temperatures. It is therefore even more likely, as stated in Chapter 3, that the reduction in saturated magnetic moment exhibited by films on $KTaO_3$ is due to strain effects, not a reduction in crystal quality.

Additional work in understanding the precise nature of the induced distortions would most likely take the form of additional, extensive reciprocal space mapping. If Riedvelt analysis, although not usually practically achievable in thin films, could provide bond length information, then a theoretical model of the modified band structure may be realized. At this time, however, this work has demonstrated the ability to easily tune the magnetic properties of $SrRuO_3$ thin films and induce a transition to high-spin Ru.

Chapter 5

Tuning Magnetic Anisotropy in $SrRuO_3$

5.1 Magnetocrystalline Anisotropy

The ability to tune the magnetic anisotropy of a material is among the most advantageous features of a magnetic material in device applications, as anisotropy plays a critical role in the performance of magnetic storage media and tunnel junctions. Once again $SrRuO_3$ represents a remarkable model system in which to test parameters for tuning magnetic anisotropy in thin films of transition metal oxides. As a consequence of the high-Z ruthenium ions, anisotropy in $SrRuO_3$ is very strong. Although some have suggested that the large variation in reported saturated magnetic moments for $SrRuO_3$ thin films (1.1-1.6 μ_B/Ru^{4+}) is due to differences in crystal quality, others have suggested that the difficulty of fully saturating a system with such large magnetocrystalline anisotropy also plays a role.[2, 16, 66, 76] The anisotropy is in fact so large that it has been reported that $SrRuO_3$ is not saturated in fields of up to 30 T.[17] There is even debate regarding whether a peak in the AC susceptibility near T_C is attributable to magnetic anisotropy or spin glass behavior.[76, 116] Given these remarkable findings, it is not surprising that the study of magnetic anisotropy in $SrRuO_3$ thin films has attracted much recent attention.[17, 55, 64, 66, 74, 79, 85, 137, 166]

Comprehensive characterization of the magnetic anisotropy performed by Ziese et al. on $SrRuO_3$ films found a temperature dependent easy axis.[166] By rotating through the $(001)_O$ and $(1\bar{1}0)_O$ planes at various temperatures, it was revealed that above 70 K the magnetic easy axis is along the $(001)_O$ axis, which corresponds to the $(100)_{pc}$ plane, at a 35° angle to the substrate normal.[166] Below 70 K, two easy axes are observed in the same $(001)_O$ plane, this time tilted by 5° and 75° relative to the substrate normal. It is generally acknowledged in the literature that, on (100) oriented $SrTiO_3$, $SrRuO_3$ films have an easy axis very near the growth axis. Remarkably, however, Palai et al. reported in 2009 that films on (110) $SrTiO_3$ *also* have an easy axis along the growth direction! Subsequently, Wang et al. reported in 2010 a significant difference in magnetic anisotropy between films grown on (001) $SrTiO_3$, (001) $LaAlO_3$, and (001) MgO.[152]. Wang et al. observed that in the films grown on $LaAlO_3$ and MgO the anisotropy effect was significantly reduced and, in the case of $LaAlO_3$ substrates, reversed.[152] This effect was attributed to differences

in growth mechanisms.[152] Even more surprising is that in the work of both Palai et al. and Wang et al., the $SrRuO_3$ thin films appear to saturate in both the easy and hard directions, but saturate to significantly different values. Along the easy axis, the "saturated" moment is significantly suppressed.[116, 152] This observation has not yet been explained, and even the reality of the effect is highly disputed. It is possible, as suggested by Wang et al., that a significant linear, completely reversible magnetization of the Ru ions is actually removed from the hysteresis loops through linear background subtraction techniques, as described in Chapter 2.4.1. Although such a perfect linear paramagnetic contribution to the magnetization is quite rare and unexpected, it may not be entirely surprising in a system which may not completely saturate in fields of less than 30 T.[17] In this case, the regime of the hard axis magnetic hysteresis loop dominated by domain growth will appear to quickly saturate to some value which is significantly suppressed relative to the easy axis. The rest of the magnetic response with increasing field up to saturation is then in the form of slow moment rotation. Based on the results of Cao et al., it is possible that as little as 10% of the difference in easy and hard axis magnetic moment will have been closed by this paramagnetic contribution by 5 T.[17] Indeed, if the magnetic anisotropy is enhanced by epitaxial strain, as discussed in this chapter, the reversible contribution may be much smaller. Thus the films may for most purposes be considered to have "saturated" along the hard axis at a significantly reduced magnetization relative to the easy axis, although it is very likely possible to truly saturate such $SrRuO_3$ films given arbitratily large applied magnetic fields.

It is of course highly desireable to be able to directly probe any linear magnetization component of the $SrRuO_3$ film as envisioned by Wang et al. One potential approach to definitively resolving the issue is to precisely determine the temperature independent diamagnetic background of the substrate through the measurement of high-temperature hysteresis loops using SQUID magnetometry. By taking magnetic moment vs. applied field loops at a temperature on the order of 400 K the film paramagnetic background can be completely suppressed and all remaining signal will come from either the substrate or ferromagnetic contaminants with high Curie temperatures such iron oxide. Assuming negligable ferromagnetic contamination, subtracting out this temperature independent background will in principle leave only the signal from the film. The disadvantage of this technique is, of course, the difficulty of determining the origin of any low-temperature linear paramagnetic signals, which have been shown to exhibit anisotropy themselves.[40] Any contamination of the sample through paramagnetic contaminants incorporated into either the substrate or the silver paint used to promote thermal contact between the substrate and the heater during deposition may reapper in low-temperature measurements as a positive linear background. As these sources of background will also be significantly suppressed at 400 K, they will contribute to and distort any observed paramagnetic slope after background subtraction. The film paramagnetic contribution is expected to be quite small, on the order of 1×10^{-5} emu at a field of 5 T, and may be very difficult to distinguish from such paramagnetic contamination. Thus, samples for which the background will be subtracted in this manner are best prepared with extreme care, avoiding the use of silver paint in the sample preparation. Since the deposition chamber used in to prepare our $SrRuO_3$ samples requires the use of silver paint, we will instead assume that the linear contribution of the film to the magnetization is quite small, as expected, and subtract a linear background during SQUID magnetometry analysis. Given that films appear to saturate to a very straight, linear background even

along the hard axes, this approximation is likely valid. For more careful confirmation of the reality and origins of this different in apparent saturated magnetic moment, we will turn to X-ray magnetic circular dichroism measurements later in this chapter. In any case, despite continued debate on the reality of an anisotropic "saturated" magnetic moment, the phenomenon continues to be observed throughout the literature and has been extended to tetragonally distorted films in which an even larger effect is observable.[85, 64]

This work will attempt to understand the origins of this remarkable magnetic anisotropy by correlating it with substrate induced strain. Through magnetometry of films on (100), (110), and (111) oriented substrates of multiple materials, it will be shown that a universal uniaxial magnetic easy axis may be induced either along the growth axis or in the film plane by compressive or tensile epitaxial strain. The extent to which the difference in saturated magnetic moments along easy and hard directions may be tuned using epitaxial strain will be probed. Finally, through X-ray Magnetic Circular Dichroism, the fundamental origins of the change in saturated magnetic moment will be explored. In the end, the reader will see that it is strain which controls the magnetic anisotropy of these films, and that $SrRuO_3$ is an excellent candidate for the precise tuning of magnetic anisotropy through the control of substrate induced lattice distortions.

5.2 Probing Anisotropy Through SQUID Magnetometry

Several signs may be used to identify a magnetic easy axis. Ziese et al. use a series of angular sweeps at constant field against which the magnetic response along the direction of applied field is plotted.[166] This is essentially a measure of film susceptibility and is a common method for identifying magnetic anisotropy. In fact, the difference in apparent saturated magnetic moment along certain axes may be considered a difference in magnetic susceptibility. Wang et al. observe differences in the remnant magnetization and the sharpness of switching at the coercive field.[152] In this work, these are the primary methods by which a magnetic easy axis will be identified. A magnetic easy axis should have a remnant magnetization very near the saturated magnetic moment and should exhibit clear, sharp switching near the coercive field. Magnetic susceptibility should be high along an easy axis relative to along a hard axis.

The samples used for the characterization of magnetic anisotropy in $SrRuO_3$ thin films have already been described in detail in Chapters 3 and 4. They include $SrRuO_3$ films of thickness varying between 20-120nm on (100) and (110) oriented $SrTiO_3$, LSAT, $LaAlO_3$, and $KTaO_3$ as well as (111) oriented $SrTiO_3$ and $KTaO_3$. This allows both compressive and tensile strain states to be probed in systems with tetragonal, monoclinic, and trigonal distortion symmetry. Magnetic hysteresis loops were obtained along the out-of-plane (growth axis) direction and along the principal in plane directions. In all compressively strained films, the out-of plane direction was the magnetic easy axis. Figure 5.1 shows hysteresis loops which demonstrate the anisotropy in a series of compressively strained films on (100), (110), and (111) oriented $SrTiO_3$. As is illustrated in Figure 5.1a and 5.1b, films on (100) and (110) $SrTiO_3$ are characterized by high remnant magnetization in the out-of-plane hysteresis loops,

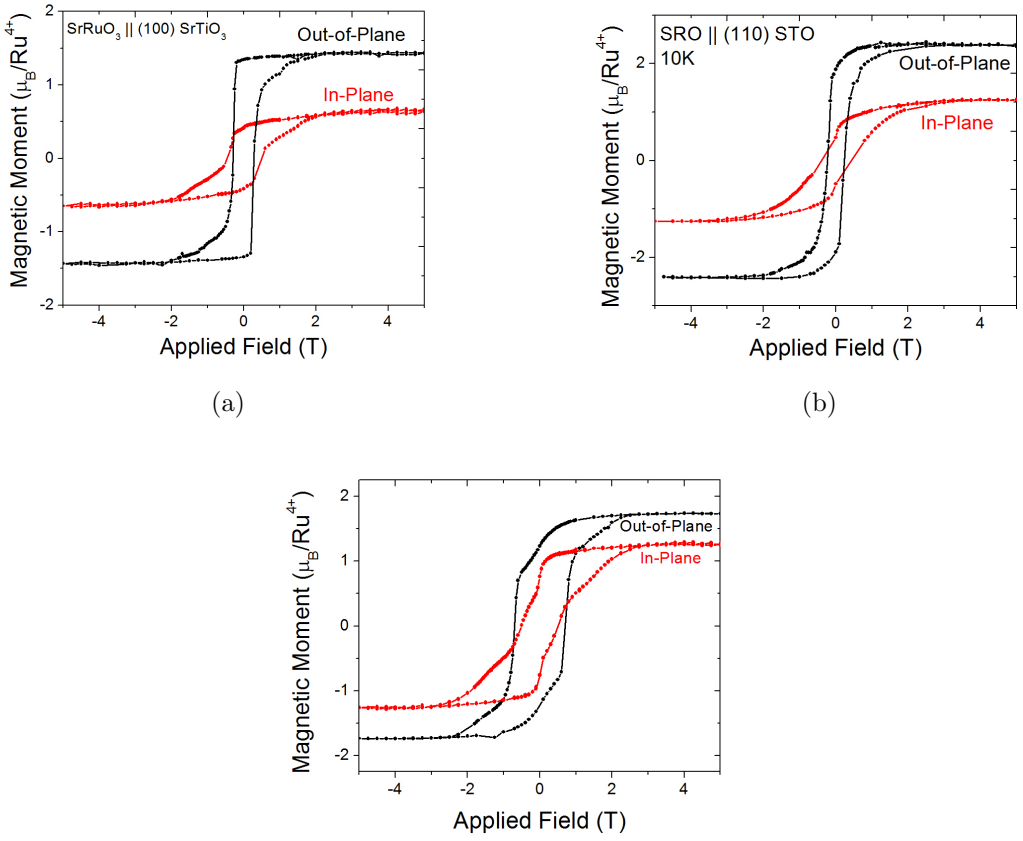

Figure 5.1: Typical magnetic hysteresis loops with the field applied out-of-plane and in-plane of $SrRuO_3$ films on a) (100), b) (110), and c) (111) oriented $SrTiO_3$

on the order of 95-100% in (100) films and 80% in (110) films. The out-of plane loops of (100) and (110) oriented films on $SrTiO_3$ switch very sharply, also indicative of a magnetic easy axis. However, in Figure 5.1a, a second regime can be seen just after the sudden, sharp switching where the net magnetization increases more slowly. This feature is indicative of a slight misalignment between the applied field and magnetic easy axis. This may be due to misalignment of the sample out-of-plane axis relative to the applied field during measurement. It could also indicate that in (100) oriented films the easy axis is actually tilted slightly relative to the out-of-plane direction. The sharp transition in slope is not observed in (110) oriented samples. Films in compression on $SrTiO_3$ exhibited the marked asymmetry in saturated magnetic moment in (111) oriented films as well as that reported on (100) and (110), with the magnetic hard axis appearing to saturate at a significantly lower magnetic moment than the easy axis. Typical ratios of hard to easy axis "saturated" magnetic moments for films on (100), (110), and (111) $SrTiO_3$ were 0.45-0.55, 0.2-0.35, and 0.4-0.7, respectively.

In all films under tensile strain, the most significant feature in the anisotropy is a reversal

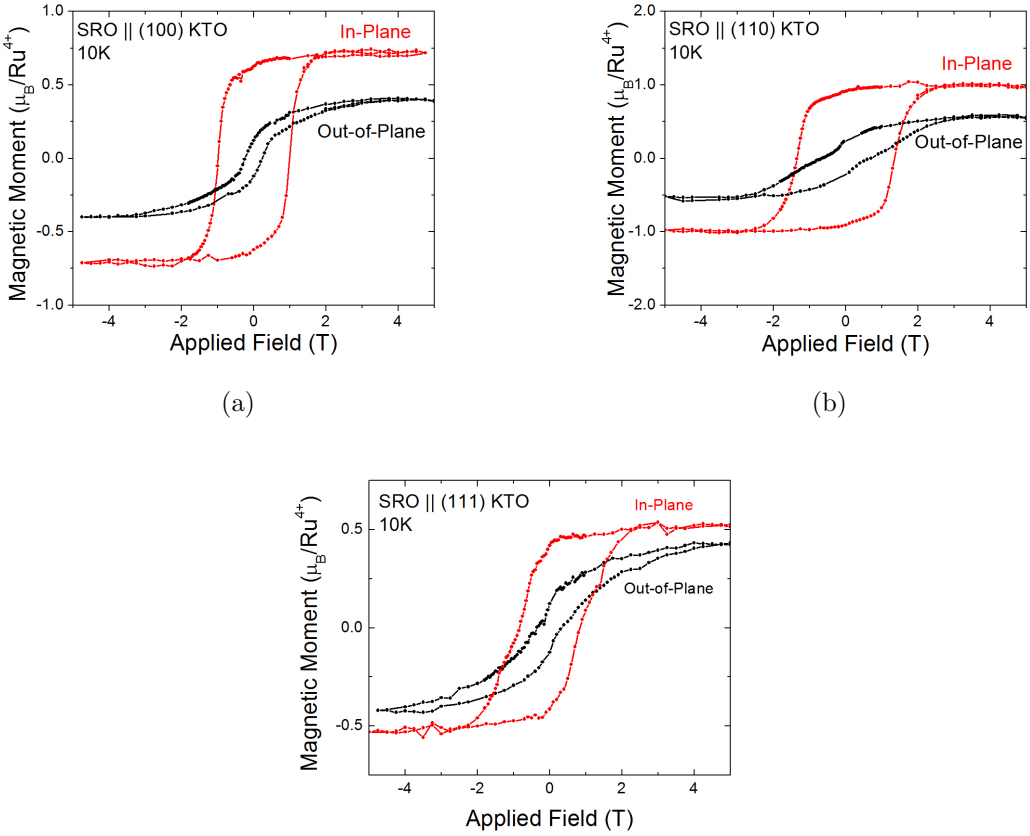

Figure 5.2: Typical magnetic hysteresis loops with the field applied out-of-plane and in-plane of $SrRuO_3$ films on a) (100), b) (110), and c) (111) oriented $KTaO_3$

of the magnetic easy axis from out-of-plane to the in-plane direction. Figure 5.2 shows the anisotropic hysteresis loops for a series of films on (100), (110), and (111) oriented films on $KTaO_3$. As in the compressively strained films, we find a significant disparity between apparent saturated magnetic moment along the easy and hard axes. Now, however, it is the in-plane direction which saturates to a higher magnetic moment. Typical ratios of hard to easy axis "saturated" magnetic moments for films on (100), (110), and (111) $KTaO_3$ ranged between 0.5-0.9, 0.6-0.75, and 0.5-0.8, respectively. Again, a very high remnant magnetization is observed along the easy axis, on the order of 87% of the saturation magnetization for (100) films, 91% in (110) oriented films, and 80% in (111) oriented films, highly indicative of a magnetic easy axis. Under tensile strain the switching of the magnetic domains, although still quite sharp, is slightly more gradual than in films under compressive strain. Additionally, there is no sudden slope change in the magnetization curve during switching. This may indicate that, although the film easy axis is in-plane and well aligned with the applied field, films in tension are slightly more defective, with more pinning sites than films on $SrTiO_3$ and LSAT.

Figure 5.3 shows the hysteresis loops of representative films on (100) and (110) LSAT and $LaAlO_3$. The LSAT films, which are under significant compressive strain, show behavior very similar to that of films on $SrTiO_3$, with out-of-plane easy axes, high remnant magnetizations, and sharp switching. Films on (100) LSAT, however, had even lower hard-axis saturated magnetic moments, with films "saturating" to magnetizations as low as 35% of the easy axis when the field is applied in-plane. Ratios on (110) LSAT reached as low as 0.4. Relaxed films on $LaAlO_3$ exhibited very little difference in saturated magnetic moment along the different axes, on the order of 6-8%. Thus, although there are some signs of an out-of-plane easy axis in $SrRuO_3$ films on (100) and (110) $LaAlO_3$, the differences are significantly reduced relative to strained films. Switching in (100) oriented films is also not as sharp as in films on $SrTiO_3$, LSAT, or $KTaO_3$. Finally, it should be noted that a significant "pinching" of the hard-axis hysteresis loop occurs in (110) oriented films on LSAT and $LaAlO_3$. This effect may be seen very weakly in films on (111) $SrTiO_3$ and $KTaO_3$. In some ways, this phenomena resembled that of a multi-phase magnetic system, but closer inspection reveals a remarkable resemblance to the "pinched" hysteresis loops observed in a number of other systems such as $BaTiO_3$ and other ferroelectrics.[123] This pinching behavior has also been observed in layered ferromagnetic/antiferromagnetic systems, magnetic nanodots, and ferritin where it has been associated with interlayer coupling, vortex states, and resonant tunneling effects.[14, 29, 38] At this time, it is difficult to ascertain the precise origin of the anomalous shape observed here.

Thus, SQUID magnetometry has revealed a strong magnetic anisotropy not just in $SrRuO_3$ films on (100) and (110) $SrTiO_3$ as previously reported, but in films on LSAT and $KTaO_3$. In the next section, the anisotropy will be compared to structural data gathered on the films, and a parameter by which it may be controlled is identified. Finally, the reality of the anisotropic saturated magnetic moment will be investigated along with the underlying physical cause.

5.3 Strain as a Control Variable for Anisotropy

It is clear from the reversal of easy axis direction from films on $SrTiO_3$ and LSAT to films on $KTaO_3$ that strain is once again an excellent candidate for a parameter by which the remarkable magnetic anisotropy of $SrRuO_3$ thin films may be tuned. Therefore, a systematic comparison of the relationship between the saturated magnetic moment ratio ($M_S^{In-Plane}/M_S^{Out-of-Plane}$) with the applied epitaxial strain has been performed in the case of (100) oriented films across all substrates. The ratio is defined by the film magnetic moment in a 5 T field applied in-plane and out-of-plane. The probing of substrate induced lattice distortions through reciprocal lattice mapping has already been extensively described in Chapters 3 and 4, so a description is omitted here. Figure 5.4 plots the relationship between the saturated magnetic moment ratio and tetragonal epitaxial strain, $\epsilon_{OOP} - \epsilon_{IP}$, for a series of (100) oriented films. Clearly, there is a strong correlation between the substrate induced lattice distortions, with the ratio being a monotonic function of the tetragonal distortion. A more positive tetragonal distortion is associated with a larger saturated moment ratio.

Although it is clearly possible to control the anisotropy of $SrRuO_3$ thin films through

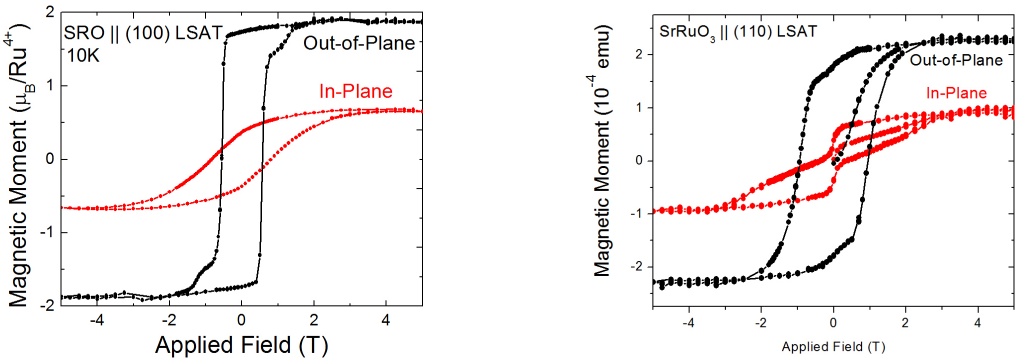

Figure 5.3: Typical magnetic hysteresis loops with the field applied out-of-plane and in-plane of $SrRuO_3$ films on a) (100) LSAT, b) (110) LSAT, and c) (100) $LaAlO_3$ and d) (110) $LaAlO_3$

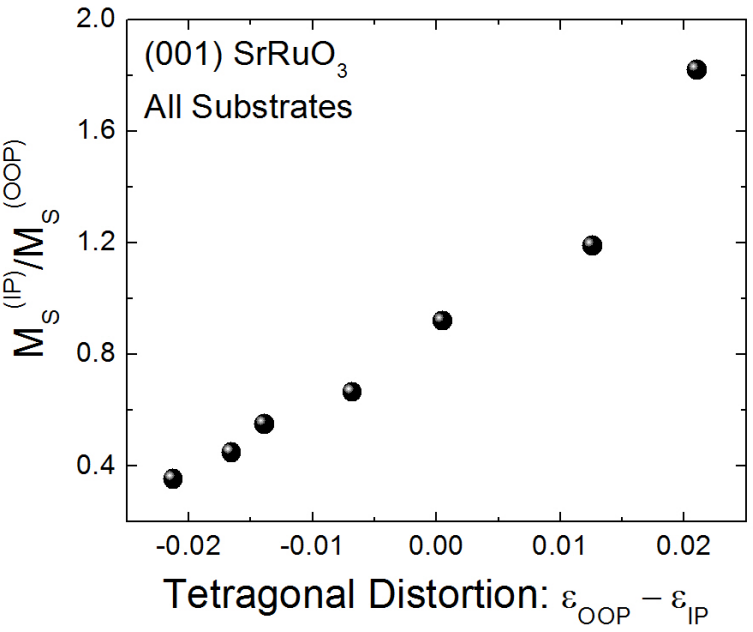

Figure 5.4: $M_S^{In-Plane}/M_S^{Out-of-Plane}$ vs. Tetragonal distortion for a series of 40-80 nm thick films on (100) $SrTiO_3$, LSAT, $LaAlO_3$, and $KTaO_3$

strain across multiple substrates and film orientations, there remain several open questions. The underlying mechanism through which strain affects magnetic anisotropy remains unclear. However, a clue may be found in the description of the orbital contribution to film magnetic moments in Chapter 3. If fully relaxed $LaAlO_3$ films, which exhibit a significantly lower out-of-plane orbital moment than compressively strained films, have very little magnetic anisotropy, perhaps the orbital magnetic moment is a relevant parameter. Thus, direction-dependent X-ray magnetic circular dichroism measurements were performed on films in tension and compression. O K and Ru $M_{5,4}$ spectra were taken with both applied field and x-ray propagation direction normal to the substrate surface, and at 30° grazing incidence relative to the in-plane direction. Samples were measured at 75-80 K to ensure switching in the ± 500 mT field available at beamline 4.0.2 of the Advanced Light Source. Beamline 6.3.1 was also used to perform similar measurements in fields of ± 1.7 T. However, the significantly reduced intensity and resolution of a bending magnet beamline such as 6.3.1 limits the statistics of these measurements. Figure 5.5 shows the resulting spectra from beamline 4.0.2 for compressively strained films, while Figure 5.6 shows the spectra for films in tension. The difference in magnetic susceptibility can be clearly seen in both cases. The strength of the dichroism, which to a certain degree represents spin polarization in a given band, confirms the magnetometry measurements. A much larger magnetic polarization is observed along the magnetic easy axis, despite the fact that at 75-80K, films will be very near saturation at the fields utilized. Clearly, the observed difference in magnetic moment is *not* an artifact of magnetometry or background subtraction.

Even more significantly, application of the X-ray magnetic circular dichroism sum rules

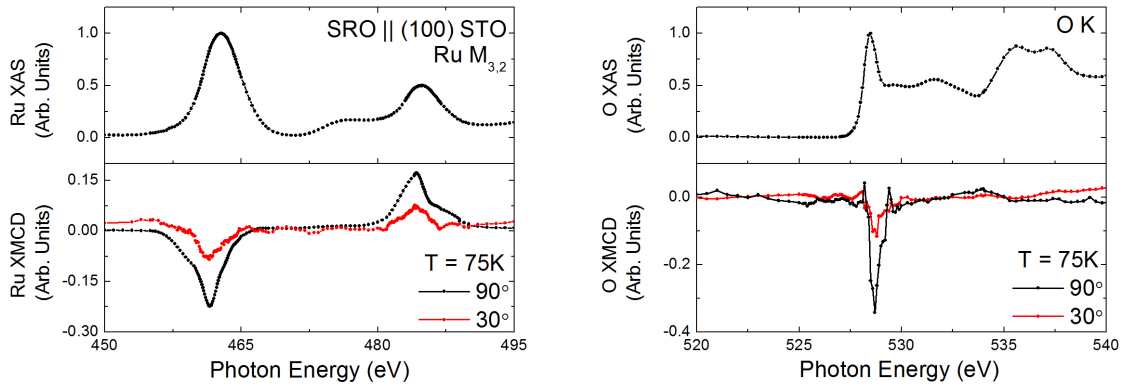

(a) (b)

Figure 5.5: X-ray absorption and X-ray magnetic circular dichroism of the a) Ru $M_{5,4}$ and b) O K edge of a representative (100) oriented $SrTiO_3$ film on $SrTiO_3$ with field applied in normal and grazing incidence

to extract a ratio of the spin and orbital contributions to the magnetic moment reveals an angular dependence in the orbital moment. Compressively strained films have a significantly larger orbital moment contribution in the out-of-plane direction, 7-8% relative to 2-4%. In contrast, films in tension had a significantly larger orbital moment along the in-plane direction: 18% as opposed to 10%. Although at first glance these values may seem to suggest that the orbital magnetic moment is larger overall in the films on $KTaO_3$, in fact scaling the orbital contribution to SQUID magnetometry values yields values of 0.13-0.15 μ_B/Ru along the easy axis and 0.036-0.072 μ_B/Ru along the hard axis for compressively strained films and values of 0.135-0.16 μ_B/Ru along the easy axis and 0.7-0.08 μ_B/Ru along the hard axis for films in tension. Thus, it is very likely that the changes in bonding which are responsible for altering the saturated magnetic moment in Chapters 3 and 4 are also anisotropically reducing the orbital overlap, weakening Ru-O bonding, and resulting in an anisotropic increase in the saturated magnetic moment. The Bruno model of magnetocrystalline anisotropy is then in excellent agreement with the creation and reversal of a universal uniaxial anisotropy in these films.[15]

5.4 Conclusions and Outlook

It has been demonstrated in this work that the magnetic anisotropy manifested as an asymmetry in apparent saturated magnetic moment reported in $SrRuO_3$ thin films is in fact a real effect rather than a magnetometry artifact. This work has shown the ability to precisely tune the magnitude of this anisotropy through the application of epitaxial strain as well as the ability to completely reverse the direction of the anisotropy in films grown on $KTaO_3$. Furthermore, it has been shown that the effects may be extended to films on many different substrates including, surprisingly, (111) oriented films. Finally X-ray magnetic circular dichroism measurements have shed light on the origins of the altered magnetic

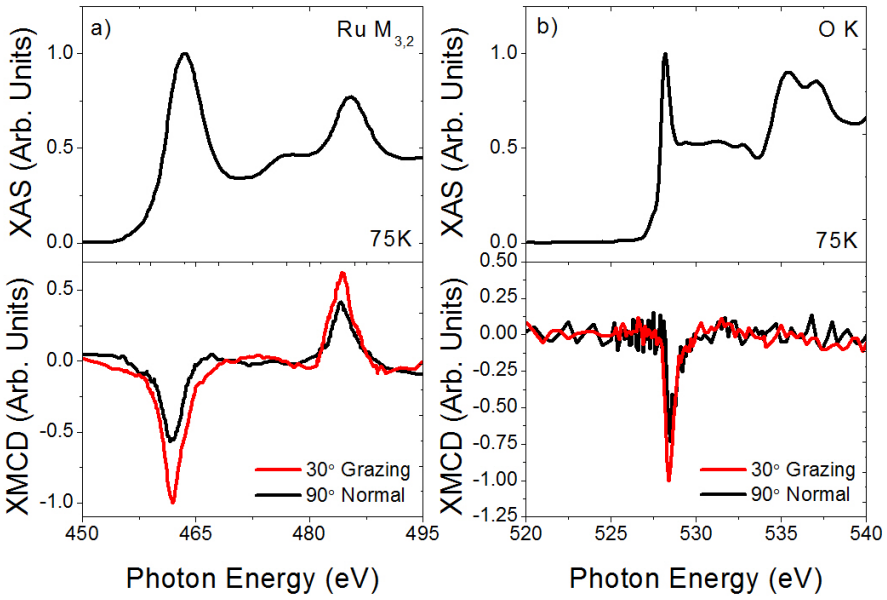

Figure 5.6: X-ray absorption and X-ray magnetic circular dichroism of the a) Ru $M_{5,4}$ and b) O K edge of a representative (100) oriented $KTaO_3$ film on $SrTiO_3$ with field applied in normal and grazing incidence

ground state in which anisotropic weakening of Ru-O bonding manifests as an increase in the relative strength of spin-orbit coupling relative to the crystal field along certain axes. Consequently, the spin-perturbation of the otherwise $l = 0$ bonding orbitals strengthens and a larger orbital moment emerges in these directions. Under these conditions, the Bruno model of magnetocrystalline anisotropy predicts a strong uniaxial anisotropy.

However, there remain a number of unanswered questions. Chief among these is the issue of eventual saturation of the magnetic moment along the hard axis. The XMCD measurements presented here suggest that any linear, reversible component to the magnetization (which may be undetected by bulk magnetometry) must be very weak, as the magnitude of the XMCD anisotropy is in excellent agreement with the anisotropy measured by SQUID magnetometry. Other questions, including the persistence of the saturated moment anisotropy in samples with very low crystal quality such as films on (111) $KTaO_3$ remain of some concern. The extent to which crystallographic quality must be preserved for the maintenance of this uniaxial anisotropy is unclear.

Part III

Inducing Magnetism at Interfaces in $CaMnO_3$-based Superlattices

Chapter 6

Probing Interfacial Ferromagnetism in $CaRuO_3/CaMnO_3$ Superlattices

The preceding chapters of Part I illustrated the power of epitaxial strain in modifying magnetic ground states. In this chapter, we will explore mechanisms for inducing and controlling ferromagnetism at otherwise non-ferromagnetic interfaces. Just as we selected $SrRuO_3$ as a model system in the preceding sections, so too will we search for model systems that allow us to better understand the underlying physical mechanisms of emergent interfacial ferromagnetism. Chapter 6 will introduce the emergent ferromagnetic ground state at the interface in superlattices of the paramagnetic metal $CaRuO_3$ and the antiferromagnetic insulator $CaMnO_3$. We will utilize a wide variety of probing techniques to form a much more cohesive picture of this unusal magnetic state, demonstrate long range antiferromagnetic order spanning the intervening $CaMnO_3$ layers, and show the importance of octahedral rotations in tuning the magnetic properties of this system.

6.1 An Introduction to Interfacial Ferromagnetism

Emergent phenomena at perovskite oxide interfaces have been studied intensively in the last decade in order to understand how mismatches in bands, valences, and interaction lengths give rise to novel interfacial ground states. Surprisingly, there have been only a handful of successful efforts demonstrating new magnetic ground states at interfaces. Some groups have realized ferromagnetic coupling between two insulating antiferromagnetic layers. For example, a ferromagnetic interaction has been reported between the Cr^{3+} and Fe^{3+} ions of $LaCrO_3/LaFeO_3$ heterostructures as predicted by the Goodenough-Kanamori rules.[150, 47, 65] Ferromagnetism has also been reported at the interface between the antiferromagnets $SrMnO_3$ and $LaMnO_3$.[7] Apart from these antiferromagnet-antiferromagnet interactions, there are very few reports of interfacial ferromagnetism. Among them is ferromagnetism (FM) attributed to the conductive layer at the interface between $LaAlO_3$ and $SrTiO_3$ that is associated with fractional charge transfer.[63] However, the nature of these new FM states is still highly controversial and not yet well understood.[34] One of the most promising systems for understanding interfacial ferromagnetism is that of $CaRuO_3/CaMnO_3$ superlattices, where FM coupling has been attributed to interfacial double exchange.[145]

Unlike the more typical antiferromagnet-antiferromagnet interfaces, $CaRuO_3/CaMnO_3$ is composed of a paramagnetic metal ($CaRuO_3$) and an antiferromagnetic insulator ($CaMnO_3$), and exhibits a number of unusual magnetic properties which show great promise in increasing our understanding and control of interfacial magnetic coupling effects.[53] However, the $CaRuO_3/CaMnO_3$ system suffers from the same difficulty as all other interfacial ferromagnetic systems already described - the difficulty of isolating intrinsic interfacial effects from alloying or bulk phenomena.

In $CaRuO_3/CaMnO_3$ superlattices, Takahashi et al. originally suggested that electron transfer occurred from the $CaRuO_3$ layer to the $CaMnO_3$ layer, facilitating a ferromagnetic double exchange interaction at the interface.[145] Takahashi et al. observed ferromagnetism with saturated magnetic moment of 1 μ_C per interfacial Mn ion and a Curie temperature of approximately 100 K, near but slightly reduced from the bulk $CaMnO_3$ Neel temperature of 123K.[145] As the saturated magnetic moment was significantly lower than the 3 μ_B per Mn expected from complete ferromagnetic alignment and the transition temperature was very near the bulk Neel temperature, it was suggested that the actual magnetic configuration is an interfacial ferromagnetic canting of the antiferromagnetic order in the bulk of the $CaMnO_3$ layer.[145] Years later, density functional theory calculations performed by Nanda et al. showed the stabilization of a canted antiferromagnetic state in a single unit cell of $CaMnO_3$ at the interface.[109] Nanda et al. concluded that a canted antiferromagnetic configuration with a net magnetic moment of 1 μ_B per interfacial Mn was consistent with an electron transfer of 0.07 e^- per Mn at the interface and exponentially decaying further in the $CaMnO_3$.[109] The excess charge on layers further into the $CaMnO_3$ was not found to be sufficient to induce ferromagnetic canting.[109] On the $CaRuO_3$ side of the interface, a very similarly shaped region of charge depletion forms and a very slight magnetic polarization results from the proximity of mobile electrons to the now ferromagnetically ordered Mn ions.[109]

Despite the apparent neatness of this picture, there are a number of issues with this interpretation, as well as some remarkable magnetic properties which have emerged through further study but are not yet understood. The most obvious point of uncertainty is that measurements of the ferromagnetic layer thickness through X-ray resonant magnetic scattering performed by Freeland et al. show a ferromagnetic polarization extending 3-4 unit cells into the $CaMnO_3$.[36] This finding contradicts the model developed by Nanda, and is attributed to the formation of magnetic polarons.[36]. The interfacial nature of the ferromagnetism is consequently called into question. Furthermore, questions regarding the role of strain continue to be difficult to address. These questions were at least partially resolved by our group through the measurement of the magnetic properties of $(CaRuO_3)_3/(CaMnO_3)_m$ superlattices, where m was varied from 3-12.[53] We found exchange bias in $(CaRuO_3)_3/(CaMnO_3)_m$ superlattices with a thickness dependence strongly favoring a ferromagnetic layer thickness of 1-1.5 unit cells.[53] This exchange bias most likely originates in strong coupling between the interfacial ferromagnetic $CaMnO_3$ layer and the antiferromagnetic layer which comprises $CaMnO_3$ layer in between the two ferromagnetic interfaces. An example of the exchange bias effect can be seen in Figure 6.1(a) and (b). When the samples are cooled through the Curie/Neel temperature in an applied field, they behave similarly to a heterostructure composed of adjacent ferromagnetic and antiferromagnetic layers, reslulting in exchange bias. Furthermore, the saturated magnetic moment of these superlattices was constant even for

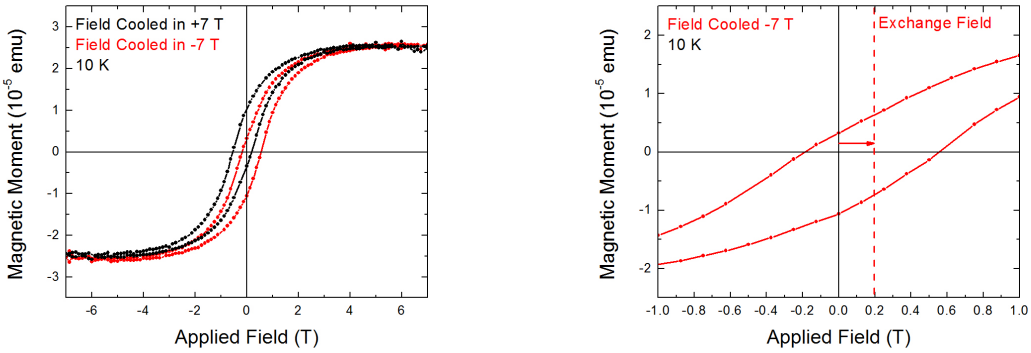

(a) (b)

Figure 6.1: a) Magnetic moment vs. applied field for a (3/15) $CaRuO_3/CaMnO_3$ superlattice after cooling to 10 K in an applied field of $\pm$ 7 T. The superlattice can be seen to exhibit both ferromagnetism and exchange bias. b) A close up view of the hysteresis loop after cooling in -7 T. The exchange field by which the hysteresis loop is biased can be clearly seen.

$CaMnO_3$ layer thicknesses less than 6 unit cells, at which point the findings of Freeland et al. would suggest modification of the magnetic properties should begin.[53] Furthermore, by growing the superlattices on $SrTiO_3$ substrates, on which the films are relaxed, we eliminated strain effects from the list of possible mechanisms for stabilizing ferromagnetism.[53]

An even more exciting phenomena emerged in this study - the dependence of the saturated magnetic moment on the $CaMnO_3$ layer thickness m. If m, the number of unit cells is even, the superlattices saturate to approximately 1.0 μ_B per interfacial Mn.[53] If m is odd, the saturated magnetic moment is the superlattices saturate to approximately 0.5 μ_B per interfacial Mn.[53] The underlying physical mechanism for such behavior is unknown. It is possible that an asymmetry exists between the $CaRuO_3/CaMnO_3$ and $CaMnO_3/CaRuO_3$ interfaces in m = odd samples such that one of them is nonmagnetic (or has a reduced saturated moment). Alternatively, the interfaces may be symmetric and simply exhibit a reduced saturated magnetic moment for m = odd. It is also possible that structural or interlayer magnetic coupling effects are altering the canting of the magnetic moments. Even the magnetic depth profile is unclear, as polarized neutron reflectometry measurements were able to access spin-splitting at only a single superlattice reflection. These measurements yielded insufficient information to distinguish either the thickness of the interfacial ferromagnetic layer or the symmetry of the interfacial magnetization.[53]

This chapter will attempt to resolve the question of ferromagnetic layer thickness through polarized neutron reflectometry. By growing samples with a significantly thicker $CaMnO_3$ layer, reciprocal space can be compressed and statistics at multiple superlattice reflections become accessible. Consequently, we have grown superlattices of thickness m = 10-18. Additionally, the interlayer coupling mechanism will be investigated through neutron diffraction, X-ray diffraction, and X-ray magnetic circular dichroism.

6.2 Samples Studied

Before introducing growth parameters and the samples studied, it is necessary to introduce the materials $CaMnO_3$ and $CaRuO_3$ that comprise the superlattice. $CaMnO_3$ is an antiferromagnetic insulator with G-type ordering of the spins on the Mn ions.[82] That is, all adjacent Mn spins are antiparallel to each other. The Neel temperature is 123 K.[88, 53, 145] In bulk, a Mn^{4+} valence is observed, corresponding to an electronic configuration of $t_{2g}^3 e_g^0$. $CaMnO_3$ is an orthorhombically distorted perovskite, with lattice parameters of a = 5.28 Å, b = 5.27 Å, and c = 7.46 Å, corresponding to a pseudocubic lattice parameter of 3.73 Å.[118] This orthorhombic distortion results in Mn-O-Mn bond angles of 156°-160°.[118] $CaRuO_3$ is a paramagnetic metal, and is also orthorhombically distorted.[53, 145] The orthorhombic lattice parameters of $CaRuO_3$ are a = 5.36 Å, b = 5.53 Å, and c = 7.67 Å, revealing a significantly more distorted structure with a pseudocubic lattice parameter of 3.84 Å.[75] The Ru-O-Ru bond angles are between 150°-151°.

Samples were grown on TiO_2 terminated (100) $SrTiO_3$ substrates according to the technique established by He et al.[54] Films were grown using pulsed laser deposition with a laser fluence of approximately 1.3 J/cm^2. Samples were grown in 20 mtorr of O_2 at a temperature of 780 °C. The thickness and quality of each superlattice layer was monitored by reflection high energy electron diffraction (RHEED). $CaMnO_3$ was found to grow in a layer-by-layer growth mode, and its thickness is consequently simple to monitor *in situ*. $CaRuO_3$, however, grows in step-flow mode and very little variation of the RHEED intensity is observed. Therefore, $CaRuO_3$ layer thickness was controlled using a series of calibration samples to determine the growth rate.

A series of thick superlattices were grown for neutron diffraction and reflectometry. These included $((CaRuO_3)_3/(CaMnO_3)_m)_x$ superlattices, where x was either 8 or 10. Additional, thinner films were grown for the purpose of X-ray absorption and X-ray magnetic circular dichroism. By making these samples thinner, the disadvantages of surface sensitivity in X-ray absorption and X-ray magnetic circular dichroism is mitigated. Additionally, to prevent possible charging, the $CaRuO_3$ layer was made thicker on some X-ray absorption films. Thus, a series of $((CaRuO_3)_n/(CaMnO_3)_m)10$ superlattices were used, where n = 3-4 and m = 3-18. Throughout this chapter, a superlattice of given periodicity n and m with a total number of repetitions x will be referred to as $(n,m)_x$

Extensive tests of film quality on $CaRuO_3/CaMnO_3$ superlattices grown using these conditions have already been performed in our group.[53, 54] Atomic force microscopy showed these samples were to be smooth, with RMS roughnesses of 0.3-0.4 nm.[53, 54] X-ray diffraction, reciprocal lattice maps, and scanning transmission electron microscopy revealed high quality epitaxial films which relax to bulk lattice parameters on $SrTiO_3$.[53, 54] Electron energy loss spectroscopy reveals that the Mn valence is at or very near the expected 4+ state, with a valence of 3.9 ± 0.15.[53, 54]

We determined the precision to which superlattice thickness was controlled using X-ray reflectometry. Figure 6.2(a) shows a typical X-ray reflectometry spectrum for a $(3,17)_1 0$ superlattice alongside a simulation used to determine thickness. In general, there was excellent agreement between the expected and actual superlattice thickness, as shown in Figure 6.2 where the expected thickness matches the actual thickness to within 1.5%. As can be seen by the persistence of total thickness fringes all the way to the fourth superlattice reflection,

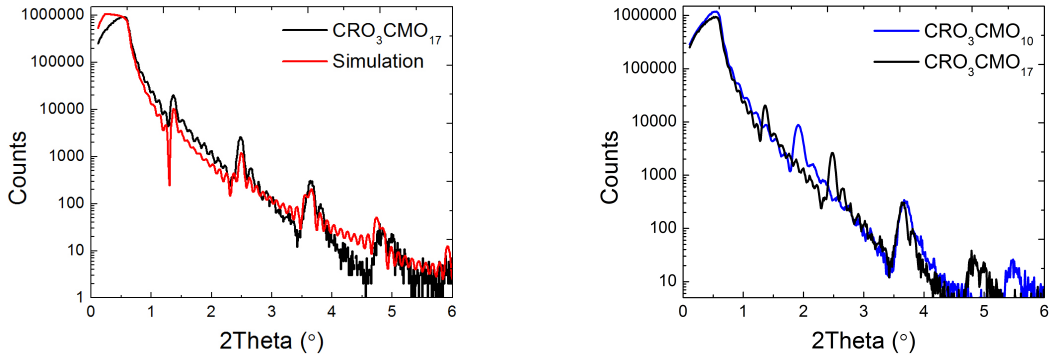

(a) (b)

Figure 6.2: X-ray reflectivity of a) a $(3,17)_{10}$ superlattice with fit and b) a $(3,17)_{10}$ and $(3,10)_{10}$ superlattice.

the top surface and interfaces are extremely sharp with an interfacial roughness on the order of 2.5 Å. Additionally, the higher order superlattice Bragg reflections can be seen to be very narrow and in excellent agreement with the simulated width as far out as the fourth superlattice peak. This implies extremely high uniformity among the individual layer thicknesses. Variation in superlattice layer thickness would be expected to result in significant peak broadening at higher order reflections, but this is not observed. These high-quality reflectivity results will allow precise constraints to be placed on fitted simulations performed on polarized neutron reflectometry spectra. Finally, the compression of reciprocal space is illustrated by Figure 6.2(b), which shows the reflectivity of a $(3,17)_{10}$ and $(3,10)_{10}$ sample side by side. Superlattice Bragg reflections are moved to much lower reflection angles with increased superlattice layer thickness.

6.3 Magnetic Characterization and Thickness Dependence

Having established the growth of superlattices with high quality interfaces, we must now demonstrate that the magnetic behavior parallels that of earlier efforts with thinner superlattice layers.[53, 145] Figure 6.3(a) shows saturated magnetic moments of superlattices grown for this study for which m = 13-18 alongside data extracted from our earlier study (m = 3-12).[53] It is readily apparent that past a thickness of 11 unit cells of $CaMnO_3$, the saturated magnetic moment of m = even and m = odd is no longer significantly different. Rather, for $m > 11$, all superlattices saturate at 0.9-1.1 μ_B per interfacial Mn. Although the thicker samples are clearly ferromagnetic and behave similarly to other reported examples of interfacial ferromagnetism in $CaRuO_3/CaMnO_3$ superlattices, they cannot be used to directly characterize the reported oscillatory magnetic coupling. To demonstrate the difference between the two sets of samples, data points in Figure 6.3(a) from samples where $m < 12$ and m = odd are colored red. All other data points, from samples where $m < 12$ and m

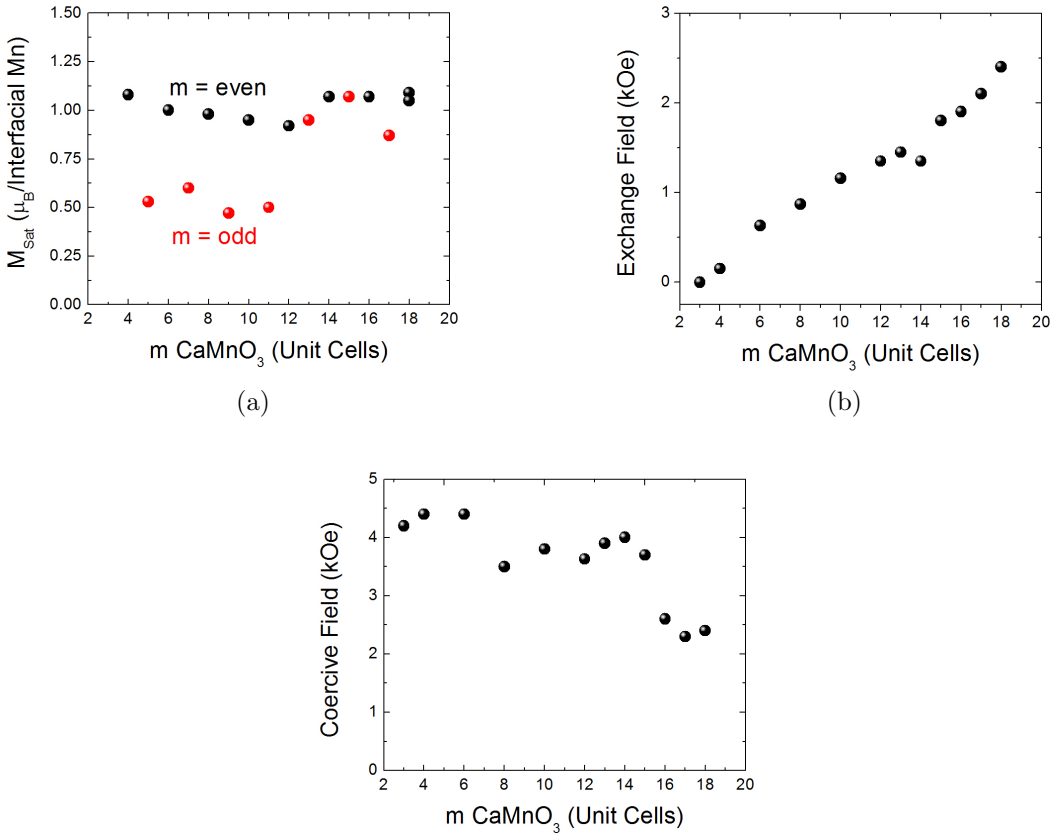

Figure 6.3: a) Saturated magnetic moment, b) exchange field, and c) coercive field of $CaRuO_3/CaMnO_3$ superlattices as a function of $CaMnO_3$ layer thickness.

= even and all samples where $m \geq 12$ are black. Additional confirmation that all $m > 11$ samples are comparable to thinner m = even films may be seen in Figure 6.3(b) and (c). For Figure 6.3(b), we characterized the exchange bias effects present in the superlattices and compared them to earlier examples by field-cooling the superlattices to 10 K in a field of ± 5 T. The exchange field was then calculated to be the field by which the center of the magnetization vs. applied field hysteresis loops were shifted relative to the origin of the applied field.[53] Figure 6.3(b) plots this exchange field as a function of the $CaMnO_3$ layer thickness. It can be clearly seen that the exchange field of the $m > 12$ superlattices increases linearly and monotonically across the entire range and agrees with the $m < 12$, m = even sample set.[53] The $m < 12$, m = odd samples (not shown) have significantly lower exchange fields. Essentially identical trends occur in Figure 6.3(c), which plots the dependence of the coercive field on m.[53]

It is in some sense surprising that such excellent agreement in magnetic properties is observed across a thickness range this wide. One of the principal alternative explanations of the "interfacial" ferromagnetism is that of intermixing to form the compound $CaRu_xMn_{1-x}O_3$,

which is ferromagnetic for $0.1 < x < 0.7$.[92] It may be expected that thicker samples will exhibit significantly more intermixing, as they are kept at elevated growth temperatures for as more than twice the time of many thinner superlattices simply because of the longer deposition times. Since only a small amount of intermixing is required to stabilize a ferromagnetic alloy, it may be expected that increased deposition times will results in greater intermixing, a thicker ferromagnetic layer, and an increase in saturated magnetic moment. As this is not observed, we speculate that interfaces remain sharp even in the thickest samples.

Having precisely determined the thickness of our superlattice layers as well as demonstrating that the magnetic properties favor comparability between the thin m = even superlattces and the $m \geq 12$ superlattices, we will now turn to polarized neutron reflectometry and attempt to probe the thickness of the interfacial ferromagnetic layer.

6.4 Constructing the Magnetic Depth Profile

Polarized neutron reflectometry was performed at the aptly named polarized beam reflectometer (PBR) beamline at the NIST Center for Neutron Research as well as the Asterix beamline at the Los Alamos Neutron Science Center. Samples were field cooled to 5-10 K in 700-800 mT and placed in a polarized neutron beam. The sample periodicities were $(3/17)_{10}$, $(3/18)_8$, and $(4/19)_8$. Since the majority of high-q information comes from the second order superlattice peak, utilizing different layer thicknesses allowed us to probe a wide range of q values. Neutron reflectometry spectra from the $(3/18)_8$, and $(4/19)_8$ samples may be seen in Figure 6.4(a) and (b) respectively. The spectra are plotted in terms of Fresnel reflectivity, which normalizes the measured reflectivity at a given q-vector by the expected reflectivity of a bare $SrTiO_3$ substrate. Also included in Figure 6.4 (a) and (b) is a fit of the thickness, nuclear scattering length density, and magnetic scattering length density. Because the fitting program used, Refl1d, weights points by statistical significance when fitting the spin asymmetry, the magnetic scattering length density, and consequently the magnitude of the theoretical spin-splitting, will be determined primarily by the splitting on the critical edge and first order Bragg reflection. We may then compare the theoretical splitting at the second order peak according to the best fit for given model depth profile with the actual observed splitting. If the calculated splitting at the second order peak does not match observation, the model may be eliminated from consideration. Determination of many parameters is simplified by our atomic force microscopy and X-ray reflectivity measurements. We are able to tightly constrain intermixing, layer thickness, and nuclear scattering length density parameters used in the fit. Figure 6.4(c) shows a typical depth profile used to obtain the fits shown. The black line is the nuclear scattering length density, while the red is the magnetic scattering length density. In this case, the profile shown is for an abrupt depth profile with no intermixing and a single magnetic unit cell at the interface. This profile was used to generate the theoretical plot shown in Figure 6.4(b).

As is illustrated in Figure 6.4, a clear splitting of the spin-up and spin-down neutron reflectometry is observed at the critical edge as well as the first and second superlattice Bragg reflections, indicating a magnetic polarization present in the samples. Integration of the spin-up and spin-down reflectometry spectra shows identical spin splitting on the first and second order Bragg reflections for the $(3/18)_8$ (Sample A) and $(4/19)_8$ (Sample

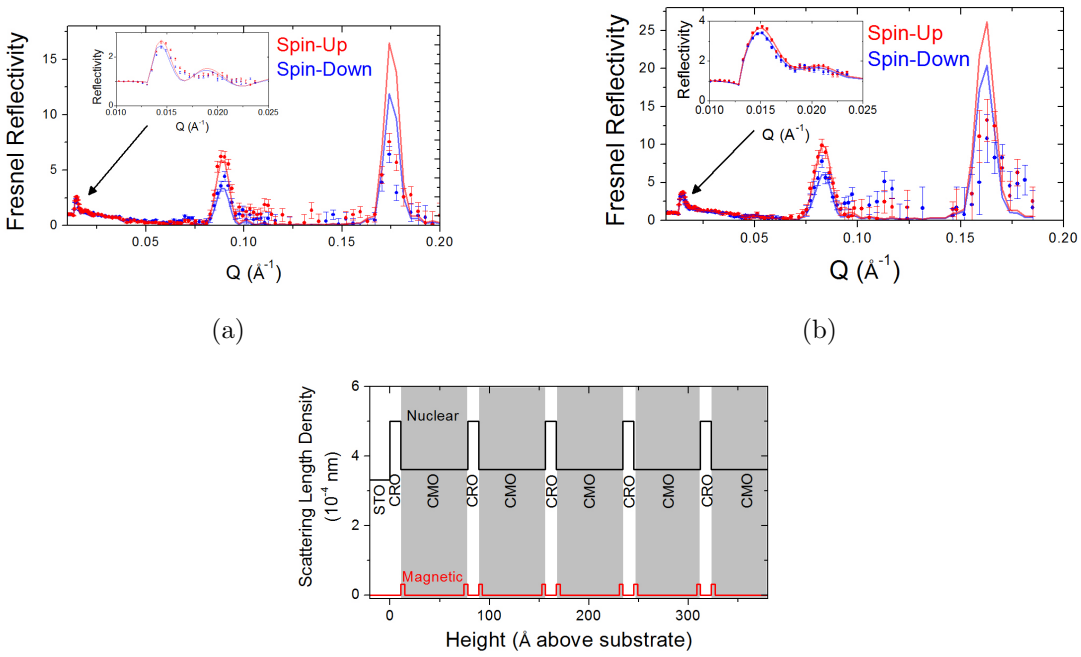

Figure 6.4: Polarized neutron reflectometry spectra with fit for a) $(3/17)_{10}$ superlattice and b) $(3/18)_8$ superlattice. In both reflectivity spectra the data points are the actual Fresnel reflectivities while the lines represent the reflectivity spectrum of best fit depth profile. Red points and lines represent spin-up neutrons while blue represents spin down neutrons. c) Typical nuclear and magnetic depth profile assuming 1 unit cell of ferromagnetism at the interface.

B) superlattice. Specifically, Sample A exhibits a spin splitting of 29% +/- 7% on the first order reflection and 42% ± 13% on the second order reflection. Although the splitting of the theoretical model on the first order peak is relatively insensitive to the thickness of the ferromagnetic layer at the interface, the splitting on the second order peak is not. Model superlattice spectra in Figure 6.5(a), (c), and (e) illustrate the sensitivity, as the splitting on the second order peak is reduced from 30% for a 1 unit cell thick layer at the interface to 16% and -15% for layers that are 2 and 3 units cells thick, respectively. This reversal of the spin splitting with increased magnetic layer thickness is a signature which we may use to determine the thickness of the magnetic layer. Thus, we may conclude from Sample A that the thickness of the interfacial magnetic layer is less than 2 unit cells. Furthermore, the magnitude of the spin-splitting at the second order Bragg reflection is inconsistent with what we calculate for a 2 unit cell thick layer (97.8% confidence), while the splitting predicted for a single unit cell thick ferromagnetic layer is within the expected error of the measurement. Therefore, based on Sample A, we are led to conclude that only a single unit cell of $CaMnO_3$ is ferromagnetic at the interface.

Turning now to Sample B, we see that once again the spin splitting is the same on the critical edge, first order, and second order peak. The splitting on the first order Bragg reflection is 44% ± 8%, while the splitting on the second order peak is 46% ± 26%. In simulations based on Sample B, the second order peak is again found to be highly sensitive to the thickness of the ferromagnetic layer at the interface, with the spin splitting disappearing at a magnetic layer thickness of 2 unit cells and reversing relative to the first order peak at a thickness greater than 3 unit cells. Consequently, we may calculate the probability that the magnetic layer is at most one unit cell thick to be 95%. Additionally, fits of the polarized neutron spectra yield the highest χ^2 values for models which assume a ferromagnetic layer thickness of 1 unit cell. Thus, polarized neutron reflectometry also rules out any model in which the ferromagnetic layer is more than 1 unit cell thick.

Unfortunately, the second order Bragg reflection for the $(4/19)_8$ (Sample C) sample falls at a q-vector at which very little spin splitting is expected. Theoretical models predict spin-splittings of 3% and -8% using models with ferromagnetic layer thicknesses of 1 and 2 unit cells, respectively. When compared to the actual splitting we observe (13% ± 16%), neither of these models can be eliminated. A model with 3 unit cells of ferromagnetism at the interface predicts a splitting of -37% and may be eliminated. Therefore, while Sample C suggests that the ferromagnetic layer thickness is less than 3 unit cells, it does not add significant insight when added to Sample A and Sample B. Based on Samples A and B alone, however, a clear picture emerges of truly interfacial ferromagnetism in which the ferromagnetic order is confined within a single unit cell of $CaMnO_3$ at the interface.

We will now discuss a number of models and issues which have been neglected. The most obvious are models in which the ferromagnetism is spread evenly across the entire film, the $CaMnO_3$ layer, or the $CaRuO_3$ layer. These first two possibilities are clearly in conflict with the polarized neutron reflectometry, spectra taken here, as well as those taken by He et al. and the resonant X-ray magnetic scattering measurements performed by Freeland et al.. Such models result in a reversal of the splitting on the first order Bragg reflection relative to our observations and are therefore clearly unreasonable.[53, 36] Additionally, it has already been clearly demonstrated that the ferromagnetic response originates in the Mn ions through X-ray magnetic circular dichroism, and we may therefore eliminate the third model as well.

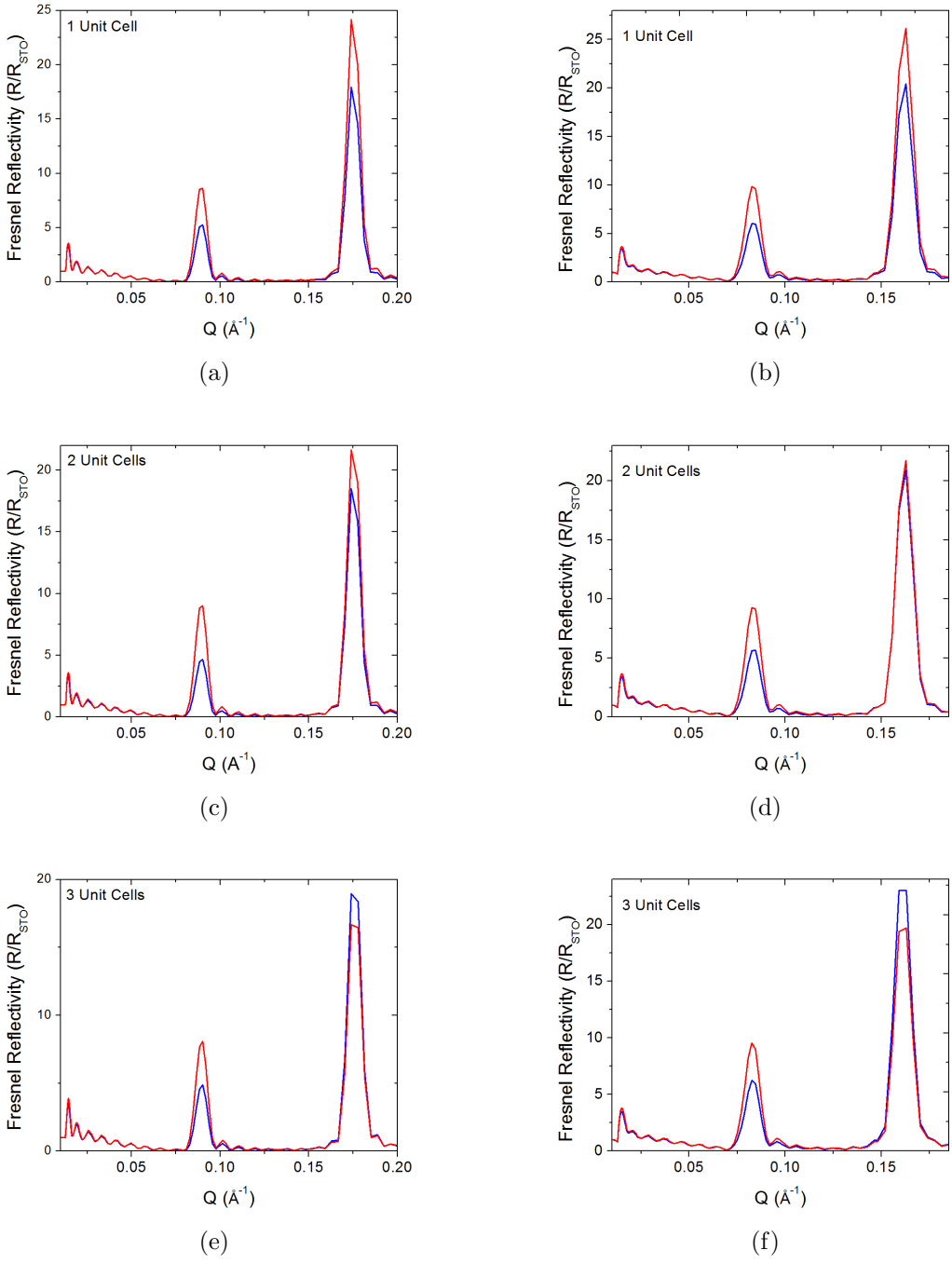

Figure 6.5: Theoretical polarized neutron reflectometry spectra. a), c), and e) are for a $(3/17)_{10}$ superlattice and assume magnetic layers 1, 2, and 3 unit cells thick. b), d), and f) are for a $(3/18)_8$ superlattice and assume magnetic layers 1, 2, and 3 unit cells thick.

Finally, the issue of roughness must be addressed. Throughout this analysis, we have used models in which it is assumed that the there is no intermixing between the various layers. Obviously, this assumption is incorrect. There are three different types of effects which will appear in neutron reflectometry (or X-ray reflectometry) as "roughness". The first is microstructural roughness as measured by atomic force microscopy. The second effect is actual intermixing of two layers to form an alloy. The third effect is one of long-range thickness variations on the scale of millimeters. Although the first two are easily accounted for using atomic force microscopy and X-ray reflectivity, the third is generally exacerbated by the much larger beam used in neutron reflectometry. While the X-ray reflectivity beam will usually interact with only a small fraction of the sample, a neutron beam will bathe the entire superlattice, significantly increasing the effects of long range variations on the measured spectra. Thus, it is possible for a film to appear extremely smooth on an atomic scale, have very smooth surface morphology, and still show significant "roughness" effects. This is the case with our films. Scanning transmission electron microscopy performed on similar films grown by our research group shows very little intermixing at the nanoscale.[53] X-ray reflectivity and atomic force microscopy on the films measured in this study limit the "roughness" to 2.5 Å. Therefore, in this study we have mostly examined models which assume minimal intermixing. However, neutron reflectivity indicates some very slight long range variation in layer thickness which would account for the small intensity discrepancies between the theoretical and measured reflectivity at high-Q. An examination of the various models already used with the addition of intermixing shows that the magnitude and sign of the splitting is negligibly affected by the addition of roughness as high as 10 Å, far in excess of that observed in our superlattices. In fact, the only significant effect is a reduction of the intensity of the superlattice peaks - the second order peak in particular, so that the theory matches our observations even more accurately.

Therefore, we have demonstrated excellent polarized neutron reflectometry spectra and have successfully fit these spectra with a model in which the ferromagnetic response is confined to a single unit cell at the interface. Furthermore, we are able to explicitly eliminate all other competing model distributions of the magnetic depth profile. This result is in excellent agreement with exchange bias measurements and observations related to the $CaMnO_3$ layer thickness dependence, but is remarkably different from findings acheived using resonant X-ray magnetic scattering from superlattices grown on $LaAlO_3$.[53, 36] It is unclear at this time whether the difference is related to the choice of substrate or strain effect, as the superlattices on $SrTiO_3$ are relaxed while those on $LaAlO_3$ are strained.

6.5 X-Ray Magnetic Circular Dichroism

Having resolved the question of the ferromagnetic layer thickness, we now return to the topic of oscillatory magnetic coupling in films with different $CaMnO_3$ thicknesses. As shown in Figure 6.3(a), the saturated magnetic moment of superlattices with $m < 12$ oscillate as a function of m. For m = even, films saturate at 1.0 μ_B per interfacial Mn while for m = odd, films saturate to 0.5 μ_B per interfacial Mn.[53] At this time, the mechanism for this oscillatory behavior is unknown. However, using XMCD, we can conclusively confirm the stark difference in saturated magnetic moments first measured by He et al. using SQUID

magnetometry. It may also be possible to address the issue of interfacial symmetry in these samples by examining the relative XMCD signal strength as a function of thickness. To that end, we have measured X-ray absorption spectra and XMCD for $(3/3)_{10}$, $(3/4)_{10}$, and $(3/5)_{10}$ $CaRuO_3/CaMnO_3$ samples, which had saturated magnetic moments of 0.9, 1.08, and 0.53 μ_B per interfacial Mn as measured by SQUID magnetometry.[53] Measurements were taken at beamline 6.3.1 of the Advanced Light Source with fixed circular polarization and alternating fields of ± 1.5 T. Samples were cooled to 20 K prior to measurement.

As already established through electron energy loss spectrometry by He et al., Mn L-edge X-ray absorption spectra were consistent with a Mn valence state very near 4+.[53] The splitting between the L_3 and L_2 edges is 10.3 eV while the L_3/L_2 peak area ratio is approximately 2.2. Both of these values are indicative of a Mn valence state of 3.83+ ± 0.1 - a state which is primarily Mn^{4+} with a smaller fraction of Mn^{3+}.[134, 142] This is in excellent agreement with the the theoretical predictions of Nanda et al. which suggest a transfer of 0.07 electrons from the $CaRuO_3$ layer to the first unit cell of $CaMnO_3$ at the interface.[109] Our measurements also agree well with previous results which report an interfacial Mn valence of 3.8+ ± 0.15+ and a bulk valence of 3.9+ ± 0.15+.[53] Although the possibility that the difference in valence across the $CaMnO_3$ layer is due to a slight oxygen deficiency at the interface cannot be entirely eliminated, such a deficiency has not been shown to induce the strong ferromagnetic behavior observed in these superlattices when studied in the bulk or as nanoparticles.[12, 97] The superlattices studied by X-ray absorption have a high proportion of interfacial $CaMnO_3$, suggesting that the measured valence should be near 3.85+ ± 0.15+. The top panels of Figure 6.6 (a)-(d) show a typical example of Mn L-edge X-ray absorption for $CaRuO_3/CaMnO_3$ superlattices. Figure 6.6(a) shows the raw XMCD of all three measured superlattices normalized by setting the maximum of the L_3 Mn absorption edge to one and the pre-edge to zero. Although there is clearly a significant difference in the measured dichroism, with the m = even sample showing much higher dichroism and consequently a larger magnetization, we cannot yet make a definitive quantitative statement regarding the relative magnitudes. Rather, we must first renormalize to account for the fact that all of the ferromagnetic signal arises at the interface.

To properly scale the dichroism magnitude relative to the X-ray absorption spectra, we must account for the exponential attenuation of the total electron yield as a function of depth. If the dichroism arises only from ferromagnetic layers at the interface, it will be reduced in magnitude relative to the dichroism from the same amount of total moment spread evenly throughout the layer. We may calculate the fraction of the signal arising from ferromagnetic layers and use that fraction to properly scale the dichroism and compare the magnitude of the ferromagnetic response at the interface using the equations below.

$$XMCD_{Interface} = XMCD_{Total}/A \tag{6.1}$$

$$A = \frac{\sum_i e^{-x_i/l}}{\sum_j e^{-x_j/l}} \tag{6.2}$$

where i is summed over all interfacial layers and j is summed over all $CaMnO_3$ layers. A is the fraction of the signal arising from layers in which there is ferromagnetism and if it is properly calculated we may use it to rescale the XMCD magnitudes of superlattices with different

periodicities so that the magnitude of the dichroism is scaled relative to the X-ray absorption signal of the interfacial ferromagnetic layers only. Thus we can compare the rescaled values to each other and ideally match the relative XMCD magnitude to that of the saturated magnetic moment per interfacial Mn ion as measured by SQUID magnetometry. The parameter l is the mean electron escape depth, an energy dependent distance which is usually on the order of 2-4 nm for probing energies between 100-1000eV.[86, 81, 13, 35, 119] Obviously, the precise value of the electron probing depth will significantly alter the magnitude of the final correction. The proponderance of the literature suggests that at the energy being probed, the expected probing depth is between 2-3 nm in total electron yield mode.[136] It is important to note that the rescaled XMCD magnitude represents the magnitude of the dichroism as a percentage of the X-ray absorption intensity of the ferromagnetic layers *only*. Thus, in order to test for the existence of an oscillatory magnetic moment, we assume a model depth profile in which the ferromagnetism is confined to a single unit cell at the interface, as required by the polarized neutron reflectometry measurements. The rescaling factor A may then be calculated for each sample.

The results of rescaling based on this model are shown in Figure 6.6(b). Note that the saturated magnetic moments of the (3/3), (3/4), and (3/5) samples as measured by SQUID magnetometry were approximately 0.9, 1.1, and 0.5 μ_B per interfacial Mn ion.[53] These values are in excellent agreement with the relative XMCD magnitudes as determined by integrating the area under the rescaled XMCD curves for each superlattice. Therefore, we can confirm the existence of an oscillatory saturated magnetic moment and show that the oscillation originates in the Mn ions. We may now also compare two alternative depth profiles of the ferromagnetic response with the SQUID measurements. We have already mentioned asymmetric interfaces as a mechanism for explaining the oscillatory coupling. Assuming that all magnetic interfaces have the same saturated magnetic moment of approximately 1 μ_B per Mn ion, we may consider models in which one of the two interfaces is nonmagnetic in the m = odd samples. Either the $CaRuO_3/CaMnO_3$ ("Top") interface is magnetic or the $CaMnO_3/CaRuO_3$ ("Bottom") interface is. Although polarized neutron reflectometry of thicker superlattices localized the ferromagnetic layer to a single unit cell of $CaMnO_3$ at the interface, reflectometry of $m < 12$ samples which exhibit the oscillatory moment was not sensitive to the difference between a symmetric model and either of the asymmetric distributions.[53] If either of the asymmetric models is true, a rescaling of the dichroism should yield the same XMCD magnitude for all superlattices since we are now scaling to half as many ferromagnetic layers in the m = odd samples, which saturate to half the total moment of the m = even samples. The "Top" model where the magnetic layer is above the $CaRuO_3$ is used to rescale the XMCD measurements and is shown in Figure 6.6(c). Obviously since the oscillation does not begin until $m > 4$, only the scaling of the (3/5) sample will change. In fact, we find that, the "Top" distribution model results in approximately the same dichroism for every superlattice, as expected. However, the "Bottom" model does not and actually requires saturated magnetic moments far in excess of what is observed. Therefore we conclude that either a symmetric model or the "Top" model may describe the magnetic depth profile, but the "Bottom" model cannot.

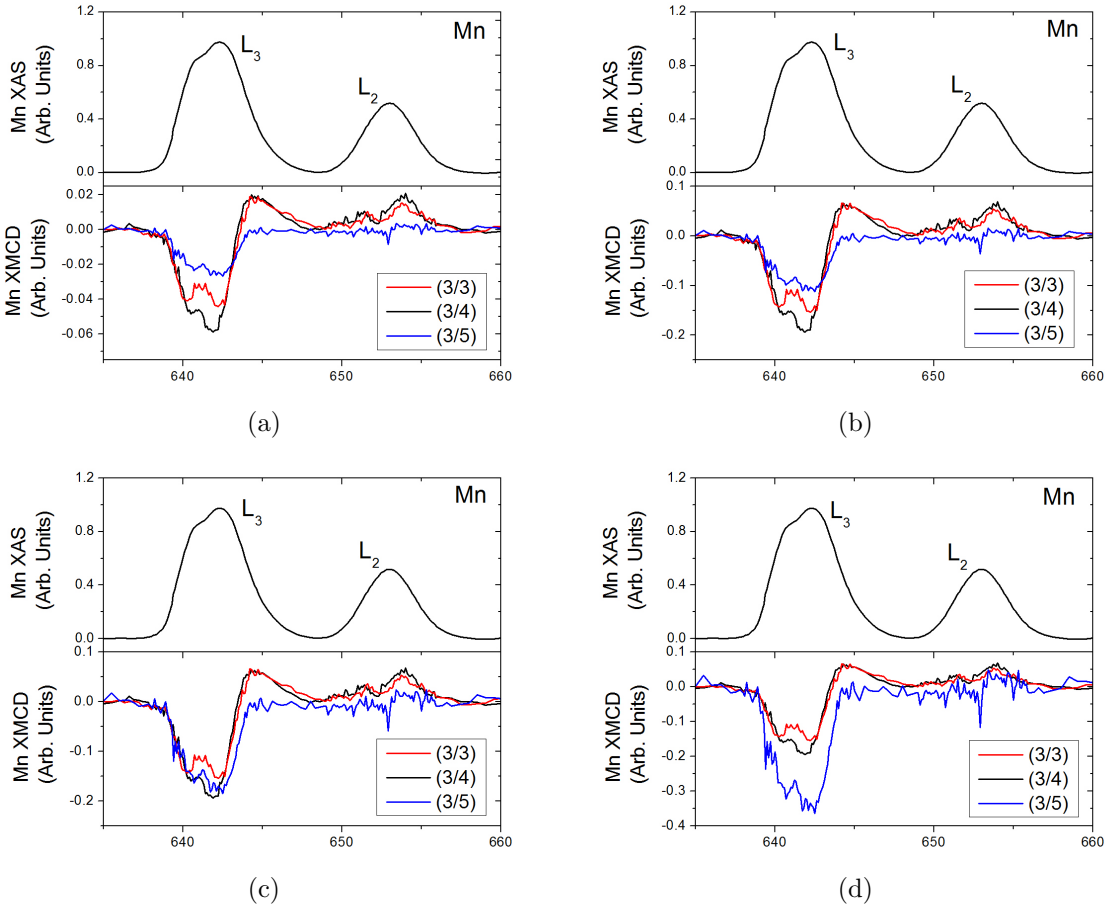

Figure 6.6: X-ray absorption and X-ray magnetic circular dichroism spectra of a $(3/3)_{10}$, $(3/4)_{10}$, and $(3/5)_{10}$ superlattice. (a) Unscaled, (b) Scaled using a symmetric interface model, (c) Scaled assuing only $CaRuO_3/CaMnO_3$ interfaces are magnetic for m = odd samples, and (d) Scaled assuing only $CaMnO_3/CaRuO_3$ interfaces are magnetic for m = odd samples,

6.6 Probing Oscillatory Coupling and Magnetic Structure Through Neutron Diffraction

Although X-ray magnetic circular dichroism measurements confirmed the oscillatory saturated moment $CaRuO_3/CaMnO_3$ superlattices with varying thickness and yielded some insights into the interfacial symmetry, it does not help to determine a mechanism to such a phenomena. For that, we will first turn to neutron diffraction. It has been observed in exchange bias measurements that (for m ¡ 12) the exchange field for superlattices with $m =$ odd is significantly reduced relative to $m =$ even samples. Additionally, the effect in question appears to have a period of 2 unit cells of $CaMnO_3$, as does the antiferromagnetic order in $CaMnO_3$. Both of these statements suggest that the ferromagnetic and antiferromagnetic states in the $CaMnO_3$ layer may be tightly linked. Therefore, we have used neutron diffraction to probe the magnetic ordering peaks in $CaMnO_3$ for signatures of long range order. Due to the extreme difficulty of resolving thin film peaks through neutron diffraction, we have used a much larger 8×8 mm^2 $(3,18)_8$ superlattice.

Neutron diffraction measurements were carried out at the BT4 and BT7 beamlines at the NIST Center for Neutron Research. It is well known that the G-type antiferromagnetism present in $CaMnO_3$ produces a strong $(^1/_2,^1/_2,^1/_2)$ magnetic scattering peak.[154, 61] By scanning the $(^1/_2,^1/_2,^1/_2)$ peak along the growth axis, we may extract an antiferromagnetic correlation length. If the various $CaMnO_3$ layers are uncorrelated and exchange information is not being transmitted across the $CaMnO_3$, we expect to find a correlation length of $18\times a_{CaMnO_3} \approx 6.7$ Å. However, if the various layers are correlated, they will be behave independently for purposes of magnetic ordering and we may find a mechanism by which oscillatory coupling may be induced. In this case, we expect a correlation length significantly greater than the width of a single $CaMnO_3$ layer.

An initial low-temperature (5 K) q-scan scan through the expected location of the $(^1/_2,^1/_2,^1/_2)$ peak revealed a surprisingly strong peak, as shown in Figure 6.7(a). This peak corresponds to the well known tetragonal distortion which occurs in the $SrTiO_3$ substrate at 105 K, as shown by its temperature dependence.[84] The $SrTiO_3$ distortion peak makes the $(^1/_2,^1/_2,^1/_2)$ antiferromagnetic peak difficult to see. However, a closer examination of the distortion peak, shown in Figure 6.7(b), reveals a shoulder which corresponds precisely to the expected position of the $(^1/_2,^1/_2,^1/_2)$ antiferromagnetic peak. This feature is present in multiple different scans, as shown in Figure 6.7(c) where tighter collimation has been employed to reduce the distortion peak width and separately resolve the $(^1/_2,^1/_2,^1/_2)$ peak. All of the measurements shown in Figure 6.7 were performed at the BT7 triple axis spectrometer with the exception of 6.6(d), which shows a similar Q-scan on the BT4 spectrometer with maximum collimation employed for the highest possible resolution.

Having demonstrated the existence of a $CaMnO_3$ $(^1/_2,^1/_2,^1/_2)$-type peak, we need to establish that it is, in fact, a magnetic peak rather than a structural half-order peak either inherent in the film or induced by the $SrTiO_3$ distortion. Unfortunately, there is at this time no other example of neutron diffraction performed on thin films of $CaMnO_3$. In fact, we are unable to find *any* example of single crystal neutron diffraction on $CaMnO_3$ in the relevant temperature regime. Therefore we must first demonstrate the temperature dependence of the peak, which may be seen in Figure 6.8, which shows the disappearance

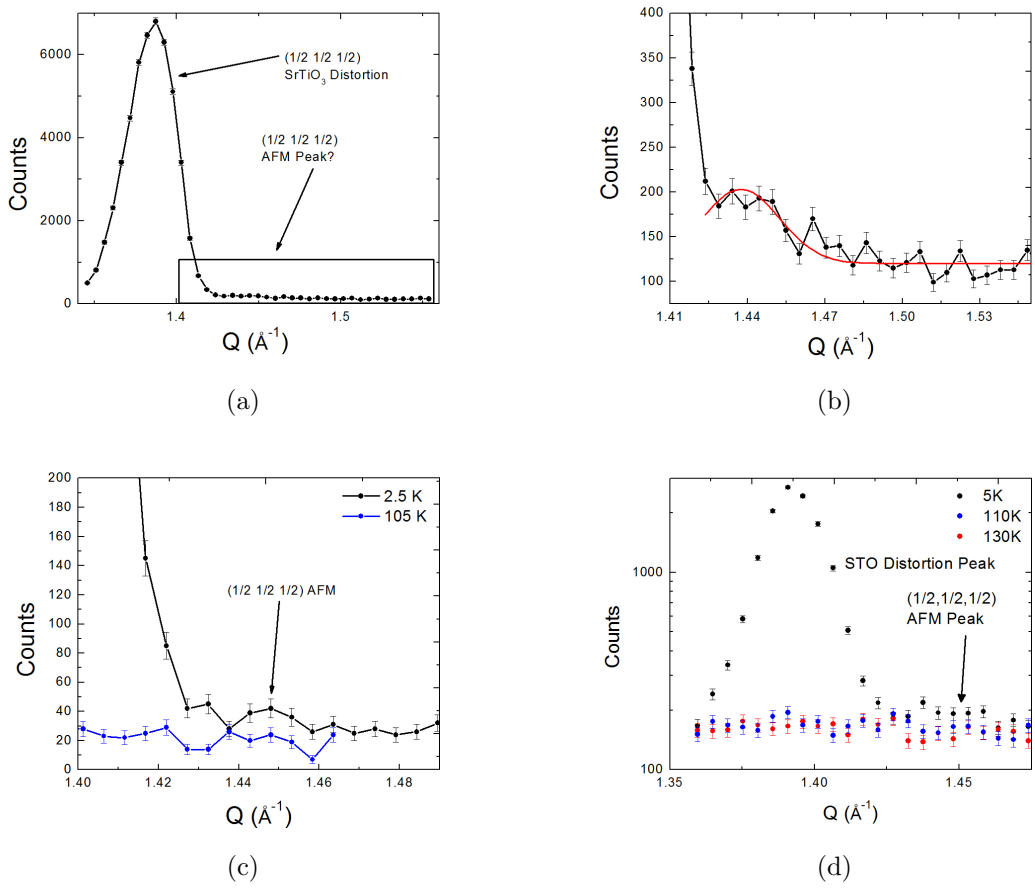

Figure 6.7: Neutron diffraction spectra of a) $(^1/_2,^1/_2,^1/_2)$ $SrTiO_3$ distortion peak with temperature dependence, b) $(^1/_2,^1/_2,^1/_2)$ $CaMnO_3$ antiferromagnetic peak as a shoulder of the $SrTiO_3$ distortion, c) Improved resolution of the $(^1/_2,^1/_2,^1/_2)$ $CaMnO_3$ antiferromagnetic peak, all taken at BT7. d) $(^1/_2,^1/_2,^1/_2)$ $SrTiO_3$ distortion peak and $CaMnO_3$ magnetic $(^1/_2,^1/_2,^1/_2)$ peak taken at BT4.

of the peak by temperatures of 105-110 K. This demonstrates that the peak in question is not an inherent structural feature of $CaMnO_3$ in thin film form. It does not, however, eliminate the possibility of a half-ordering peak induced on the film by the tetragonal distortion of the $SrTiO_3$ substrate. Unfortunately, it it not possible to distinguish these two peaks based on their temperature dependence. As has been thoroughly demonstrated in examples of $CaRuO_3/CaMnO_3$ superlattices, the canted antiferromagnetic state has a Curie temperature in the range of 100-110 K on both $LaAlO_3$ and $SrTiO_3$ substrates.[53] This is most likely an indication that the Neel temperture of $CaMnO_3$ is slightly suppressed in $CaRuO_3/CaMnO_3$ superlattices. Even if the ferromagnetic ordering temperature were at a bulk value of 123 K it would be very difficult to distinguish between the two second order transitions based on temperature dependence. With a Neel temperature suppressed to between 100 and 110 K it is certainly not possible. To address this issue, we first remind the reader that the film is relaxed, and there is consequently no strong reason to believe that the superlattice will distort along with the substrate. However, we may make a more convincing argument by comparing the relative peak strengths of the $SrTiO_3$ distortion peak with the (111) $SrTiO_3$ peak and extrapolating the expected intensity of any distortion peak induced in the superlattice. At constant experimental configuration, we found that the $SrTiO_3$ (111) peak had an intensity of 37500 counts per second, while the $(^1/_2,^1/_2,^1/_2)$ distortion peak yielded 22 counts per second, a ratio of 0.05%. From Wiebe et al., it is known that the ratio of $CaMnO_3$ antiferromagnetic $(^1/_2,^1/_2,^1/_2)$ peak intensity to (111) peak intensity is approximately 15%. If the ratio between the (111) peak and the $(^1/_2,^1/_2,^1/_2)$ distortion peak intensity holds approximately constant for $CaMnO_3$ and $SrTiO_3$, we would expect any film distortion peak to be 0.3% of the intensity of the magnetic peak. Alternatively, if the peak intensity of the $SrTiO_3$ distortion is the same per unit volume as in $CaMnO_3$, a simple volumetric ratio shows that the expected peak intensity would be 0.0025 counts per second. As the scans shown in Figure 6.7 were 5 minute scans, we therefore expect at most 0.75 counts per point to be contributed by any distortion peak in $CaMnO_3$. It is extremely unlikely, therefore, that the peak in question is anything but the expected $CaMnO_3$ $(^1/_2,^1/_2,^1/_2)$ magnetic peak.

We scanned through the peak along the growth axis direction and, using the full width at half maximum of the peaks, extracted the antiferromagnetic correlation length along the growth direction. As can be seen in Figure 6.8, which plots the peak at 25 K, 50 K, 75 K, and 100 K, the antiferromagnetic peak stands out even more clearly in the growth axis scan. Figure 6.9 shows the reciprocal space geometry in which a film diffraction peak (blue) may overlap with a substrate diffraction peak (purple) along the Q-axis yet appear as a freestanding peak in a scan along the growth or in-plane axis. In fact, if the peaks were not clearly separated along these axes, we would expect to see a strong increasing background in either a growth axis or in-plane scan as Q approached the edge of the substrate peak. Moreover, we may be even more confident that we are seeing a film peak, rather than slicing through a section of the substrate reciprocal lattice point, because the maximum intensity occurs far from the center of the substrate peak as determined by Q, growth axis, and in-plane scans. In fact, the center of the film peak occurs at $Q_{GA} = 0.831$ Å^{-1}, $Q_{IP} = 0.831$ Å^{-1} while the center of the substrate distortion peak occurs at $Q_{GA} = 0.798$ Å^{-1}, $Q_{IP} = 0.802$ Å^{-1}. From the FWHM of the $(^1/_2,^1/_2,^1/_2)$ antiferromagnetic peak we extract a correlation length in the range of 22-27 nm. This corresponds to a correlation length that

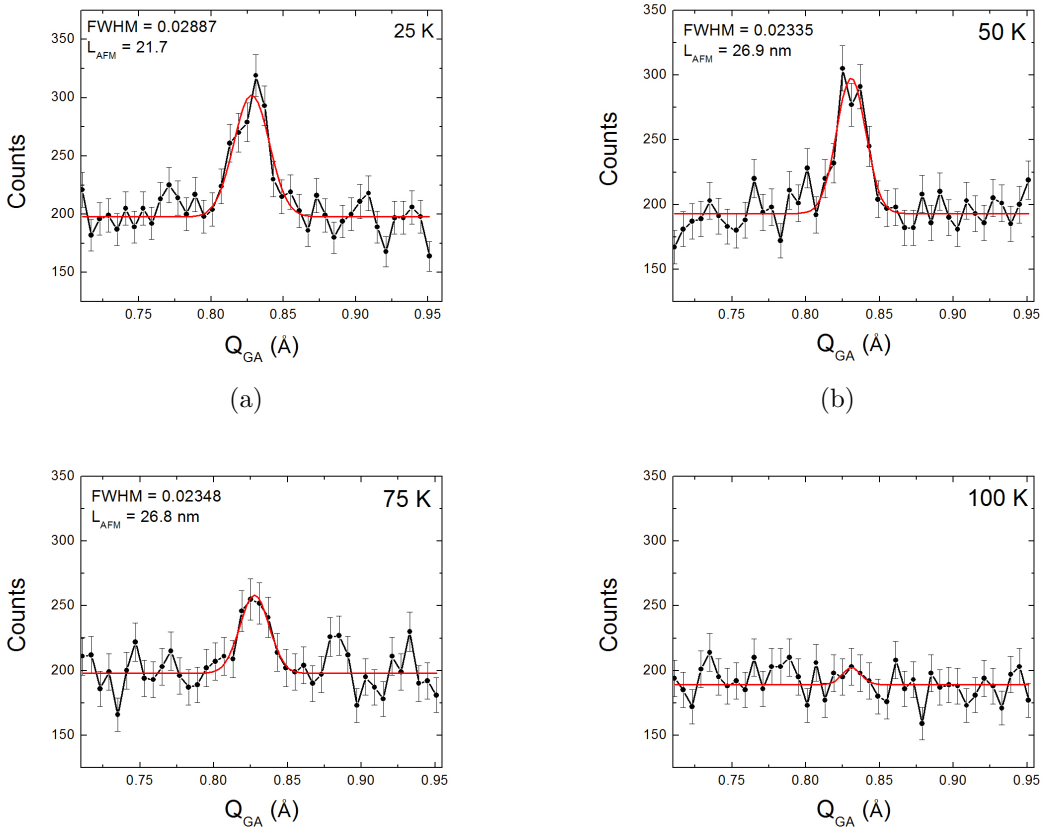

Figure 6.8: Neutron diffraction spectra of $(^1/_2, ^1/_2, ^1/_2)$ $CaMnO_3$ antiferromagnetic peak at a) 25 K, b) 50 K, c) 75 K, d) 100 K. All spectra taken at beamline BT7.

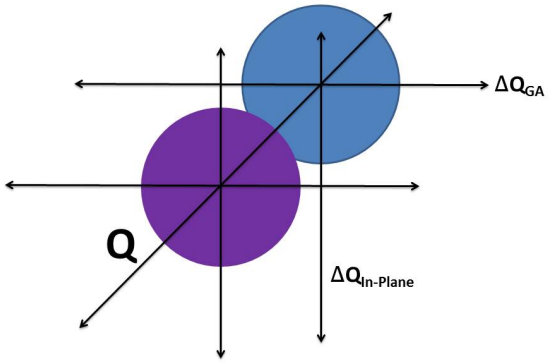

Figure 6.9: Schematic reciprocal lattice arrangement showing Q, Growth Axis, and In-Plane scanning directions used in neutron diffraction. Peaks appearing in Q-scans may not appear in Growth Axis or In-Plane scans.

is 3.3-4.0 times the thickness of any given $CaMnO_3$ layer. Consequently, it is clear that the $CaRuO_3$ layers do not inhibit long range magnetic order in $CaRuO_3/CaMnO_3$ superlattices, even along the growth axis. For the first time, we have a mechanism by which an oscillatory magnetic coupling may be manifest in this system.

In addition to growth order scans of the $(^1/_2,^1/_2,^1/_2)$ antiferromagnetic reflection, we also searched for the $(^1/_2,^1/_2,0)$ type antiferromagnetic reflection known to occur in some examples of doped $CaMnO_3$.[154, 130, 111, 82] In these doped systems, the C-type phase is frequently associated with the emergence of ferromagnetic clusters in the $CaMnO_3$. However, a scan through the expected location, which can be seen in Figure 6.10(a), shows no such peak.[154, 130, 111, 82] Correspondingly, it is highly unlikely that a significant amount of doping or oxygen deficiency has occurred in the measured superlattice. Finally, neutron diffraction also revealed a strong half-order film peak (Figure 6.10(b)) which indexes to a $CaRuO_3$ or $CaMnO_3$ $(^3/_2,^1/_2,^1/_2)$ and does not disappear with increasing temperature, indicating that structural half order is indeed present. Although not surprising in orthorhombically distorted perovskites, the peak is quite strong and demands additional attention.

Although the large growth axis antiferromagnetic correlation length remains an important step in understanding the nature of oscillatory coupling and magnetic order in $CaRuO_3/CaMnO_3$ superlattices, it remains to be seen whether it is an underlying cause, or merely a manifestation of usual structual half order. To address that question, we turn now to X-ray diffraction experiments carried out with synchrotron radiation.

6.7 Detailed Crystal Structure Probing

The manifestation of antiferromagnetism with phase coherence across several superlattice layers is almost as surprising as the modulation of saturated magnetic moment with superlattice layer thickness. As already discussed, such long range order requires a mecha-

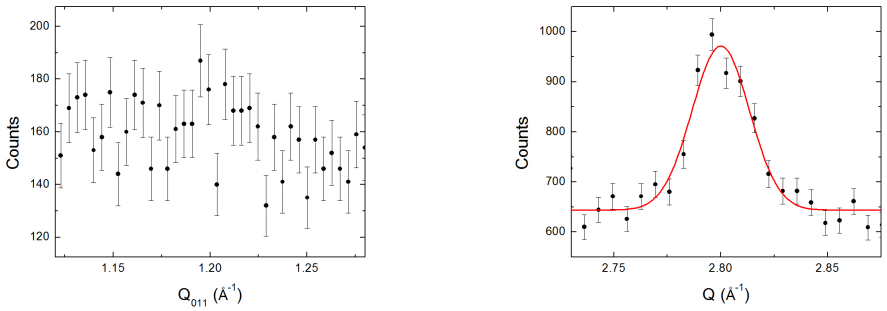

(a) (b)

Figure 6.10: a) Neutron diffraction scan of the expected C-type antiferromagnetic peak location taken at 5 K. b) ($^3/_2$,$^1/_2$,$^1/_2$) $CaMnO_3$ structural peak.

nism by which coherence is maintained through the intervening $CaRuO_3$ layers. Although it is not clear at this time whether the long range antiferromagnetic order is influencing the canted antiferromagnetic state, it is easy to speculate that "even" and "odd" $CaMnO_3$ layers might exhibit different coupling between the antiferromagnetic and canted antiferromagnetic regions. In this case, long range antiferromagnetic coherence may provide an explanation for the oscillatory magnetic moment. However, this neither explains the long range antiferromangetism nor eliminates the possibility of a structural mechanism for explaining the magnetic moment oscillation. Therefore, we used X-ray diffraction to provide a detailed structural analysis of a pair of $(3/4)_{10}$ and $(3/5)_{10}$ superlattices which have been confirmed to show the observed oscillatory magnetic moment. By using the thin film diffraction setup at beamline 2-1 of the Stanford Synchrotron Radiation Laboratory (SSRL), it was possible to perform X-ray diffraction with much higher intensity than otherwise achievable using a typical X-ray diffractometer. All synchrotron diffraction measurements were performed by Dr. Arturas Vailionis of Stanford University and SLAC National Accelerator Laboratory. Thus, we could resolve a number of features not observable through the use of lower-intensity mechanisms, such as asymmetric scans through orthorhombic distortion peaks in samples with superlattice layers as thin as 4 unit cells. We observe structural "half-order" diffraction peaks which have the same 2 pseudocubic unit cell periodicity as both the antiferromagnetism and oscillatory saturated magnetic moment. These orthorhombic distortions present in $CaRuO_3/CaMnO_3$ superlattices are very promising for explaining the magnetic behavior.

We first examined a pair of reciprocal lattice maps of the $(\bar{1}03)$ $CaMnO_3$ peak for the $(3/4)_{10}$ and $(3/5)_{10}$ superlattices are shown in Figure 6.11. These lattice maps reveal a strain state which is very similar in both superlattices, with in-plane and growth axis strains of 2% and 1.2% respectively in the $(3/4)_{10}$ sample and in-plane and growth strains of 1.8% and 0.9% respectively in in the $(3/5)_{10}$ sample. It is worth noting that the slight shift towards bulk $CaMnO_3$ parameters in the (3/5) sample is likely caused by the thicker $CaMnO_3$ layer. This will be a continuous trend as a function of thickness and is unlikely to result in an oscillatory magnetic behavior. In Figure 6.11, we observed no trace of the $CaRuO_3$ peak which is expected to appear between the $SrTiO_3$ and $CaMnO_3$ peaks near Q_{IP} = -1.68 $Å^{-1}$

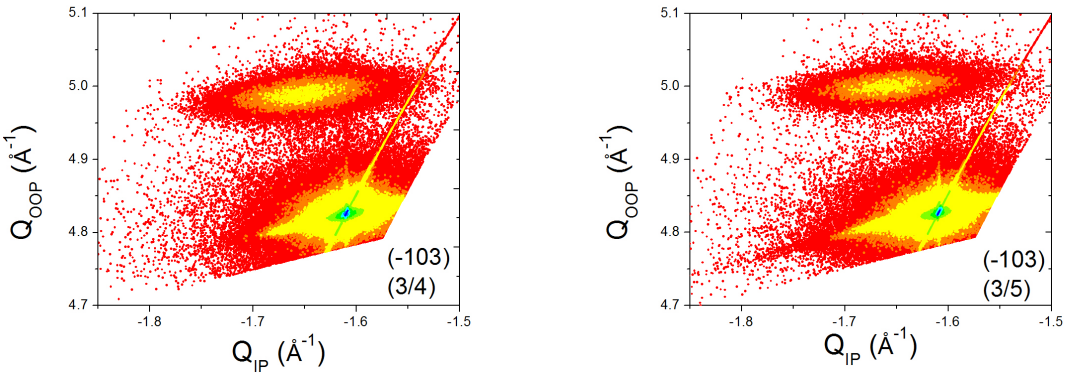

Figure 6.11: Reciprocal lattice maps of the $(\bar{1}03)$ peak of $CaRuO_3/CaMnO_3$ superlattices with periodicities of a) (3/4) and b) (3/5). Significant relaxation is evident.

and $Q_{OOP} = 4.91$ Å^{-1}. Observataion of this peak has been previously reported near the expected reciprocal space location in examples of $((CaRuO_3)_3/(CaMnO_3)_{12})_{10}$ superlattices on $SrTiO_3$.[54] These examples show the $CaRuO_3$ and $CaMnO_3$ to be relaxed relative to the substrate, as shown in Figure 6.11, but also that the two layers have identical in-plane lattice parameters. It is possible that in superlattices with thinner layers and lattice parameters which deviate more extensively from bulk values the $CaRuO_3$ peak is significantly weakened or merges with the $CaMnO_3$ peak. Finally, we note that the $CaMnO_3$ peaks shows positive strain values along both in-plane and growth-axis directions. This indicates a slight volume expansion in these layers, which is in excellent agreement with a slight oxygen deficiency as suggested by earlier EELS results.[53]

ω rocking curves of the (200) film peaks were taken using high intensity radiation at SSRL for a number of samples, and typical examples are shown in Figure 6.12. These scans revealed two overlapping peaks in all samples. One is sharp central peak while the other is a much wider feature. The layer thicknesses of samples exhibiting this behavior varied extensively, with periodicities of (3/4), (3/5), (3/10), (3/11), and (3/18). In all cases, we observed the same set of overlapping peaks. In general, the broader peak becomes stronger relative to the sharp central peak with increasing $CaMnO_3$ layer thickness. It is possible that these overlapping features represent the relative mosaicity of the $CaRuO_3$ and $CaMnO_3$ layers. If so, the wider feature which increases in relative intensity with increasing $CaMnO_3$ thickness is most likely the $CaMnO_3$ peak while the sharper feature is the $CaRuO_3$ peak. This suggests that the $CaRuO_3$ layers are of significantly higher quality that the $CaMnO_3$ layers, as may be expected given the greater substrate mismatch and relaxation expected to be present in the $CaMnO_3$. However, as the two overlapping peaks do not appear in symmetric $\theta - 2\theta$ scans, it is also possible that the double peak represents an in-plane feature such as nanoscale phase segregation. The phase segregation of small nanocrystalline regions in a much larger crystal matrix is well known in the manganites but was not observed in previous studies utilizing transmission electron microscopy.[53] Alternatively, the wider peaks may indicate small variations on the structural order across individual superlattice layers.

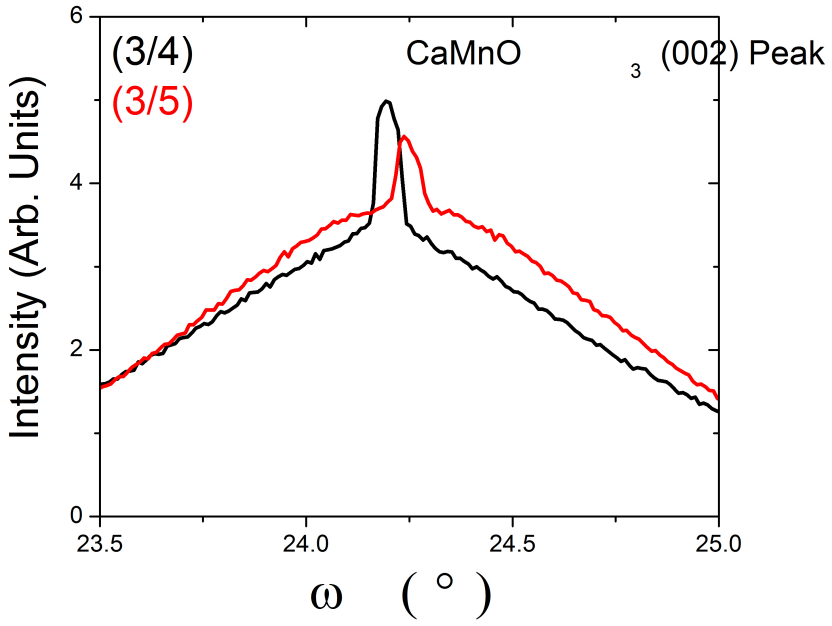

Figure 6.12: ω rocking curves of the (200) film peaks of (3/4) and (3/5) superlattices taken at SSRL beamline 2-1

Finally, we used beamline 2-1 at the SSRL to probe the orthorhombic distortion or "half-order" peaks present in our superlattices. The high intensity of synchrotron radiation allowed these weak diffraction peaks to be resolved even in such thin $(3/4)_{10}$ and $(3/5)_{10}$ samples, as can be seen in Figure 6.13 which shows the pseudocubic $(10^5/_2)$ and $(01^5/_2)$ peaks for (3/4) and (3/5) samples scanned along the l direction (as in hkl indices). When we say $(01^5/_2)$ peaks we are of course referring to the pseudocubic system, in which these peaks are not expected to exist. Alternatively we may refer to these peaks in a system with doubled lattice parameters as 205 type peaks. Both superlattices showed two distinct distortion peaks, one at $l = 2.589$ Å^{-1} and another at 2.535 Å^{-1}, with one peak being significantly stronger than the other. However, in the (3/4) sample the peak at 2.589 Å^{-1} was significantly stronger while in the (3/5) sample the peak at 2.535 Å^{-1} was stronger. The peak at 2.589 corresponds to a $CaMnO_3$ distortion peak while the peak at 2.535 Å^{-1} corresponds to a $CaRuO_3$ distortion peak. Therefore, the "even" and "odd" samples have distortions which match $CaMnO_3$ and $CaRuO_3$, respectively! Thus, we have uncovered a structural difference between "even" and "odd" samples which may explain the oscillatory magnetic moment.

These preliminary results clearly warrant further investigation. Showing long range structural order along the film growth axis is highly suggestive of a system which may preserve long range antiferromagnetic phase coherence. It is possible that the two ranges of structural order revealed by symmetric diffraction scans correspond to the individual superlattice layers as well as a long range structure which is propagated through the entire superlattice through the orthorhombic distortion in the system. This theory is lent significant credence by Figure

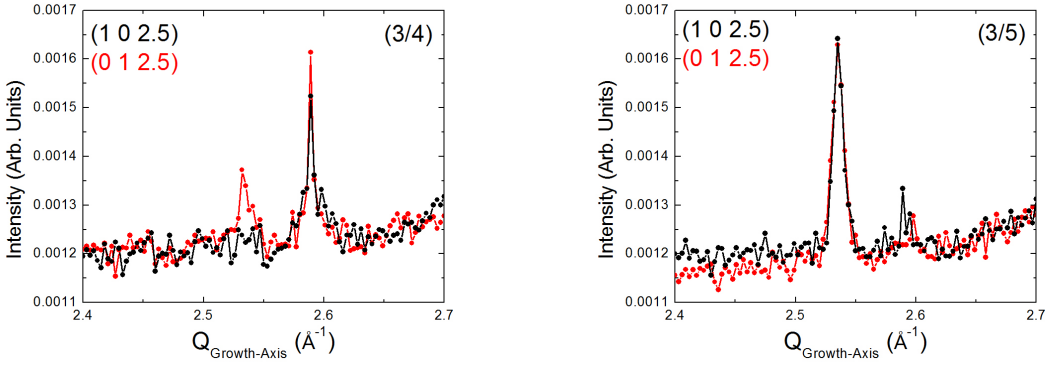

(a) (b)

Figure 6.13: l direction scans of the a) $(10^5/_2)$ and b) $(01^5/_2)$ diffraction peaks for (3/4) and (3/5) superlattices taken at SSRL beamline 2-1

6.13, which clearly demonstrated that rather than a series of coexisting distortions in each superlattice, each sample stabilizes only a single distortion symmetry which corresponds either to that present in bulk $CaMnO_3$ or bulk $CaRuO_3$. Such consistent periodicity in the sample may be reponsible for the sharp peak observed in the symmetric scans. Additionally, the stabilization of different distortion in the "even" and "odd" samples is an excellent candidate for explaining the modulation of the saturated magnetic moment. Before such a theory may be accepted, however, it must be shown that other samples show the same behavior.

6.8 Concluding Thoughts

In this chapter, we have spent considerable time attempting to understand the complex magnetic coupling interactions in $CaRuO_3/CaMnO_3$ superlattices. We have, for the first time, conclusively demonstrated that the ferromagnetism in this system is confined to a single unit cell of $CaMnO_3$ at the interface. In exploring the magnetic coupling, we have uncovered several surprising mechanisms by which oscillatory magnetic coupling may be accomplished in $CaRuO_3/CaMnO_3$ superlattices. We have shown, through neutron diffraction measurements, long range antiferromagnetic order with a growth axis coherence length 3-4 times that of an individual superlattice $CaMnO_3$ layer and crossing the $CaRuO_3$ layers. It is not yet clear whether or not this long range magnetic order is a cause of the oscillatory coupling itself, or if both effects are the result of the underlying half order structure present in this system. Despite the progress this represents, there are many unanswered questions remaining about the roles and interactions of these competing types of order in determining the final magnetic state. What is clear, however, is that the system is much more complex than previously thought.

What this chapter has *not* addressed, however, is the issue of intermixing at the interface. It is well known that $CaRu_xMn_{1-x}$ form a ferromagnetic solid solution for a very wide

compositional range. Might not this provide a very simple explanation for the observed magnetic properties? Finally, although our understanding of the underlying physics of the system is now much clearer, the critical issue of how to tune the interfacial magnetism has also not yet been discussed. Chapter 7 will be devoted to exploring and answering these questions by replacing $CaRuO_3$ with another paramagnetic metal, $LaNiO_3$.

Chapter 7

Inducing Ferromagnetism at the $LaNiO_3/CaMnO_3$ Interface

Having established the highly interfacial nature of the magnetism at $CaRuO_3/CaMnO_3$ interfaces in Chapter 6, Chapter 7 will attempt to definitively isolate interfacial double exchange effects from those of intermixing. This chapter is also concerned with the search for parameters by which the interfacial magnetic ordering in the system may be tuned. To accomplish both of these goals, we replaced the highly correlated metal $CaRuO_3$ with an alternative system, $LaNiO_3$. The resulting superlattices show interfacial ferromagnetism which is highly tunable in terms of saturated magnetic moment as well as the stabilization of emergent interfacial ferromagnetism itself.

7.1 The Challenge of Intermixing at Interfaces

As discussed in Chapter 6, the interface ferromagnetism in $CaRuO_3/CaMnO_3$ superlattices is attributed to itinerant electrons in the $CaRuO_3$ mediating a canted antiferromagnetic state among the Mn ions in $CaMnO_3$ at the interfaces.[145, 109, 53, 36] However, interdiffusion may give rise to ferromagnetism, since the solid solution $CaRu_xMn_{1-x}O_3$ is ferromagnetic for $0.1 < x < 0.7$.[92] Although it is difficult to imagine that a ferromagnetic state induced by intermixing would be confined to a single unit cell, especially given the low threshold for magnetic ordering in such an alloy, it is also extremely difficult to rule out. In order to completely satisfy our skepticism, it would be desireable to have examples of an interfacial double exchange interaction which may be modulated using a parameter independent of intermixing. Such a system would not only allow us to rule out intermixing effects, but would also allow control of an interfacial double exchange interaction for the first time. To that end, we turn to a material which has attracted a great deal of attention in the past few years - $LaNiO_3$.

$LaNiO_3$ is a correlated paramagnetic metal with the electronic configuration $t_{2g}^6e_g^1$. It is an orthorhombically distorted perovskite with a pseudocubic lattice parameter of 0.384 Å, very similar to $CaRuO_3$.[105, 104, 106, 75] It is also commonly grown in higher oxygen pressures such as 30 mtorr O_2, as are $CaRuO_3$ and $CaMnO_3$.[131, 144] It is, consequently, an excellent candidate for replacing $CaRuO_3$. Although the electron configuration is quite

different, the e_g levels are typically more mobile than the t_{2g} and represent an excellent opportunity for stabilizing double exchange through electron leakage. Most importantly, $LaNiO_3$ is thought to be on the verge of a metal-insulator transition as well as a transition to a charge ordered antiferromagnetic state.[45, 132, 42] In such a state, the Ni^{3+} ions will segregate into Ni^{2+} ($t_{2g}^6 e_g^2$) and Ni^{4+} ($t_{2g}^6 e_g^0$). This is expected to result in an insulating antiferromagnet, and is common in other rare earth nickelates but not realized in bulk $LaNiO_3$.[46, 32, 101, 148, 99, 42]

However, it has been recently reported that a metal insulator transition may be induced by reducing the $LaNiO_3$ thickness in thin film and superlattice form.[132, 11, 98] The origin of this thickness dependent MIT is not well understood but several mechanisms have been proposed, including strain, confinement effects, and charge disproportionation.[8, 11, 83, 41, 45, 98, 120, 132, 139] Although the MIT is observed in both $LaNiO_3$-based superlattices and $LaNiO_3$ ultrathin films, the critical thickness varies somewhat across the studied systems and it is generally agreed that there may be different or competing mechanisms at work.[8] For example, in $LaNiO_3/LaAlO_3$ films the critical thickness is most commonly reported to be 3 unit cells and the mechanism is suggested to be charge disproportionation of the Ni^{3+} into Ni^{2+} ($t_{2g}^6 e_g^2$) and Ni^{4+} ($t_{2g}^6 e_g^0$).[11, 83] Density functional theory calculations support this interpretation and suggest an antiferromagnetic ground state strongly reminiscent of the related rare earth nickelates.[8, 120] In addition, X-ray absorption measurements in these superlattices show strong evidence that a confinement induced enhancement of electron correlation effects plays a significant role in the MIT, as do the Al ions at the interface.[83] The Ni-O-Al bond is expected to exhibit significantly reduced covalency, contribution the the localization of the otherwise conducting Ni electrons.[8, 83] A similar MIT has been reported in $LaNiO_3/SrMnO_3$ superlattices, with a critical thickness of 3-4 unit cells of $LaNiO_3$. Is is both surprising and convenient that the behavior and critical thickness are so similar in $LaNiO_3/LaAlO_3$ and $LaNiO_3/SrMnO_3$ superlattices, given that the first is an example of a polar/polar interface while the second is a polar/nonpolar interface. Ultrathin films of $LaNiO_3$ appear to undergo a somewhat more gradual thickness dependent metal-insulator transition, with critical thicknesses on the order of 5-8 unit cells.[132, 139] Again, there is evidence for the proximity of $LaNiO_3$ to a charge ordered antiferromagnetic state, although is has also been suggested that weak localization and epitaxial strain also play a role.[132, 139] Thus, it appears likely that quantum confinement and localization introduce competition between the bulk $LaNiO_3$ state and a change ordered antiferromagentic state. As electrons are increasing localized by the proximity of interfaces, charge disproportionation and ordering begins to occur, increasing localization and driving a MIT. In superlattices, it seems clear that the bonding at interfaces also plays a significant role in determining the critical thickness.

Many other exciting magnetic interactions have been recently reported in $LaNiO_3$ films and superlattices. For example, ferromagnetism and exchange biasing has been reported to be induced in typically paramagnetic $LaNiO_3$ by adjacent ferromagnetic $LaMnO_3$ in $LaMnO_3/LaNiO_3$ superlattices.[45] Although mechanistically very different from $CaRuO_3$ / $CaMnO_3$ superlattices, in both cases ultrathin strongly correlated metallic layers are essential for the generation of ferromagnetism. There is also some evidence for spin density wave formation in $LaNinO_3$ films and superlattices.[45, 132] Much of the underlying physics behind this behavior has not yet been elucidated. However, despite these open questions, epitaxial $LaNiO_3$ layers are excellent candidates for exploring the origin of interfacial fer-

romagnetism in systems where itinerant electrons may mediate ferromagnetic exchange. In particular, the metal insulator transition offers a unique tool for separating the effects of itinerant electrons at the interface from others such as intermixing, epitaxial strain, and defects.

When considering $LaNiO_3$ as a replacement for $CaRuO_3$, it is of course critical to note the magnetic properties of the alloy $La_{1-x}Ca_xNi_{1-x}Mn_xO_3$. However, we are not able to find any study of such a compound in the literature. There has of course been extensive study of the alloy $La_{1-x}Ca_xMnO_3$. $La_xCa_{1-x}MnO_3$ is a ferromagnetic insulator for the compositional range $0 < x < 0.18$, a ferromagnetic metal for the range $0.18 < x < 0.5$, and an antiferromagnetic insulator for $0.5 < x < 1.0$.[133] Curie temperatures for the ferromagnetic phase range from 160-250 K, while the Neel temperature of the antiferromagnetic phase increases sharply as the La-content incrases from 123 K at $x = 1$ to as high as 260 K at $x = 0.65$.[133] Although the magnetic phase diagram just described may grant us considerable insight into the effects of significant La-doping of the $CaMnO_3$ layer, it tells us very little about any alloyed layer at the interface. It is clear, however, that the system we have selected requires considerably more intermixing to induce ferromagnetism that that of the $CaRuO_3/CaMnO_3$ system. La-doping of the $CaMnO_3$ sufficient to induce ferromagnetism will be easily observable in transmission electron microsopy as well as X-ray absorption and EELS spectra. Far more important, however, is the potential for a magnetic $La_{1-x}Ca_xNi_{1-x}Mn_xO_3$ state, and such an alloy must be fabricated and characterized magnetically as well.

Therefore, in this work we attempt to induce ferromagnetism in $LaNiO_3/CaMnO_3$ superlattices and to tune the ferromagnetism through modulation of the $LaNiO_3$ layer thickness and conducting state. If interfacial ferromagnetism indeed results from the leakage of highly mobile electrons into the $CaMnO_3$ layer, a decrease in the number of electrons leaking into the $CaMnO_3$ layer will destroy the double exchange based ferromagnetism among Mn ions. If, however, ferromagnetism results through intermixing, the metal insulator transition should have no effect on the magnetic alloy at the interface. Therefore, we have grown and characterized high quality (n,m) superlattices where n and m are the number of $LaNiO_3$ and $CaMnO_3$ unit cells per layer, respectively. The $LaNiO_3$ layer thickness, n, was varied from 2-9 unit cells while the $CaMnO_3$ layer thickness was set at 8, 14, and 20 unit cells to test the effects of increased $CaMnO_3$ thickness. Although for most samples the number of superlattice repetitions was 8, several examples of 6 or 10 repitition superlattices were also fabricated to examine the effect of altered film thickness at constant periodicity. The $LaNiO_3/CaMnO_3$ superlattices were grown by pulsed laser deposition with a KrF excimer laser at 700 °C in 4 Pa of O_2 on (100) oriented $LaAlO_3$ substrates.

7.2 Superlattice Structure and Quality

As with other samples throughout this dissertation, the quality of our $LaNiO_3/CaMnO_3$ superlattices was characterized using atomic force microscopy, X-ray reflectometry, and X-ray diffraction. Since the abruptness of the interfaces is extremely important in this case, scanning transmission electron microscopy was also employed. Finally, since this is the first time, as far as we are aware, that a $LaNiO_3/CaMnO_3$ heterostructure has been fabricated, it is critical to ensure that we are obtaining the expected stoichiometry and valence states. To

that end, electron energy loss spectrometry and extensive X-ray absorption measurements were performed to precisely determine the B-site valences.

Atomic force micrographs show extremely smooth terraced films with typical RMS roughnesses of 0.13-0.14 nm, on the order of half a unit cell, as shown in Figure 7.1(a). Even more encouraging is the fact that the significant majority of the detected surface roughness results from the terraces. If the roughness is measured on an area confined to a single terrace, it is reduced significantly and may be as low as a quarter of a unit cell. Thus, from a surface morphology standpoint, the superlattices are as close to ideally flat as possible. X-ray reflectometry confirmed the existence of both highly abrupt interfaces and precisely controllable layer thicknesses. A representative XRR of a $(6,8)_{10}$ sample can be seen in Figure 7.1(b). The high frequency fringes correspond to the total thickness while the larger low frequency peaks correspond to the superlattice Bragg reflections. This spectrum is very well fit by a model with an interfacial roughness of 0.18 nm, suggesting very little mixing at the interface. The slight disagreement between AFM and X-ray reflectivity roughness may be a result of the larger sample size of the X-ray beam, which extends in a line across the majority of the sample. Across such a large range, even minute variations in thickness may still have a noticeable effect. Agreement between the expected total (53 nm) and measured (54.3 nm) superlattice thicknesses is within the expected error of the measurement, indicating that the deposited layer thicknesses closely match the intended value.

X-ray diffraction θ-2θ scans of superlattices revealed high quality growth in the expected (100) orientation, with multiple visible superlattice peaks, as shown in Figure 7.1(c). In addition, ω rocking curves were used to characterize the mosaic spreads of single layer $LaNiO_3$ and $CaMnO_3$ films and were normalized to the substrate mosaic spread. We found that both $CaMnO_3$ films and $LaNiO_3$ films deposited at the same conditions as the superlattices had normalized mosaic spreads ($\Delta\omega_{film}/\Delta\omega_{LaAlO_3}$) between 1.7-2.3, indicating high quality growth. Finally, we evaluated the strain state of the films using reciprocal lattice maps of the (301) reflection, which showed both the $CaMnO_3$ and $LaNiO_3$ films to be strained to the substrate, as shown in Figure 7.1(d).

To probe structural quality and interfacial abruptness more directly, we performed cross sectional high resolution scanning transmission electron microscopy (STEM) on a (6,8) superlattice, for which a typical image may be seen in Figure 7.2. In the Z-contrast image shown in Figure 7.2, the majority of the contrast originates in the A-site cations La and Ca. STEM shows that we have fabricated high quality films with excellent epitaxial registry across interfaces. Although small local variations in layer thickness are observed, the results are consistent with expected thicknesses determined through XRR measurements. Thus, Z-contrast imaging shows that the interfaces are atomically smooth and very abrupt, with at most a single unit cell of intermixing at the interface. At the same time, we performed high-resolution electron energy loss spectroscopy (EELS) on the Mn $L_{3,2}$ edge to probe for spatial variation in the Mn valence state that would suggest ferromagnetism induced by intermixing. The Mn valence was determined using both constrained multiple linear least squares fitting and $L_{3,2}$ peak heights, yielding oxidation states of $4^+ \pm 0.3^+$ and $3.75^+ \pm 0.2^+$, respectively.[146, 129] Neither technique showed a statistically significant difference in valence between Mn at the interface and in the middle of the $CaMnO_3$ layer, suggesting very little modification of the Mn valence through La-doping of the $CaMnO_3$ at the interface. Although a slight Mn valence modification through leakage of Ni e_g electrons cannot be

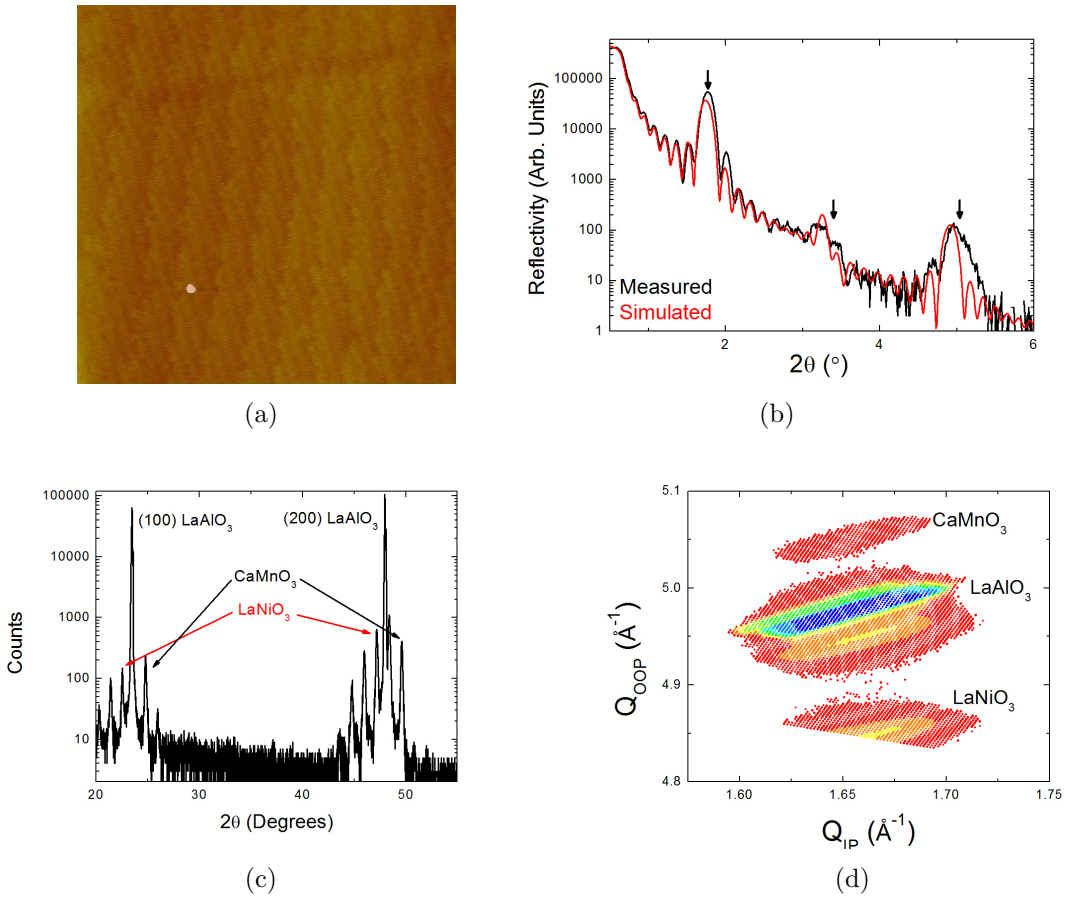

Figure 7.1: a) 5 micron atomic force micrograph showing smooth atomic terraces on the film surface. b) X-ray reflectivity and theoretical fit of a $(6,8)_{10}$ film showing total thickness fringes as well as first, second, and third order superlattice reflections (marked by arrows). c) X-ray diffraction scan of a (6/14) sample showing substrate, film, and superlattice peaks. d) Reciprocal lattice map of the (301) reflection of a typical (6/20) superlattice.

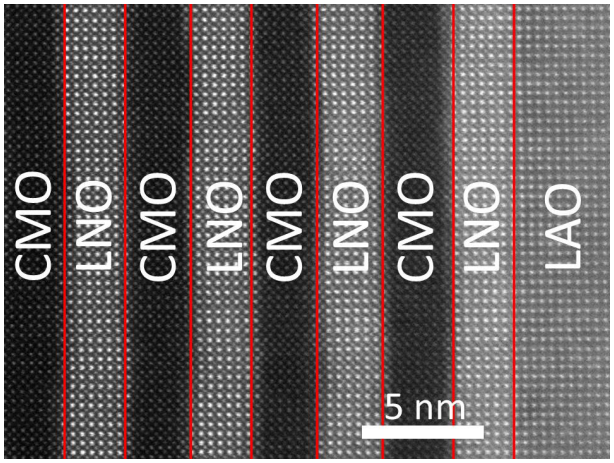

Figure 7.2: High resolution STEM Z-constrast image of a (6/8) superlattice.

detected to within the error of the EELS measurements, we can eliminate a ferromagnetic $La_xCa_{(1-x)}MnO_3$ phase ($0.5 < x < 1$ corresponding to a Mn valence $\leq 3.5+$). Thus, it is very unlikely that La-doping significant enough to induce ferromagnetism has occurred.[133]

Finally, to precisely confirm the Mn and Ni valence states, we performed X-ray absorption spectroscopy at beamline 4.0.2 and 6.3.1 at the Advanced Light Source. Measurements were performed in total electron yield mode at 20K. In order to establish the Mn valence, we examined three key features of the Mn L-edge spectra. First, it has been shown empirically that the relative ratio of the L_3 and L_2 peak energy values as well as the relative ratio of the L_3 and L_2 peak areas can be correlated with Mn valence.[142, 134, 153] We find a typical area ratio of approximately 1.94, corresponding to an average Mn valence between 3.9+ and 4.0+. Secondly, a Mn^{4+} X-ray absorption spectra is expected to show a clearly defined doublet.[121] We see signatures of multiplet splitting in the X-ray absorption lineshape of superlattices sample on spectra from both beamline 4.0.2 and 6.3.1- although much more distinctly in spectra taken at BL 4.0.2 which has an elliptically polarizing undulator and high resolution monochromator as opposed to the bending magnet of 6.3.1. The lineshape and magnitude of the observed multiplet splitting is in excellent agreement with a valence that is very near 4+. The Mn^{4+} valence requires a multiplet splitting feature separated from the main L_3 peak by 2.5 eV, precisely what we observe in high-resolution X-ray absorption measurements on beamline 4.0.2.[121] Finally, Mn valence may be characterized by the splitting between the L_3 and L_2 peaks. A Mn^{4+} valence is expected to have a splitting near 10.0 eV while a Mn^{3+} valence will show a splitting of 10.8 eV.[142] A typical spectra taken at BL4.0.2 which highlights these features is shown in Figure 7.3(a). The precision with which the spectra match the expected features of a 4+ Mn valence allow us to establish an average Mn valence of $4+ \pm 0.05+$, although without the spatial resolution of STEM/EELS. This does not, however, preclude a small amount of electron leakage at the interface, predicted by Nanda et al. to result in a valence of $Mn^{3.93+}$ in the interfacial layers of $CaRuO_3/CaMnO_3$ superlattices.[109]

With respect to the Ni valence, it is more difficult to use the Ni X-ray absorption spectra to resolve small variations in the Ni valence as the La M edge overlaps with and distorts

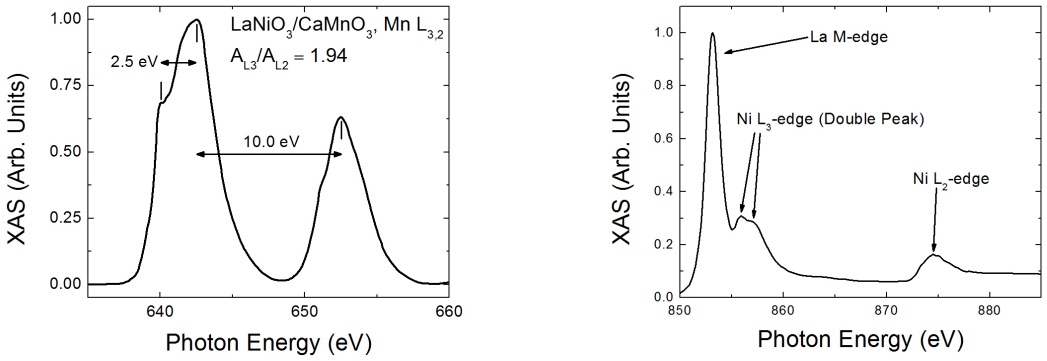

(a) (b)

Figure 7.3: a) Mn L-edge spectra for a typical (6,8) $LaNiO_3/CaMnO_3$ superlattice highlighting the signatures of Mn^{4+}. b) Ni L-edge spectra for a typical (6,8) $LaNiO_3/CaMnO_3$ superlattice. Despite overlap with the La M-edge, clear signatures of Ni^{3+} are observable.

the Ni L_3 edge. Thus, if there are small deviations of the Ni valence from 3+, it would be very difficult to extract them. However, we have achieved sufficient resolution to observe general signatures of Ni-valence, such as a double peak on the L_3, that indicate excellent agreement with Ni^{3+}.[100, 37] Additionally, some groups have focused on the Ni L_2 edge, which is expected to display two distinct peaks in the Ni^{2+} configuration for valence determination.[100, 77, 37] We see no evidence of such a splitting, and the resolvable portion of the Ni L_3 edge also supports a Ni^{3+} configuration. However, a small deviation from the 3+ configuration may not be resolvable. A typical Ni L-edge (and partial La M-edge) appears in Figure 7.3(b).

Having carefully characterized the crystal structure, interface quality, and valence states of the $LaNiO_3$ superlattices, it appears that we have grown extremely high quality superlattices with atomically smooth interfaces and excellent crystalline registry. The valence states are precisely as expected, and indicate excellent stoichiometry and very little intermixing. The extremely high structural and interface quality as well as the agreement with bulk stoichiometry and valence made these samples ideal candidates for extensive magnetic characterization, in which it is preferable to identify the magnetic properties of specific ions and construct an accurate magnetic depth profile.

7.3 Magnetism and Conductivity

Of course, the high quality of the samples is of limited interest if the metal insulator transition is not realized or the desired magnetic properties do not emerge. Therefore we have performed transport measurements taken in the van der Pauw geometry to extract the resistivity as a function of temperature. ρ vs T curves in a range of 5-350 K show the expected thickness dependent metal insulator transition in the $LaNiO_3$ layers. Samples for which $n \geq 4$ were metallic. Assuming conduction only across the thickness of the $LaNiO_3$

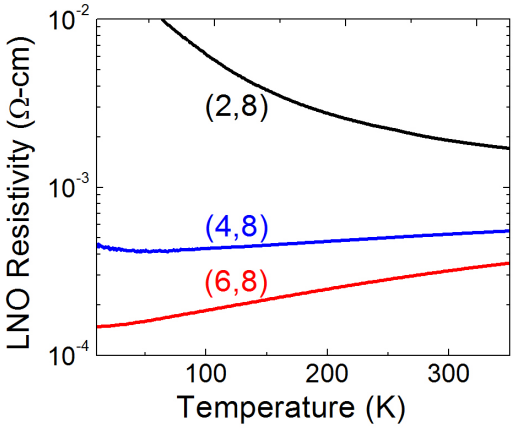

Figure 7.4: Resistivity vs. Temperature of a series of (n,8) superlattices

layers, we found the samples to have resistivities at 5K on the order of 1×10^{-4} Ω-cm. These values are in good agreement with other examples of PLD grown $LaNiO_3$.[98, 83, 132, 139] At $LaNiO_3$ thicknesses of n = 2, the samples are insulating, showing an exponential temperature dependence indicative of thermally activated hopping conduction. Measured resistivities were comparable to those reported for other $LaNiO_3$ films of similar thickness grown on (100) $LaAlO_3$. Figure 7.4 illustrates the transition, showing the conductivity of typical (2,8), (4,8), and (6,8) superlattices.

We used SQUID magnetometry to probe the bulk magnetic properties of the films. Magnetic moment vs. applied field measurements, taken at 10 K with ± 5 T fields applied parallel to the substrate surface (in-plane), show hysteretic loops indicative of ferromagnetism in superlattices where $n \geq 4$ but not in those where $n < 4$. Figure 7.5(a) shows magnetic moment vs. applied field for typical ferromagnetic (2,8), (4,8), (6,8) samples. For magnetization vs. temperature measurements, shown in Figure 7.5(b) samples were cooled to 10 K in a field of 1 T and magnetization measurements were taken while warming in a field of 0.01 T. The magnetization of ferromagnetic films exhibits linear, non-Curie-Weiss, temperature dependence with a clear T_C of 75-80 K while non-ferromagnetic $n < 4$ films show no indication of a transition. No magnetic transitions were observed between 160-260 K, the range of T_Cs expected for a ferromagnetic alloy of $La_xCa_{1-x}MnO_3$.[133] The temperature dependence is also different from that expected from isolated ferromagnetic clusters in the $CaMn_3$ layer.[97] Thus, on the basis of temperature dependence alone we may eliminate most conventional sources of ferromagnetism in the superlattices. Assuming a model with a single magnetic monolayer of $CaMnO_3$ at the interface, we we find that the n = even FM films saturated to approximately 0.5 μ_B per interfacial Mn while the n = odd FM films saturated to approximately 1.0 μ_B. Figure 7.5(c) shows the remarkable difference in saturated moments between n = odd and n = even films. Saturated magnetic moment was independent of $CaMnO_3$ thickness, as demonstrated in Figure 7.5(d) by a comparison of similar ferromagnetic (6,8), (6,14), and (6,20) films, which all saturate at 0.5 μ_B per interfacial Mn. It is important to note when discussing the saturated magnetic moment of these superlattices that the small signals associated with interfacial ferromagnetism make extrinsic contributions to the mea-

sured magnetic moment a serious concern. Although paramagnetic contamination of the substrate was not observed in the $SrTiO_3$ substrates in chapter 6, the $LaAlO_3$ substrates used here do exhibit just such an effect. To address this, as discussed in Chapter 2.4.1, we have fit the background using the expected field dependence of an ideal paramagnetic signal and subtracted it from the final measurement. The paramagnetic contamination appears to be extremely consistent across substrates, and normalizing the expected contamination signal for substrate volume generally produced an excellent background subtraction. Of course, the accuracy of a saturated magnetic moment determined in this way is somewhat suspect. Consequently we have used both X-ray magnetic circular dichroism and polarized neutron reflectometry measurements to confirm the magnitude of the ferromagnetic signal and determine its origin. Finally, we found that increased superlattice thickness for larger m results in a larger coercive field, which may be a result of an increase in antiferromagnetic material pinning the ferromagnetic domains or a slight roughening of the superlattice with increasing overall film thickness.

As with all weak ferromagnetic signals, contamination must be eliminated as a potential source. We note that only one temperature dependent magnetic transition is observed in magnetization vs. temperature scans. Additionally, no hysteresis is observed at temperatures above 80 K, well below the expected T_Cs of contaminants such as iron. Finally, we deposited an alloyed film of $La_{0.5}Ca_{0.5}Ni_{0.5}Mn_{0.5}O_3$ on $LaAlO_3$ and characterized it magnetically using SQUID magnetometry under the same conditions as the superlattice measurement. We found no evidence for ferromagnetism in the alloyed film, suggesting that any magnetism present is much too weak to explain the observed effects in superlattice films.

The most important observation, apart from the emergence of ferromagnetism, is the coincident disappearance of ferromagnetism as the thickness of the $LaNiO_3$ layer is decreased and the LNO layer becomes insulating. This correlation is a strong indication that the ferromagnetism is closely tied to the metallicity of the $LaNiO_3$ layer. We theorize that mobile electrons in the Ni^{3+} e_g band extend into the interfacial $CaMnO_3$ and mediate ferromagnetism in the form of a double exchange interaction. As the $LaNiO_3$ thickness is decreased, the Ni electrons are localized and no longer extend into the $CaMnO_3$ layer. Thus the mechanism that mediates ferromagnetic ordering is destroyed and the ferromagnetism disappears.

7.4 Probing the Magnetic Depth Profile

Having demonstrated that ferromagnetism emerges in $LaNiO_3/CaMnO_3$, we must now establish the interfacial nature of the magnetic response. The SQUID magnetometry results represent an excellent first step. The oscillatory dependence on the thickness of the $LaNiO_3$ layer is very reminiscent of the interfacial oscillation in $CaRuO_3/CaMnO_3$ superlattices. Additionally, the independence of the saturated moment from the $CaMnO_3$ thickness is suggestive of an interfacial interaction. However, X-ray magnetic circular dichroism and polarized neutron reflectometry will allow for a much more precise localization of the ferromagnetism.

First, to identify the magnetic ions, we obtained element specific magnetic information using X-ray magnetic circular dichroism measurements performed at beamline 6.3.1 of the Advanced Light Source. Measurements were performed in total electron yield mode at 20K.

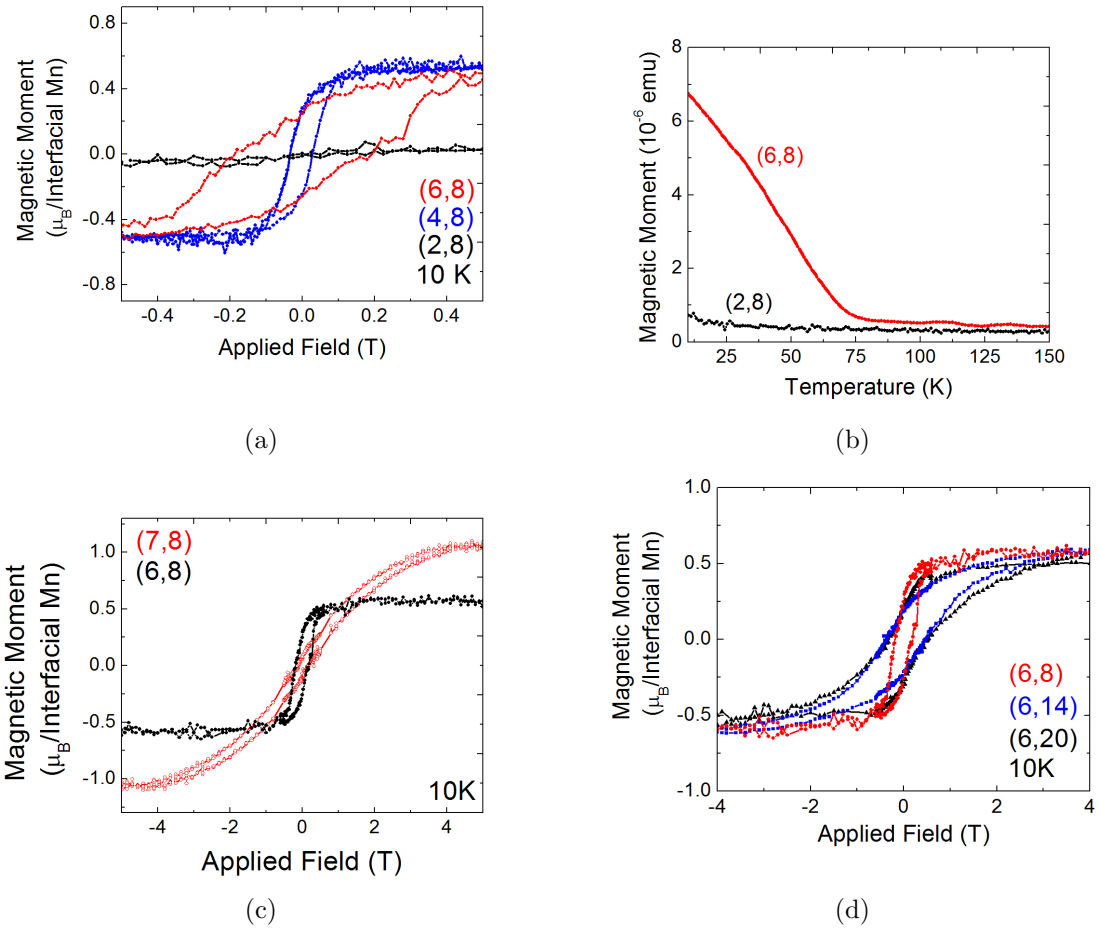

Figure 7.5: a) Magnetic hysteresis loops for a series of typical (2,8), (4,8), and (6,8) superlattices. b) Magnetic moment vs. temperature from 10-150 K. A ferromagnetic transition is observed between 75-80 K only in n $\geq$ 4 superlattices. c) Hysteresis loops for typical (6,8) and (7,8) superlattice illustrating the significant difference in saturated moments of n = even and n = odd samples. d) Magnetic hysteresis loops showing scaling of the magnetic moment with the number of interfaces rather than $CaMnO_3$ layer thickness.

The field was parallel to the direction of X-ray propagation and both were at a 30° angle of incidence to the in-plane direction of the film. The incident light was maintained at a constant circular polarization. XMCD was obtained from the difference in XA signal in ± 1.7 T applied along the direction to X-ray propagation. The difference signal was normalized to its sum to obtain the data shown in Figure 7.6(a). In this figure, the Mn $L_{3,2}$ X-ray absorption and raw dichroism signal normalized to the total X-ray absorption intensity of a (6,8) superlattice is displayed. As in chapter 6, we expect a significant reduction in the magnitude of the dichroism if the magnetism is localized to a buried interface. Also as in chapter 6, we may use a model in which only a single unit cell at the interface is ferromagnetic to calculate the expected magnitude. Figure 7.6(b) plots the Mn $L_{3,2}$ dichroism after it has been rescaled to the expected interfacial contribution to the X-ray absorption spectra, as calculated for an electron escape depth of 2.5 nm. Once normalized to the saturated moment measured using SQUID magnetometry, the magnitude of the $LaNiO_3/CaMnO_3$ superlattice dichroism is in excellent agreement with both the measured dichroism of $CaRuO_3/CaMnO_3$ superlattices as well as a $LaMnO_3$ film.

This agreement can be seen in Figure 7.6(c), which plots the integrated area under the XMCD curve as a function of electron escape depth for a typical $LaNiO_3/CaMnO_3$ sample, two $CaRuO_3/CaMnO_3$ superlattices, and a $LaMnO_3$ standard. All curves are rescaled to account for the interfacial nature of the magnetism and normalized to their saturation magnetization. As the expected saturation magnetization from a $LaMnO_3$ standard varies somewhat across the literature, Figure 7.6(c) shows an upper and lower bound for $LaMnO_3$. In this way, Figure 7.6(c) tests the validity of the interfacial model. If the magnetic moment measured through SQUID magnetometry is accurate, the scaled XMCD area normalized to saturation magnetization should be the same magnitude for all superlattices *and* the $LaMnO_3$ standard. The reader will note that there is excellent agreement between all samples and that the best agreement occurs at an electron escape depth of 2-3 nm, precisely the predicted probing depth in total electron yield mode. Alternatively we may state that, when properly scaled, XMCD shows the representative (6/8) $LaNiO_3/CaMnO_3$ to have half the magnetic polarization of a (3/4) $CaRuO_3/CaMnO_3$ superlattice, the same magnetic polarization as a a (3/5) $CaRuO_3/CaMnO_3$ superlattice, and approximately $^1/_4$ the magnetic polarization of a $LaMnO_3$ film. This is in precise agreement with both our SQUID measurements and the literature. Thus, the model of a single ferromagnetic unit cell of $CaMnO_3$ at the interface accurately represents the magnitude of the X-ray magnetic circular dichroism and confirms the saturated moments measured by SQUID magnetometry. In contrast, explaining the observed dichroism with a model in which the magnetism is evenly distributed through the $CaMnO_3$ layers results in a magnetic moment much lower than what we observe through SQUID magnetometry. The Mn X-ray magnetic circular dichroism is in excellent agreement with an interfacial model, not a bulk ferromagnetic system.

We must also establish whether or not the Ni ions are contributing to the magnetism. We do not observe any XMCD signal at the Ni $L_{3,2}$ edges, thus indicating that, to within experimental resolution, there is no magnetic response associated with the Ni ions in $LaNiO_3$. This shows not only that there is no ferromagnetism originating in the Ni ions, but also that any paramagnetic contribution to the magnetization by the $LaNiO_3$ is so small it is likely undetectable through SQUID magnetometry. Because the rapid shifts in intensity around the La M-edge and Ni L_3 edge create a fairly noisy XMCD spectra, we will focus on the

smoother L_2 edge, which is plotted along with the observed dichroism in Figure 7.6(d). As is clearly shown, no dichroism can be resolved and these observations conclusively demonstrate a magnetic response occurring only in the $CaMnO_3$ layers.

To more precisely probe the magnetic depth profile, we performed PNR on a (5,8) sample using the Asterix beamline at Los Alamos National Lab. The superlattice was cooled to 15 K in a 0.7 T magnetic field applied in the plane of the sample. Incident neutrons were polarized to be spin-up or spin-down with respect to this field. The specular reflectivity of spin-polarized neutrons is dependent on the depth profile of the nuclear composition and the depth profile of the sample magnetization component parallel to the applied field. Thus, sample magnetization manifests as a splitting of the spin-up and spin-down reflectivities. Such splitting is evident in Figure 7.7(a), which shows the spin-dependent reflectivities as functions of wavevector transfer along the surface normal (Q_Z) near the 1st order superlattice Bragg reflection. The measured reflectivity in Figure 7.7 is scaled by the theoretical reflectivity of the $LaAlO_3$ substrate. The PNR data were then fitted using the Refl1D software package.[71] Figure 7.7(b) shows a model with periodic ferromagnetism in the superlattice which is consistent with the data.

Constraints imposed by atomic force microscopy, XMCD, and XRR measurements require a model in which intermixing is limited to less than 2 Å, all magnetism originates in the $CaMnO_3$ layer, and layer thickness and nuclear scattering length density are within 10% of expected values. Using this model, we find that only a magnetic depth profile in which the magnetization is confined to within one unit cell of the interface can reproduce the observed spectrum. As shown in Figure 7.7, the calculated reflectivity corresponding to this model accurately reproduces the spin-dependent Bragg reflection. All other possible thicknesses of the ferromagnetic layer (2-4 unit cells) result in a reversal of the splitting on the first superlattice Bragg reflection. We conclude therefore that the ferromagnetism in the $CaMnO_3$ layer is confined to one unit cell at the interface.

7.5 Discussion and Concluding Thoughts

In this chapter, we have demonstrated interfacially confined ferromagnetism in $LaNiO_3$ / $CaMnO_3$ superlattices and will now address alternative explanations of the magnetism. Intermixing induced ferromagnetism would be expected to persist through the $LaNiO_3$ metal-insulator transition, while an interfacial effect in which mobile electrons from the $LaNiO_3$ mediate ferromagnetism in the $CaMnO_3$ would be expected to be closely tied to the $LaNiO_3$ conducting state. Intermixing induced ferromagnetism would also be expected to increase with thicker $CaMnO_3$ layers due to the greater deposition time resulting in increased intermixing. However, no such effect is observed. TEM and EELS show no evidence of intermixing at the levels required to induce a ferromagnetic moment.[133] Similarly, PNR and XMCD measurements explicitly rule out uniform magnetization of $CaMnO_3$ that might arise from oxygen vacancies or other defects. The T_Cs of the materials are also inconsistent with both La-dopant and defect induced ferromagnetism in $CaMnO_3$, which are expected to exhibit T_Cs of at least 160-260K and 130K, respectively.[110, 133] The observed saturated magnetic moments are much too strong to be consistent with defect induced ferromagnetism such as that observed in $CaMnO_3$ nanoparticles.[97] In any case, magnetism arising throughout the

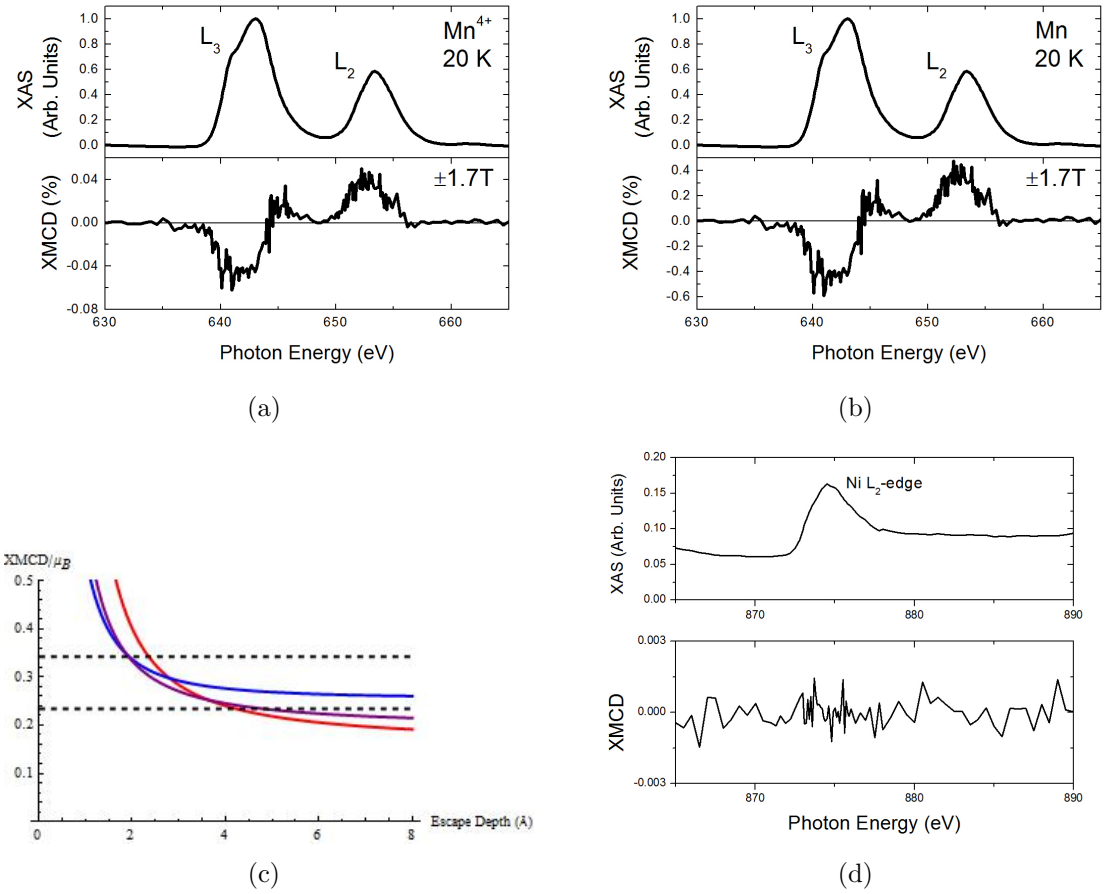

Figure 7.6: a) Mn L-edge X-ray absorption and XMCD of a typical (6/8) $LaNiO_3$ superlattice. The X-ray absorption linshape is in excellent agreement with a Mn^{4+} state and indicates that the Mn^{3+} contribution must be at most 5%. The Mn XMCD linshape is also in excellent agreement with examples in the literature of Mn^{4+} XMCD b) Rescaling of the XMCD signal to reflect the interfacial nature of the ferromagnetism, as in Chapter 6.6 c) Plot comparing the area of rescaled Mn $L_{3,2}$ XMCD curves of the (6/8) $LaNiO_3/CaMnO_3$ superlattice with a $LaMnO_3$ standard as well as the $CaRuO_3/CaMnO_3$ samples shown in Chapter 6.6 as a function of electron escape depth. Note the excellent agreement at the theoretically expected scattering length of 2-3 nm. d) Ni L_2 edge X-ray absorption and XMCD showing no discerable dichroism. This indicates not only a lack of ferromagnetism in the Ni ions, but also a very weak paramagnetic response. All measurements shown were taken at 20 K and (for XMCD) at fields of ± 1.5 T.

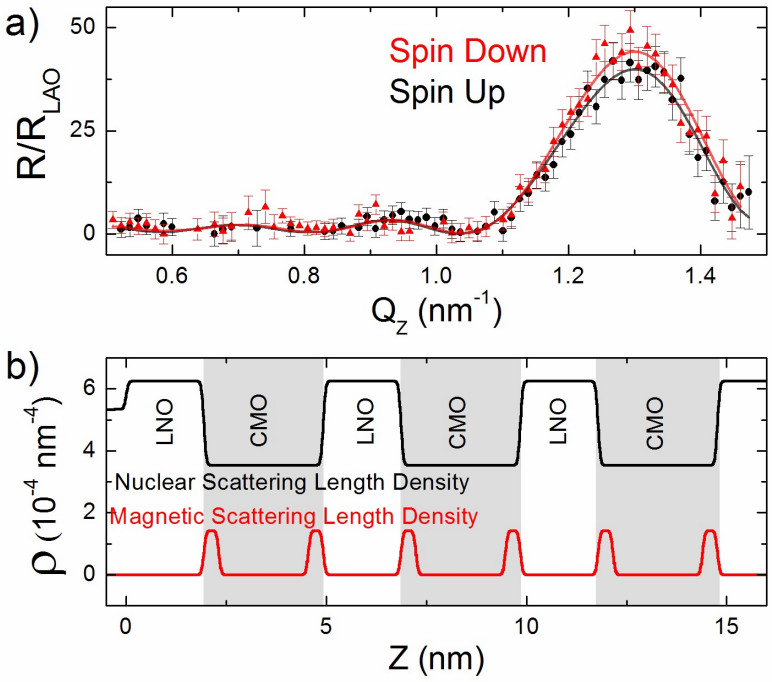

Figure 7.7: (color online) a) Fitted polarized neutron reflectivity with standard error at 800 mT and 15 K at the first order superlattice reflection of a (5,8) superlattice. b) We show below the model used to obtain this fit, in which we assume one unit cell of magnetized $CaMnO_3$.

$CaMnO_3$ layer must scale with the $CaMnO_3$ thickness, which we do not observe.

Therefore we believe that the only remaining explanation is that of an interfacial magnetic interaction between the $LaNiO_3$ and $CaMnO_3$ which results in 1 unit cell thick ferromagnetic layers as indicated by the PNR measurements. Such an exchange mechanism is likely analogous to that shown in $CaRuO_3/CaMnO_3$ superlattices, in which it has been proposed that mobile electrons from $CaRuO_3$ mediate canted ferromagnetism in the $CaMnO_3$.[145, 109, 53] In this model, mobile Ni e_g electrons leak into the first unit cell of the adjacent $CaMnO_3$ layer, facilitating double exchange among the Mn ions. Unlike ferromagnetism corresponding to intermixing, such a small electron leakage is expected to result in only a very slight reduction of the Mn valence similar to that predicted for $CaRuO_3/CaMnO_3$.[109] This change is unlikely to be detected by either X-ray absorption or EELS measurements. A transition of the $LaNiO_3$ to an insulating, potentially antiferromagnetic state in the superlattices with thin $LaNiO_3$ layers results in localization of the electrons, a reduction in leakage, and the loss of the interfacial ferromagnetism.

Finally, the saturated magnetic moment of the superlattice oscillates as a function of LNO layer thickness. Since we do not observe a similar effect as the thickness of the CMO layers is varied for fixed LNO layer thickness, it is likely that the coupling occurs through the LNO layer. Although such a coupling could be described in terms of a RKKY-type interaction, it may also be an indication of a spin-density wave in the LNO.[45, 132] Indeed, despite the fact that the electron mean free path in LNO (> 31 Å) is long enough to support an RKKY interaction across the thickness of the LNO layers, the expected oscillation period (~ 3 nm) calculated from the resistance and Fermi velocity is significantly larger than the observed period of 2 unit cells.[11, 96] A modulation of the LNO spin-density with a much smaller period (2-5 unit cells) has been suggested in $LaNiO_3/LaMnO_3$ superlattices, where Ni spins are theorized to become polarized at the interface due to interactions with the Mn. This explanation more closely matches our observations.[45] It is possible that in this case, the Ni spins in the middle of the layer tend to be antiparallel to those at the interface, which can result in either a very small net magnetic moment or no net moment.[45]

In conclusion, we have demonstrated ferromagnetism in $LaNiO_3/CaMnO_3$ superlattices that can only be explained in terms of an interfacial double exchange interaction. We find that $LaNiO_3$ undergoes a metal-insulator transition as the $LaNiO_3$ layer thickness is decreased. We observe ferromagnetism with a T_C of 70 K in the conducting superlattices but not in the insulating ones. We believe that a preponderance of evidence from SQUID magnetometry, XMCD, and PNR points to the ferromagnetism originating in one unit cell of $CaMnO_3$ at the interface. In particular, the strong dependence of the ferromagnetism on the conducting state of $LaNiO_3$ is indicative of an interfacial double exchange interaction mediated by the $LaNiO_3$ e_g band. Although the mechanism for controlling the ferromagnetic state is, at this point, a thickness dependence that must be determined at the time of fabrication, it is our hope that in the near future it will be possible to utilize other parameters. An excellent stepping stone to this goal can be found in other rare-earth nickelates, which have temperature-dependent metal-insulator transitions. Even more exciting is the potential for room temperature functionality. Although $CaMnO_3$ has a Neel temperature of 123 K which most likely represents the upper limit to magnetic ordering in the system, other antiferromagnetic such as $LaFeO_3$ with a $t_{2g}^3 e_g^2$ electronic configuration have much higher Neel temperatures and are excellent candidates for magnetic interactions mediated by a donated

Ni e_g electron. One can easily imagine a system in which a superlattice of (Sm,Nd)NiO_3 is tuned to have a metal-insulator transition of 300 K and combined with $LaFeO_3$ to realize a room temperature effect. The results discussed in this dissertation are an important step toward this result.

Chapter 8

Summary and Outlook

Throughout this work, we have emphasized the importance of better understanding the interrelationship between the many competing types of order and disorder in transition metal complex oxides. In these systems, where electron localization, mixed valences, and complex structural distortions already coexist in the bulk, we have intentionally added tuning parameters such as interfaces and epitaxial strain. In addition, oxide thin film deposition commonly introduce defects and stoichiometric variations. As the entire field moves towards the development of oxide heterostructure devices that combine emergent magnetic phenomena with electronic control and room temperature functionality, one of the most consistent challenges is our limited understanding of the parameters that control the sharp deviations from bulk behavior in thin films, heterostructures, and superlattices. To that end, it is critical to develop methods by which we may isolate and control the effects of parameters such as strain and electronic reconstruction independently.

In this work, we performed an exhaustive analysis of the effects of strain on $SrRuO_3$ thin films. We found a tunable saturated magnetic moment, tunable Curie temperatures, and completely tunable reversible uniaxial anisotropy. We also induced a transition to a high-spin Ru *and* a low-spin nonmagnetic Ru state. Just as importantly, we traced origins of these effects to the epitaxial strain through changes in bonding, orbital magnetic moment, and the density of states at the Fermi level. Although there is considerable work remaining before a complete understanding of the distortion in these films is attained, this work represents a large step forward in the control of magnetic properties using epitaxial strain. By using $SrRuO_3$ as a model system, it may be possible to tune the magnetic moment, anisotropy, or spin state of many other systems in the future.

There are a number of remaining opportunities for better understanding the detailed and complex interactions between strain, electronic structure, and the magnetic ground state. The most promising of these are X-ray diffraction studies that reveal the true unit cell of the coherently strained and partially relaxed films, especially those of (111) oriented films on $SrTiO_3$. These investigations require very extensive mapping of reciprocal space, but are fairly straighforward and likely to be successful. The alternative technique of Rietveld analysis would yield much more extensive information on atomic positions, bond lengths, and bond angles which would be invaluable in modeling the electronic structure of the system. Although it is known to be very difficult to achieve sufficient signal strength to apply Rietveld analysis to thin films, the potential insights in this case make it worth the attempt. Finally,

if there is a strain gradient along the growth axis of partially relaxed films, this is very likely to result in a gradient in the magnetization as well. The application of polarized neutron reflectometry may be helpful in establishing such a dependence and would yield additional information about the various competing magnetic states.

In the $CaRuO_3/CaMnO_3$ system, this work showed conclusively that it is possible to create an interfacial magnetic state confined to a single unit cell of $CaMnO_3$. We also explored the magnetic coupling mechanisms, exposing antiferromagnetic coupling through the paramagnetic $CaRuO_3$ layer and revealing potential mechanisms for the stabilization of an oscillatory magnetic moment with a 2 unit cell oscillation period. We explored the underlying structural half-order of $CaRuO_3/CaMnO_3$ systems, finding a significant difference in the orthorhombic distortion present in "even" and "odd" samples. It is entirely possible that, coupling through the long range antiferromagnetic order, the difference in structural distortions is responsible for the modulation of the saturated magnetic moment. This represents an opportunity for advancing our understanding of magnetic exchange through an interfacial double exchange interaction. Clearly, on such small scales the effects of structural distortions and antiferromagnetic coupling cannot be neglected, as they may have a significant impact on the final magnetic ground state.

Further investigation is warranted. Characterization of the orthorhomic distortion additional samples with $CaMnO_3$ layer thicknesses ranging from 6-12 unit cells thick must be measured to confirm the results of the 4-5 unit cell samples. Additionally, the dependence of the oscillatory magnetic moment on the $CaRuO_3$ layer thickness must be investigated, as it remains to be seen whether the total number of unit cells per superlattice layer is the controlling parameter as opposed to the number of unit cells per $CaMnO_3$ layer. We have already grown a sample for which the thickness of both the $CaRuO_3$ and $CaMnO_3$ layers is 4 unit cells each, which will hopefully answer this question in the near future.

We next utilized the principles of interfacial double exchange in the $CaMnO_3$/ $CaRuO_3$ system to induce ferromagnetism in a single unit cell of $CaMnO_3$ at the interface in $LaNiO_3$ / $CaMnO_3$ superlattices. By tying the ferromagnetism to the conducting state of the $LaNiO_3$ layers, we showed conclusively that interfacial double exchange rather than intermixing is responsible for the ferromagnetism in these system. Furthermore, we demonstrated a remarkable new mechanism for controlling ferromagnetism at an interface. Although the metal-insulator transition in $LaNiO_3$ films is thickness dependent, many other rare-earth nickelates are excellent candidates for similar interfacial ferromagnetic states. These alternative materials have temperature dependent metal-insulator transitions, some of which extent to room temperature. This represents an excellent model for attaining room-temperature functionality.

There is much more work to be done in studying magnetism at the interface between a paramagnetic metal and antiferromagnetic insulator. In this thesis we proposed that the oscillation of the saturated magnetic moment in $LaNiO_3/CaMnO_3$ superlattices was due to a spin density wave in the $LaNiO_3$ layer, as has been reported in other studies of the $LaNiO_3$ system. First principles calculations would greatly aid our investigation of this phenomena, as would increasing the thickness of the $LaNiO_3$ layer until the oscillation dies away. We have not yet achieved such thicknesses. Finally, it is highly desireable to show both an interfacial ferromagnetic and a nonmagnetic state in a single sample. To acheive this goal, we propose the incorporation of other rare earth nickelates into $CaMnO_3$-based superlattices. It has

been shown that there is a tunable temperature dependent metal insulator transition in such rare-earth nickelate alloys. If a magnetic state can be achieved in such a system, it should be possible to activate and deactivate the emergent ferromagnetism at a tunable temperature.

It is our hope that this work has convinced the reader of the importance of carefully examining and separating out the many possible parameters that can contribute to emergent phenomena in transition metal complex oxides. In the next decade, it is highly likely that more and more heterostructure devices based on these oxides will become practical for electronic applications, but only if a better understanding of the underlying physics is achieved.

Bibliography

[1] C. H. Ahn, R. H. Hammond, T. H. Geballe, M. R. Beasley, J.-M. Triscone, M. Decroux, O. Fischer, L. Antognazza, and K. Char. Ferroelectric field effect in ultrathin $SrRuO_3$ films. *Applied Physics Letters*, 70:206, 1997.

[2] P. B. Allen, H. Berger, O. Chauvet, L. Forro, T. Jarlborg, A. Junod, B. Revaz, and G. Santi. Transport properties, thermodynamic properties, and electronic structure of $SrRuO_3$. *Physical Review B*, 53:4393, 1996.

[3] E. Arenholz and M. Liberati. Personal communication. 2009.

[4] Neil W Ashcroft and N David Mermin. Solid state physics, 1976.

[5] Julie A Bert, Beena Kalisky, Christopher Bell, Minu Kim, Yasuyuki Hikita, Harold Y Hwang, and Kathryn A Moler. Direct imaging of the coexistence of ferromagnetism and superconductivity at the $LaAlO_3/SrTiO_3$ interface. *Nature physics*, 7(10):767–771, 2011.

[6] J. S. Bettinger, C. Piamonteze, R. V. Chopdekar, M. Liberati, E. Arenholz, and Y. Suzuki. Room-temperature photomagnetism in the spinel ferrite $(Mn,Zn,Fe)_3O_4$ as seen via soft x-ray magnetic circular dichroism. *Phys. Rev. B*, 80:140413, Oct 2009.

[7] A. Bhattacharya, S. J. May, S. G. E. te Velthuis, M. Warusawithana, X. Zhai, B. Jiang, J.-M. Zuo, M. R. Fitzsimmons, S. D. Bader, and J. N. Eckstein. Metal-insulator transition and its relation to magnetic structure in $(LaMnO_3)_{2n}/(SrMnO_3)_n$ superlattices. *Physical Review Letters*, 100:257203, 2008.

[8] Ariadna Blanca-Romero and Rossitza Pentcheva. Confinement-induced metal-to-insulator transition in strained $LaNiO_3/LaAlO_3$ superlattices. *Physical Review B*, 84(19):195450, 2011.

[9] Murtaza Bohra, CP Wu, HJ Yeh, YH Cheng, CC Peng, and H Chou. Role of Ru vacancies in the magnetism of strain relaxed $SrRuO_3$ films on $srtio_3$ substrates. *Journal of Applied Physics*, 109(7):07D728–07D728, 2011.

[10] JA Borchers, BJ Kirby, and CF Majkrzak. Polarized beam reflectometer. page http://ncnr.nist.gov/instruments/ng1refl/, Retrieved 2013.

[11] A. V. Boris, Y. Matiks, E. Benckiser, A. Frano, P. Popovich, V. Hinkov, P. Wochner, M. Castro-Colin, E. Detemple, V. K. Malik, C. Bernhard, T. Prokscha, A. Suter, Z. Salman, E. Morenzoni, G. Cristiani, H.-U. Habermeier, and B. Keimer. Dimensionality control of electronic phase transitions in nickel-oxide superlattices. *Science*, 20:937, 2011.

[12] J Briatico, B Alascio, R Allub, A Butera, A Caneiro, MT Causa, and M Tovar. Double-exchange interaction in electron-doped $CaMnO_{3-\delta}$ perovskites. *Physical Review B*, 53(21):14020, 1996.

[13] D. Briggs and M. P. Seah. *Practical surface analysis Vol. 1: Auger and X-ray photoelectron spectroscopy*. Wiley, Chichester, 1990.

[14] M.E. Brubaker, J.E. Mattson, C.H. Sowers, and S.D. Bader. Oscillatory interlayer magnetic coupling of sputtered Fe/Mo superlattices. *Applied Physics Letters*, 58:2306, 1991.

[15] P. Bruno. Physical origins and theoretical models of magnetic anisotropy. *Ferienkurse des Forschungszentrums Julich, Julich*, 1993.

[16] S. N. Bushmeleva, V. Yu. Pomjakushin, E. V. Pomjakushina, D. V. Sheptyakovand, and A. M. Balagurov. Evidence for the band ferromagnetism in $SrRuO_3$ from neutron diffraction. *Journal of Magnetism and Magnetic Materials*, 305:491, 2006.

[17] G. Cao, S. McCall, M. Shepard, J.E. Crow, and R.P. Guertin. Thermal, magnetic, and transport properties of single-crystal $Sr_{1-x}Ca_xRuO_3$ ($0< x < 1.0$). *Physical Review B*, 56:321, 1997.

[18] P. Carra, B.T. Thole, M. Altarelli, and X. Wang. X-ray circular dichroism and local magnetic fields. *Physical Review Letters*, 70:694, 1993.

[19] Y. J. Chang, J. I. Kim, and C. U. Jung. Electrical properties of $SrRuO_3$ thin films with varying c-axis lattice constant. *Journal of Magnetics*, 13(2):31–64, 2008.

[20] E. Chason and T.M. Mayer. Thin film and surface characterization by specular x-ray reflectivity. *Critical Reviews in Solid State and Materials Science*, 22:1, 1997.

[21] Peter P Chow. Molecular beam epitaxy. *Academic Press, Inc., Thin Film Processes II(USA), 1991,*, pages 133–175, 1991.

[22] H. M Christen and G. Eres. Recent advances in pulsed-laser deposition of complex oxides. *Journal of Physics: Condensed Matter*, 20:264005, 2008.

[23] J. M. D. Coey. *Magnetism and Magnetic Materials*. Cambridge University Press, New York, New York, 2010.

[24] B.D. Cullity and S.R. Stock. *Elements of X-ray Diffraction*. Prentice Hall, Upper Saddle River, New Jersey, 2001.

[25] B. Dabrowski, O. Chmaissem, P. W. Klamut, S. Kolesnik, M. Maxwell, J. Mais, Y. Ito, , B. D. Armstrong, J. D. Jorgensen, and S. Short. Reduced ferromagnetic transition temperatures in $SrRu_{1-v}O_3$ perovskites from Ru-site vacancies. *Physical Review B*, 70:014423, 2004.

[26] B Dabrowski, O Chmaissem, PW Klamut, S Kolesnik, M Maxwell, J Mais, Y Ito, BD Armstrong, JD Jorgensen, and S Short. Reduced ferromagnetic transition temperatures in $SrRu_{1-c}O_3$ perovskites from Ru-site vacancies. *Physical Review B*, 70(1):014423, 2004.

[27] Jean Daillant and Alain Gibaud. *X-ray and neutron reflectivity: principles and applications*, volume 770. Springer Verlag, 2009.

[28] A Demuer, D Jaccard, JW Reiner, CH Ahn, and J-M Triscone. Magnetism of $SrRuO_3$ thin films under high hydrostatic pressure. *Annalen der Physik*, 13(1-2):72–73, 2004.

[29] R.K. Dumas, K Liu, C.-P. Li, I.V. Roshchin, and I.K. Schuller. Temperature induced single domainvortex state transition in sub-100 nm Fe nanodots. *Applied Physics Letters*, 91:202501, 2007.

[30] V Dusastre, J Heber, F Pulizzi, A Stoddart, P Pamies, and C Martin. The interface is still the device. *Nature Materials*, 11:91, 2012.

[31] C. B. Eom, R. J. Cava, R. M. Fleming, J. M. Phillips, R. B. van Dover, J. H. Marshall, J. W. P. Hsu, J. J. Krajewski, and W. F. Peck Jr. Single-crystal epitaxial thin films of the isotropic metallic oxides $Sr_{1x}Ca_xRuO_3$. *Science*, 258:1766, 1992.

[32] P Fernando, Cínthia Piamonteze, Néstor E Massa, Horacio Salva, José Antonio Alonso, María Jesús Martínez-Lope, and María Teresa Casais. Possible common ground for the metal-insulator phase transition in the rare-earth nickelates $RNiO_3$ (R= Eu, Ho, Y). *Physical Review B*, 66(15):153104, 2002.

[33] M. R. Fitzsimmons and C. F. Majkrzak. Application of polarized neutron reflectometry to studies of artificially structured magnetic materials. *NIST Website*, Retrieved 2012.

[34] M.R. Fitzsimmons, N.W. Hengartner, S. Singh, M. Zhernenkov, F.Y. Bruno, J. Santamaria, A. Brinkman, M. Huijben, H.J.A. Molegraaf, J. de la Venta, and I.K. Schuller. Upper limit to magnetism in $LaAlO_3/SrTiO_3$ heterostructures. *Physical Review Letters*, 107:217201, 2012.

[35] Bradley H Frazer, Benjamin Gilbert, Brandon R Sonderegger, and Gelsomina De Stasio. The probing depth of total electron yield in the sub-kev range: TEY-XAS and X-PEEM. *Surface science*, 537(1):161–167, 2003.

[36] J. W. Freeland, J. Chakhalian, A. V. Boris, J.-M. Tonnerre, J. J. Kavich, P. Yordanov, S. Grenier, P. Zschack, E. Karapetrova, P. Popovich, H. N. Lee, and B. Keimer. Charge transport and magnetization profile at the interface between the correlated metal $CaRuO_3$ and the antiferromagnetic insulator $CaMnO_3$. *Physical Review B*, 81:094414, 2010.

[37] JW Freeland, Jian Liu, M Kareev, B Gray, JW Kim, P Ryan, R Pentcheva, and J Chakhalian. Orbital control in strained ultra-thin $LaNiO_3/LaAlO_3$ superlattices. *EPL (Europhysics Letters)*, 96(5):57004, 2011.

[38] J.R. Friedman, U. Voskoboynik, and M.P. Sarachik. Anomalous magnetic relaxation in ferritin. *Physical Review B*, 56:10793, 1997.

[39] Q. Gan, R. A. Rao, C. B. Eom, J. L. Garrett, and M. Lee. Direct measurement of strain effects on magnetic and electrical properties of epitaxial $SrRuO_3$ thin films. *Applied Physics Letters*, 72:978, 1998.

[40] MA Garcia, E Fernandez Pinel, J De la Venta, Adrián Quesada, V Bouzas, JF Fernández, JJ Romero, Martín González, and JL Costa-Kramer. Sources of experimental errors in the observation of nanoscale magnetism. *Journal of Applied Physics*, 105(1):013925–013925, 2009.

[41] J. L. Garcia-Munoz, J. Rodriguez-Carvajal, and P. Lacorre. Sudden appearance of an unusual spin density wave at the metal-insulator transition in the perovskites $RNiO_3$ (R = Pr, Nd). *Europhysics Letters*, 20:241, 1992.

[42] JL García-Muñoz, MAG Aranda, JA Alonso, and MJ Martinez-Lope. Structure and charge order in the antiferromagnetic band-insulating phase of $NdNiO_3$. *Physical Review B*, 79(13):134432, 2009.

[43] JS Gardner, G Balakrishnan, and D McK Paul. Neutron powder diffraction studies of Sr_2RuO_4 and $SrRuO_3$. *Physica C: Superconductivity*, 252(3):303–307, 1995.

[44] S. C. Gausepohl, M. Lee, R. A. Rao, and C. B. Eom. Hall-effect sign reversal in $CaRuO_3$ and $SrRuO_3$ thin films. *Physical Review B*, 54:8996, 1996.

[45] Marta Gibert, Pavlo Zubko, Raoul Scherwitzl, Jorge Iniguez, and Jean-Marc Triscone. Exchange bias in $LaNiO_3LaMnO_3$ superlattices. *Nature Materials*, 11:195, 2012.

[46] C Girardot, J Kreisel, S Pignard, N Caillault, and F Weiss. Raman scattering investigation across the magnetic and metal-insulator transition in rare earth nickelate $RNiO_3$ (R= Sm, Nd) thin films. *Physical Review B*, 78(10):104101, 2008.

[47] J.B. Goodenough. Theory of the role of covalence in the perovskite-type manganites [La,M(II)]MnO_3. *Physical Review*, 100:564, 1955.

[48] CE Gough, MS Colclough, EM Forgan, RG Jordan, M Keene, CM Muirhead, AIM Rae, N Thomas, JS Abell, and S Sutton. Flux quantization in a high-tc superconductor. *Nature*, 326(6116):855–855, 1987.

[49] AJ Grutter, FJ Wong, E Arenholz, A Vailionis, and Y Suzuki. Evidence of high-spin Ru and universal magnetic anisotropy in $SrRuO_3$ thin films. *Physical Review B*, 85(13):134429, 2012.

[50] Alexander Grutter, Franklin Wong, Elke Arenholz, Marco Liberati, and Yuri Suzuki. Enhanced magnetization in epitaxial $SrRuO_3$ thin films via substrate-induced strain. *Journal of Applied Physics*, 107(9):09E138–09E138, 2010.

[51] Alexander Grutter, Franklin Wong, Elke Arenholz, Marco Liberati, Arturas Vailionis, and Yuri Suzuki. Enhanced magnetism in epitaxial $SrRuO_3$ thin films. *Applied Physics Letters*, 96(8):082509–082509, 2010.

[52] E. Haller. Rutherford backscattering spectroscopy. *Course Notes*, 2011.

[53] C. He, A. J. Grutter, M. Gu, N. D. Browning, Y. Takamura, B. J. Kirby, J. A. Borchers, J.W. Kim, M. R. Fitzsimmons, X. Zhai, V.V. Mehta F. J. Wong, and Y. Suzuki. Interfacial ferromagnetism and exchange bias in $CaRuO_3/CaMnO_3$ superlattices. *Physical Review Letters*, 109:197202, 2012.

[54] C. He, X. Zhai, V.V. Mehta, F.J. Wong, and Y. Suzuki. Interfacial magnetism in $CaRuO_3/CaMnO_3$ superlattices grown on (001) $SrTiO_3$. *Journal of Applied Physics*, 109:07D729, 2011.

[55] G. Herranz, F. Sanchez, N. Dix, D. Hrabovsky, I.C. Infante, J. Fontcuberta, M.V. Garcia-Cuenca, C. Ferrater, and M. Varela. Controlled magnetic anisotropy of $SrRuO_3$ thin films grown on nominally exact $SrTiO_3$ (001) substrates. *Applied Physics Letters*, 89:152501, 2006.

[56] J. H. Hubbell and S. M. Seltzer. Tables of x-ray mass attenuation coefficients and mass energy-absorption coefficients from 1 keV to 20 MeV for elements Z = 1 to 92 and 48 additional substances of dosimetric interest. *NIST Standard Reference Database*, 126, 2004.

[57] M. Itoh, M. Shikano, and T. Shimura. High- and low-spin transition of Ru^{4+} in the perovskite-related layered system $Sr_{n+1}Ru_nO_{3n+1}$ with the change in n. *Physical Review B*, 51:16432, 1995.

[58] N. Jalili and K. Laxminarayana. A review of atomic force microscopy imaging systems: application to molecular metrology and biological sciences. *Mechatronics*, 14:907, 2004.

[59] QX Jia, F Chu, CD Adams, XD Wu, M Hawley, JH Cho, AT Findikoglu, SR Foltyn, JL Smith, and TE Mitchell. Characteristics of conductive $SrRuO_3$ thin films with different microstructures. *Journal of materials research*, 11(9):2263, 1996.

[60] JC Jiang, W Tian, XQ Pan, Q Gan, and CB Eom. Domain structure of epitaxial $SrRuO_3$ thin films on miscut (001) $SrTiO_3$ substrates. *Applied physics letters*, 72:2963, 1998.

[61] Z Jirak, S Krupička, Z Šimša, M Dlouha, and S Vratislav. Neutron diffraction study of $Pr_{1-x}Ca_xMnO_3$ perovskites. *Journal of magnetism and magnetic materials*, 53(1):153–166, 1985.

[62] C. W. Jones, P. D. Battle, P. Lightfoo, , and W. T. A. Harrison. The structure of $SrRuO_3$ by time-of-flight neutron powder diffraction. *Acta Crystallographica*, C45:365, 1988.

[63] B. Kalisky, J. A. Bert, B. B. Klopfer, C. Bell, H. K. Sato, M. Hosoda, Y. Hikita, H. Y. Hwang, and K. A. Moler. Critical thickness for ferromagnetism in $LaAlO_3/SrTiO_3$ heterostructures. *Nature Communications*, 3:922, 2012.

[64] D. Kan, R. Aso, H. Kurata, and Y. Shimakawa. Epitaxial strain effect in tetragonal $SrRuO_3$ thin films. *Journal of Applied Physics*, 113:173912, 2013.

[65] J. Kanamori. Superexchange interaction and symmetry properties of electron orbitals. *Journal of Physics and Chemistry of Solids*, 10:87, 1959.

[66] A. Kanbayasi. Magnetic properties of $SrRuO_3$ single crystal. *Journal of the Physical Society of Japan*, 41:1876, 1976.

[67] Y. Kats, I. Genish, L. Klein, J. W. Reiner, and M. R. Beasley. Testing the berry phase model for extraordinary hall effect in $SrRuO_3$. *Physical Review B*, 70:180407, 2004.

[68] David M Kelly, Eric E Fullerton, Jacobo Santa-Maria, and Ivan K Schuller. A simple closed-form expression for the x-ray reflectivity from multilayers with cumulative roughness. *Scripta metallurgica et materialia*, 33(10):1603–1608, 1995.

[69] Peter Khalifah, I Ohkubo, Hans M Christen, and DG Mandrus. Evolution of transport and magnetic properties near the ferromagnetic quantum critical point in the series $Ca_xSr_{1-x}RuO_3$. *Physical Review B*, 70(13):134426, 2004.

[70] M.-H. Kim, G. Acbas, M.-H. Yang, M. Eginligil, P. Khalifah, I. Ohkubo, H. Christen, D. Mandrus, Z. Fang, and J. Cerne. Infrared anomalous hall effect in $SrRuO_3$: Exploring evidence for crossover to intrinsic behavior. *Physical Review B*, 70:180407, 2004.

[71] B.J. Kirby, P.A. Kienzle, B.B. Maranville, N.F. Berk, J. Krycka, F. Heinrich, and C.F. Majkrzak. Phase-sensitive specular neutron reflectometry for imaging the nanometer scale composition depth profile of thin-film materials. *Current Opinion in Colloid and Interface Science*, 17:44, 2012.

[72] Charles Kittel and Paul McEuen. *Introduction to solid state physics*, volume 7. Wiley New York, 1996.

[73] L Klein, JS Dodge, CH Ahn, JW Reiner, L Mieville, TH Geballe, MR Beasley, and A Kapitulnik. Transport and magnetization in the badly metallic itinerant ferromagnet. *Journal of Physics: Condensed Matter*, 8(48):10111, 1996.

[74] L. Klein, J.S. Dodge, T.H. Geballe, A. Kapitulnik, A.F. Marshall, L. Antognazza, and K. Char. Perpendicular magnetic anisotropy and strong magneto-optic properties of $SrRuO_3$ epitaxial films. *Applied Physics Letters*, 66:2427, 1995.

[75] H. Kojitani, Y. Shirako, and M. Akaogi. Post-perovskite phase transition in $CaRuO_3$. *Physics of the Earth and Planetary Interiors*, 165:127, 2007.

[76] P. S. Anil Kumar, P. A. Joy, and S. K. Date. On the irreversible magnetic behavior of the anisotropic ferromagnetic system $SrRuO_3$. *Physica B*, 269:356, 1999.

[77] Yogesh Kumar, Abhinav Pratap Singh, P Thakur, and Ravi Kumar. X-ray absorption study of epitaxial $LaNiO_3$ thin films. In *AIP Conference Proceedings*, volume 1349, page 697, 2011.

[78] CCY Kwan, J Basinski, and JC Woolley. Analysis of the two-band hall effect and magnetoresistance. *physica status solidi (b)*, 48(2):699–704, 1971.

[79] B.W. Lee, C.U. Jung, M. Kawasaki, and Y. Tokura. Tuning of magnetism in $SrRuO_3$ thin flms on $SrTiO_3$ (001) substrate by control of the twin and strain amount in the buffer layer. *Journal of Applied Physics*, 104:103909, 2008.

[80] H. N. Lee, H. M. Christen, M. F. Chisholm, C. M. Rouleau, and D. H. Lowndes. Strong polarization enhancement in asymmetric three-component ferroelectric superlattices. *Nature*, 433:396, 2005.

[81] I Lindau and WE Spicer. The probing depth in photoemission and Auger-electron spectroscopy. *Journal of Electron Spectroscopy and Related Phenomena*, 3(5):409–413, 1974.

[82] C. D. Ling, E. Granado, J. J. Neumeier, J. W. Lynn, and D. N. Argyriou. Inhomogeneous magnetism in La-doped $CaMnO_3$. I. mesoscopic phase separation due to lattice-coupled ferromagnetic interactions. *Physical Review B*, 68:134439, 2003.

[83] J. Liu, S. Okamoto, M. van Veenendaal, M. Kareev, B. Gray, P. Ryan, J. W. Freeland, and J. Chakhalian. Quantum confinement of mott electrons in ultrathin $LaNiO_3/LaAlO_3$ superlattices. *Physical Review B*, 83:161102(R), 2011.

[84] Mao Liu, Trevor R Finlayson, and T Fred Smith. High-resolution dilatometry measurements of $SrTiO_3$ salong cubic and tetragonal axes. *Physical Review B*, 55(6):3480, 1997.

[85] W. Lu, W.D. Song, K. He, J. Chai, C.-J. Sun, G.-M. Chow, and J.-S. Chen. Perpendicular magnetic anisotropy and strong magneto-optic properties of $SrRuO_3$ epitaxial films. *Journal of Applied Physics*, 113:063901, 2013.

[86] J Lüning, F Nolting, A Scholl, H Ohldag, Jin Won Seo, J Fompeyrine, J-P Locquet, and J Stöhr. Determination of the antiferromagnetic spin axis in epitaxial $LaFeO_3$ films by x-ray magnetic linear dichroism spectroscopy. *Physical Review B*, 67(21):214433, 2003.

[87] JW Lynn, Y Chen, S Chang, Y Zhao, S Chi, W Ratcliff II, BG Ueland, and RW Erwin. Double-focusing thermal triple-axis spectrometer at the ncnr.

[88] J. B. MacChesney, H. J. Williams, J. F. Potter, and R. C. Sherwood. Magnetic study of the manganate phases: $CaMnO_3$, $Ca_4Mn_3O_{10}$, $Ca_3Mn_2O_7$, Ca_2MnO_4. *Physical Review*, 164:779, 1967.

[89] AP Mackenzie, SR Julian, AJ Diver, GJ McMullan, MP Ray, GG Lonzarich, Y Maeno, S Nishizaki, and T Fujita. Quantum oscillations in the layered perovskite superconductor sr_2ruo_4. *Physical review letters*, 76(20):3786–3789, 1996.

[90] P. Mahadevan, F. Aryasetiawan, A. Janotti, and T. Sasaki. Evolution of the electronic structure of a ferromagnetic metal: Case of $SrRuO_3$. *Physical Review B*, 80:035106, 2009.

[91] John E. Mahan, Kent M. Geib, G. Y. Robinson, and Robert G. Long. A review of the geometrical fundamentals of reflection high-energy electron diffraction with application to silicon surfaces. *Journal of Vacuum Science and Technology A*, 8:3692, 1990.

[92] A. Maignan, C. Martin, M. Hervieu, and B. Raveau. Ferromagnetism and metallicity in the $CaMn_{1-x}Ru_xO_3$ perovskites: a highly inhomogeneous system. *Solid State Communications*, 117:377, 2001.

[93] K. Maiti. Role of covalency in the ground-state properties of perovskite ruthenates: A first-principles study using local spin density approximations. *Physical Review B*, 73:235110, 2006.

[94] C. F. Majkrzak, K. V. ODonovan, and N. F. Berk. Polarized neutron reflectometry. *NIST Website*, 2004.

[95] K. Maki, B.T. Liu, H. Vu, V. Nagarajan, R. Ramesh, Y. Fujimori, T. Nakamura, and H. Takasu. Controlling crystallization of $Pb(Zr,Ti)O_3$ thin films on IrO_2 electrodes at low temperature through interface engineering. *Applied Physics Letters*, 82:1263, 2003.

[96] GP Mambrini, ER Leite, MT Escote, AJ Chiquito, E Longo, JA Varela, and RF Jardim. Structural, microstructural, and transport properties of highly oriented $LaNiO_3$ thin films deposited on $SrTiO_3$ (100) single crystal. *Journal of Applied Physics*, 102(4):043708–043708, 2007.

[97] V. Markovich, I. Fita, A. Wisniewski, R. Puzniak, D. Mogilyansky, L. Titelman, L. Vradman, M. Herskowitz, and G. Gorodetsky. Surface and exchange-bias effects in compacted $CaMnO_{3-d}$ nanoparticles. *Physical Review B*, 77:054410, 2008.

[98] S. J. May, T. S. Santos, and A. Bhattacharya. Onset of metallic behavior in strained $(LaNiO_3)_n/(SrMnO_3)_2$ superlattices. *Physical Review B*, 79:115127, 2009.

[99] II Mazin, DI Khomskii, R Lengsdorf, JA Alonso, WG Marshall, RM Ibberson, A Podlesnyak, MJ Martinez-Lope, and MM Abd-Elmeguid. Charge ordering as alternative to jahn-teller distortion. *Physical review letters*, 98(17):176406, 2007.

[100] M. Medarde, A. Fontaine, J. L. Garcia-Muñoz, J. Rodriguez-Carvajal, M. de Santis, M. Sacchi, G. Rossi, and P. Lacorre. $RNiO_3$ perovskites (R=Pr,Nd): Nickel valence and the metal-insulator transition investigated by x-ray-absorption spectroscopy. *Phys. Rev. B*, 46:14975–14984, Dec 1992.

[101] M Medarde, P Lacorre, K Conder, F Fauth, and A Furrer. Giant ^{16}O-^{18}O isotope effect on the metal-insulator transition of $RNiO_3$ perovskites (R= rare earth). *Physical review letters*, 80(11):2397–2400, 1998.

[102] Virat Mehta and Yuri Suzuki. Ferromagnetism enhanced by structural relaxation of biaxially compressed $LaCoO_3$ films. *Journal of Applied Physics*, 109:07D717, 2011.

[103] Virat Vasav Mehta, Marco Liberati, Franklin J Wong, Rajesh Vilas Chopdekar, Elke Arenholz, and Yuri Suzuki. Ferromagnetism in tetragonally distorted $LaCoO_3$ thin films. *Journal of Applied Physics*, 105(7):07E503–07E503, 2009.

[104] Xiang-Jian Meng, Jing-Lan Sun, Jian Yu, Hong-Juan Ye, Shao-Ling Guo, and Jun-Hao Chu. Preparation of highly (100)-oriented metallic $LaNiO_3$ films on Si substrates by a modified metalorganic decomposition technique. *Applied surface science*, 171(1):68–70, 2001.

[105] XJ Meng, JG Cheng, JL Sun, HJ Ye, SL Guo, and JH Chu. Growth of (100)-oriented $LaNiO_3$ thin films directly on Si substrates by a simple metalorganic decomposition technique for the highly oriented pzt thin films. *Journal of crystal growth*, 220(1):100–104, 2000.

[106] Hidetoshi Miyazaki, Takashi Goto, Yuki Miwa, Tomoya Ohno, Hisao Suzuki, Toshitaka Ota, and Minoru Takahashi. Preparation and evaluation of $lanio_3$ thin film electrode with chemical solution deposition. *Journal of the European Ceramic Society*, 24(6):1005–1008, 2004.

[107] Nevill F Mott. The basis of the electron theory of metals, with special reference to the transition metals. *Proceedings of the Physical Society. Section A*, 62(7):416, 1949.

[108] N. Nagaosa, J. Sinova, S. Onoda, A. H. MacDonald, and N. P. Ong. Anomalous hall effect. *Reviews of Modern Physics*, 82:1539, 2010.

[109] B. R. K Nanda, S. Satpathy, , and M. S. Springborg. Electron leakage and double-exchange ferromagnetism at the interface between a metal and an antiferromagnetic insulator: $CaRuO_3/CaMnO_3$. *Physical Review Letters*, 98:216804, 2007.

[110] J. J. Neumeier and D. H. Goodwin. Unusually strong ferromagnetic correlations in La-doped $CaMnO_3$. *Journal of Applied Physics*, 85:5591, 1999.

[111] JJ Neumeier and JL Cohn. Possible signatures of magnetic phase segregation in electron-doped antiferromagnetic $CaMnO_3$. *Physical Review-Series B*, 61(21):14319–14322, 2000.

[112] David P. Norton. Synthesis and properties of epitaxial electronic oxide thin-film materials. *Materials Science and Engineering R*, 43:139, 2004.

[113] J. F. Nye. *Physical Properties of Crystals: Their Representation by Tensors and Matricesics*. Clarendon, 1985.

[114] A Ohtomo and HY Hwang. A high-mobility electron gas at the laalo$_3$/srtio$_3$ heterointerface. *Nature*, 427(6973):423–426, 2004.

[115] J. Okamoto, T. Okane, Y. Saitoh, K. Terai, S.-I. Fujimori, Y. Muramatsu, K. Yoshii, K. Mamiya, T. Koide, A. Fujimori, Z. Fang, Y. Takeda, and M. Takano. Soft x-ray magnetic circular dichroism study of $Ca_{1-x}Sr_xRuO_3$ across the ferromagnetic quantum phase transition. *Physical Review B*, 76:184441, 2007.

[116] R. Palai, H. Huhtinen, J.F. Scott, and R.S. Katiyar. Observation of spin-glass-like behavior in $SrRuO_3$ epitaxial thin films. *Physical Review B*, 79:104413, 2009.

[117] Morton B Panish. Molecular beam epitaxy. *Science*, 208(4446):916–922, 1980.

[118] W. Paszkowicz, J. Pietosa, S. M. Woodley, P. A. Dluzewski, M. Kozlowski, and C. Martin. Lattice parameters and orthorhombic distortion of $CaMnO_3$. *Powder Diffraction*, 25:46, 2010.

[119] C. J. Powell and A. Jablonski. *NIST Electron Inelastic-Mean-Free-Path Database - Version 1.2*. National Institute of Standards and Technology, Gaithersburg, MD, 2010.

[120] Danilo Puggioni, Alessio Filippetti, and Vincenzo Fiorentini. Ordering and multiple phase transitions in ultrathin nickelate superlattices. *Physical Review B*, 86(19):195132, 2012.

[121] Ruimin Qiao, Timothy Chin, Stephen J Harris, Shishen Yan, and Wanli Yang. Spectroscopic fingerprints of valence and spin states in manganese oxides and fluorides. *Current Applied Physics*, 2012.

[122] R. Ramesh and D.G. Schlom. Orienting ferroelectric films. *Science*, 296:1975, 2002.

[123] M. Rao and R. Pandit. Magnetic and thermal hysteresis in the o(n)-symmetric $(\phi^2)^3$ model. *Physical Review B*, 43:3373, 1991.

[124] M. V. Rama Rao, V. G. Sathe, D. Sornadurai, and B. Panigrahi and T. Shripathi. Electronic Structure of $ARuO_3$ (A = Ca, Sr and Ba) Compounds. *Journal of Physics and Chemistry of Solids*, 62:797, 2001.

[125] Bernard Raveau. *Colossal magnetoresistance, charge ordering and related properties of manganese oxides*. World Scientific Publishing Company Incorporated, 1998.

[126] G.J.H.M. Rijnders, G. Koster, D.H.A. Blank, and H. Rogalla. In-situ monitoring during PLD of complex oxides using RHEED at high oxygen pressure. *MRS Proceedings*, 502:209, 1997.

[127] J. M. Rondinelli, N. M. Caffrey, S. Sanvito, and N. A. Spaldin. Electronic properties of bulk and thin film $SrRuO_3$: Search for the metal-insulator transition. *Physical Review B*, 78:155107, 2008.

[128] James M. Rondinelli, Steven J. May, and John W. Freeland. Control of octahedral connectivity in perovskite oxide heterostructures: An emerging route to multifunctional materials discovery. *MRS Bulletin*, 37:261, 2012.

[129] G. Sanchez-Santolino, J. Tornos, F.Y. Bruno, F.A. Cuellar, C. Leon, J. Santamaria, S.J. Pennycook, and M. Varela. Characterization of surface metallic states in $SrTiO_3$ by means of aberration corrected electron microscopy. *Ultramicroscopy*, 127:109, 2013.

[130] PN Santhosh, J Goldberger, PM Woodward, T Vogt, WP Lee, and AJ Epstein. Phase separation over an extended compositional range: Studies of the $Ca_{1-x}Bi_xMnO_3$(x<$\sim$ 0.25) phase diagram. *Physical Review B*, 62(22):14928, 2000.

[131] KM Satyalakshmi, RM Mallya, KV Ramanathan, XD Wu, B Brainard, DC Gautier, NY Vasanthacharya, and MS Hegde. Epitaxial metallic $LaNiO_3$ thin films grown by pulsed laser deposition. *Applied physics letters*, 62(11):1233–1235, 1993.

[132] R. Scherwitzl, S. Gariglio, M. Gabay, P. Zubko, M. Gibert, and J.-M. Triscone. Metal-insulator transition in ultrathin $LaNiO_3$ films. *Physical Review Letters*, 106:246403, 2011.

[133] P. Schiffer, A. P. Ramirez, W. Bao, , and S.-W. Cheong. Low temperature magnetoresistance and the magnetic phase diagram of $La_{1-x}Ca_xMnO_3$. *Physical Review Letters*, 75:3336, 1995.

[134] H.K. Schmid and W. Mader. Oxidation states of Mn and Fe in various compound oxide systems. *Micron*, 37:426, 2006.

[135] J. Schou1. Physical aspects of the pulsed laser deposition technique: The stoichiometric transfer of material from target to film. *Applied Surface Science*, 255:5191, 2009.

[136] MP Seah and WA Dench. Quantitative electron spectroscopy of surfaces: a standard data base for electron inelastic mean free paths in solids. *Surface and interface analysis*, 1(1):2–11, 1979.

[137] Y. Shperber, I. Genish, J.W. Reiner, and L. Klein. Field induced resistivity anisotropy in $SrRuO_3$ films. *Journal of Applied Physics*, 105:07B106, 2009.

[138] Wolter Siemons, Gertjan Koster, Arturas Vailionis, Hideki Yamamoto, Dave Blank, and Beasleym Malcolm R. Strain-induced single-domain growth of epitaxial $SrRuO_3$ layers on $SrTiO_3$: A high-temperature x-ray diffraction study. *Physical Review B*, 76:075126, 2007.

[139] J. Son, P. Moetakef, J. M. LeBeau, D. Ouellette, L. Balents, S. J. Allen, and S. Stemmer. Low-dimensional mott material: Transport in ultrathin epitaxial $LaNiO_3$ films. *Applied Physics Letters*, 96:062114, 2010.

[140] J. Stohr and H. Konig. Determination of spin- and orbital-moment anisotropies in transition metals by angle-dependent X-ray magnetic circular dichroism. *Physical Review Letters*, 75:3748, 1995.

[141] Joachim Stöhr and Hans Christoph Siegmann. *Magnetism: from fundamentals to nanoscale dynamics*, volume 152. Springer, 2006.

[142] G. Subas, J. Garcia, M. C. Sanchez, J. Blasco, and M. G. Proietti. Soft x-ray absorption spectroscopy (Mn $L_{2,3}$ and O K) in mixed valence manganites. *Surface Review Letters*, 9:1071, 2002.

[143] Kazu Suenaga, Yuta Sato, Zheng Liu, Hiromichi Kataura, Toshiya Okazaki, Koji Kimoto, Hidetaka Sawada, Takeo Sasaki, Kazuya Omoto, Takeshi Tomita, et al. Visualizing and identifying single atoms using electron energy-loss spectroscopy with low accelerating voltage. *Nature chemistry*, 1(5):415–418, 2009.

[144] Li Sun, Tao Yu, Yan-Feng Chen, Jun Zhou, and Nai-Ben Ming. Conductive $LaNiO_3$ electrode grown by pulsed laser ablation on si substrate. *Journal of materials research*, 12(4):931–935, 1997.

[145] K.S. Takahashi, M. Kawasaki, and Y. Tokura. Interface ferromagnetism in oxide superlattices of $CaMnO_3/CaRuO_3$. *Applied Physics Letters*, 79:1324, 2001.

[146] H. Tan, J. Verbeeck, A. Abakumov, and G. Van Tendeloo. Oxidation state and chemical shift investigation in transition metal oxides by EELS. *Ultramicroscopy*, 116:24, 2012.

[147] B.T. Thole, P. Carra, F. Sette, and G. van der Laan. X-ray circular dichroism as a probe of orbital magnetization. *Physical Review Letters*, 68:1943, 1992.

[148] JB Torrance, P Lacorre, AI Nazzal, EJ Ansaldo, and Ch Niedermayer. Systematic study of insulator-metal transitions in perovskites $RNiO_3$(R= Pr, Nd, Sm, Eu) due to closing of charge-transfer gap. *Physical Review B*, 45(14):8209, 1992.

[149] D. Toyota, I. Ohkubo, H. Kumigashira, M. Oshima, T. Ohnishi, M. Lippmaa, M. Takizawa, A. Fujimori, K. Ono, M. Kawasaki, and H. Koinuma. Thickness-dependent electronic structure of ultrathin $SrRuO_3$ films studied by in situ photoemission spectroscopy. *Applied Physics Letters*, 87:162508, 2008.

[150] K. Ueda, H. Tabata, and T. Kawai. Ferromagnetism in $LaFeO_3$-$LaCrO_3$ superlattices. *Science*, 280:1064, 1998.

[151] Arturas Vailionis, Wolter Siemons, and Gertjan Koster. Strain-induced single-domain growth of epitaxial $SrRuO_3$ layers on $SrTiO_3$: A high-temperature x-ray diffraction study. *Applied Physics Letters*, 91(7):071907–071907, 2007.

[152] X. W. Wang, Y. Q. Zhang, H. Meng, Z. J. Wang, D. Li, and Z. D. Zhang. Magnetic anisotropy and transport properties of 70 nm $SrRuO_3$ films grown on different substrates. *Journal of Applied Physics*, 109:07D707, 2011.

[153] Z.L. Wang, J.S. Yin, and Y.D. Jiang. EELS analysis of cation valence states and oxygen vacancies in magnetic oxides. *Micron*, 31:571, 2000.

[154] CR Wiebe, JE Greedan, JS Gardner, Z Zeng, and M Greenblatt. Charge and magnetic ordering in the electron-doped magnetoresistive materials $CaMnO_{3-\delta}$ (δ= 0.06, 0.11). *Physical Review B*, 64(6):064421, 2001.

[155] P. R. Willmott. Deposition of complex multielemental thin films. *Progress in Surface Science*, 76:163, 2004.

[156] M Wissinger, D Fuchs, L Dieterle, H Leiste, R Schneider, D Gerthsen, and HV Löhneysen. Anisotropic lattice changes and ferromagnetic order in $Sr_{1-x}Ca_xRuO_3$. *Physical Review B*, 83(14):144430, 2011.

[157] Franklin Wong. Electronic transitions in perovskite oxide heterostructures. *Doctoral Thesis*, 2011.

[158] Shinsuke Yamanaka, Takuji Maekawa, Hiroaki Muta, Tetsushi Matsuda, Shin-ichi Kobayashi, and Ken Kurosaki. Thermophysical properties of $SrHfO_3$ and $SrRuO_3$. *Journal of Solid State Chemistry*, 177(10):3484–3489, 2004.

[159] GZ Yang, HB Lu, F Chen, T Zhao, and ZH Chen. Laser molecular beam epitaxy and characterization of perovskite oxide thin films. *Journal of crystal growth*, 227:929–935, 2001.

[160] YZ Yoo, O Chmaissem, S Kolesnik, B Dabrowski, M Maxwell, CW Kimball, L McAnelly, M Haji-Sheikh, and AP Genis. Contribution of oxygen partial pressures investigated over a wide range to $SrRuO_3$ thin-film properties in laser deposition processing. *Journal of applied physics*, 97(10):103525–103525, 2005.

[161] A. T. Zayak, X. Huang, J. B. Neaton, and K. M. Rabe. Structural, electronic, and magnetic properties of $SrRuO_3$ under epitaxial strain. *Physical Review B*, 74:094104, 2006.

[162] A. T. Zayak, X. Huang, J. B. Neaton, and K. M. Rabe. Manipulating magnetic properties of $SrRuO_3$ and $CaRuO_3$ with epitaxial and uniaxial strains. *Physical Review B*, 77:214410, 2008.

[163] H. Zheng, J. Wang, S. E. Lofland, Z. Ma, L. Mohaddes-Ardabili, T. Zhao, L. Salamanca-Riba, S. R. Shinde, S. B. Ogale, F. Bai, D. Viehland, Y. Jia, D. G. Schlom, M. Wuttig, A. Roytburd, and R. Ramesh. Multiferroic $BaTiO_3$-$CoFe_2O_4$ nanostructures. *Science*, 303:661, 2004.

[164] Xiao-Lin Zhou and Sow-Hsin Chen. Theoretical foundation of x-ray and neutron reflectometry. *Physics Reports*, 257(4):223–348, 1995.

[165] X. Zhu, D. Zheng, W. Peng, J. Miao, and J. Li. Structural and electrical properties of epitaxial $Ba_{0.5}Sr_{0.5}TiO_3/SrRuO_3$ heterostructures grown by pulsed laser deposition. *Journal of Crystal Growth*, 268:192, 2004.

[166] M. Ziese, I. Vrejoiu, and D. Hesse. Structural symmetry and magnetocrystalline anisotropy of $SrRuO_3$ films on $SrTiO_3$. *Physical Review B*, 81:2010, 2010.

[167] Bin Zou, Peter K Petrov, and Neil McN Alford. $SrRuO_3$ thin films grown on MgO substrates at different oxygen partial pressures. *Journal of Materials Research*, 28:702–707, 2013.

Appendix A

X-ray Magnetic Circular Dichroism

Derived from X-ray absorption spectroscopy, X-ray magnetic circular dichroism is a magnetic characterization technique which utilizes the difference in X-ray absorption, or dichroism, of positively and negatively circularly polarized light as a detector of electron spin in a material. In describing the mechanisms of X-ray magnetic circular dichroism, this work fill follow the description of Stohr before examining in detail an example of how dichroism is achieved and moving on to the derivation and application of the sum rules for X-ray magnetic circular dichroism.[141]

A.1 Theoretical Basis

In order to observe dichroism in the X-ray absorption spectra for the cases of positively and negatively circularly polarized light, there are three elementary requirements. The first is a spin-polarized photon source. The second is a spin-polarized valence band into which electrons may be excited. The third is spin-orbit coupling in the core levels from which electrons are excited into the valence band. Thus, the band picture of X-ray magnetic circular dichroism is typically approached in terms of using the magnetic electron energy band, typically the $3d$, as a detector of electron spin. The quantum mechanical selection rules for transitions between electron energy levels through absorption of a photon are

$$\begin{aligned} \Delta l &= \pm 1 \\ \Delta m_l = q &= 0, \pm 1 \\ \Delta s &= 0 \\ \Delta m_s &= 0 \end{aligned} \tag{A.1}$$

where q$\hbar$ is the angular momentum of the incoming photon (± 1). Equation A.1 requires that there are no spin-flip transitions. That is, an electron which begins spin-up remains spin-up. From Figure 1.6(b), which shows a typical ferromagnetic d-band, it is apparent that a spin-split system must have more total unoccupied states into which to excite on electron spin than the other. The probability of a transition from a single core state to a set of unoccupied states with energy E_f in a magnetic valence band is described by Fermi's golden rule, typically written as shown below

$$T_{i\to f} = \frac{2\pi}{\hbar} H_{fi}\rho_f \delta(E_f - E_i - \hbar\omega) \tag{A.2}$$

where $T_{i\to f}$ is the transition probability between initial state and the final states, H_{fi} is the transfer matrix element $\langle f|H|i\rangle$, ρ_f is the density of states in the destination band at a given energy, and $\delta(E_f - E_i - \hbar\omega)$ enforces energy conservation. Of course, when we probe a system with photons of a given energy, we are not specifically picking out states, but rather probing the number of transitions from an initial energy to a final energy. Therefore, the probability of an absorption event is also proportional to the number of initial and final states available at the given energy. Additionally, in a more localized ionic picture relying on a superexchange mechanism, ρ_f may not accurately describe the number of accessible final states. Thus, we may alternatively write the transition probability as

$$T_{i\to f} = \sum_f \frac{2\pi}{\hbar} H_{fi}\delta(E_f - E_i - \hbar\omega) \tag{A.3}$$

However, the intensity of the entire absorption edge also depends on the number of initial states from which electrons are being excited. Thus, the most complete description of the absorption edge intensity is

$$T_{absorption} = \sum_{if} T_{i\to f} = \sum_{if} \frac{2\pi}{\hbar} H_{fi}\delta(E_f - E_i - \hbar\omega) \tag{A.4}$$

It is clear from expression A.4 that whichever spin has a higher density of available states ρ_f at a given energy is more likely to be excited. However, the destination shell does not yet act as a spin detector and dichroism will not be observed, as the incoming light will excite equal numbers of spin-up and spin-down electrons. That is, the initial state $|i\rangle$ does not distinguish between positively and negatively circularly polarized light and the total absorption does not change as the direction of photon polarization is reversed relative to the magnetization axis. It is in fact an additional contribution from the interaction between the spin-orbit split initial bands (usually p-bands) that result in dichroism.

In effect, the spin-orbit coupling in the initial core states allows transitions in which some of the photon angular momentum is transferred to the electron spin. The resulting excited photoelectrons are consequently spin-polarized. With a spin polarized source of electrons and a spin polarized final state, dichroism may be observed on certain absorption edges. The importance of spin orbit coupling is the reason that X-ray magnetic circular dichroism is generally not observed in K-edge excitations. Because the spin-polarization is opposite at the $l + s$ and $l - s$, the dichroism on the L^3 or M^5 edges must be opposite that of the L^2 or M^4. To understand the details of the spin-orbit interaction and its influence on absorption, the previously undefined transition matrix element H_{fi} must be examined in detail. It is defined below in equation A.5.

$$H_{fi} = < f|P_\alpha^q|i > \tag{A.5}$$

where f is the final state, i is the initial state, and P_α^q is the dipole operator which represents the perturbation of the photon electric field on the electron. X-ray magnetic circular

dichroism addresses the case of photon propagation and circular polarization direction along the axis of magnetization, so that[141]

$$P_z^{\pm 1} = rC_{\pm 1}^{(1)} \tag{A.6}$$

where $C_a^{(b)}$ is Racah's spherical tensor operator and may be found defined in [141]. In this case, the transition matrix element for two hydrogenic wave functions simplifies to

$$< f|P_z^q|i >= \delta(m_s', m_s) < R_{n'l'}|r|R_{nl} > \sum_{m_l, m_l'} < l', m_l'|C_{\pm 1}^{(1)}|l, m_l > \tag{A.7}$$

which may be easily evaluated for most hydrogenic wave functions, as will be seen in the next section. In any case, the fundamentals of X-ray magnetic circular dichroism may now be understood as a source of spin-polarized photoelectrons excited to a spin-polarized valence band. Varying the relative orientations of X-ray polarization and magnetization, it is possible to detect magnetism at specific elemental absorption edges through the resulting dichroism.

A.2 Example System

The details of the X-ray magnetic circular dichroism effect will now be examined in an example system. The model system will consist of a perfectly spin-polarized $3d$ band, which will serve as the final state, a $2p$ band, which will serve as the initial state, and a perfectly spin-polarized beam of incoming photons. The total transition probability will be determined for the $2p_{3/2} \rightarrow 3d$ and $2p_{1/2} \rightarrow 3d$ transitions for the cases of positively (+) and negatively (-) circularly polarized light. The difference between the two will be the X-ray magnetic circular dichroism effect. As this will be done in a localized, rather than band, picture, the density of states in equation A.2 will be replaced by the enumeration and summation of the interactions between individual states. All constants in the expression will be incorporated into a single term N, while the radial term, which is constant across all $2p \rightarrow 3d$ transitions will be simply referred to as R. Therefore, equation A.6 is rewritten simply as:

$$T_{i \rightarrow f} = AR^2| < l_f, m_f|C_{\pm 1}^{(1)}|l_i, m_i >< m_s^f|m_s^i > |^2 \tag{A.8}$$

Individual terms may be evaluated as

$$\begin{aligned} < l-1, m+1|C_1^{(1)}|l, m >&= -\sqrt{\frac{(l-m)(l+1)}{2(2l-1)(2l+1)}} \\ < l+1, m-1|C_{-1}^{(1)}|l, m >&= -\sqrt{\frac{(l-m+2)(l-m+1)}{2(2l+3)(2l+1)}} \end{aligned} \tag{A.9}$$

These represent the only nonzero elements. That is, only a matrix element in which m_l^{final} = $\mathrm{m}_l^{initial}$+q satisfies the quantum mechanical selection rules stated in equation A.1. The matrix element coefficients for all allowable transitions between $2p$ and $3d$ states have been

Positive Helicity				
L_i	L_f	m_l^i	m_l^f	Coefficient
1	2	-1	0	$\frac{1}{\sqrt{3}\sqrt{5}}$
1	2	0	1	$\frac{1}{\sqrt{5}}$
1	2	1	2	$\sqrt{\frac{2}{5}}$

Table A.1: Transition matrix element coefficients for positively circularly polarized light

Negative Helicity				
L_i	L_f	m_l^i	m_l^f	Coefficient
1	2	-1	-2	$\sqrt{\frac{2}{5}}$
1	2	0	-1	$\frac{1}{\sqrt{5}}$
1	2	1	0	$\frac{1}{\sqrt{3}\sqrt{5}}$

Table A.2: Transition matrix element coefficients for negatively circularly polarized light

evaluated and may be found in table A.1 for the case of positive Helicity and A.2 for the case of negative helicity.

The states of interest in the $2p$ band are strongly spin orbit coupled and split according to the total angular momentum j. Therefore, the state $|l, m_l> |\alpha>$ may also be described in terms of the total angular momentum j so that the states are represented by $|j, m_j>$. Therefore, when enumerating the $2p$ bonding states below, the state will be written first as $|j, m_j>$ and then broken into its spin and orbital components. Thus

$$\overbrace{|^3/_2, ^3/_2\rangle}^{\mathrm{j,m}_j} = \overbrace{|1,1\rangle|\uparrow\rangle}^{\mathrm{l,m}_l,\mathrm{spin}} \tag{A.10}$$

Therefore all of the $2p_{3/2}$ states may be written as

$$\begin{aligned}
|^3/_2, ^3/_2\rangle =& |1,1\rangle|\uparrow\rangle \\
|^3/_2, ^1/_2\rangle =& \frac{1}{\sqrt{3}}\left(|1,1\rangle|\downarrow\rangle + \sqrt{(}2)|1,0\rangle|\uparrow\rangle\right) \\
|^3/_2, -^1/_2\rangle =& \frac{1}{\sqrt{3}}\left(|1,-1\rangle|\uparrow\rangle + \sqrt{(}2)|1,0\rangle|\downarrow\rangle\right) \\
|^3/_2, -^3/_2\rangle =& |1,-1\rangle|\downarrow\rangle
\end{aligned} \tag{A.11}$$

and the $2p_{1/2}$ states are written as

$$\begin{aligned}
|^1/_2, ^1/_2\rangle =& \frac{1}{\sqrt{3}}\left(|1,0\rangle|\uparrow\rangle - \sqrt{(}2)|1,1\rangle|\downarrow\rangle\right) \\
|^1/_2, -^1/_2\rangle =& \frac{1}{\sqrt{3}}\left(|1,0\rangle|\downarrow\rangle - \sqrt{(}2)|1,-1\rangle|\uparrow\rangle\right)
\end{aligned} \tag{A.12}$$

The available $3d$ levels are written below in terms of the hydrogenic wave functions. Because the case being considered is completely spin polarized, only a single spin band will be written. The $|\uparrow\rangle$ is arbitrarily chosen as the minority spin-band.

$$\begin{aligned}
|d_{z^2}\rangle =& |2,0\rangle|\uparrow\rangle \\
|d_{xz}\rangle =& \frac{1}{\sqrt{2}}\left(|2,1\rangle|\uparrow\rangle + |2,-1\rangle|\uparrow\rangle\right) \\
|d_{yz}\rangle =& \frac{1}{\sqrt{2}i}\left(|2,1\rangle|\uparrow\rangle - |2,-1\rangle|\uparrow\rangle\right) \\
|d_{x^2-y^2}\rangle =& \frac{1}{\sqrt{2}}\left(|2,2\rangle|\uparrow\rangle + |2,-2\rangle|\uparrow\rangle\right) \\
|d_{xy}\rangle =& \frac{1}{\sqrt{2}i}\left(|2,2\rangle|\uparrow\rangle - |2,-2\rangle|\uparrow\rangle\right)
\end{aligned} \tag{A.13}$$

Now the transfer matrix elements for all possible transitions are considered for the case of positively circularly polarized light. They are presented below:

$$\begin{aligned}
&\mathbf{d_{z^2}}: \\
\langle d_{z^2}|C_1^{(1)}|^3/_2,^3/_2\rangle =& 0 \\
\langle d_{z^2}|C_1^{(1)}|^3/_2,^1/_2\rangle =& 0 \\
\langle d_{z^2}|C_1^{(1)}|^3/_2,-^1/_2\rangle =& \langle 2,0|\langle\uparrow|\frac{1}{\sqrt{3}}\left(|1,-1\rangle|\uparrow\rangle + \sqrt{2}|1,0\rangle|\downarrow\rangle\right) \\
=& \frac{1}{\sqrt{3}}\langle\uparrow|\uparrow\rangle\langle 2,0|1,-1\rangle \\
=& \frac{1}{\sqrt{3}}\left(\frac{1}{\sqrt{3}\sqrt{5}}\right) = \frac{1}{3\sqrt{5}} \\
\langle d_{z^2}|C_1^{(1)}|^3/_2,-^3/_2\rangle =& 0 \\
\langle d_{z^2}|C_1^{(1)}|^1/_2,^1/_2\rangle =& 0 \\
\langle d_{z^2}|C_1^{(1)}|^1/_2,-^1/_2\rangle =& \langle 2,0|\langle\uparrow|\frac{1}{\sqrt{3}}\left(|1,0\rangle|\downarrow\rangle - \sqrt{2}|1,-1\rangle|\uparrow\rangle\right) \\
=& -\langle\uparrow|\uparrow\rangle\frac{\sqrt{2}}{\sqrt{3}}\langle 2,0|1,-1\rangle \\
=& -\frac{\sqrt{2}}{\sqrt{3}}\frac{1}{\sqrt{3}\sqrt{5}} = -\frac{\sqrt{2}}{3\sqrt{5}}
\end{aligned} \tag{A.14}$$

$$\mathbf{d_{xz}}:$$

$$\begin{aligned}
\langle d_{xz}|C_1^{(1)}|^3/_2,^3/_2\rangle =& 0\\
\langle d_{xz}|C_1^{(1)}|^3/_2,^1/_2\rangle =& \frac{1}{\sqrt{2}}\left(\langle\uparrow|\langle 2,1| + \langle\uparrow|\langle 2,-1|\right)\frac{1}{\sqrt{3}}\left(|1,1\rangle|\downarrow\rangle + \sqrt{2}|1,0\rangle|\uparrow\rangle\right)\\
=& \frac{1}{\sqrt{3}}\langle\uparrow|\uparrow\rangle\left(\langle 2,1|1,0\rangle\right)\\
=& \frac{1}{\sqrt{3}}\frac{1}{\sqrt{5}} = \frac{1}{\sqrt{3}\sqrt{5}}\\
\langle d_{xz}|C_1^{(1)}|^3/_2,-^1/_2\rangle =& 0\\
\langle d_{xz}|C_1^{(1)}|^3/_2,-^3/_2\rangle =& 0\\
\langle d_{xz}|C_1^{(1)}|^1/_2,^1/_2\rangle =& \frac{1}{\sqrt{2}}\left(\langle\uparrow|\langle 2,1| + \langle\uparrow|\langle 2,-1|\right)\frac{1}{\sqrt{3}}\left(|1,0\rangle|\uparrow\rangle - \sqrt{2}|1,1\rangle|\downarrow\rangle\right)\\
=& \frac{1}{\sqrt{2}\sqrt{3}}\langle\uparrow|\uparrow\rangle\langle 2,1|1,0\rangle\\
=& \frac{1}{\sqrt{2}\sqrt{3}\sqrt{5}}\\
\langle d_{xz}|C_1^{(1)}|^1/_2,-^1/_2\rangle =& 0
\end{aligned} \tag{A.15}$$

$$\mathbf{d_{yz}}:$$

$$\begin{aligned}
\langle d_{yz}|C_1^{(1)}|^3/_2,^3/_2\rangle =& 0\\
\langle d_{yz}|C_1^{(1)}|^3/_2,^1/_2\rangle =& \frac{1}{\sqrt{2}i}\left(\langle\uparrow|\langle 2,1| - \langle\uparrow|\langle 2,-1|\right)\frac{1}{\sqrt{3}}\left(|1,1\rangle|\downarrow\rangle + \sqrt{2}|1,0\rangle|\uparrow\rangle\right)\\
=& \frac{1}{\sqrt{3}i}\langle\uparrow|\uparrow\rangle\left(\langle 2,1|1,0\rangle\right)\\
=& \frac{1}{\sqrt{3}i}\frac{1}{\sqrt{5}} = \frac{1}{\sqrt{3}\sqrt{5}i}\\
\langle d_{yz}|C_1^{(1)}|^3/_2,-^1/_2\rangle =& 0\\
\langle d_{yz}|C_1^{(1)}|^3/_2,-^3/_2\rangle =& 0\\
\langle d_{yz}|C_1^{(1)}|^1/_2,^1/_2\rangle =& \frac{1}{\sqrt{2}i}\left(\langle\uparrow|\langle 2,1| - \langle\uparrow|\langle 2,-1|\right)\frac{1}{\sqrt{3}}\left(|1,0\rangle|\uparrow\rangle - \sqrt{2}|1,1\rangle|\downarrow\rangle\right)\\
=& \frac{1}{\sqrt{2}\sqrt{3}i}\langle\uparrow|\uparrow\rangle\langle 2,1|1,0\rangle\\
=& \frac{1}{\sqrt{2}\sqrt{3}\sqrt{5}i}\\
\langle d_{xz}|C_1^{(1)}|^1/_2,-^1/_2\rangle =& 0
\end{aligned} \tag{A.16}$$

$$
\begin{aligned}
&\mathbf{d_{x^2-y^2}}: \\
\langle d_{x^2-y^2}|C_1^{(1)}|^3/_2,^3/_2\rangle =& \frac{1}{\sqrt{2}}\left(\langle\uparrow|\langle 2,2|+\langle\uparrow|\langle 2,-2|\right)|1,1\rangle|\uparrow\rangle \\
=& \frac{1}{\sqrt{2}}\langle\uparrow|\uparrow\rangle\langle 2,2|1,1\rangle \\
=& \frac{1}{\sqrt{2}}\frac{\sqrt{2}}{\sqrt{5}} = \frac{1}{\sqrt{5}} \\
\langle d_{x^2-y^2}|C_1^{(1)}|^3/_2,^1/_2\rangle =& 0 \\
\langle d_{x^2-y^2}|C_1^{(1)}|^3/_2,-^1/_2\rangle =& 0 \\
\langle d_{x^2-y^2}|C_1^{(1)}|^3/_2,-^3/_2\rangle =& 0 \\
\langle d_{x^2-y^2}|C_1^{(1)}|^1/_2,^1/_2\rangle =& 0 \\
\langle d_{x^2-y^2}|C_1^{(1)}|^1/_2,-^1/_2\rangle =& 0
\end{aligned}
\tag{A.17}
$$

$$
\begin{aligned}
&\mathbf{d_{xy}}: \\
\langle d_{xy}|C_1^{(1)}|^3/_2,^3/_2\rangle =& \frac{1}{\sqrt{2}i}\left(\langle\uparrow|\langle 2,2|-\langle\uparrow|\langle 2,-2|\right)|1,1\rangle|\uparrow\rangle \\
=& \frac{1}{\sqrt{2}i}\langle\uparrow|\uparrow\rangle\langle 2,2|1,1\rangle \\
=& \frac{1}{\sqrt{2}i}\frac{\sqrt{2}}{\sqrt{5}} = \frac{1}{\sqrt{5}i} \\
\langle d_{xy}|C_1^{(1)}|^3/_2,^1/_2\rangle =& 0 \\
\langle d_{xy}|C_1^{(1)}|^3/_2,-^1/_2\rangle =& 0 \\
\langle d_{xy}|C_1^{(1)}|^3/_2,-^3/_2\rangle =& 0 \\
\langle d_{xy}|C_1^{(1)}|^1/_2,^1/_2\rangle =& 0 \\
\langle d_{xy}|C_1^{(1)}|^1/_2,-^1/_2\rangle =& 0
\end{aligned}
\tag{A.18}
$$

The interactions can be similarly written in the case of negatively circularly polarized light, shown below:

$$\mathbf{d_{z^2}}:$$

$$\begin{aligned}
\langle d_{z^2}|C^{(1)}_{-1}|^3/_2,^3/_2\rangle =& \langle 2,0|1,1\rangle\langle\uparrow|\uparrow\rangle \\
=& \frac{1}{\sqrt{3}\sqrt{5}} \\
\langle d_{z^2}|C^{(1)}_{-1}|^3/_2,^1/_2\rangle =& 0 \\
\langle d_{z^2}|C^{(1)}_{-1}|^3/_2,-^1/_2\rangle =& 0 \\
\langle d_{z^2}|C^{(1)}_{-1}|^3/_2,-^3/_2\rangle =& 0 \\
\langle d_{z^2}|C^{(1)}_{-1}|^1/_2,^1/_2\rangle =& 0 \\
\langle d_{z^2}|C^{(1)}_{-1}|^1/_2,-^1/_2\rangle =& 0
\end{aligned} \tag{A.19}$$

$$\mathbf{d_{xz}}:$$

$$\begin{aligned}
\langle d_{xz}|C^{(1)}_{-1}|^3/_2,^3/_2\rangle =& 0 \\
\langle d_{xz}|C^{(1)}_{-1}|^3/_2,^1/_2\rangle =& \frac{1}{\sqrt{2}}\left(\langle\uparrow|\langle 2,1| + \langle\uparrow|\langle 2,-1|\right)\frac{1}{\sqrt{3}}\left(|1,1\rangle|\downarrow\rangle + \sqrt{2}|1,0\rangle|\uparrow\rangle\right) \\
=& \frac{1}{\sqrt{3}}\langle\uparrow|\uparrow\rangle\left(\langle 2,-1|1,0\rangle\right) \\
=& \frac{1}{\sqrt{3}}\frac{1}{\sqrt{5}} = \frac{1}{\sqrt{3}\sqrt{5}} \\
\langle d_{xz}|C^{(1)}_{-1}|^3/_2,-^1/_2\rangle =& 0 \\
\langle d_{xz}|C^{(1)}_{-1}|^3/_2,-^3/_2\rangle =& 0 \\
\langle d_{xz}|C^{(1)}_{-1}|^1/_2,^1/_2\rangle =& \frac{1}{\sqrt{2}}\left(\langle\uparrow|\langle 2,1| + \langle\uparrow|\langle 2,-1|\right)\frac{1}{\sqrt{3}}\left(|1,0\rangle|\uparrow\rangle - \sqrt{2}|1,1\rangle|\downarrow\rangle\right) \\
=& \frac{1}{\sqrt{2}\sqrt{3}}\langle\uparrow|\uparrow\rangle\langle 2,-1|1,0\rangle \\
=& \frac{1}{\sqrt{2}\sqrt{3}\sqrt{5}} \\
\langle d_{xz}|C^{(1)}_{-1}|^1/_2,-^1/_2\rangle =& 0
\end{aligned} \tag{A.20}$$

$$
\begin{aligned}
&\mathbf{d_{yz}}: \\
\langle d_{yz}|C^{(1)}_{-1}|^3/_2,^3/_2\rangle =&0 \\
\langle d_{yz}|C^{(1)}_{-1}|^3/_2,^1/_2\rangle =&\frac{1}{\sqrt{2}i}\left(\langle\uparrow|\langle 2,1|-\langle\uparrow|\langle 2,-1|\right)\frac{1}{\sqrt{3}}\left(|1,1\rangle|\downarrow\rangle+\sqrt{2}|1,0\rangle|\uparrow\rangle\right) \\
=&-\frac{1}{\sqrt{3}i}\langle\uparrow|\uparrow\rangle\left(\langle 2,-1|1,0\rangle\right) \\
=&-\frac{1}{\sqrt{3}i}\frac{1}{\sqrt{5}}=-\frac{1}{\sqrt{3}\sqrt{5}i} \\
\langle d_{yz}|C^{(1)}_{-1}|^3/_2,-^1/_2\rangle =&0 \\
\langle d_{yz}|C^{(1)}_{-1}|^3/_2,-^3/_2\rangle =&0 \\
\langle d_{yz}|C^{(1)}_{-1}|^1/_2,^1/_2\rangle =&\frac{1}{\sqrt{2}i}\left(\langle\uparrow|\langle 2,1|-\langle\uparrow|\langle 2,-1|\right)\frac{1}{\sqrt{3}}\left(|1,0\rangle|\uparrow\rangle-\sqrt{2}|1,1\rangle|\downarrow\rangle\right) \\
=&-\frac{1}{\sqrt{2}\sqrt{3}i}\langle\uparrow|\uparrow\rangle\langle 2,-1|1,0\rangle \\
=&-\frac{1}{\sqrt{2}\sqrt{3}\sqrt{5}i} \\
\langle d_{xz}|C^{(1)}_{-1}|^1/_2,-^1/_2\rangle =&0
\end{aligned}
\tag{A.21}
$$

$$
\begin{aligned}
&\mathbf{d_{x^2-y^2}}: \\
\langle d_{x^2-y^2}|C^{(1)}_{-1}|^3/_2,^3/_2\rangle =&0 \\
\langle d_{x^2-y^2}|C^{(1)}_{-1}|^3/_2,^1/_2\rangle =&0 \\
\langle d_{x^2-y^2}|C^{(1)}_{-1}|^3/_2,-^1/_2\rangle =&\frac{1}{\sqrt{2}}\left(\langle\uparrow|\langle 2,2|+\langle\uparrow|\langle 2,-2|\right)\frac{1}{\sqrt{3}}\left(|1,-1\rangle|\uparrow\rangle+\sqrt{2}|1,0\rangle|\downarrow\rangle\right) \\
=&\frac{1}{\sqrt{2}\sqrt{3}}\langle 2,-2|1,-1\rangle\langle\uparrow|\uparrow\rangle \\
=&\frac{1}{\sqrt{2}\sqrt{3}}\frac{\sqrt{2}}{\sqrt{5}}=\frac{1}{\sqrt{3}\sqrt{5}} \\
\langle d_{x^2-y^2}|C^{(1)}_{-1}|^3/_2,-^3/_2\rangle =&0 \\
\langle d_{x^2-y^2}|C^{(1)}_{-1}|^1/_2,^1/_2\rangle =&0 \\
\langle d_{x^2-y^2}|C^{(1)}_{-1}|^1/_2,-^1/_2\rangle =&\frac{1}{\sqrt{2}}\left(\langle\uparrow|\langle 2,2|+\langle\uparrow|\langle 2,-2|\right)\frac{1}{\sqrt{3}}\left(|1,0\rangle|\downarrow\rangle-\sqrt{2}|1,-1\rangle|\uparrow\rangle\right) \\
=&-\frac{1}{\sqrt{2}\sqrt{3}}\langle\uparrow|\uparrow\rangle\sqrt{2}\langle 2,-2|1,-1\rangle \\
=&-\frac{\sqrt{2}}{\sqrt{3}\sqrt{5}}
\end{aligned}
\tag{A.22}
$$

$$
\begin{aligned}
&\mathbf{d_{xy}}: \\
\langle d_{xy}|C^{(1)}_{-1}|^3/_2,^3/_2\rangle =& 0 \\
\langle d_{xy}|C^{(1)}_{-1}|^3/_2,^1/_2\rangle =& 0 \\
\langle d_{xy}|C^{(1)}_{-1}|^3/_2,-^1/_2\rangle =& \frac{1}{\sqrt{2}i}\left(\langle\uparrow|\langle 2,2|-\langle\uparrow|\langle 2,-2|\right)\frac{1}{\sqrt{3}}\left(|1,-1\rangle|\uparrow\rangle+\sqrt{2}|1,0\rangle|\downarrow\rangle\right) \\
=& -\frac{1}{\sqrt{2}\sqrt{3}i}\langle 2,-2|1,-1\rangle\langle\uparrow|\uparrow\rangle \\
=& -\frac{1}{\sqrt{2}\sqrt{3}i}\frac{\sqrt{2}}{\sqrt{5}}=\frac{1}{\sqrt{3}\sqrt{5}i} \\
\langle d_{xy}|C^{(1)}_{-1}|^3/_2,-^3/_2\rangle =& 0 \\
\langle d_{xy}|C^{(1)}_{-1}|^1/_2,^1/_2\rangle =& 0 \\
\langle d_{xy}|C^{(1)}_{-1}|^1/_2,-^1/_2\rangle =& \frac{1}{\sqrt{2}i}\left(\langle\uparrow|\langle 2,2|-\langle\uparrow|\langle 2,-2|\right)\frac{1}{\sqrt{3}}\left(|1,0\rangle|\downarrow\rangle-\sqrt{2}|1,-1\rangle|\uparrow\rangle\right) \\
=& -\frac{1}{\sqrt{2}\sqrt{3}i}\langle\uparrow|\uparrow\rangle\sqrt{2}\langle 2,-2|1,-1\rangle \\
=& -\frac{\sqrt{2}}{\sqrt{3}\sqrt{5}i}
\end{aligned}
\tag{A.23}
$$

The intensity of the induced transitions from the $2p_{3/2}$ to the $3d$ states and the $2p_{1/2}$ to the $3d$ may now be determined. These transitions are, of course, the L^3 and L^2 edges, respectively. In the case of positively circularly polarized light, the intensities are:

$$
\begin{aligned}
I^+_{3/2} =& AR^2\sum|\langle d_i||C^{(1)}_1|^3/_2,m_j\rangle|^2 \\
=& AR^2\left(\frac{1}{5}+\frac{1}{5}+\frac{1}{15}+\frac{1}{15}+\frac{1}{45}\right) \\
=& \frac{5}{9}AR^2
\end{aligned}
\tag{A.24}
$$

$$
\begin{aligned}
I^+_{1/2} =& AR^2\sum|\langle d_i||C^{(1)}_1|^1/_2,m_j\rangle|^2 \\
=& AR^2\left(\frac{1}{30}+\frac{1}{30}+\frac{2}{45}\right) \\
=& \frac{1}{9}AR^2
\end{aligned}
\tag{A.25}
$$

while the intensities for negatively circularly polarized light are

$$\begin{aligned} I^{-}_{3/2} =& AR^2 \sum |\langle d_i||C^{(1)}_{-1}|^3/_2, m_j\rangle|^2 \\ =& AR^2 \left(\frac{1}{15}+\frac{1}{15}+\frac{1}{15}+\frac{1}{15}+\frac{1}{15}\right) \\ =& \frac{1}{3}AR^2 \end{aligned} \tag{A.26}$$

$$\begin{aligned} I^{-}_{1/2} =& AR^2 \sum |\langle d_i||C^{(1)}_{-1}|^1/_2, m_j\rangle|^2 \\ =& AR^2 \left(\frac{1}{30}+\frac{1}{30}+\frac{2}{15}+\frac{2}{15}\right) \\ =& \frac{1}{3}AR^2 \end{aligned} \tag{A.27}$$

and the dichroism is determined by the difference in L^3 and L^2 intensity for positive and negative photon helicity.

$$\begin{aligned} XMCD_{L^3} &= I^{+}_{3/2} - I^{-}_{1/2} = \frac{2}{9}AR^2 \\ XMCD_{L^2} &= I^{+}_{3/2} - I^{-}_{1/2} = -\frac{2}{9}AR^2 \end{aligned} \tag{A.28}$$

Thus, the dichroism on the L^3 and L^2 edges is equal in magnitude but opposite in sign. Through this example, it can be seen that the X-ray magnetic circular dichroism effect originates in two separate effects. The spin-splitting of the final state allows detection of the spin state of the excited electrons by introducing a spin-dependent density of states. In the example shown, this is manifested as $|\uparrow\rangle$ states exclusively appearing in the transfer matrix element. Equally important is the spin-orbit coupling of the initial state. It is the spin orbit coupling that separates the L^3 and L^2 edges in energy. The spin-orbit coupling is also responsible for creating a difference in the probability of exciting a spin up electron, as the spin-state becomes correlated with the orbital moment, and the orbital moment determines the allowed transitions through the selection rules.

A.3 Sum Rules

In the previous section it was noted that the magnitude of the X-ray magnetic circular dichroism effect is expected to be equal and opposite on the L^3 and L^2 edges. In practice, this is not always the case. In addition to using the total magnitude of the dichroism to determine the magnitude of the spin magnetic moment, it is possible to determine the magnitude of the orbital contribution from the difference in L^3 and L^2 dichroism. The spin and orbital sum rules, as written by Stohr are[141]

$$m_s = \frac{\mu_B}{C}\left(-XMCD_{L^3} + 2XMCD_{L^2}\right) \tag{A.29}$$

$$m_l = -\frac{2}{3}\frac{\mu_B}{C}\left(XMCD_{L^3} + XMCD_{L^2}\right) \tag{A.30}$$

where XMCD is the dichroism associated with a particular absorption edge. Although the choice of the edge to which a negative dichroism is assigned is arbitrary, convention defined the L^3 dichroism as negative and the L^2 as positive. Therefore the orbital moment is proportional to the difference in magnitudes while the spin moment is proportional to the sum of the dichroism magnitudes. C is a constant defined by Stohr as[141]

$$C = \frac{4\pi^2\hbar\omega}{137}R^2\frac{L}{3(2L+1)} \tag{A.31}$$

Alternatively, it is possible to use the intensity of the absorption edge to determine C for a given experiment. According to the charge sum rule[141]

$$I = CN_h \tag{A.32}$$

where N_h is the number of holes in the final valence state. Therefore it is possible to apply the X-ray magnetic circular dichroism sum rules through a careful normalization of the X-ray absorption spectra.[3] In order to obtain the proper normalization, it is first necessary to subtract the step function absorption associated with passing through an absorption edge. Therefore, beginning with an X-ray absorption spectrum taken using an unpolarized beam, the following correction must be made[3]

$$I_{new}(E_{photon}) = I_{raw}(E_{photon}) - I_{step}(E_{photon}) \tag{A.33}$$

$$I_{step}(E_{photon}) = \frac{2}{3}\left(0.5 + 0.5Erf\left(\frac{E-E_3}{W_{L^3}}\right)\right) + \frac{1}{3}\left(0.5 + 0.5Erf\left(\frac{E-E_2}{W_{L^@}}\right)\right) - c \tag{A.34}$$

where E_3 and E_2 are the energies of the inflection points on the rising edge of the L^3 and L^2 absorption edges and W is the width of the associated absorption edge. The relative heights of the step functions mirror the relative heights of the edge intensities. c is the background or constant offset in the absorption data. It is often necessary to measure absorption in a large region on either side of the edges and fit a straight line to this background. After such a background subtraction, the absorption data should be relatively flat with respect to energy and is ready for step function subtraction. Once the normalization has been performed, the dichroism may be determined by[3]

$$m_s = \frac{1}{Pcos(\phi)}N_h\frac{XMCD_{L3} + 2XMCD_{L2}}{A_{L3} + A_{L2}} \tag{A.35}$$

$$m_s = \frac{2}{3Pcos(\phi)}N_h\frac{XMCD_{L3} - XMCD_{L2}}{A_{L3} + A_{L2}} \tag{A.36}$$

where P is the fractional polarization of the incoming beam and allows for the realistic condition of imperfect beam polarization. ϕ is the angle between the X-ray polarization and magnetization direction. This is usually 0, but corrections for other cases may now be made.

It is obvious that these background subtractions are imprecise and therefore extreme caution must be used before applying the sum rules for X-ray magnetic circular dichroism. Any minor error may drastically alter the magnitudes of the extracted moments. In particular, situations in which the X-ray absorption edges are weak or include significant drift may not provide enough statistics to accurately determine the moments. In these cases, it is sometimes useful to determine the much more robust parameter of the orbital-spin magnetic moment ratio.

$$\frac{m_l}{m_s} = \frac{2}{3}\frac{XMCD_{L3} - XMCD_{L2}}{XMCD_{L3} + XMCD_{L2}} \tag{A.37}$$

A complete derivation of the sum rules discussed throughout this section is highly involved and not included here. However, the reader is encouraged to consult Stohr and Konig, Carra et al., and Thole et al.[140, 18, 147]

Appendix B

Strain in Epitaxial Thin Films

B.1 Stress/Strain Notation

Throughout this dissertation, an important theme has been the effect of different distortion symmetries imposed by substrates of varying orientations on the magnetic properties of films. In order to better understand these distortions, this section will explicitly describe the stresses imposed by (100), (110), and (111) oriented substrates and utilize the compliance tensor to translate these into the resulting strains for a cubic system. Although the majority of the systems described in this work are orthorhombically distorted from the ideal cubic system, in most cases the distortion is minor and this formalism represents an excellent starting point in understanding the final symmetry of the system. For a much more complete description of stress and strain in materials, we recommend consulting the book by Nye, which was used extensively as a reference for this section.[113]

It is well known that stress may be described by a rank two tensor, the 3×3 matrix

$$\sigma = \begin{pmatrix} \sigma_{11} & \sigma_{12} & \sigma_{13} \\ \sigma_{21} & \sigma_{22} & \sigma_{23} \\ \sigma_{31} & \sigma_{32} & \sigma_{33} \end{pmatrix} \tag{B.1}$$

where we have defined principal axes 1, 2, and 3 so that they correspond any arbitrary set of orthogonal basis vectors describing the system. In general, we will select these to be to the (100), (010), and (001) directions of our structure for convenience. If we define the stress as the force per unit area applied to plane i along axis j, we will see two different categories of stresses appear. These categories are the normal stresses, σ_{ik} where i = j, and the shear stresses, σ_{ij} where i ≠ j. Normal stresses are applied (unsurprisingly) in the direction of the plane normal, while shear stresses are applied in the plane.

Similarly, we can define the strain in a system as

$$\epsilon = \begin{pmatrix} \epsilon_{11} & \epsilon_{12} & \epsilon_{13} \\ \epsilon_{21} & \epsilon_{22} & \epsilon_{23} \\ \epsilon_{31} & \epsilon_{32} & \epsilon_{33} \end{pmatrix} \tag{B.2}$$

where ϵ_{ij} is the displacement of a reference point in the crystal normalized to a reference length, typically the crystal lattice parameter in the i^{th} direction.

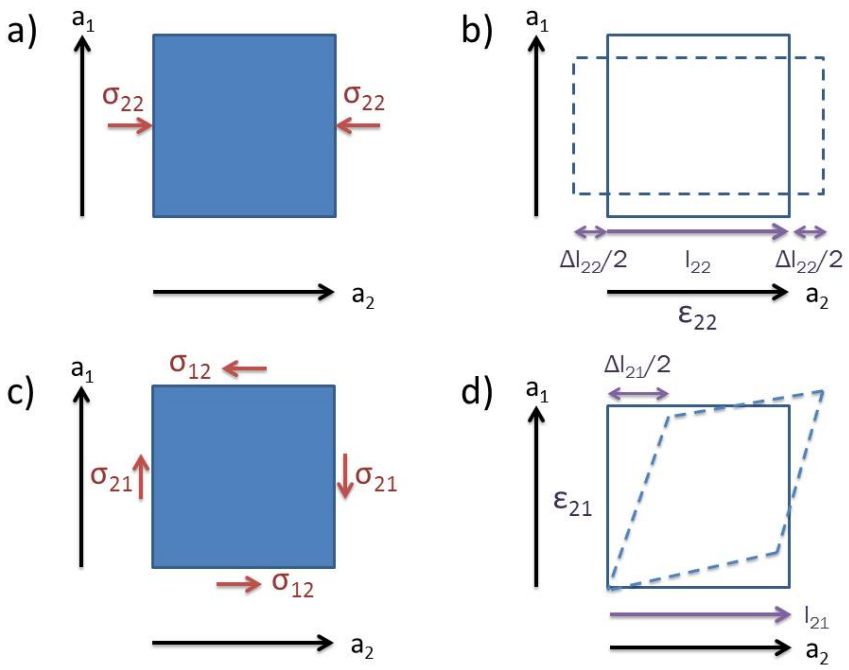

Figure B.1: a) Normal stress b) Normal strain c) Shear stress d) Shear strain

$$\epsilon_{ij} = \frac{\Delta l_i}{l_j} \tag{B.3}$$

As in the case of stress, two types of strain clearly emerge - normal strain and shear strain. Figure B.1 illustrates normal sress and strain as well as shear stress and strain. Although this model has many parameters to keep track of, it can be simplified somewhat by remembering that stress and strain are concerned only with static deformations rather than forces which produce an acceleration or rotation. Thus it becomes clear that, the stress and strain tensors must be symmetric about the diagonal elements so that

$$\sigma = \begin{pmatrix} \sigma_{11} & \sigma_{12} & \sigma_{13} \\ \sigma_{12} & \sigma_{22} & \sigma_{23} \\ \sigma_{13} & \sigma_{23} & \sigma_{33} \end{pmatrix} \tag{B.4}$$

and

$$\epsilon = \begin{pmatrix} \epsilon_{11} & \epsilon_{12} & \epsilon_{13} \\ \epsilon_{12} & \epsilon_{22} & \epsilon_{23} \\ \epsilon_{13} & \epsilon_{23} & \epsilon_{33} \end{pmatrix} \tag{B.5}$$

It is tempting to assume that a single strain σ_{ij} will lead only to a single associated stress ϵ_{ij}, if only because everything would be so much simpler. Sadly, however, it is well known that a even single normal stress will, in a cubic crystal, lead to normal strains along all three directions. For example, a compression of the c-axis will lead to expansion along the a and b-axes. Thus, the stress and strain matrices are actually related by a rank four tensor, called

the C_{ijkl}. For sufficiently small strains, it is generally assumed that Hooke's law applies and there is a linear relationship between stress and strain so that we may write

$$\epsilon_{ij} = C_{ijkl}\sigma_{kl} \tag{B.6}$$

At the small strains that are typically applied in heteroexpitaxy ($\leq 2\%$) this equation is usually applicable. Fortunately, the difficulty in visualizing and interacting with the compliance tensor has lead to a number of tricks which exploit the inherent symmetries of the stress, strain, and crystal structure. For example, in a completely isotropic system the compliance tensor can be reduced to the bulk modulus and the shear modulus. More generally, however, it is typical to take advantage of symmetry to rewrite the stress and strain as vectors and the compliance tensor as a second rank tensor, so that

$$\begin{pmatrix} \sigma_{11} & \sigma_{12} & \sigma_{13} \\ \sigma_{12} & \sigma_{22} & \sigma_{23} \\ \sigma_{13} & \sigma_{23} & \sigma_{33} \end{pmatrix} = \begin{pmatrix} \sigma_1 & \sigma_6 & \sigma_5 \\ \sigma_6 & \sigma_2 & \sigma_4 \\ \sigma_5 & \sigma_4 & \sigma_3 \end{pmatrix} \tag{B.7}$$

and

$$\begin{pmatrix} \epsilon_{11} & \epsilon_{12} & \epsilon_{13} \\ \epsilon_{12} & \epsilon_{22} & \epsilon_{23} \\ \epsilon_{13} & \epsilon_{23} & \epsilon_{33} \end{pmatrix} = \begin{pmatrix} \epsilon_1 & \frac{1}{2}\epsilon_6 & \frac{1}{2}\epsilon_5 \\ \frac{1}{2}\epsilon_6 & \epsilon_2 & \frac{1}{2}\epsilon_4 \\ \frac{1}{2}\epsilon_5 & \frac{1}{2}\epsilon_4 & \epsilon_3 \end{pmatrix} \tag{B.8}$$

then finally we can rewrite Hooke's law as

$$\begin{pmatrix} \epsilon_1 \\ \epsilon_2 \\ \epsilon_3 \\ \epsilon_4 \\ \epsilon_5 \\ \epsilon_6 \end{pmatrix} = \begin{pmatrix} C_{11} & C_{12} & C_{13} & C_{14} & C_{15} & C_{16} \\ C_{21} & C_{22} & C_{23} & C_{24} & C_{25} & C_{26} \\ C_{31} & C_{32} & C_{33} & C_{34} & C_{35} & C_{36} \\ C_{41} & C_{42} & C_{43} & C_{44} & C_{45} & C_{46} \\ C_{51} & C_{52} & C_{53} & C_{54} & C_{55} & C_{56} \\ C_{61} & C_{62} & C_{63} & C_{64} & C_{65} & C_{66} \end{pmatrix} \begin{pmatrix} \sigma_1 \\ \sigma_2 \\ \sigma_3 \\ \sigma_4 \\ \sigma_5 \\ \sigma_6 \end{pmatrix} \tag{B.9}$$

finally, by exploiting the cubic symmetry of the crystal, the compliance tensor can be rewritten as

$$\begin{pmatrix} \epsilon_1 \\ \epsilon_2 \\ \epsilon_3 \\ \epsilon_4 \\ \epsilon_5 \\ \epsilon_6 \end{pmatrix} = \begin{pmatrix} C_{11} & C_{12} & C_{12} & 0 & 0 & 0 \\ C_{12} & C_{11} & C_{12} & 0 & 0 & 0 \\ C_{12} & C_{12} & C_{11} & 0 & 0 & 0 \\ 0 & 0 & 0 & C_{44} & 0 & 0 \\ 0 & 0 & 0 & 0 & C_{44} & 0 \\ 0 & 0 & 0 & 0 & 0 & C_{44} \end{pmatrix} \begin{pmatrix} \sigma_1 \\ \sigma_2 \\ \sigma_3 \\ \sigma_4 \\ \sigma_5 \\ \sigma_6 \end{pmatrix} \tag{B.10}$$

It is now possible to calculate the strain imposed by various substrate orientations.

B.2 (100) Oriented substrates

We will begin with substrates in the (100) orientation. Assuming heteroepitaxy, we find that the strain that will be applied is

$$\sigma = \begin{pmatrix} 0 & 0 & 0 \\ 0 & \sigma_0 & 0 \\ 0 & 0 & \sigma_0 \end{pmatrix} \tag{B.11}$$

yielding a Hooke's law equation of

$$\begin{pmatrix} \epsilon_1 \\ \epsilon_2 \\ \epsilon_3 \\ \epsilon_4 \\ \epsilon_5 \\ \epsilon_6 \end{pmatrix} = \begin{pmatrix} C_{11} & C_{12} & C_{12} & 0 & 0 & 0 \\ C_{12} & C_{11} & C_{12} & 0 & 0 & 0 \\ C_{12} & C_{12} & C_{11} & 0 & 0 & 0 \\ 0 & 0 & 0 & C_{44} & 0 & 0 \\ 0 & 0 & 0 & 0 & C_{44} & 0 \\ 0 & 0 & 0 & 0 & 0 & C_{44} \end{pmatrix} \begin{pmatrix} 0 \\ \sigma_0 \\ \sigma_0 \\ 0 \\ 0 \\ 0 \end{pmatrix} \tag{B.12}$$

so the strain vector is

$$\epsilon = \begin{pmatrix} 2\sigma_0 C_{12} \\ \sigma_0(C_{11} + C_{12}) \\ \sigma_0(C_{11} + C_{12}) \\ 0 \\ 0 \\ 0 \end{pmatrix} \tag{B.13}$$

and the strain tensor is

$$\begin{pmatrix} 2\sigma_0 C_{12} & 0 & 0 \\ 0 & \sigma_0(C_{11} + C_{12}) & 0 \\ 0 & 0 & \sigma_0(C_{11} + C_{12}) \end{pmatrix} \tag{B.14}$$

This matrix can easily be separated into a volume expansion/contraction and a volume preserving tetragonal distortion

$$\epsilon = \frac{\sigma_0}{3}(4C_{12} + 2C_{11}) \begin{pmatrix} 1 & 0 & 0 \\ 0 & 1 & 0 \\ 0 & 0 & 1 \end{pmatrix} + \frac{\sigma_0}{3}(C_{12} - C_{11}) \begin{pmatrix} 2 & 0 & 0 \\ 0 & -1 & 0 \\ 0 & 0 & -1 \end{pmatrix} \tag{B.15}$$

Therefore we can see that a (100) oriented substrate is expected to yield a volume change and a tetragonal distortion of the film.

B.3 (110) Oriented Substrates

A film grown on a (110) oriented substrate will experience strain along the $[1\bar{1}0]$ and [001] in-plane directions. If we still define our principal directions as (100), (010), and (001), we must decompose the stress in the $[1\bar{1}0]$ direction into it's composite components. Not only is the $(1\bar{1}0)$ plane at a 45° angle to the (100) and (010) planes, but so is the stress. This results in a combination of normal and shear stresses such that, if we define $\sigma_{(1\bar{1}0)} = 2\sigma_0$ and $\sigma_{(001)} = \sigma_1$ we find a stress tensor of

$$\sigma = \begin{pmatrix} \sigma_0 & -\sigma_0 & 0 \\ -\sigma_0 & \sigma_0 & 0 \\ 0 & 0 & \sigma_1 \end{pmatrix} \tag{B.16}$$

We can determine the resulting strain using

$$\begin{pmatrix} \epsilon_1 \\ \epsilon_2 \\ \epsilon_3 \\ \epsilon_4 \\ \epsilon_5 \\ \epsilon_6 \end{pmatrix} = \begin{pmatrix} C_{11} & C_{12} & C_{12} & 0 & 0 & 0 \\ C_{12} & C_{11} & C_{12} & 0 & 0 & 0 \\ C_{12} & C_{12} & C_{11} & 0 & 0 & 0 \\ 0 & 0 & 0 & C_{44} & 0 & 0 \\ 0 & 0 & 0 & 0 & C_{44} & 0 \\ 0 & 0 & 0 & 0 & 0 & C_{44} \end{pmatrix} \begin{pmatrix} \sigma_0 \\ \sigma_0 \\ \sigma_1 \\ 0 \\ 0 \\ -\sigma_0 \end{pmatrix} \tag{B.17}$$

which yields

$$\begin{aligned} \epsilon_1 =& \sigma_0(C_{11} + C_{12}) + \sigma_1 C_{12} \\ \epsilon_2 =& \sigma_0(C_{11} + C_{12}) + \sigma_1 C_{12} \\ \epsilon_3 =& \sigma_0(2C_{12}) + \sigma_1 C_{11} \\ \epsilon_4 =& -\sigma_0 C_{44} \end{aligned} \tag{B.18}$$

So now we may construct the strain matrix

$$\begin{pmatrix} \sigma_0(C_{11} + C_{12}) + \sigma_1 C_{12} & -\frac{1}{2}\sigma_0 C_{44} & 0 \\ -\frac{1}{2}\sigma_0 C_{44} & \sigma_0(C_{11} + C_{12}) + \sigma_1 C_{12} & 0 \\ 0 & 0 & \sigma_0(2C_{12}) + \sigma_1 C_{11} \end{pmatrix} \tag{B.19}$$

which we alternatively write

$$\begin{pmatrix} \epsilon_{11} & \epsilon_{12} & 0 \\ \epsilon_{12} & \epsilon_{11} & 0 \\ 0 & 0 & \epsilon_{33} \end{pmatrix} \tag{B.20}$$

We can easily see that this will have the same volume change and tetragonal distortion components of the (100) orientation, plus the following pure shear contribution:

$$\epsilon_{Shear} = \begin{pmatrix} 0 & \epsilon_{12} & 0 \\ \epsilon_{12} & 0 & 0 \\ 0 & 0 & 0 \end{pmatrix} \tag{B.21}$$

Substrates in the (110) orientation therefore induce a volume expansion/contraction, a tetragonal distortion, and a shear strain.

B.4 (111) Oriented Substrates

Finally, we turn our attention to films on (111) oriented substrates. The principal stresses induced by (111) oriented substrates may be decomposed into principal stresses along any

two orthogonal in-plane directions, and it is most convenient to choose the $[\bar{1}\bar{1}2]$ and $[\bar{1}10]$ directions. Since the transformation of this strain into a [100], [010], [001] system is highly tedious rather than instructive, we shall simply look up the answer and find that the resulting stress may be expressed as

$$\sigma = \begin{pmatrix} 2\sigma_0 & -\sigma_0 & -\sigma_0 \\ -\sigma_0 & 2\sigma_0 & -\sigma_0 \\ -\sigma_0 & -\sigma_0 & 2\sigma_0 \end{pmatrix} \tag{B.22}$$

The entire stress-strain relationship may therefore be written as

$$\begin{pmatrix} \epsilon_1 \\ \epsilon_2 \\ \epsilon_3 \\ \epsilon_4 \\ \epsilon_5 \\ \epsilon_6 \end{pmatrix} = \begin{pmatrix} C_{11} & C_{12} & C_{12} & 0 & 0 & 0 \\ C_{12} & C_{11} & C_{12} & 0 & 0 & 0 \\ C_{12} & C_{12} & C_{11} & 0 & 0 & 0 \\ 0 & 0 & 0 & C_{44} & 0 & 0 \\ 0 & 0 & 0 & 0 & C_{44} & 0 \\ 0 & 0 & 0 & 0 & 0 & C_{44} \end{pmatrix} \begin{pmatrix} 2\sigma_0 \\ 2\sigma_0 \\ 2\sigma_0 \\ -\sigma_0 \\ -\sigma_0 \\ -\sigma_0 \end{pmatrix} \tag{B.23}$$

The strains, therefore, are

$$\begin{aligned} \epsilon_1 =& 2\sigma_0 C_{11} + 4\sigma_0 C_{12} \\ \epsilon_2 =& 2\sigma_0 C_{11} + 4\sigma_0 C_{12} \\ \epsilon_3 =& 2\sigma_0 C_{11} + 4\sigma_0 C_{12} \\ \epsilon_4 =& -\sigma_0 C_{44} \\ \epsilon_5 =& -\sigma_0 C_{44} \\ \epsilon_6 =& -\sigma_0 C_{44} \end{aligned} \tag{B.24}$$

which strongly suggests that we define

$$\begin{aligned} \epsilon_{11} =& 2\sigma_0 C_{11} + 4\sigma_0 C_{12} \\ \epsilon_{12} =& -\frac{1}{2}\sigma_0 C_{44} \end{aligned} \tag{B.25}$$

and write the strain matrix as

$$\begin{pmatrix} \epsilon_{11} & \epsilon_{12} & \epsilon_{12} \\ \epsilon_{12} & \epsilon_{11} & \epsilon_{12} \\ \epsilon_{12} & \epsilon_{12} & \epsilon_{11} \end{pmatrix} \tag{B.26}$$

From this rewrite, it is obvious that (111) oriented substrates induce a volume expansion or contraction and have a pure shear component. However, because all of the diagonal elements are identical, there is no tetragonal or orthorhombic distortion induced in the film.